Charge and Thermoelectric Transport in Semicrystalline Conjugated Polymers and Single-Walled Carbon Nanotube Networks

Martin Statz
Churchill College
University of Cambridge

This thesis is submitted for the degree of
Doctor of Philosophy
September 2020

In memory of my loving mother
and
to my supporting and loving father, fiancée and family.

Declaration

This thesis is the result of my own work and includes nothing which is the outcome of work done in collaboration except as outlined in the preface and specified in the text and captions.
It is not substantially the same as any that I have submitted, or, is being concurrently submitted for a degree, diploma or other qualification at the University of Cambridge or any other University or similar institution except as declared in the preface and specified in the text. I further state that no substantial part of my dissertation has already been submitted, or, is being concurrently submitted for any such degree, diploma or other qualification at the University of Cambridge or any other University of similar institution except as declared in the preface and specified in the text.
The thesis does not exceed the prescribed word limit of 60,000 words, including abstract, tables, footnotes and appendices.

Martin Statz,
4 December 2020

Martin Statz

Abstract:

Charge and Thermoelectric Transport in Semicrystalline Conjugated Polymers and Single-Walled Carbon Nanotube Networks

Due to their flexibility, solution-processability and continuously improving electronic performance, conjugated polymer semiconductors and single-walled carbon nanotube (SWCNT) networks are promising candidates for wearable electronics, flexible optoelectronic devices and thermoelectric generators. In the past two decades the development of high-mobility donor-acceptor copolymers outperforming amorphous silicon, employed in commercial display technologies, and the ability to tune the diameter distribution in SWCNT networks via selective dispersion with conjugated polymers and other sorting methods have been major breakthroughs for these material systems.

This thesis provides an improved understanding of their charge and thermoelectric transport. In particular, the charge density and temperature dependence of their field-effect mobility and gated Seebeck coefficient are investigated. When a temperature difference is applied to a conducting system, a thermal voltage builds up as a response. The Seebeck coefficient is the ratio of the thermal voltage to the temperature difference and characterizes the entropy transported by a carrier divided by its charge. Consequently, it offers insights into the transport energetics and the density of states (DoS). It can be used to identify the prevailing transport mechanisms, such as phonon-assisted hopping between localized states or scattering-limited transport through delocalized states, scattering mechanisms and carrier-carrier interactions as well as the extent of charge carrier trapping.

Firstly, it is demonstrated that charge transport in semicrystalline high-mobility copolymers is incompatible with disorder-based transport models that were developed for preceding, more disordered polymers. Instead the charge density and temperature

dependence of the field-effect mobility and gated Seebeck coefficient of the semicrystalline n-type polymer P(NDI2OD-T2) with varying degrees of crystallinity provides direct evidence for low-disorder, narrow-band conduction. The inclusion of short-range electron-electron interactions and the consideration of a spatially inhomogeneous DoS allow to explain both the measured mobility and Seebeck coefficient. These findings outline the extension of crystalline domains as a mean for improved thermoelectric conversion efficiencies.

Subsequently, the charge density and temperature-dependent field-effect mobility and gated Seebeck coefficient of polymer-sorted monochiral small diameter (6,5) (0.76 nm) and mixed large diameter SWCNT (1.17-1.55 nm) networks with different network densities and length distributions are reported. It is shown that charge and thermoelectric transport in SWCNT networks can be modelled by the Boltzmann transport formalism incorporating transport in heterogeneous media and fluctuation-induced tunneling. The charge density and temperature dependence of the Seebeck coefficient can be simulated via the consideration of the diameter-dependent one-dimensional DoS of the SWCNTs composing the network. Due to the carrier relaxation time being anti-proportional to energy, the simulations further point towards a more two-dimensional character of scattering, as opposed to one-dimensional acoustic and optical phonon scattering in single SWCNTs, as well as the potential necessity to consider scattering at SWCNT junctions. Trap-free, narrow DoS distribution, large diameter SWCNT networks, allowing low tunnel barriers and a large thermally accessible DoS, are proposed for both electronic and thermoelectric applications.

Finally, the thermoelectric performance of the molecularly doped semicrystalline polymer PBTTT is presented in the high charge density limit, which is relevant for applications in thermoelectric generators. Using the recently reported ion-exchange doping routine charge densities on the order of one carrier per monomer repeat unit can be obtained, allowing to attain a highly conductive system. Ongoing investigations of the impact of polymer alignment on charge and thermoelectric transport in this regime are presented.

Acknowledgements

The results presented in this PhD thesis are the outcomes of my work during the past four years, starting in October 2016, in the Optoelectronics Group of the Cavendish Laboratory, University of Cambridge. It goes without saying that this work would not have been possible without the collaboration with and support of many respectable people, who I would like to acknowledge here.

Firstly, I would like to thank my supervisor Prof. Henning Sirringhaus for giving me the opportunity to conduct research in his group. Henning and I had many fruitful scientific discussions during the course of my PhD and his attentive attitude always had a positive impact on my progress and research projects. He gave me the freedom to explore new project ideas and offered support as well as encouragement in difficult parts of research projects. Furthermore, I would like to thank him for the financial support I received through one of his research grants from the European Research Council. Concomitantly, I would like to thank the Engineering and Physical Science Research Council for the support via an EPSRC studentship.

I would also like to thank my colleagues and collaborators for their contributions and the positive impact they made on my time during my PhD. I am particularly thankful to Dr. Riccardo Di Pietro, who has been like a second supervisor to me for the work relating to semicrystalline conjugated polymers. Our collaboration started already during my Masters thesis for my MSc degree from ETH Zürich, for which I worked between November 2015 and July 2016 in the group. I had the chance to engage in many scientific discussions with him and am grateful for the introductions he gave me to many experimental techniques when I commenced working in the lab. Furthermore, I would like to thank Dr. Deepak Venkateshvaran for introducing me to the field-effect-modulated Seebeck coefficient measurements, showing me the patterning process of the organic layers and allowing me to employ his device architecture for the first project on charge and thermoelectric transport in semicrystalline conjugated polymers presented

in this thesis. For the same project I would like to acknowledge Dr. Sam Schott for preparing the samples for grazing incidence wide-angle X-ray scattering (GIWAXS) measurements. Sam has been a great colleague, is a good friend of mine and we had many enjoyable scientific and non-scientific discussions in and outside the lab. The GIWAXS measurements for both this and the project of molecularly doped, aligned semicrystalline polymers were performed by Dr. Xuechen Jiao and Prof. Chris McNeill from the Monash University in Australia at the Australian Synchrotron. In addition, I would like to thank Adj. Prof. David Emin from the University of New Mexico as well as Riccardo and Henning, for their support in developing the theoretical model discussed in chapter 4.

I would like to thank Dr. Mark Nikolka for giving me the opportunity to continue working on his efforts towards molecularly doped SWCNT networks, which gave me the chance to collaborate with Prof. Jana Zaumseil's group at the University of Heidelberg. For the project on charge and thermoelectric transport in SWCNT networks presented in chapter 5, I would like to thank Severin Schneider and Felix Berger from Jana's group, who have fabricated the thermoelectric devices based on my improved device architecture and performed the optical and structural characterization of the SWCNT networks. For this project I would also like to acknowledge William Wood, who has written the drivers for the measurement electronics employed for the electric and thermoelectric characterization and provided support with the implementation of the Java code for the measurement routines. Furthermore, Dr. Mojtaba Abdi-Jalebi has contributed to the project through photothermal deflection spectroscopy measurements as well as Simone Leingang and Prof. Hans-Jörg Himmel from the University of Heidelberg with the synthesis of ttmgb molecules.

For the ongoing investigations on the impact of polymer-chain alignment on charge and thermoelectric transport of molecularly doped, aligned conjugated polymers, I would like to acknowledge the Heeney group at Imperial College London for the synthesis of PBTTT-C_{12}. Furthermore, I would like to thank Yuxuan Huang and Dr. Ian Jacobs for fabricating the thermoelectric devices based on my improved device design, as well as for their optical characterization of the aligned PBTTT films and their preparation of GIWAXS samples.

In addition, I would like to thank Dimitrios Simatos for his significant efforts towards improving the operational state of lab equipment. In line with this I would like to acknowledge Dr. Radoslav Chakalov for his great maintenance of the lab equipment, as well as Roger Beadle and Tom Sharp for their support with the installation of the Lake Shore Cryotronics Inc. CRX-4K closed-cycle cryogenic probe station.

I would also like to very much acknowledge and thank my friends in and outside of the 'Cambridge bubble', who have contributed to my great experience here. Playing together with Mark for the Churchill College badminton club for several years has been a lot of fun and spending many fun cooking, formal dinner and board game evenings with Sam, Angela, Swastika, Surabhi, Chiara and particularly my fiancée Aditi has been really nice. Further, I would like to give special thanks to my school and university friends Jurek, Markus, Max and Matthias for their great friendships and support.
It most certainly has been the most invaluable experience of my time in Cambridge to meet my fiancée Aditi and I am deeply thankful for her coming into my life. I would like to thank her for her endless love and support, for all the great times we had during my PhD and for her cheerful attitude that always fills me with happiness and a smile.
Last but not least I would like to thank my loving and supporting father, brother and entire family. It has been a great journey with many ups and downs since I left my hometown Aachen nine years ago to commence my studies at ETH Zürich and I am deeply grateful for them always being there for me.

Martin Statz,
29 September 2020

Contents

Abstract **v**

Acknowledgements **vii**

1 Introduction **1**

1.1 Electronic and thermoelectric applications 1

1.2 Organic semiconductors 7

1.2.1 Electronic structure 7

1.2.2 Conjugated polymers 9

1.3 Single-walled carbon nanotubes 12

1.3.1 Structural properties and electronic structure 12

1.3.2 Synthesis and sorting techniques 19

1.4 Thin-film transistors 22

2 Background and theory **29**

2.1 Charge transport in organic semiconductors 29

2.1.1 Disorder-based transport models for conjugated polymers 32

2.1.2 Narrow-band transport in high-mobility conjugated copolymers . 36

2.2 Charge transport in SWCNT networks 39

2.2.1 Transport in single SWCNTs 39

2.2.2 Disorder-based and heterogeneous transport models for SWCNT networks 41

2.3 The Seebeck coefficient 44

2.3.1 The Seebeck coefficient from Boltzmann transport equation . . . 48

2.3.2 The Seebeck coefficient in organic semiconductors 51

2.3.3 The Seebeck coefficient in SWCNT networks 55

3 Experimental methods **57**
3.1 Materials and dispersions 57
3.1.1 Conjuated polymers, small molecules and SWCNTs 57
3.1.2 SWCNT dispersions 59
3.1.3 Dielectrics 59
3.2 Fabrication of thermoelectric devices 60
3.2.1 Conjugated polymer-based gated Seebeck devices 60
3.2.2 SWCNT network-based gated Seebeck devices 61
3.2.3 Multifunctional devices for conducting material systems 63
3.3 Electric and thermoelectric characterization 65
3.3.1 Measurement routines 65
3.3.2 Error analysis and accurate Seebeck coefficient measurements . . 79
3.4 Structural characterization 82
3.4.1 Atomic force microscopy 82
3.4.2 Grazing incidence wide-angle X-ray scattering 82
3.5 Optical characterization 82
3.5.1 Absorbance measurements 82
3.5.2 Raman spectroscopy 83
3.5.3 Photothermal deflection spectroscopy 83

4 Charge and thermoelectric transport in low-disorder, semicrystalline conjugated polymers **85**
4.1 Motivation and outline 86
4.2 Thermoelectric transport in the non-degenerate regime 88
4.3 Structural characterization 90
4.4 Electric and thermoelectric characterization 92
4.5 Evidence of low-disorder narrow-band conduction 95
4.6 Modelling transport with the inclusion of electron-electron interactions . 105
4.7 Conclusions 114

5 Charge and thermoelectric transport in polymer-sorted semiconducting SWCNT networks **115**
5.1 Motivation and outline 116
5.2 SWCNT network characterization 118
5.3 Electric and thermoelectric characterization at 300 K 123
5.4 Fluctuation-induced tunneling in SWCNT networks 128
5.5 Temperature-dependent thermoelectric transport in SWCNT networks . 133

5.6 Implications for SWCNT network FETs and thermoelectrics 143
5.7 Conclusions 145

6 Charge and thermoelectric transport in molecularly doped, aligned conducting polymers 147
6.1 Motivation and outline 147
6.2 Optical and structural characterization 151
6.3 Temperature-dependent charge and thermoelectric transport 156
6.4 Conclusions 163

7 Conclusions and outlook 165

Appendices 169

A Publications and presentations 169

References 173

Chapter 1

Introduction

1.1 Electronic and thermoelectric applications

Since the pioneering works by Hideki Shirakawa, Alan MacDiarmid and Alan Heeger on halogen and arsenic pentafluoride-doped polyacetylene,[1] awarded with the Nobel Prize in Chemistry in 2000, a wide range of research branches and technological applications in the field of organic electronics have emerged. The most prominent examples include organic field-effect transistors (OFETs), organic light-emitting diodes (OLEDs), organic solar cells and more recently organic sensing applications, organic thermoelectrics and organic spintronics. Amongst those, OLEDs currently display by far the most commercially impactful technology. Following the eminent contributions by Ching Wan Tang and Steven Van Slyke on OLEDs based on organic small molecules at Eastman Kodak in the 1980s and those by Jeremy Burroughes, Richard Friend and coworkers on OLEDs based on conjugated polymers at the Cavendish Laboratory in the 1990s,[2,3] OLEDs have been established as a key component of a competitive display technology. Nowadays, they are employed by essentially all leading electronic companies for TV, smartphone, camera and further electronic device displays.

Similarly, broad are the potential application areas of single-walled carbon nanotube (SWCNT) electronics that evolved since the seminal works by Sumio Iijima, Mildred Dresselhaus and coworkers on SWCNTs and their electronic structure in the 1990s.[4–6] With respect to the focus of this thesis on the charge and thermoelectric transport in semicrystalline conjugated polymers and SWCNT networks, further background should particularly be provided on field-effect transistor (FET) and thermoelectric applications of these systems.

Over the past decades the performance of conjugated polymer and SWCNT-based FETs has improved more than six orders of magnitude.[7–11] For organic semiconductors this development has facilitated the evolution from proof-of-concept devices to simple flexible electronic circuits such as complementary (CMOS) inverters, ring oscillators or control circuitry for active-matrix LED displays (Fig. 1.1a).[12–14] While conjugated

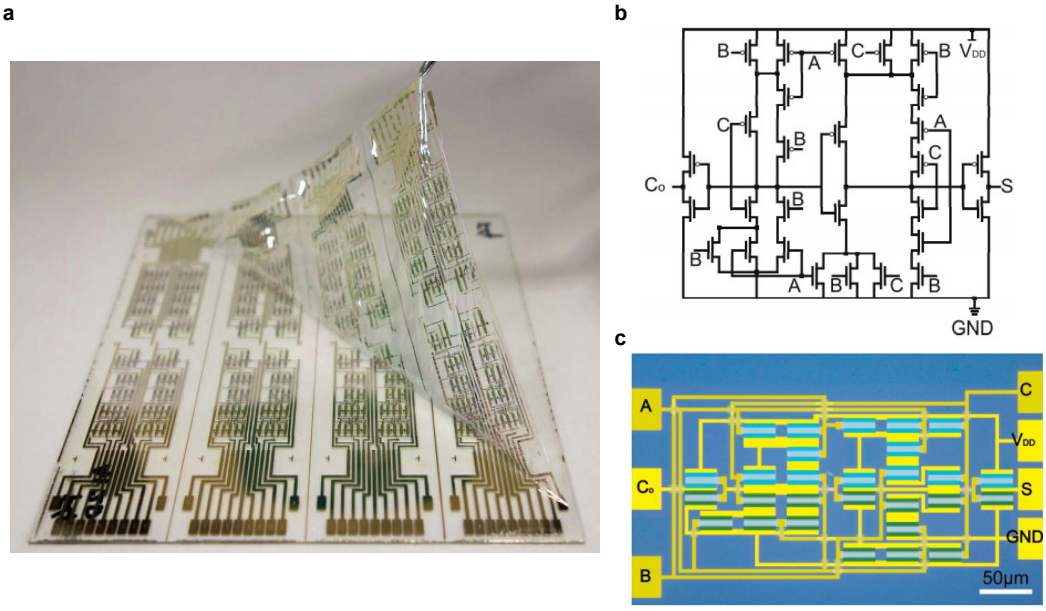

Figure 1.1. Organic semiconductor and SWCNT network FET applications. A photograph of an organic CMOS logic circuit on a flexible, 1 µm thick substrate (a) as well as the circuit diagram (b) and micrograph (c) of a SWCNT network CMOS 1-bit full adder are shown. The figures have been adapted from refs. [13] and [15].

polymers have greater potential for scalable uniform film fabrication processes, their performance tends to be lower than their small molecule semiconductor competitors.[8] In terms of the carrier mobility, which is one of the key performance parameters governing the switching speed of FETs, both conjugated polymers as well as SWCNT networks have outperformed their commercial competitor amorphous silicon, which is commonly employed in active-matrix LED displays. Nevertheless, further improvement of their operational and environmental stability is necessary to allow widespread commercial application.[8,11,16] For SWCNT-based FETs, single SWCNT FETs respectively SWCNT array-based FETs and SWCNT network-based FETs need to be distinguished. Single and array-based SWCNT FETs have essentially outperformed state-of-the-art silicon devices,[10] widely employed in any kind of consumer electronics (such as PCs), due to their ballistic and quasi-ballistic transport properties in the low and high-field regime.[17–19] Even small SWCNT FET-based computers have been developed, but commercial breakthrough relies on improvements of both stability and reliability as well as routes for easier mass production.[10,20] SWCNT network FETs cannot reach the performance limits of single SWCNT transistors due to the existence of SWCNT junctions and enhanced electron scattering, but they still display the SWCNT technology

that to date allows for the fastest SWCNT-based integrated circuits (ICs) with GHz switching frequencies (Fig. 1.1b, c).[15,21] SWCNT networks offer easier uniform and scalable fabrication and are therefore also strong candidates for active-matrix LED display backplanes and a broad range of flexible sensing applications such as wearable sensor-based health monitoring.[11,22]

More recently conjugated polymers and SWCNT networks have emerged as promising materials for thermoelectric applications.[23,24] Thermoelectric generators (TEGs) are solid state heat engines without any mechanically moving parts, designed to convert waste heat to electricity. Considering that approximately two thirds of the energy consumed in the United States is wasted primarily as heat, TEGs, Rankine, Stirling and other heat engines have an immense potential to improve global energy management.[24] The underlying mechanism of the operation principle of TEGs is the Seebeck effect. If a temperature difference (ΔT) is applied to a conducting system, carriers thermally diffuse from the hot to the cold side, where they accumulate and establish an opposing electric field. Eventually a new steady state with zero current flow is reached if the system is kept in open-circuit condition. The Seebeck coefficient is defined as the ratio of the electric voltage (V_{th}) that has built up to the applied temperature difference ($S = \frac{V_{\mathrm{th}}}{\Delta T}$). The material performance in converting heat to electricity based on this operation principle is characterized by the dimensionless figure of merit (zT):

$$zT = \frac{PF}{\kappa} \cdot T = \frac{\sigma \cdot S^2 \cdot T}{\kappa_{\mathrm{l}} + \kappa_{\mathrm{e}}}, \tag{1.1}$$

with the temperature T, the power factor $PF = \sigma \cdot S^2$, σ the electrical conductivity, S the Seebeck coefficient and $\kappa = \kappa_{\mathrm{l}} + \kappa_{\mathrm{e}}$ the thermal conductivity which has contributions from both lattice (κ_{l}) and charge carrier (κ_{e}) thermal conductivity.[25] Since a single material has very small power outputs, TEGs consisting of both a p-type and n-type leg, are typically connected electrically in series and thermally in parallel to form a thermoelectric module with sufficient power output for practical applications (Fig. 1.2). As a heat engine the conversion efficiency of a TEG (η) is limited by the Carnot efficiency ($\eta_{\mathrm{C}} = \frac{T_{\mathrm{hot}} - T_{\mathrm{cold}}}{T_{\mathrm{hot}}}$) and can be expressed as:

$$\eta = \eta_{\mathrm{C}} \cdot \frac{\sqrt{1 + ZT_{\mathrm{av}}} - 1}{\sqrt{1 + ZT_{\mathrm{av}}} + \frac{T_{\mathrm{cold}}}{T_{\mathrm{hot}}}}, \tag{1.2}$$

with the average temperature $T_{\mathrm{av}} = \frac{T_{\mathrm{hot}} + T_{\mathrm{cold}}}{2}$ and the device figure of merit $ZT_{\mathrm{av}} = \frac{(S_{\mathrm{p}} - S_{\mathrm{n}})^2 T_{\mathrm{av}}}{K \cdot R}$. Here S_{p} and S_{n} are the Seebeck coefficients of the p-type and n-type leg respectively, $R = \frac{L_{\mathrm{p}} \rho_{\mathrm{p}}}{A_{\mathrm{p}}} + \frac{L_{\mathrm{n}} \rho_{\mathrm{n}}}{A_{\mathrm{n}}}$ is the electrical resistance of the two legs in series and $K = \frac{\kappa_{\mathrm{p}} A_{\mathrm{p}}}{L_{\mathrm{p}}} + \frac{\kappa_{\mathrm{n}} A_{\mathrm{n}}}{L_{\mathrm{n}}}$ is the thermal conductance of the two legs in parallel.[25,27] In

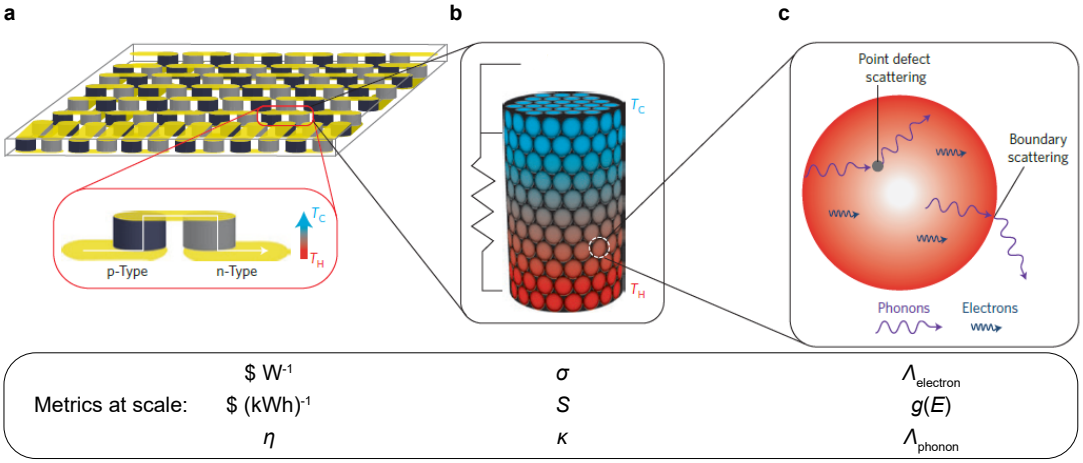

Figure 1.2. Thermoelectric modules and material parameters. An illustration of a thermoelectric module consisting of many TEGs (a), an illustration of the temperature profile across one of the generator legs consisting of a specific material (b) and an illustration of the microscopic transport processes (c) are shown. While on a module and device level (a) the conversion efficiency (η) and the costs per power output are the governing metrics of thermoelectric modules, they in turn depend on the transport coefficients of the material ((b), electrical conductivity (σ), Seebeck coefficient (S) and thermal conductivity (κ)), which are dictated by the density of states (DoS, $g(E)$) and microscopic transport processes (such as point defect and boundary scattering, (c)) that govern the mean free path of electrons ($\Lambda_{\mathrm{electron}}$) and phonons ($\Lambda_{\mathrm{phonon}}$). The figure has been adapted from ref. [26].

order to maximize the conversion efficiency, the geometry of the two legs and their temperature-dependent transport coefficients need to be matched ($\frac{L_{\mathrm{n}}A_{\mathrm{p}}}{L_{\mathrm{p}}A_{\mathrm{n}}} = \left(\frac{\rho_{\mathrm{p}}\kappa_{\mathrm{n}}}{\rho_{\mathrm{n}}\kappa_{\mathrm{p}}}\right)^{\frac{1}{2}}$).[25,27] Nevertheless, for simplicity in materials research the optimization of the figure of merit according to Eq. 1.1 is considered. Due to their low conversion efficiencies and comparatively high costs (Fig. 1.3a), the application of TEGs has so far been restricted to niche applications, such as radioisotope TEGs in the Mars rover or NASA's deep space missions (e.g. in the Voyager), where costs and efficiency are less important and weight as well as reliability are the decisive factors.[24,28] Since other sources of energy are not available in these space applications, the power supply of their electronics relies on the conversion of heat generated from the nuclear fission of a radioisotope via a TEG. In order to enable more widespread application of TEGs, e.g. for the conversion of waste heat of power stations to boost their generation efficiencies or to power car electronics via a thermoelectric module located at the exhaust pipe, their efficiency (Eq. 1.2) has to be increased via optimization of the figure of merit zT (Eq. 1.1 and Fig. 1.3b).[24] State-of-the-art materials employed in TEGs typically have zT-values close to $zT = 1$.[25] As evident from Eq. 1.1, a high Seebeck coefficient (S), high electrical conductivity (σ) and low thermal conductivity (κ) are required for efficient thermoelectric materials.

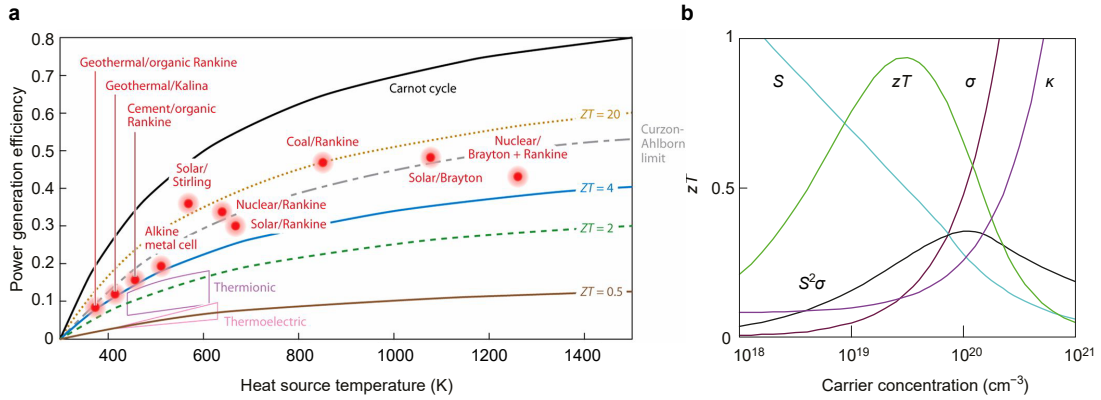

Figure 1.3. TEG conversion efficiencies and zT optimization. A comparison of the conversion efficiency of TEGs for different values of ZT with other heat conversion technologies is shown in panel (a). Here the heat sink temperature has been set to 300 K and the ZT values were assumed to be temperature independent. Panel (b) shows the modelled dependence of zT, the Seebeck coefficient (S, 0-500 $\frac{\mu V}{K}$) as well as the electrical and thermal conductivity (σ, 0-5000 S cm^{-1}, and κ, 0-10 W m^{-1} K^{-1}, respectively) of Bi_2Te_3 on charge density. The figures have been adapted from refs. [25] and [28].

However, these transport coefficients are interdependent and show opposite trends with varying charge density (Fig. 1.3b). Typically the Seebeck coefficient decreases with increasing charge density due to entropic considerations (further discussion in section 2.3), while both electrical as well as thermal conductivity increase with increasing charge density. For instance, the Wiedemann-Franz law directly relates the electronic contribution of the thermal conductivity (κ_e) to the electrical conductivity in metals ($L \equiv \frac{\kappa_e}{\sigma T} = \frac{\pi^2}{3}\left(\frac{k_B}{e}\right)^2 \equiv L_0$, with k_B the Boltzmann constant, e the electron charge and L the Lorenz ratio) and dictates such concomitant increase of both transport coefficients with increasing charge density.[25,29] Nevertheless, metals are usually not employed for TEGs due to their very small Seebeck coefficients on the order of a few $\frac{\mu V}{K}$ (originating from their wide bands and the proximity of transport- and Fermi-level, see section 2.3). Instead narrow-bandgap degenerate semiconductors such as Bi_2Te_3, Sb_2Te_3 and their alloys are employed, because they offer high Seebeck coefficients while displaying high electrical conductivities. As shown representatively in Fig. 1.3b for Bi_2Te_3, the zT of these degenerate semiconductors typically peaks for charge densities between 10^{19} cm^{-3} and 10^{21} cm^{-3} ($zT \sim 1$).[25] In the attempt of achieving zT-values in excess of 3, great efforts towards decoupling of the transport coefficients via nanostructuring and defect engineering have been undertaken in the past three decades and zT-values on the order of 2 have been obtained.[30–32] The conceptual idea behind these approaches is to implement an electron-crystal phonon-glass system, where the transport of charge carriers is not significantly impeded by the nanostructure, while heat-transporting phonons

(lattice vibrations) are scattered in order to reduce the lattice thermal conductivity (κ_l, illustrated in Fig. 1.2c). Further promising approaches have been the implementation of band convergence to increase band degeneracies as well as the reduction of the material dimensionality to introduce sharp peaks in the density of states (DoS), in order to at least maintain electrical and thermal conductivity while enhancing the Seebeck coefficient.[33–35] The highest reported zT of approximately 2.6 ± 0.3 at 923 K, corresponding to 20-25 % conversion efficiency (Fig. 1.3a), has been obtained for bulk inorganic SnSe crystals and further enhancements employing novel concepts such as topological states and using the spin degree of freedom seem feasible.[28,36]

Beyond waste heat recovery at high temperatures (>400 K), cost-effective low-grade (300-400 K) heat conversion and cooling applications are of significant interest particularly for wearable electronics and health monitoring applications. Due to their flexibility, solution-processability and low-cost fabrication routines, the investigated conjugated polymers and SWCNT networks in this thesis are very promising candidates for these applications.[23,24] The van der Waals bonded nature of conjugated polymers not only facilitates flexibility, but also leads to intrinsically low thermal conductivities on the order of 0.2-0.3 W m^{-1} K^{-1}.[37] Considering these low thermal conductivities and the fact that conjugated polymers usually have wide bandgaps around 1-3 eV leading to low intrinsic carrier concentrations, the optimization of their zT is typically more focused on tuning the charge density via doping in order to maximize their power factor (σS^2).[23,38] This optimization has been particularly successful in conducting polymers such as poly(3,4-ethylenedioxythiophene) (PEDOT) doped by poly(styrenesulphonate) (PSS) and mixed with dimethyl-sulphoxide (DMSO), which is the highest performing organic thermoelectric material system to date, reaching power factors close to 470 $\frac{\mu W}{m \cdot K^2}$ and a zT of approximately 0.42 at room temperature.[39] Further notable p-type conjugated polymer thermoelectric materials are oxidation level controlled PEDOT-Tosylate achieving a zT of approximately 0.25 at room temperature as well as [2,3,5,6- tetrafluoro-7,7,8,8-tetracyanoquinodimethane (F_4TCNQ)- respectively bis(trifluoromethanesulfonyl)imide (TFSI)-doped poly(2,5-bis(3-tetradecylthiophen-2-yl)thieno[3,2-*b*]thiophene) (PBTTT) displaying power factors around 100 $\frac{\mu W}{m \cdot K^2}$.[40–43] Efficient n-type conjugated polymer semiconductors are scarce instead, with the most efficient one being the recently reported fluorinated benzodifurandione-based poly(*p*-phenylene vinylene) (FBDPPV) doped with a triaminomethane-based dopant (TAM) reaching a power factor of approximately 51 $\frac{\mu W}{m \cdot K^2}$.[38,44] In the same study Yang *et al.* presented the first flexible all-polymer solution-processed TEG with a power output of 77 nW (with air as a heat sink and T_{hot} at 150 °C) based on FBDPPV-TAM n-type and PEDOT-PSS p-type legs.[44]

SWCNT networks cannot offer as low thermal conductivities as conjugated polymers. Nevertheless, considering that individual SWCNTs display thermal conductivities on the order of several thousand W m^{-1} K^{-1},[45] it is remarkable that values as low as 1.3 W m^{-1} K^{-1} have been reported for doped polymer-sorted semiconducting SWCNT networks.[46] These low thermal conductivities combined with both p- and n-type power factors in excess of 500 $\frac{\mu W}{m \cdot K^2}$ facilitated a zT of approximately 0.12 at room temperature.[46] Such high ambipolar power factors (up to ∼700 $\frac{\mu W}{m \cdot K^2}$) render polymer-sorted semiconducting SWCNT networks as strong candidates for thermoelectric applications, particularly in wearable electronics.[46,47]

The objective of this thesis is to study the charge and thermoelectric transport of these conjugated polymers and polymer-sorted semiconducting SWCNT networks, in order to get insights into their electronic structure as well as the microscopic transport mechanisms and the interaction of carriers with their environment (as e.g. illustrated in Fig. 1.2b, c). This understanding is then employed to propose new design guidelines for further improvements of their electronic and thermoelectric performance. For this purpose firstly some fundamental properties of these systems as well as some background on their charge and thermoelectric transport properties is provided in chapters 1 and 2. Chapter 3 outlines the employed materials, fabrication as well as characterization routines. The most important outcomes of this work on charge and thermoelectric transport in semicrystalline conjugated polymers, polymer-sorted semiconducting SWCNT networks as well as molecularly doped, aligned conjugated polymers is subsequently presented in chapters 4-6. Finally, chapter 7 provides the concluding remarks of the presented work.

1.2 Organic semiconductors

1.2.1 Electronic structure

Organic semiconductors are predominantly carbon and hydrogen-based materials exhibiting semiconducting properties due to their π-conjugation originating from their alternating single and double bonded carbon atoms. In its ground state carbon has only two unpaired electrons in the $2p$ orbitals. Nevertheless, upon proximity to any binding partners, it is energetically favourable to compensate for the energy difference between the $2s$ and three $2p$ orbitals, rendering them as degenerate and leading to their hybridization. In case of organic semiconductors, three sp^2 orbitals are formed equally spaced in the molecular plane as a linear combination of the $2s$ and two $2p$ orbitals, leaving one unpaired out-of-plane p_z orbital. While the three sp^2 orbitals are involved in the

formation of strong covalent σ bonds with the electron density localized along the axis between the two bonding atoms, the p_z orbital hybridizes with the p_z orbitals of neighbouring carbon atoms to form covalent π bonds with a delocalized out-of-plane charge density. If the orbitals are combined with opposite phases as opposed to the bonding case, the corresponding unoccupied anti-bonding π^* and σ^* orbitals are obtained from the p_z and sp^2 orbitals respectively. Since the orbital energy splitting is proportional to the exchange integral ($\beta = \int \phi_i H \phi_j d\vec{r}$, with H the Hamiltonian of the system and ϕ_i as well as ϕ_j the overlapping electron wavefunctions), which is antiproportional to the distance between nuclei and orbital interaction, the energy splitting between the σ and σ^* orbitals formed by the strongly in-plane overlapping $2sp^2$ orbitals is larger than the π-π^* splitting. Consequently, the π and π^* orbitals are also referred to as the highest occupied molecular orbital (HOMO) and lowest unoccupied molecular orbital (LUMO).[48] The resulting energy diagram and the bond formation process is illustrated for the simple case of ethene in Fig. 1.4a, b. When these considerations are extended

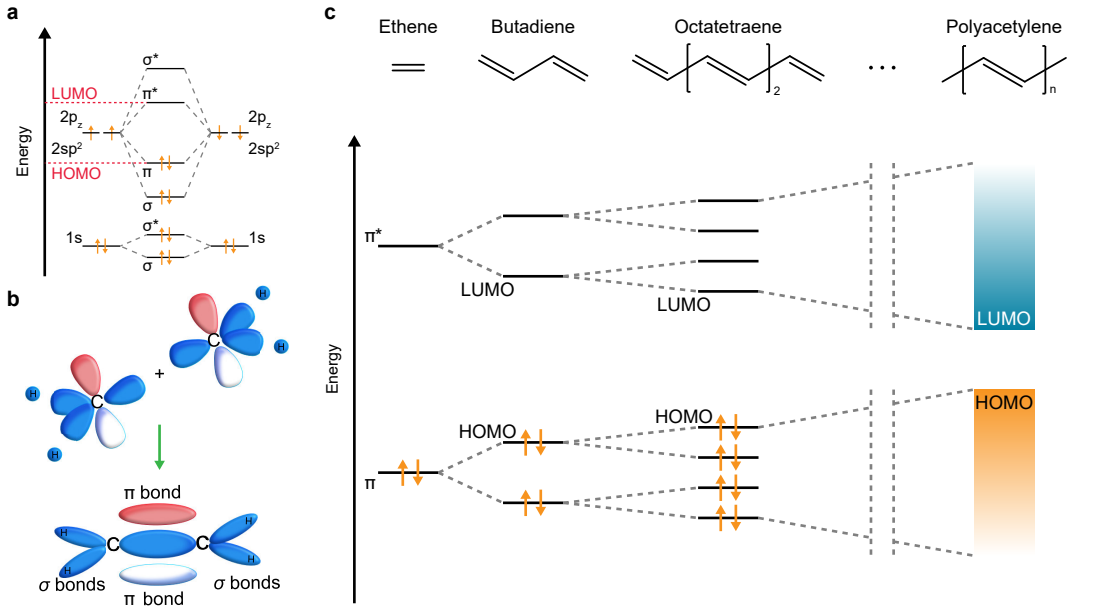

Figure 1.4. Formation of electronic structure in organic semiconductors. The energy diagram considering only carbon-carbon interactions as well as the bond formation process for ethene are shown in panel (a) and (b). Panel (c) shows the extension of these considerations from ethene to polyacetylene, illustrating the electronic structure formation in organic semiconductors.

to a polymer chain with $N \gg 1$ monomer units, the number of linear combinations of p_z orbitals increases and the spacing between the π and π^* orbitals decreases (Fig. 1.4c). These simple considerations would suggest a half-filled quasi-continuous band of bonding

and anti-bonding states and therefore a conducting system. However, the conjugated system is still semiconducting, due to the following two reasons: On the one hand, the polymer chain is subject to a Peierls distortion, an energetically favourable configuration in which the lengths of the single and double bonds are not equal. This dimerization causes an additional energy splitting around the Fermi-level between the bonding and anti-bonding states.[49,50] On the other hand, amongst others Kohler has shown that the additional incorporation of electron-electron correlation (that has been neglected in the previous arguments) within Hückel theory through the consideration of configurational interaction leads to a more accurate description of the electronic structure.[48,51,52] Due to the fact that organic small molecules and conjugated polymers in deposited films interact via weak van der Waals forces with each other, resulting in weak electronic coupling, the band widths of their energy bands are typically narrow and on the order of 100 meV.[53] Furthermore, both positional disorder e.g. due to torsions along the polymer backbone or paracrystalline disorder (absence of long range order despite short and medium range order), as well as energetic disorder e.g. due to different dipolar environments, leads to a Gaussian broadening of the described energy levels (further discussion in section 2.1).[54,55] While organic molecular semiconductors such as pentacene and rubrene are an important class of organic semiconductors which offer the highest performance (with field-effect saturation mobilities (μ_{sat}) in excess of 15 $\text{cm}^2\ \text{V}^{-1}\ \text{s}^{-1}$), this thesis focuses on conjugated polymers that offer better large-area film uniformity and are easier employable for scalable fabrication techniques such as roll-to-roll printing.[56,57]

1.2.2 Conjugated polymers

Compared to oligomeric small molecule semiconductors, conjugated polymers are substantially longer (∼100 nm) as they typically have on the order of 100 monomer repeat units (depending on their molecular weight). Considering that their persistence length (length over which the polymer bends on average 90°) is on the order of 3-30 nm, many of them behave as semiflexible chains, instead of rod-like systems.[58] The polymer backbone constitutes the core of the polymer chain and mostly consists of heteroatom-substituted aromatic rings (e.g. thiophene or selenophene rings). Furthermore, alkyl side chains flank the polymer backbone in order to enable solubility as well as to tune aggregation and molecular packing.[59] Due to their semiflexible nature, structural and energetic disorder are often a direct consequence of their microstructural and morphological properties and many conjugated polymers adopt semicrystalline structures with coexisting amorphous and crystalline domains.[8,55,60] While the first conjugated semiconductors employed in FETs formed amorphous films and displayed

very low carrier mobilities ($\sim 10^{-6} - 10^{-3}$ cm^2 V^{-1} s^{-1}),[7,61] substantial progress towards higher performance conjugated polymer semiconductors has been made in the 1990s and 2000s, using highly ordered polythiophene-based conjugated polymers such as poly(3-hexylthiophene) (P3HT) and PBTTT (Fig. 1.5a, b), with field-effect mobilities up to 1 cm^2 V^{-1} s^{-1}.[62–64] In the past decade a new class of high-mobility donor-acceptor copolymers has been developed, of which many consistently show carrier mobilities greater than 1 cm^2 V^{-1} s^{-1}.[65–68] Widely employed building blocks are the electron-deficient diketopyrrolopyrrole (DPP), indacenodithiophene (IDT), cyclopentadithiophene (CDT), isoindigo (II) and naphtalenediimide (NDI) units as well as the electron-rich thiophene (T), benzothiadiazole (BT) and benzotriazole (BTz) units (Fig. 1.5c-g).[65–69] In contrast to the polythiophene-based conjugated polymers, these donor-acceptor copolymers frequently display ambipolar transport properties due to their relatively small bandgaps of approximately 1.2-1.8 eV.[65,66] Notably, high-mobility n-type polymers such as the NDI-based poly[*N*,*N*'-bis(2-octyldodecyl)-naphthalene-1,4,5,8-bis(dicarboximide)-2,6-diyl]-*alt*-5,5'-(2,2'-bithiophene) (P(NDI2OD-T2)) with comparable mobilities of approximately 1 cm^2 V^{-1} s^{-1} have also been realized.[69] Some of these copolymers display less order than polythiophene-based conjugated polymers, yet they achieve significantly higher mobilities due to their highly planar torsion-free backbone configurations enabled by extended fused aromatic units.[70,71] Additionally, further performance improvements have been realized via tuning of the polymer crystallinity and polymer stacking by the choice of solvent controlling pre-aggregation in solution and thermal annealing processes affecting the morphological phase of the polymer films.[72,73] The interconnectivity of crystalline domains via tie chains through increased polymer molecular weight and backbone planarity has also been a key design guideline.[55] The implications of these molecular design guidelines on charge transport in conjugated polymers will be discussed in section 2.1. Uniaxial alignment routines have been employed to achieve the highest mobilities in conjugated polymers, up to 5-10 cm^2 V^{-1} s^{-1} in the case of DPP-BTz and cyclopentadithiophene-benzothiadiazole (CDT-BTZ).[74–76]

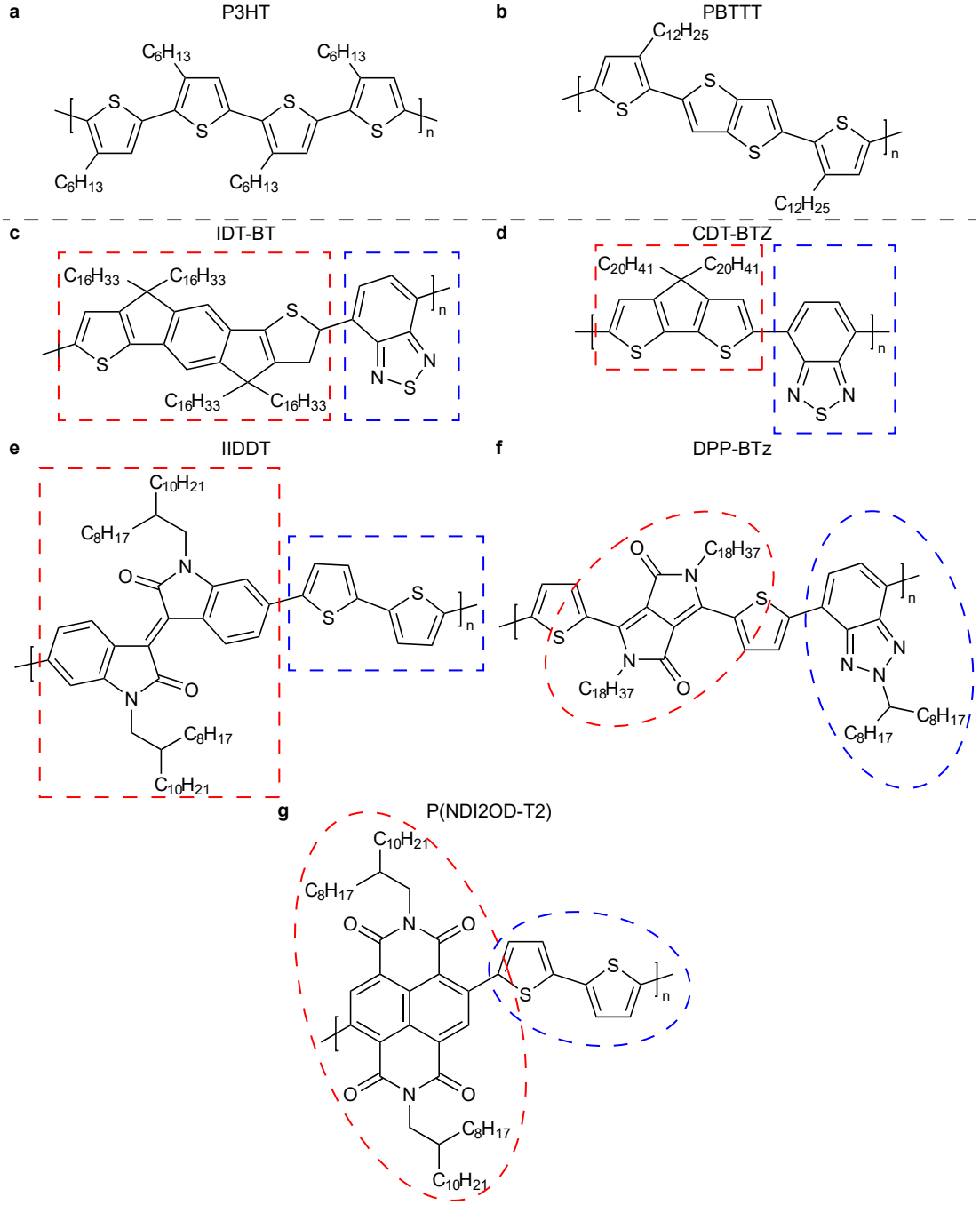

Figure 1.5. Molecular structures of conjugated polymers. The molecular structures of the highly ordered polythiophene-based P3HT (a) and PBTTT as well as the more recently developed high-mobility donor-acceptor copolymers IDT-BT (c), CDT-BTZ (d), IIDDT (e), DPP-BTz (f) and P(NDI2OD-T2) (g) are shown. The electron-deficient units of the donor-acceptor copolymers are highlighted by red-dashed surrounding lines and the electron-rich units by blue-dashed lines respectively.

1.3 Single-walled carbon nanotubes

1.3.1 Structural properties and electronic structure

The structural properties of single-walled carbon nanotubes (SWCNTs) are very closely related to those of the carbon allotropes graphene and closed fullerenes (such as C_{60}), whose discoveries were awarded with the Nobel prize in 2010 and 1996 respectively.[77,78] Graphene consists of a single layer of carbon atoms arranged in a hexagonal lattice and stacking of such layers results in the well-known carbon allotrope graphite. Closed fullerenes instead are closed structures assembled from carbon penta-, hexa- and heptagons. SWCNTs are hollow cylindrical tubes of carbon atoms, whose structure can be conceptually obtained by virtually rolling up a graphene sheet to form a cylinder, with some of them capped by a hemisphere of a closed fullerene.[79] Nevertheless, due to their exceptionally large aspect ratios based on their diameters in the range of approximately 0.5-5 nm and lengths of several hundred nanometers to several centimeters, their potential end-caps are usually ignored when characterizing their structural and electronic properties. Multi-walled carbon nanotubes which consist of multiple nested SWCNTs and are typically more defective will not be further discussed in this thesis. The chiral vector $\vec{C}_\mathrm{h}$ along which the graphene sheet is virtually rolled up to obtain a SWCNT, defines the structure of a SWCNT (Fig. 1.6a).[79] It is a linear combination of the graphene primitive lattice vectors $\vec{a}_1 = \frac{a}{2} \cdot (\sqrt{3},\, 1)$ and $\vec{a}_2 = \frac{a}{2} \cdot (\sqrt{3},\, -1)$, with the graphene Bravais lattice constant $a = \sqrt{3} a_{\mathrm{C-C}} = 2.46$ Å and $a_{\mathrm{C-C}}$ the carbon-carbon bond length (~ 1.42 Å):

$$\vec{C}_\mathrm{h} = n\vec{a}_1 + m\vec{a}_2, \tag{1.3}$$

with n and m being positive integers and satisfying the condition $0 \leq m \leq n$. The integer pair (n, m) is referred to as the chirality of a SWCNT and based on their chirality three classes of SWCNTs are distinguished: (n, n) and $(n, 0)$ SWCNTs are armchair and zigzag SWCNTs respectively, considering the shape of the bonding carbon atoms seen from the cross-section along the chiral vector (Fig. 1.6), while all other SWCNTs are termed chiral SWCNTs. The structure of such (6,6) armchair, (6,0) zigzag and (6,5) chiral SWCNTs is illustrated in Fig. 1.6b-d. The structure of a SWCNT is equivalently defined by its diameter $d_\mathrm{t} = \frac{\|\vec{C}_\mathrm{h}\|}{\pi} = \frac{a}{\pi}\sqrt{n^2 + nm + m^2}$ (with the length of the chiral vector ($\|\vec{C}_\mathrm{h}\| = C_\mathrm{h}$) being the circumference of the tube) and its chiral angle:

$$\theta = \arccos\left(\frac{\vec{C}_\mathrm{h} \cdot \vec{a}_1}{\|\vec{C}_\mathrm{h}\| \cdot \|\vec{a}_1\|}\right) = \arccos\left(\frac{2n + m}{2\sqrt{n^2 + nm + m^2}}\right), \tag{1.4}$$

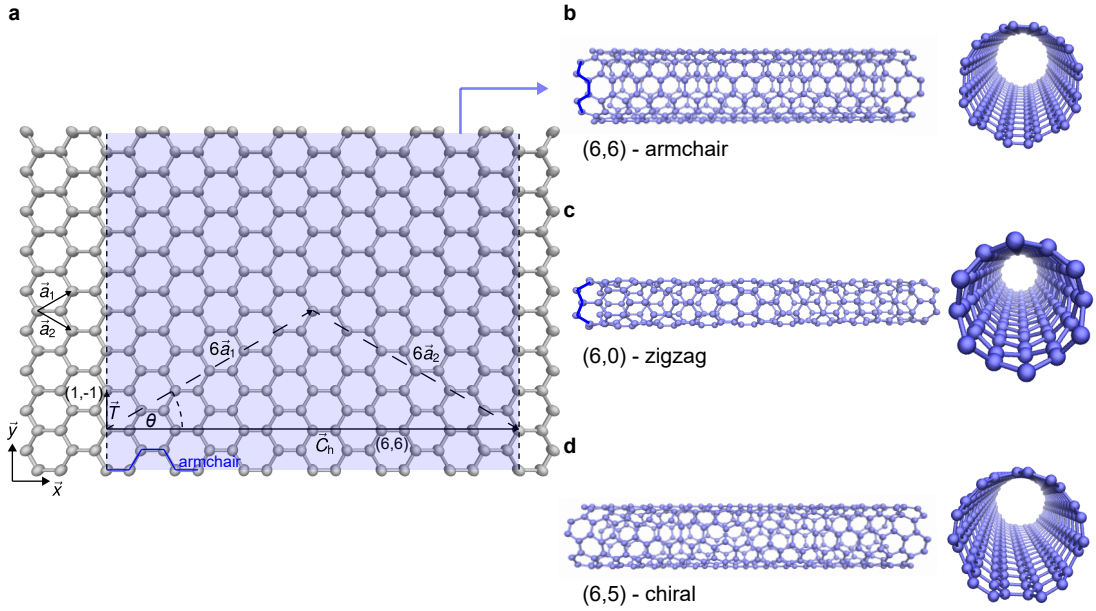

Figure 1.6. Structural relation between graphene and SWCNTs. The conceptual rolling up process from a 2D graphene sheet to a (6,6) armchair SWCNT (a) and its resulting molecular structure (b) as well as the molecular structure of a (6,0) zigzag (c) and a (6,5) chiral (d) SWCNT are shown. Furthermore, the most relevant structural parameters, the primitive lattice vectors of graphene ($\vec{a}_1$, $\vec{a}_2$) and the chiral vector ($\vec{C}_\mathrm{h}$, Eq. 1.3), the chiral angle (θ, Eq. 1.4) as well as the translation vector ($\vec{T}$, Eq. 1.5) of the (6,6) SWCNT are highlighted (a). The molecular structures were created with the visual molecular dynamics (VMD) software.[80]

with unique values restricted to $0° \leq \theta \leq 30°$. For zigzag SWCNTs with the chiral vector along $\vec{a}_1$, the chiral angle is 0° and for armchair SWCNTs it is 30°. Another less frequently considered property distinguishing the structure of SWCNTs is their handedness. The mirror image of the right-handed (n, m) SWCNT $(n > m)$ is the left-handed (m, n) tube $(m > n)$. SWCNT samples with only one enantiomer (non-superimposable mirror image form) show optical activity.[81] Further important parameters commonly used to characterize the structure of SWCNTs are the translation vector of the SWCNT unit cell:

$$\vec{T} = \frac{2m+n}{g_\mathrm{d}}\vec{a}_1 - \frac{2n+m}{g_\mathrm{d}}\vec{a}_2, \tag{1.5}$$

with the greatest common divisor $g_\mathrm{d} \equiv \gcd(2m+n, 2n+m)$, the translation vector length $\|\vec{T}\| = T = \frac{\sqrt{3}C_\mathrm{h}}{g_\mathrm{d}}$ as well as the number of carbon hexagons per SWCNT unit cell:

$$N = \frac{\|\vec{C}_\mathrm{h} \times \vec{T}\|}{\|\vec{a}_1 \times \vec{a}_2\|} = \frac{2\,\|\vec{C}_\mathrm{h}\|^2}{a^2 g_\mathrm{d}}. \tag{1.6}$$

Due to the structural relation between SWCNTs and graphene, the electronic structure of SWCNTs can be derived from that of graphene as well.[5,82] Following the considerations in section 1.2.1, every carbon atom in the 2D hexagonal lattice of graphene forms three σ bonds to its nearest neighbours, based on the three hybridized $2sp^2$ orbitals of each carbon atom. The remaining p_z orbitals form the π and π^* bands which are also the valence and conduction band for energies less than 3 eV away from the Fermi-energy (E_F), which is the case for many transport as well as low-excitation energy optical and Raman spectroscopy measurements.[79,83] While for higher energy excitations more than 3 eV away from the Fermi-level numerical *ab initio* calculations of the band structure of graphene and hence SWCNTs become inevitable, for low energy excitations less than 3 eV away from the Fermi-level, nearest neighbour tight-binding (TB) calculations give very good approximations in agreement with experiments.[79,84] Considering only the wavefunction overlap of nearest neighbours to be significant, the following dispersion relation is obtained for graphene:[79,84]

$$E^{\pm}_{g,\,2D}(\vec{k}) = \frac{\epsilon_{2p} \pm \gamma_0 w(\vec{k})}{1 \mp s w(\vec{k})}. \tag{1.7}$$

Here $\epsilon_{2p} = \int \phi^*(\vec{r} - \vec{R}_j) H \phi(\vec{r} - \vec{R}_j) d\vec{r}$ ($\vec{R}_j$ is the position of a carbon atom in the hexagonal lattice) is approximately the energy of a $2p$ orbital (ϕ) in isolated carbon (except from the fact that the Hamiltonian H of graphene contains a periodic Coulombic potential and not that of a single atom), $\gamma_0 = \int \phi^*(\vec{r} - \vec{R}_j) H \phi(\vec{r} - \vec{R}_j - \vec{R}_{nn,\,j,\,i=1-3}) d\vec{r}$ is the nearest neighbour overlap energy ($\vec{R}_{nn,\,j,\,i=1-3}$ are the vectors connecting atom j to its three nearest neighbours), $s = \int \phi^*(\vec{r} - \vec{R}_j) \phi(\vec{r} - \vec{R}_j - \vec{R}_{nn,\,j,\,i=1-3}) d\vec{r}$ is the tight-binding overlap integral and $w(\vec{k})$ is given by:

$$w(\vec{k}) = \sqrt{1 + \cos\frac{\sqrt{3}k_x a}{2} \cos\frac{k_y a}{2} + 4\cos^2\frac{k_y a}{2}}. \tag{1.8}$$

While $\gamma_0 = 3.033$ eV and $s = 0.129$ have been found to fit the first-principles *ab initio* calculations particularly well, it is common practice to approximate $s = 0$, since for low energies $E < 3$ eV the differences are negligible.[84] Considering non-zero values of the overlap integral s introduces an asymmetry of the valence and conduction bands, which is non-negligible for energies $E > 3$ eV. The hexagonal Brillouin zone of graphene and its high symmetry points (Γ: (0, 0), K: $\left(\frac{2\pi}{\sqrt{3}a}, \frac{2\pi}{3a}\right)$, K': $\left(\frac{2\pi}{\sqrt{3}a}, -\frac{2\pi}{3a}\right)$ and M: $\left(\frac{2\pi}{\sqrt{3}a}, 0\right)$) as well as the 2D dispersion relation (Eq. 1.7) for $\gamma_0 = 2.9$ eV and $s = 0$ are shown in Fig. 1.7a, c, e. The K and K' points which are called Dirac points are the only points in the Brillouin zone for which graphene does not have a bandgap. Instead at these points

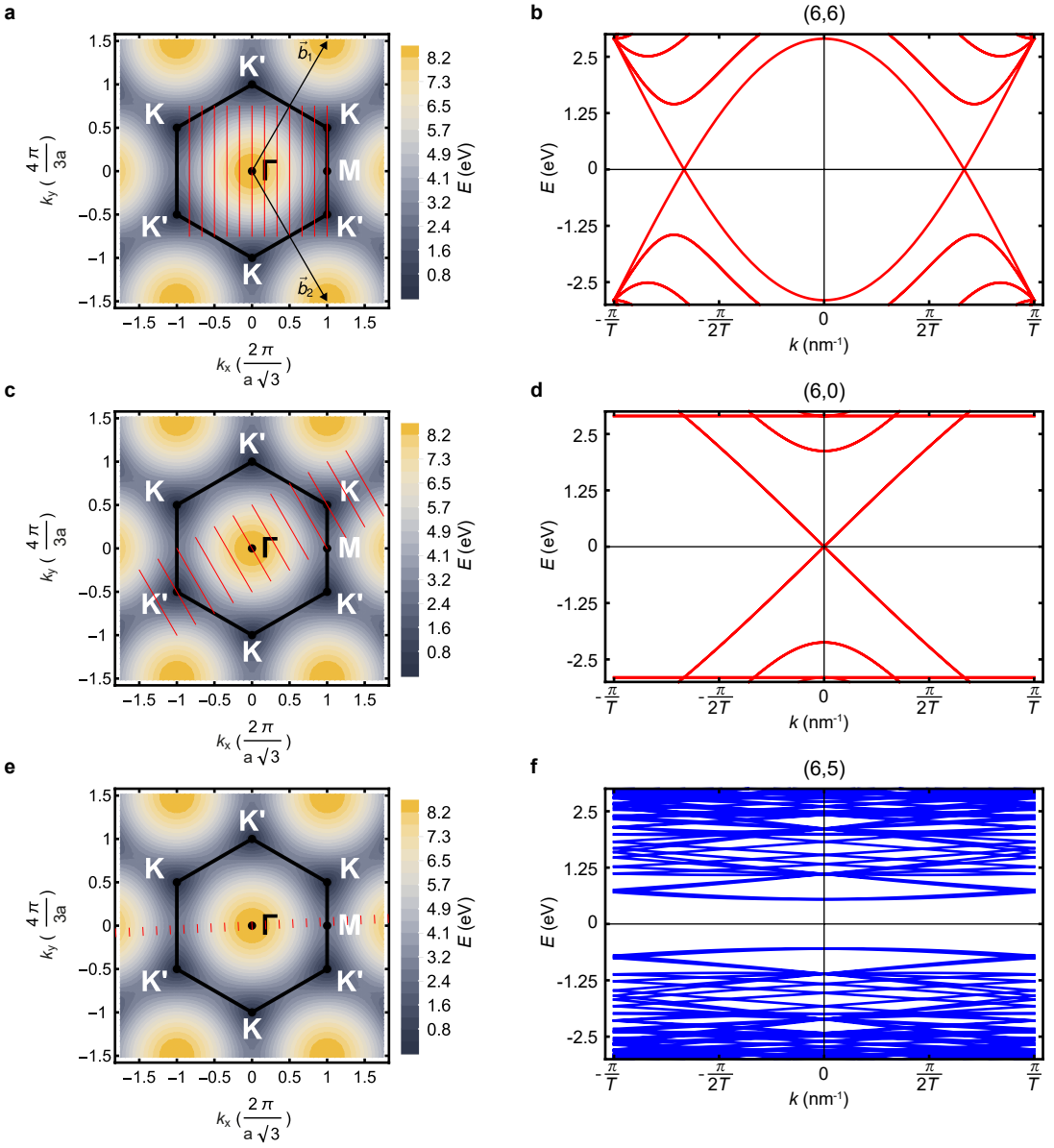

Figure 1.7. Tight-binding energy dispersion of graphene and SWCNTs. The 2D tight-binding nearest neighbour conduction band dispersion of graphene (Eq. 1.7, $\gamma_0 = 2.9$ eV, $s = 0$, (a), (c), (e)) as well as the energy dispersions of the (6,6), (6,0) and (6,5) SWCNTs based on the zone folding approximation (Eq. 1.11, (b), (d), (f)) are shown. The corresponding cutting lines due to the quantization of the wavevector in circumferential direction (q) are shown in panels (a), (c) and (e). Most of the 182 cutting lines for the (6,5) SWCNTs are not shown since they exceed the plot range and the increasing complexity for chiral SWCNTs is further evident from the energy dispersions shown in panel (f). The Brillouin zone, reciprocal lattice vectors ($\vec{b}_1$ and $\vec{b}_2$) as well as high-symmetry points of graphene are also presented ((a), (c), (e)).

the valence and conduction band touch each other and in the vicinity of the Fermi-level (approximately ±0.6 eV) the dispersion relation is linear and hence carriers behave as massless Dirac fermions:

$$E(\vec{k}) \approx \pm\frac{\sqrt{3}}{2}\gamma_0|\vec{k}|a = \pm\hbar|\vec{k}|v_\mathrm{F}, \tag{1.9}$$

with v_F being the Fermi velocity.[79,84] Consequently graphene is typically considered as a semi-metal, since despite having no bandgap the DoS at the Fermi-level is zero in contrast to regular metals.

The electronic structure of SWCNTs can be derived from the graphene dispersion within the zone folding approximation. From the reciprocal lattice vectors of graphene $\vec{b}_1 = \frac{2\pi}{a}\cdot\left(\frac{1}{\sqrt{3}}, 1\right)$ and $\vec{b}_2 = \frac{2\pi}{a}\cdot\left(\frac{1}{\sqrt{3}}, -1\right)$, the reciprocal lattice vectors along the nanotube axis ($\vec{K}_\mathrm{a}$) and along the circumferential direction ($\vec{K}_\mathrm{c}$) are determined from the reciprocity condition ($\exp[\mathrm{i}(\vec{K}_\mathrm{a}+\vec{K}_\mathrm{c})(\vec{C}_\mathrm{h}+\vec{T})] = 1$):

$$\begin{aligned}\vec{K}_\mathrm{a} &= \frac{1}{N}(m\vec{b}_1 - n\vec{b}_2)\\ \vec{K}_\mathrm{c} &= \frac{(2n+m)\vec{b}_1 + (n+2m)\vec{b}_2}{2(n^2+nm+m^2)},\end{aligned} \tag{1.10}$$

with $\|\vec{K}_\mathrm{c}\| = \frac{2\pi}{C_\mathrm{h}}$ and $\|\vec{K}_\mathrm{a}\| = \frac{2\pi}{T}$. Considering the periodic boundary conditions $\psi(0) = \psi(L_\mathrm{t}) = \exp(\mathrm{i}kN_\mathrm{uc}T)$ (with the length of the tube $L_\mathrm{t} = N_\mathrm{uc}T$ given by T times the number of unit cells N_uc and k the wavevector along the nanotube axis) and $\psi(0) = \psi(C_\mathrm{h}) = \exp(\mathrm{i}qC_\mathrm{h})$ (and hence for the wavevectors along the circumferential direction $q = \frac{2\pi}{C_\mathrm{h}}j$), the 1D SWCNT dispersion relations follow from that of graphene as:[79,84]

$$\begin{aligned}E_j(\vec{k}) = E^{\pm}_{\mathrm{g,\,2D}}&\left(k\frac{\vec{K}_\mathrm{a}}{\|\vec{K}_\mathrm{a}\|} + j\vec{K}_\mathrm{c}\right),\\ &\left(j = 0, \ldots, N-1 \,\text{and}\, -\frac{\pi}{T} < k < \frac{\pi}{T}\right).\end{aligned} \tag{1.11}$$

Since $L_\mathrm{t} \gg T$ and hence $N_\mathrm{uc} \gg 1$ it is evident that k is quasi-continuous, while due to $L_\mathrm{t} \gg C_\mathrm{h}$, q is quantized and much more widely spaced. The N pairs (valence and conduction band) of 1D dispersion relations of SWCNTs can be visualized as N cutting lines of the 2D graphene band structure with a width of $\frac{2\pi}{T}$, that are orthogonal to $\vec{K}_\mathrm{c}$ and parallel to $\vec{K}_\mathrm{a}$ as well as $\frac{2\pi}{C_\mathrm{h}}$-spaced. This process is illustrated for (6,6), (6,0) and (6,5) SWCNTs in Fig. 1.7a, c, e and the corresponding 1D dispersion relations are shown in Fig. 1.7b, d, f. Since the K point $\left(\frac{2\pi}{\sqrt{3}a}, \frac{2\pi}{3a}\right)$ is the point in the Brillouin zone of graphene where valence and conduction band touch, it immediately follows that if one

of the N cutting lines respectively one of the N pairs of 1D dispersions of a SWCNT crosses this K point it is metallic and otherwise it is semiconducting. This condition can be written as $\vec{K} \cdot \vec{C}_{\mathrm{h}} = 2\pi j$ and it follows that all SWCNTs for which $(n - m)$ is zero or an integer multiple of 3 are metallic and all others are semiconducting. Another consequence is that based on a random chirality distribution two thirds of all SWCNTs are semiconducting and one third is metallic.[79] Using the N pairs of 1D dispersion relations of SWCNTs (Eq. 1.11) their 1D DoS in units of states per carbon atom per eV can be calculated as:[84]

$$D(E) = \frac{2}{N} \sum_{j=0}^{N-1} \int \frac{1}{\left| \frac{dE_j(k)}{dk} \right|} \delta(E_j(k) - E) dE. \tag{1.12}$$

The correspondingly calculated DoS of the (6,6), (6,0) and (6,5) SWCNTs is shown in Fig. 1.8. The SWCNT DoS based on this zone folding approximation has been found to

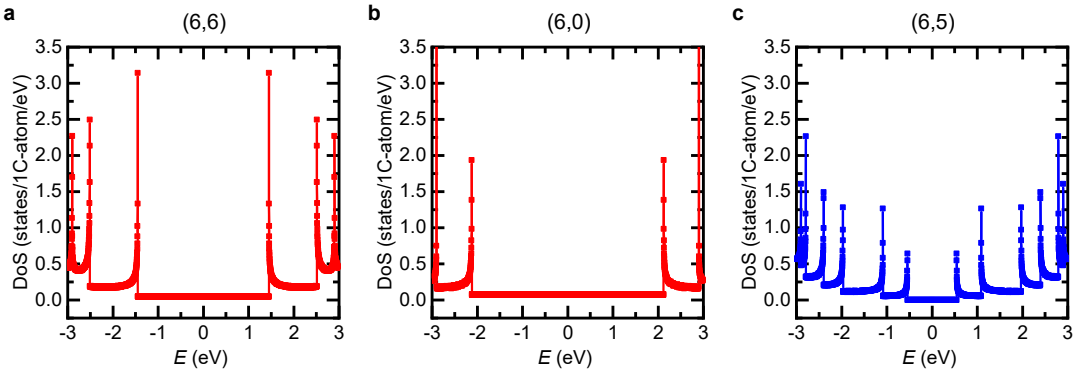

Figure 1.8. SWCNT density of states. The DoS of the (6,6) (a), (6,0) (b) and (6,5) (c) SWCNTs based on the zone folding approximation using Eqs. 1.7, 1.8 and 1.10-1.12 with $\gamma_0 = 2.9$ eV, $s = 0$ and $a_{\mathrm{C-C}} = 1.44$ Å are shown. The data was obtained from ref. [85].

be in good agreement with scanning tunneling, optical and Raman spectroscopy.[86–89] Of particular importance are the spikes in the DoS which are typical for 1D semiconductors and referred to as van Hove singularities. SWCNTs display a direct bandgap between the energies of these singularities and optical transitions between these energies are possible. When the dispersion relation of graphene is linearised around the Fermi-level (Eq. 1.9), the energy difference between the highest energy valence band singularity and lowest energy conduction band singularity for metallic (E_{11}^{M}) and semiconducting (E_{11}^{S}) SWCNTs can be expressed as:[84]

$$\begin{aligned} E_{11}^{\mathrm{M}}(d_{\mathrm{t}}) &\approx 6a_{\mathrm{C-C}} \frac{\gamma_0}{d_{\mathrm{t}}} \\ E_{11}^{\mathrm{S}}(d_{\mathrm{t}}) &\approx 2a_{\mathrm{C-C}} \frac{\gamma_0}{d_{\mathrm{t}}}. \end{aligned} \tag{1.13}$$

It has also been shown that for semiconducting SWCNTs of moderately large diameter ($d_\mathrm{t} > 1$ nm) the DoS per unit length of the lowest subband can be universally (for all chiralities) expressed as:[79,90]

$$g_\mathrm{s}(E,j) = \frac{8}{\sqrt{3}a\pi E_\mathrm{vh2}} \frac{|E|}{\sqrt{E^2 - E_\mathrm{vh1}^2}}, \tag{1.14}$$

with $E_\mathrm{vh1}(j) = \pm\gamma_0 \left|1 + 2\cos\left(\frac{ja}{d_\mathrm{t}}\right)\right|$ and $E_\mathrm{vh2}(j) = \pm\gamma_0 \left|1 - 2\cos\left(\frac{ja}{d_\mathrm{t}}\right)\right|$.
The linearisation of the graphene dispersion underlying Eq. 1.13 is only applicable for low energies (approximately ± 0.6 eV) and therefore the effect of trigonal warping has to be considered. This refers to the fact that with increasing energy seen from the K (and K') points of the Brillouin zone of graphene, the equi-energy contours deviate more and more from circles and eventually become triangles that connect the three neighbouring M points (e.g. Fig. 1.7a). As a consequence the DoS peaks of metallic SWCNTs split into two peaks. The energy splitting increases monotonically with decreasing chiral angle and diameter. Hence, the splitting is most pronounced for small diameter metallic zigzag SWCNTs ($\theta = 0°$) and there is no splitting for armchair SWCNTs ($\theta = 30°$). Despite the fact that the trigonal warping effect does not induce a DoS peak splitting for semiconducting SWCNTs, it still leads to a broadening (compared to Eq. 1.13) of the $E_{ii}^\mathrm{S}(d_\mathrm{t})$ dependence. The broadening of this relation for the smallest energy differences for metallic and semiconducting SWCNTs can be expressed as:[84]

$$\begin{aligned} \Delta E_{11}^\mathrm{M}(d_\mathrm{t}) &= 8\gamma_0 \sin^2\left(\frac{a}{2d_\mathrm{t}}\right) \\ \Delta E_{11}^\mathrm{S}(d_\mathrm{t}) &= 8\gamma_0 \sin^2\left(\frac{a}{6d_\mathrm{t}}\right) \end{aligned} \tag{1.15}$$

and the resulting seminal Kataura plot of $E_{ii}^\mathrm{M}(d_\mathrm{t})$ and $E_{ii}^\mathrm{S}(d_\mathrm{t})$ based on Eqs. 1.7, 1.8 and 1.11 is shown in Fig. 1.9.[88,91] Despite the agreement with many spectroscopic and transport measurements, the limitations of this approach should be outlined in more detail. Apart from the already discussed restricted energy range ($E < 3$ eV) due to deviations from *ab initio* calculations and the significance of σ bands for higher energies, curvature effects particularly in small diameter SWCNTs ($\sim d_\mathrm{t} < 1$ nm) and the impact of bundling of SWCNTs on the electronic structure need to be considered. Prominent curvature effects are asymmetries of the carbon-carbon bond length ($a_\mathrm{C-C}$) and the hybridization of π ($/\pi^*$) and σ ($/\sigma^*$) orbitals due to the fact that the $2sp^2$ and p_z orbitals are not strictly orthogonal any more.[92,93] The effect of stretched carbon-carbon bond lengths can however usually be neglected, since even for small SWCNTs such as the (5,5) tube, the nearest neighbour overlap energy γ_0 is only modified about 2 %.[84]

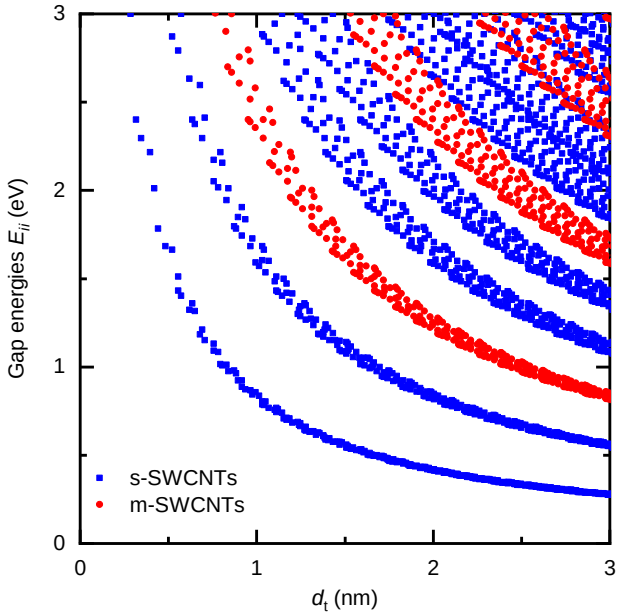

Figure 1.9. Kataura plot of the SWCNT gap energies. Based on the zone folding approximation of the DoS of SWCNTs (Fig. 1.8 and Eqs. 1.7, 1.8 and 1.10-1.12 with $\gamma_0 = 2.9$ eV, $s = 0$ and $a_{C-C} = 1.44$ Å), the gap energies for semiconducting ($E^{S}_{ii}(d_t)$, blue squares) and metallic ($E^{M}_{ii}(d_t)$, red circles) SWCNTs in dependence of their diameter (d_t) are shown. The data was obtained from ref. [91] and is based on the work by Kataura *et al.*.[88]

Hybridization effects can instead have more significant corrections to the zone folding approximation. For energies ($E > 1$ eV) corrections to the conduction band on the order of 200 meV have been found. Furthermore, hybridization effects can cause the opening of a secondary bandgap on the order of 20 meV in small diameter metallic tubes (such as the (9,3) tube).[93] Similarly bundling of SWCNTs due to van der Waals interactions can further modify the electronic structure. It can induce a bandgap opening in armchair SWCNTs, e.g. on the order of 50 meV in (6,6) tubes, and can cause bandgap variations (e.g. a reduction of around 20 % for (8,4) tubes).[93]
Absorption, photoluminescence excitation and Raman spectroscopy are widely employed measurement techniques to characterize the composition of SWCNT networks.[94–96] In particular a Sivarajan Chart that relates the E_{11} and E_{22} resonance peaks to the radial breathing mode (RBM) of the SWCNTs is of significant applicability.[96] Further details on these characterization techniques will be given where relevant in chapters 3 and 5.

1.3.2 Synthesis and sorting techniques

Over the past three decades a multitude of synthesis methods for the preparation of SWCNTs have been developed.[97,98] Amongst those are chemical vapour deposition

(CVD),[99–101] arc discharge,[102] laser ablation,[103] arc plasma jet[104] as well as plasma torch growth.[105,106] The produced SWCNTs typically display a broad range of diameters on the order of 1-3 nm with the statistical distribution of approximately two third semiconducting and one third metallic SWCNTs discussed in the previous section.[98] Due to its large scalability and the high purity of the prepared SWCNTs, CVD is the most commonly employed synthesis technique.[97,98] The process relies on the decomposition of carbon sources such as alkenes, alcohols or carbon monoxide (CO) and their deposition at moderate temperatures (< 1000 °C) onto metal catalysts (e.g. iron (Fe) or cobalt/molybdenum (CoMo)) in the gaseous phase or on substrates (e.g. SiO_2 or MgO).[97,98] The produced SWCNTs of the widely employed commercial processes HipCO® and CoMoCat® have small diameters around 0.7-1.2 nm.[99–101] Notably, the CoMoCat® process allows to produce highly preferential growth of (6,5) and (7,5) SWCNTs, highly relevant for the transport studies presented in chapter 5.[101] While arc discharge, laser ablation and arc plasma jet processes, relying on the vaporization of carbon in an inert atmosphere at high temperatures (> 1000 °C), display high quality SWCNTs, their diameter range is often wider (1-3 nm) and they are less scalable.[97,98] Instead the plasma torch process, which utilizes a direct current-driven or radio frequency-induced thermal plasma of very high temperatures (1000-15000 K) that evaporates carbon sources such as carbon black together with metallic catalysts, is highly scalable and produces SWCNTs with diameters on the order of 1.2-1.6 nm.[98,105,106] This is the underlying synthesis process of the mixed chirality, large diameter SWCNT networks discussed in chapter 5.[107]

Considering that most scalable SWCNT growth processes produce mixtures of semiconducting and metallic SWCNTs as well as amorphous carbon and potentially other carbonaceous particles or catalyst residues, further purification and sorting is necessary before they can be employed as metallic electrodes or semiconducting layers in electronic applications.[97,98,108–110] While methods of purification after the deposition of SWCNTs have been reported,[109,111] scalable fabrication methods such as ink-jet printing, require to dissolve or disperse SWCNTs in common solvents. However, SWCNTs are poorly soluble in most solvents and display bundling and aggregation due to their strong inter-nanotube van der Waals interactions.[112] Consequently, they need to be dispersed and debundled via ultrasonciation or shear-force mixing, while further stabilization is necessary to prevent re-aggregation.[113] Such stabilization as well as the basis for the subsequent purification can be achieved via covalent or non-covalent selective chemical functionalization.[108] Non-covalent funcionalization is preferential since it does not modify the electronic structure of the SWCNTs. While the first sorting methods via

non-covalent DNA wrapping of SWCNTs are selective and have more recently also demonstrated selectivity to the handedness of many SWCNTs,[114–117] their scalability is still limited.[98] Scalable and highly selective separation methods include dispersion of SWCNTs with surfactants such as sodium dodecyl sulphate (SDS) and cholates and subsequent density gradient ultracentrifugation (DGU),[108,118] gel chromatography of SWCNTs dispersed in SDS (relying on the different interaction strength of semiconducting and metallic SWCNTs with the gel)[119] as well as wrapping of the SWCNTs with conjugated polymers by mixing them in organic solvents such as toluene or xylene and subsequent centrifugation steps.[109,120,121]

The diameter-selected SWCNT networks presented in this thesis were obtained via polymer wrapping (see section 3.1.2 and chapter 5). This process relies on the non-covalent π-π interactions of the conjugated polymers and the SWCNTs, while its yield and selectivity depend on the SWCNT raw material, the choice of solvent as well as the employed polymer.[98,109] The most widely used conjugated polymers, which are all selective to semiconducting SWCNTs, are polyfluorenes, polyfluorene copolymers and regio-regular polythiophenes, while other NDI and DPP-based conjugated polymers have also been employed successfully.[98,109,120,121] There is currently no complete understanding of the polymer wrapping process, although it is e.g. proposed that the selectivity to semiconducting SWCNTs originates from the difference in polarity between these and the metallic SWCNTs.[109] It is suggested that the stronger polarizability of metallic SWCNTs leads to the formation of stronger dipoles in polymer-wrapped metallic SWCNTs which then lead to a higher likelihood of bundling and sedimentation during the subsequent centrifugation steps.[109] Despite the lack of a complete understanding a broad range of parameters such as the polarity of the solvent, the polymer to SWCNT ratio, the ultrasonication temperature as well as the side chain length and molecular weight of the conjugated polymers have been found to influence the yield and selectivity.[98,109] The solvent should be a good solvent for the conjugated polymer, but simultaneously a poor one for the SWCNTs, leading to the dispersion of only polymer-wrapped SWCNTs. The density of the solvent should be lower than that of SWCNTs, allowing the sedimentation of SWCNT bundles during the centrifugation step. It is suggested that highly polar solvents such as tetrahydrofuran (THF) prevent the interaction of stronger dipoles of polymer-wrapped metallic SWCNTs and thereby impede their aggregation as well as sedimentation and hence the selectivity of the process.[109] With respect to the conjugated polymers, it has been found that lower molecular weight increases the yield but decreases the selectivity of the dispersion, which has been ascribed to the increased viscosity of the high molecular weight polymer

solution.[122] Furthermore, longer alkyl side chains lead to the dispersion of larger diameter SWCNTs, but also lower selectivity.[121,123] Before using the dispersions for device fabrication, further filtration and solvent washing is necessary to remove the detrimental unbound polymer (see section 3.1.2). Another synthetically more challenging but elegant route is to employ removable and recyclable conjugated polymers such as poly[(9,9-di-*n*-dodecyl-2,7-fluorendiyl-dimethine)-(1,4-phenylene-dinitrilomethine)] (PF-PD), which can be depolymerized after SWCNT separation under mild acidic conditions.[124]
With the application of these sorting techniques it has been possible to achieve more than 40 kinds of enriched (n, m) SWCNTs and their enantiomers (non-superimposable mirror image and hence selectivity of their handedness) in the diameter range of 0.6-1.5 nm, which are summarized in Fig. 1.10.[110] While purities of > 96 % for polymer-wrapping

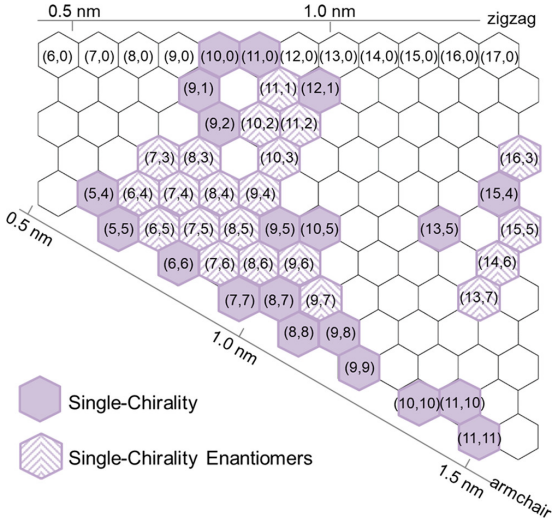

Figure 1.10. Overview of separated enriched SWCNT species. More than 40 different (n, m) SWCNT chiralities and some of their enantiomers have been successfully enriched with high purity using the discussed sorting techniques. The figure has been adopted from ref. [110].

and > 99 % for other techniques such as gel chromatography have been realized,[125,126] further improvements of selectivity and yield are necessary for widespread commercial application of SWCNTs.[110]

1.4 Thin-film transistors

Thin-film transistors (TFTs) are a class of metal-oxide-semiconductor field-effect transistors (MOSFETs), which are widely employed for active-matrix addressing in LED displays (section 1.1) as well as frequently used to study charge transport in thin-film

semiconductors.[12,98,127] TFTs are composed of an active thin-film semiconducting layer, which is in contact with two metallic source and drain electrodes of width W, separated by the channel length L and used for charge carrier injection and extraction, as well as an insulating dielectric separating the semiconducting layer from the metallic gate electrode (Fig. 1.11a). Consequently, TFTs are usually three terminal devices in which

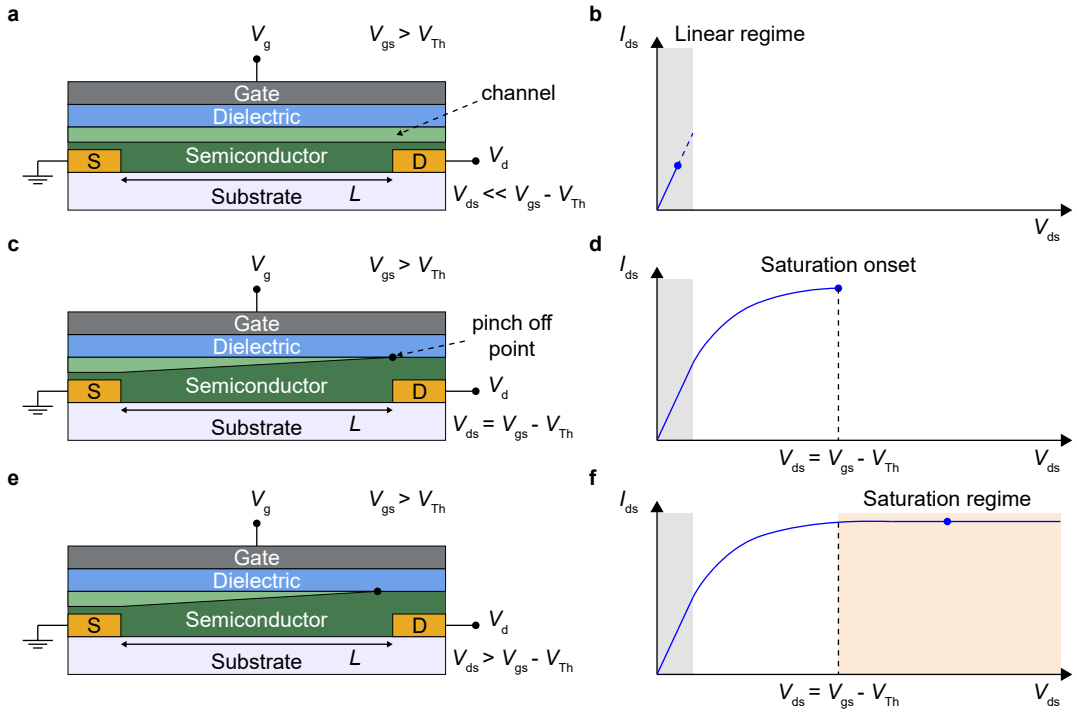

Figure 1.11. TFT structure and operation principle. Schematics of a TFT structure including the charge accumulation channel (light green) as well as the corresponding output characteristics in the linear regime (a, c), at the onset of saturation (b, d) and the saturation regime (e, f) are shown. The source (S) and drain (D) electrodes are shown in golden colour. It is worth to note that the dimensions of the schematics are chosen for clarity of illustration. In practise, the substrate is typically hundreds of µm thick, while all other layers are only tens to hundreds of nanometer thick. The charge accumulation channel is only a few nm in height and a larger channel height in the schematic represents a higher charge density.

the charge density and thereby conductivity in the semiconducting layer is tuned via the applied gate voltage (V_{gs}), controlling the current flow between source and drain electrode (I_{ds}). The most widely applied TFT structures are the coplanar bottom-contact, bottom-gate (BC/BG) architecture as well as the staggered configurations top-contact, bottom-gate (TC/BG) and bottom-contact, top-gate (BC/TG), which is employed throughout this thesis.[127] In contrast to enhancement-mode MOSFETs, which operate in the inversion mode, TFTs based on undoped organic semiconductors and semiconducting SWCNT networks, discussed in this thesis, operate in the accumulation

mode, since these active layers display low intrinsic carrier concentrations. The source electrode is typically grounded and the drain as well as gate voltage (V_{ds} and V_{gs} respectively) are applied with respect to this grounded source potential. In order to deduce the general operation principle of accumulation-mode TFTs, unipolar charge accumulation is considered. Depending on the polarity of the applied gate voltage either holes for negative gate voltages or electrons for positive gate voltages are injected from the source electrode and accumulated at the semiconductor-dielectric interface. The following considerations are explained for electron accumulation (V_{gs}, $V_{\mathrm{ds}} > 0$), while the argumentation for hole accumulation (V_{gs}, $V_{\mathrm{ds}} < 0$) is obtained analogously. Once the applied gate voltage exceeds the threshold voltage (V_{Th}), which marks the onset of mobile carrier accumulation and is usually non-zero due to built-in dipoles, interface states, impurities and particularly the existence of trap states, the uniformly distributed mobile charge density per unit area is given by $Q_{\mathrm{mob}} = C_{\mathrm{i}}(V_{\mathrm{gs}} - V_{\mathrm{Th}})$, with C_{i} being the areal capacitance (Fig. 1.11a).[127] It should be noted that the concept of a threshold voltage in accumulation-mode TFTs can be misleading and that this voltage is not related to the onset of any inversion layer as it was introduced originally for MOSFETs.[128] Upon further application of a drain voltage, the potential along the channel ($V(x)$) becomes dependent on its position ($x \in (0, L)$). Within the gradual channel approximation,[129] which assumes that the vertical electric field due to the gate voltage is much larger than the lateral field due to the source-drain voltage and ensures that the charge distribution along the channel is determined by the gate voltage, the charge density along the channel is expressed as:

$$Q_{\mathrm{mob}} = C_{\mathrm{i}}(V_{\mathrm{gs}} - V_{\mathrm{Th}} - V(x)). \tag{1.16}$$

Neglecting any diffusion contribution to the drain-source current, it is given by:

$$I_{\mathrm{ds}} = W\mu Q_{\mathrm{mob}} E_{\mathrm{x}} = W\mu C_{\mathrm{i}}(V_{\mathrm{gs}} - V_{\mathrm{Th}} - V(x))\frac{dV(x)}{dx}, \tag{1.17}$$

with μ the field-effect carrier mobility and E_{x} the lateral electric field at position x. Furthermore, neglecting any contact resistance effects as well as the charge density dependence of the field-effect mobility (further discussion below), the variables can be separated and integration from 0 to L respectively 0 to V_{ds}, leads to:

$$I_{\mathrm{ds}} = \frac{W}{L}\mu C_{\mathrm{i}}\left[(V_{\mathrm{gs}} - V_{\mathrm{Th}})V_{\mathrm{ds}} - \frac{1}{2}V_{\mathrm{ds}}^2\right]. \tag{1.18}$$

Based on this relation both output (I_{ds} versus V_{ds} for fixed V_{gs}, Fig. 1.11) as well as transfer (I_{ds} versus V_{gs} for fixed V_{ds}) curves are the characterizing current-voltage

relations of an FET. Two regimes of operation, the linear regime with $V_{ds} \ll V_{gs} - V_{Th}$ as well as the saturation regime with $V_{ds} \geq V_{gs} - V_{Th}$ are distinguished. For small drain-source voltages ($V_{ds} \ll V_{gs} - V_{Th}$) Eq. 1.18 simplifies to:

$$I_{ds} = \frac{W}{L}\mu_{lin}C_i(V_{gs} - V_{Th})V_{ds}. \tag{1.19}$$

Hence, in this linear regime the source-drain current increases linearly with the source-drain voltage (V_{ds}) for a fixed gate voltage (Fig. 1.11b). Neglecting contact resistance effects the linear field-effect mobility is found as:

$$\mu_{lin} = \frac{L}{WC_iV_{ds}}\frac{\partial I_{ds}}{\partial V_{gs}}. \tag{1.20}$$

When the drain voltage is further increased to $V_{ds} = V_{gs} - V_{Th}$, the channel is pinched off (Fig. 1.11c, d) and a depletion region forms near the drain electrode since the difference between the local potential $V(x)$ and the gate voltage is smaller than the threshold voltage. Upon further increase of the source-drain voltage, the depletion region extends, which slightly narrows the length of the channel, while the potential at the pinch off point remains $V_{gs} - V_{Th}$ and hence the source-drain current I_{ds} saturates (Fig. 1.11e, f). Consequently, $V_{ds} = V_{gs} - V_{Th}$ marks the onset of the saturation regime, for which the source-drain current is obtained from Eq. 1.18 via substitution of $V_{ds} = V_{gs} - V_{Th}$:

$$I_{ds} = \frac{W}{2L}\mu_{sat}C_i(V_{gs} - V_{Th})^2. \tag{1.21}$$

Therefore, when neglecting contact resistance and the gate voltage dependence of the mobility, the saturation mobility reads as:

$$\mu_{sat} = \frac{2L}{WC_i}\left(\frac{\partial\sqrt{|I_{ds}|}}{\partial V_{gs}}\right)^2. \tag{1.22}$$

While the presented analysis is instructive for an understanding of the operation principle of TFTs and Eqs. 1.20 and 1.22 are frequently employed in literature to study charge transport in organic semiconductors and SWCNT networks, their underlying assumptions of negligible contact resistance and a gate voltage independent field-effect mobility are usually not satisfied.[130,131] Particularly in the field of organic semiconductors, the application of these simplified equations for the extraction of mobilities from non-ideal current-voltage characteristics has lead to significant overestimations of the field-effect mobilities in the past decade.[131] In order to ensure a more accurate extraction of the field-effect mobilities both contact resistance and the gate-voltage dependence of the mobilities should be considered. Due to the energy differences between the metal work

functions of the electrodes and the HOMO (respectively valence band) as well as LUMO (respectively conduction band), and surface states that cause Fermi-level pinning, the injecting contacts are usually not ohmic but Schottky contacts. Contact engineering via the treatment of the contacts with self-assembled monolayers to induce surface dipoles that modify the injection barrier or insertion layers that tune the work function of the metal electrodes has established as a viable route to reduce contact resistance and obtain more ideal FET characteristics.[132,133] Furthermore, careful investigation of the potential overestimation and underestimation of the field-effect mobilities due to contact resistance as well as refined measurement routines such as the transfer length method or less prone to device variations, gated four-point-probe (4pp) measurements have been devised.[130,132–134] For gated 4pp measurements, the 4pp linear mobility can be expressed as:

$$\mu_{4\mathrm{pp}} = \frac{D}{WC_\mathrm{i}} \frac{\partial}{\partial V_\mathrm{gs}} \left(\frac{I_\mathrm{ds}}{V_{4\mathrm{pp}}} \right), \tag{1.23}$$

with D the centre-to-centre spacing and $V_{4\mathrm{pp}}$ the potential difference between the 4pp voltage probes.[130] The broad Gaussian state distribution in strongly disordered organic semiconductors, Coulomb interactions between charge carriers in narrow-band semicrystalline polymer semiconductors as well as the one dimensional nature of the DoS in SWCNTs, can for instance further lead to an intrinsic dependence of the field-effect mobility on charge density (further discussion in chapter 2).[61,135–137] Equation 1.23 is used for the extraction of linear field-effect mobilities in this thesis since it can be used even if the mobility is intrinsically charge density dependent.[130] In addition to gated 4pp measurements, another approach based on ref. [138], considering both gate voltage dependence of the mobility and contact resistance is used for the extraction of saturation mobilities in chapter 4. In this approach the source-drain current in the gradual channel approximation is expressed as:[138]

$$I_\mathrm{ds} = \frac{W}{L} C_\mathrm{i} \int_{V_{\mathrm{S}^*}}^{V_{\mathrm{D}^*}} \left(\int_0^{V_\mathrm{gs} - V_\mathrm{on} - V(x)} \mu(v) dv \right) dV(x), \tag{1.24}$$

with $\mu(v)$ the charge density dependent mobility, V_{S^*} and V_{D^*} the effective source and drain potentials (which are different from 0 and V_ds due to the contact resistance related voltage drops across the semiconductor-electrode interfaces) and V_on the onset voltage of charge accumulation in the channel. Assuming the increase of the voltage drop across the source resistance with applied gate voltage to be limited ($\frac{dV_{\mathrm{S}^*}}{dV_\mathrm{gs}} \ll 1$), the saturation mobility is obtained analogously to Eq. 1.22 with an additional gate voltage dependent correction factor $k(V_\mathrm{gs})$ arising from the gate voltage dependence of the mobility.[138] In case of organic semiconductors for which the mobility often follows a power law

relation $\mu_{\mathrm{sat}} \propto (V_{\mathrm{gs}} - V_{\mathrm{on}})^{\beta}$, with $\beta > 0$ characterizing the steepness of the gate voltage dependence, the correction factor becomes gate-voltage independent and the saturation mobility is obtained as:[138]

$$\mu_{\mathrm{sat}} = \frac{2L}{WC_{\mathrm{i}}} \left(\frac{\partial \sqrt{|I_{\mathrm{ds}}|}}{\partial V_{\mathrm{gs}}} \right)^2 \frac{2(\beta + 1)}{\beta + 2}. \tag{1.25}$$

From this gate voltage dependent saturation mobility of the charges that are added in the interval dV_{gs}, the effective gate voltage dependent saturation mobility of the total charge density at gate voltage V_{gs} is obtained as $\mu_{\mathrm{sat,\,eff}} = \frac{1}{V_{\mathrm{gs}} - V_{\mathrm{on}}} \int_{V_{\mathrm{on}}}^{V_{\mathrm{gs}}} \mu_{\mathrm{sat}}(V'_{\mathrm{gs}}) dV'_{\mathrm{gs}}$.[138] The temperature and charge density dependence of the field-effect mobility provides insights into the charge transport of the active semiconducting layer, which will be further discussed in chapter 2 for conjugated polymers and semiconducting SWCNT networks.

Chapter 2

Background and theory

2.1 Charge transport in organic semiconductors

In conventional crystalline, covalently bound inorganic semiconductors charge transport is characterized by Bloch-Boltzmann theory which considers a perfect lattice in which electrons are described by fully delocalized Bloch waves with well-defined wave vectors ($\vec{k}$). Interactions of electrons with lattice vibrations and ionized impurities are much weaker than the electronic interactions (transfer integrals J_{ij}) and can therefore be treated perturbatively.[139,140] However, such band transport treatment is only appropriate as long as the mean-free-path of carriers (distance between two subsequent scattering events) is greater than the atomic spacing ($l \gtrsim a$, Mott-Ioffe-Regel limit) or equivalently when the semiclassical scattering rate $1/\tau$ is much smaller than the electronic transfer rate $J/\hbar$ between lattice sites.[8,139] In van der Waals bonded molecular semiconductors as well as conjugated polymer semiconductors positional and energetic disorder due to e.g. torsions along the polymer backbone, paracrystalline disorder, variations in the conjugation length as well as molecular packing distances or different local dipolar environments of the molecules or repeat units, as well as strong electron-phonon interactions, have prompted the development of new transport theories. Charge carriers in these materials are able to lower their energy with respect to the HOMO and LUMO energies (see section 1.2.1) through these strong electron-phonon interactions, thereby forming polarons, which are quasiparticles that consist of the charge carrier and a surrounding region of molecular distortions.[141,142] The polaronic nature of charge carriers has been demonstrated for both molecular semiconductors as well as conjugated polymer semiconductors via the observations of new optical transitions in charge modulation spectroscopy (CMS) which measures the change in transmission upon charge accumulation in an FET.[141,143] However, energetic disorder typically dominates over polaron relaxation effects in the electrical characteristics of organic FETs respectively the temperature activation of the field-effect mobility.[141,144,145] Neglecting Coulombic electron-electron interactions (see further discussion in section 2.3.2) and considering

the linear electron-phonon coupling approximation, the outlined electron-phonon interactions and energetic considerations can be expressed by the Holstein-Peierls model Hamiltonian:[140,143]

$$\begin{aligned} H &= H^0_{\mathrm{el}} + H^0_{\mathrm{ph}} + V^{\mathrm{local}}_{\mathrm{el-ph}} + V^{\mathrm{non-local}}_{\mathrm{el-ph}}, \\ H^0_{\mathrm{el}} &= \sum_j \epsilon_j a^\dagger_j a_{\mathrm{j}} + \sum_{\substack{i,\,j \\ i \neq j}} J_{ij} a^\dagger_i a_{\mathrm{j}}, \\ H^0_{\mathrm{ph}} &= \sum_{\vec{q},\,s} \hbar\omega_{\vec{q},\,s} \left(b^\dagger_{\vec{q},\,s} b_{\vec{q},\,s} + \frac{1}{2} \right), \\ V^{\mathrm{local}}_{\mathrm{el-ph}} &= \sum_{\vec{q},\,s} \sum_j \hbar\omega_{\vec{q},\,s} g_{jj,\,\vec{q},\,s} \left(b^\dagger_{\vec{q},\,s} + b_{-\vec{q},\,s} \right) a^\dagger_j a_j, \\ V^{\mathrm{non-local}}_{\mathrm{el-ph}} &= \sum_{\vec{q},\,s} \sum_{\substack{i,\,j \\ i \neq j}} \hbar\omega_{\vec{q},\,s} g_{ij,\,\vec{q},\,s} \left(b^\dagger_{\vec{q},\,s} + b_{-\vec{q},\,s} \right) a^\dagger_i a_j. \end{aligned} \tag{2.1}$$

The Holstein-Peierls Hamiltonian consists of the pure electronic Hamiltonian (H^0_{el}), the Hamiltonian of the phonon subsystem (H^0_{ph}), as well as the local electron-phonon interactions ($V^{\mathrm{local}}_{\mathrm{el-ph}}$) modifying the site energies ϵ_j and the non-local electron-phonon interactions ($V^{\mathrm{non-local}}_{\mathrm{el-ph}}$) modulating the transfer integrals J_{ij} between sites. Furthermore, $a^\dagger_j$ and a_j denote the creation and annihilation operators of an electron at site j respectively, $b^\dagger_{\vec{q},\,s}$ and $b_{\vec{q},\,s}$ are the creation and annihilation operators of a phonon of branch s with energy $\hbar\omega_{\vec{q},\,s}$ and wave vector $\vec{q}$ respectively and $g_{jj,\,\vec{q},\,s}$ as well as $g_{ij,\,\vec{q},\,s}$ are the local and non-local electron-phonon coupling constants respectively. Static on-site diagonal disorder (σ) in the distribution of site energies ϵ_j and off-diagonal disorder (Σ) in the transfer integrals J_{ij} can be considered in their distribution.[143]
The formulation of the Hamiltonian in Eq. 2.1 is very general and in the appropriate limits different transport regimes such as polaron band transport, disorder-based transport, small polaron based hopping transport or transient localization can emerge.[139] In order to distinguish these vastly different regimes the relative energy scales of the electronic coupling (transfer integrals J_{ij}), the vibrational energies ($\hbar\omega_{\vec{q},\,s}$), the electron-phonon couplings ($g_{jj,\,\vec{q},\,s}$ and $g_{ij,\,\vec{q},\,s}$) and the thermal energy ($k_{\mathrm{B}}T$) need to be evaluated.[139,146]
The breakdown of semiclassical transport theory due to estimated mean-free paths on the order of the intermolecular spacing ($l \sim a$) based on the typical magnitude of transfer integrals, phonon frequencies and electron-lattice coupling strengths for organic molecular crystals (e.g. $J_{ij} = J = 143$ meV, $\omega_0 = 6.2$ meV and $\lambda = \alpha^2 \frac{\hbar}{2M\omega_0} \frac{J}{\hbar\omega_0} = 0.17$ for rubrene, where α defines the coupling strength in real space modulating the transfer integrals $J_{ij,\,\mathrm{mod}} = J[1 - \alpha(u_i - u_j)]$, $u_i - u_j$ the relative molecular displacements), has been traditionally interpreted as a manifestation of polaronic localization of carriers.[139]

Consequently, following the first studies in the 1950s of such small polaron transport by Holstein for molecular crystals,[147,148] many further studies of such Holstein-type Hamiltonians considering only local electron phonon coupling ($g_{ij,\vec{q},s} = 0$) and their extensions to non-local electron phonon coupling (such as the Su-Schrieffer-Heeger Hamiltonian[50]) have been investigated.[149,150] These theories are based on a polaron transformation of the Holstein-Peierls Hamiltonian (Eq.2.1) to effectively cancel the electron-phonon interaction terms by changing the electron operators into "dressed" polaron operators. The kinetic energy terms still contain phonon operators which cannot be treated exactly and therefore the crucial band-narrowing approximation, treating the polaron kinetic energy by averaging the phonons over their thermal state, is applied.[139,150] This approximation is only valid when the phonon cloud can instantaneously follow the motion of the carrier, which is when the phonon frequencies are much larger than the transfer integrals ($J \ll \hbar\omega_0$, non-adiabatic limit). However, as outlined for rubrene above, this condition is usually not fulfilled in organic semiconductors, which are typically in the adiabatic limit ($J \gg \hbar\omega_0$) where the electron can follow the slow motion of the molecular vibrations instantaneously.[139] Due to the insufficient description of charge transport by both semiclassical as well as small polaron transport theories, the transient localization transport regime has been proposed for organic molecular semiconductors. The fundamental mechanism of this transport regime is that large amplitude thermal molecular vibrations lead to dynamic disorder which in turn leads to localization of the wavefunction on timescales shorter than the molecular vibrations, which strongly limits carrier diffusion.[139,151,152] This description is in agreement with the bandlike field-effect mobility in molecular crystals decreasing as a power law with increasing temperature at higher temperatures (approx. > 200 K) due to a decreased localization length caused by increased thermal disorder. For lower temperatures extrinsic disorder is dominant leading to a temperature-activated field-effect mobility.[8,152]

Not only molecular organic semiconductors but also conjugated polymer semiconductors, have been studied in the Holstein-type polaron model ($g_{ij,\vec{q},s} = 0$) in the non-adiabatic limit ($J \ll \hbar\omega_0$), particularly in the case of weak electronic coupling ($J \approx 0$). In this regime the electron wavefunction localizes on a single site and the Hamiltonian can be exactly diagonalized, with the site energies ϵ_j being stabilized by the polaron binding energy $E_\mathrm{p} = \frac{1}{N}\sum_{\vec{q},s} \hbar\omega_{\vec{q},s} \left| g_{jj,\vec{q},s} \right|^2$. The polaron binding energy is equal to half the reorganization energy associated with an intermolecular electron transfer reaction and can be further simplified when a single optical dispersionless phonon mode ($\omega_{\vec{q},s} = \omega_0$, $g_{jj,\vec{q},s} = g$) is considered ($E_\mathrm{p} = \frac{\lambda_\mathrm{reorg}}{2} = \hbar\omega_0 g^2$).[140,143] Further considering the classical

limit of high temperatures ($\hbar\omega_0 \ll k_\mathrm{B}T$), the electron transfer rate respectively the hopping rate for phonon-assisted incoherent hopping between localized states from one site to another, obeys an Arrhenius-type law and equals the Marcus equation for electron transfer:[140,141,153]

$$k_\mathrm{ET} = \frac{J^2}{\hbar}\left(\frac{\pi}{2E_\mathrm{p}k_\mathrm{B}T}\right)^{1/2}\exp\left(-\frac{E_\mathrm{p}}{2k_\mathrm{B}T}\right). \tag{2.2}$$

Consequently, the mobility in this non-adiabatic, high-temperature limit can be expressed as:[140,141]

$$\mu = \frac{ea^2}{k_\mathrm{B}T}\frac{J^2}{\hbar}\left(\frac{\pi}{2E_\mathrm{p}k_\mathrm{B}T}\right)^{1/2}\exp\left(-\frac{E_\mathrm{p}}{2k_\mathrm{B}T}\right) = \frac{ea^2}{k_\mathrm{B}T}\nu\exp\left(-\frac{E_\mathrm{p}}{2k_\mathrm{B}T}\right), \tag{2.3}$$

where ν is the attempt frequency. However, as discussed above the non-adiabatic limit is usually not justified and additionally effects of static disorder (in the on-site energies (σ) and transfer integrals (Σ)) typically outweigh such polaronic effects.[141,146] Therefore, the next section discusses such disorder-based transport models which have been and are still widely employed to explain charge transport in conjugated polymers.[61,154–162]

2.1.1 Disorder-based transport models for conjugated polymers

The origin of localization in disorder-based transport models is the presence of strong disorder leading to Anderson localization of carriers.[163] This is in contrast to small polaron theories, which consider the formation of "self-trapped" charges in the non-adiabatic limit ($J \ll \hbar\omega_0$) via localized polaron formation even in the absence of disorder. Phonon-assisted hopping motion between such localized states was originally discussed by Mott for strongly disordered inorganic semiconductors such as amorphous silicon as well as impurity conduction in weakly doped and compensated crystalline inorganic semiconductors.[155,164] Depending on the degree of disorder of the conjugated polymers, solely hopping between localized states or for less disordered systems trapped charges below and delocalized transport above a mobility edge (ME models) as well as hybrid models of these two have been considered (Fig. 2.1).[61,144,156,165] These disorder-based transport models are originally based on phenomenological assumptions of specific hopping rates and energetic site distributions, rather than (molecular dynamics) simulations of the polymer morphology and first-principle calculations of site energies and transfer integrals that are further discussed in the following section. The distribution of on-site energies due to the variation of polymer conjugation lengths and different local dielectric environments is represented by an exponential, Gaussian or more complex density of

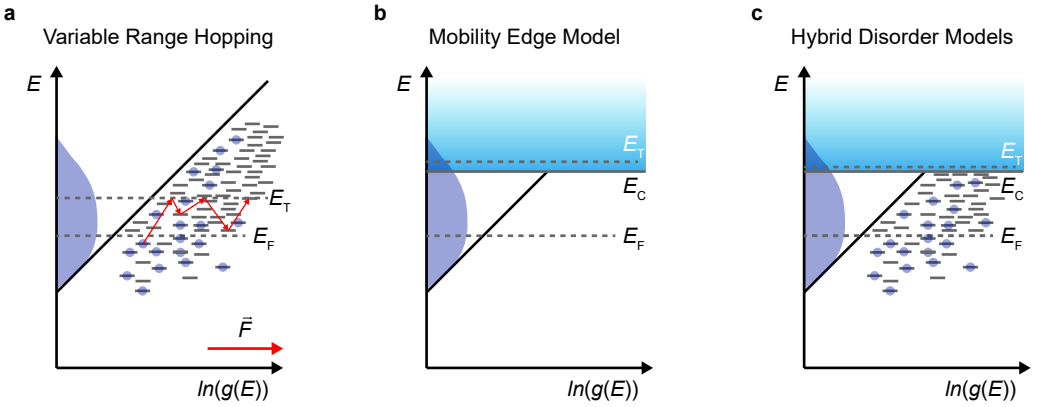

Figure 2.1. Simplistic illustration of disorder-based transport models. Simplified illustrations of the DoS (logarithmic axis) and characteristic energies of the most widely employed disorder-based transport models, the variable range hopping model (a), the mobility edge (ME) model (b) and their hybrid models (c) are shown. The hopping of electrons (with either Miller-Abrahams or extended Marcus rate, Eqs. 2.4 and 2.5) upon application of an electric field $\vec{F}$ is illustrated, with predominant hopping to the transport level E_T ((a), further discussion in section 2.3, Eq. 2.26), the accumulated charge density is shown in dark blue, delocalized states in the band are shown in light blue and in this region the DoS is not explicitly shown. The band edge E_C and Fermi level E_F are indicated. For the ME model (b) the localized states below the band edge are not illustrated. These states are all considered to be trap states in the original model.

states (DoS).[61,144,156] The shape of this DoS has been reasoned by the Gaussian shape of absorption spectra of disordered conjugated polymers and both uncorrelated and correlated site distributions due to long range permanent electric dipole moments have been considered.[156,166] The most widely employed hopping rates are the Miller-Abrahams rate as well as extensions of the Marcus hopping rate (Eq. 2.2) when considering both polaronic and energetic disorder effects.[140]

The Miller-Abrahams rate was computed for weakly doped and compensated crystalline inorganic semiconductors in the low (liquid helium) temperature limit and under these conditions in the weak electron-phonon coupling limit the hopping rate W_{ij} from site i to site j can be expressed as:[140,167]

$$W_{ij} = \nu \exp(-2\gamma R_{ij}) \begin{cases} \exp\left(-\frac{\epsilon_j - \epsilon_i - e\vec{R}_{ij}\vec{F}}{k_\mathrm{B}T}\right), & \epsilon_j \geq \epsilon_i + e\vec{R}_{ij}\vec{F} \\ 1, & \epsilon_j < \epsilon_i + e\vec{R}_{ij}\vec{F} \end{cases}, \tag{2.4}$$

with ν being the attempt hopping frequency, R_{ij} the hopping distance between sites i and j, γ the inverse localization length of the localized wavefunction and $\vec{F}$ the applied electric field. The first term takes into account that with increasing distance between the localized states (R_{ij}), the electronic overlap and therefore the tunnel probability decreases. The second factor accounts for the fact that upward hopping between sites of large energetic

difference ($\epsilon_j - \epsilon_i$) is unlikely as it requires the absorption and emission of high-energy phonons or multi-phonon processes which are however not considered in Eq. 2.4.[140,168] Application of an electric field ($\vec{F}$) can further reduce the energetic difference between sites and increase the upward hopping rate. Downward hops are instead assumed to be independent of the site energies and therefore also independent of the electric field. The formulation of the hopping rate in Eq. 2.4 assumes that site i is occupied and site j is unoccupied, the corresponding occupation probabilities p_i and p_j need to be considered separately in the calculation of the macroscopic transport coefficients. Although Emin has been pointed out that the applicability of the Miller-Abrahams rate is limited to the very low temperature limit and that multi-phonon processes need to be considered at higher temperatures, Eq. 2.4 has been employed frequently outside its range of validity to explain charge transport in disordered conjugated polymers at room temperature.[149,156,159,162,168] However, potentially supported by the multitude of fitting (parameterization) parameters, good agreement with transport in low-mobility disordered conjugated polymers has been found.[159]

The other widely employed hopping rate, an extension of the Marcus rate to non-uniform site distributions, which is valid in the weak electronic coupling and strong electron-phonon coupling regime at high temperatures ($J \ll \hbar\omega_0 \ll k_\mathrm{B}T$) can be expressed as:[140,162]

$$W_{ij} = \frac{J^2}{\hbar}\left(\frac{\pi}{2E_\mathrm{p}k_\mathrm{B}T}\right)^{1/2}\exp(-2\gamma R_{ij})\exp\left[-\frac{(2E_\mathrm{p}+\epsilon_j-\epsilon_i)^2}{8E_\mathrm{p}k_\mathrm{B}T}\right]. \tag{2.5}$$

The underlying assumptions as well as the fact that the rate does not keep increasing for $\epsilon_j - \epsilon_i < -2E_\mathrm{p}$, in contrast to the constant factor in the Miller-Abrahams rate independent of the energetic difference for downward hops, render the extended Marcus rate likely more applicable to disordered conjugated polymers.[140,162]

The most common approaches to calculate the macroscopic transport coefficients, most notably the electrical conductivity as well as field-effect mobility, from the introduced hopping rates, are Monte Carlo simulations, numerical solution of the Master equation and the development of analytic approximations using percolation and effective medium theory.[61,154,156,159,162,169,170] The frequently employed approaches by Pasveer *et al.* as well as Vissenberg and Matters are representatively briefly outlined. Pasveer *et al.* considered a Gaussian DoS and iteratively solved the steady-state Master equation:

$$\sum_{i\neq j}[W_{ij}p_i(1-p_j) - W_{ji}p_j(1-p_i)] = 0, \tag{2.6}$$

using the Miller-Abrahams hopping rate (Eq. 2.4) for W_{ij} as well as the Fermi-Dirac distribution as an initialization of the occupancy probability p_i in the absence an

electric field, for the site occupancy probabilities p_i in the presence of an electric field in x-direction (F).[159] The factors $p_i(1-p_j)$ ensure that the initial sites are occupied and the final sites unoccupied. They further considered a cubic lattice, allowed for variable range hopping (generally referring to the dependence of W_{ij} on R_{ij} and $\epsilon_j - \epsilon_i$ in Eqs. 2.4 and 2.5) and consequently obtained the mobility according to Ohm's law:

$$\mu = \frac{\sum_{i,j} eW_{ij}p_i(1-p_j)R_{ij,x}}{pFV}, \tag{2.7}$$

with $R_{ij,x}$ the hopping distance in x-direction, the charge density $p = \frac{e<p_i>}{a^3}$, a the lattice constant and a system volume up to $V = (150\,a)^3$.[159]
Vissenberg and Matters instead consider an exponential DoS ($g(\epsilon) = \frac{N_\mathrm{t}}{k_\mathrm{B}T_0}\exp(\frac{\epsilon}{k_\mathrm{B}T_0})$, $-\infty < \epsilon \leq 0$, N_t the total DoS and T_0 characterizing the width of the DoS) as an approximation of the Gaussian DoS since they further consider low carrier densities ($-E_\mathrm{F} \gg k_\mathrm{B}T_0$).[61] In the low field regime they represent the system as a resistor network with conductances $G_{ij} = G_0\exp(-s_{ij})$ between site i and j, considering variable range hopping as in Eqs. 2.4 and 2.5 via $s_{ij} = 2\gamma R_{ij} + \frac{|\epsilon_i - E_\mathrm{F}| + |\epsilon_j - E_\mathrm{F}| + |\epsilon_i - \epsilon_j|}{2k_\mathrm{B}T}$.[61,154,170] Using percolation theory they write the conductivity of the system as:

$$\sigma = \sigma_0\exp(-s_\mathrm{c}), \tag{2.8}$$

where σ_0 is a fitting parameter and s_c is the exponent of the critical percolation conductance $G_\mathrm{c} = G_0\exp(-s_\mathrm{c})$. It is determined by the critical bond number $B_\mathrm{c} \approx 2.8$ for three dimensional amorphous systems. For this average bond number per site, the resistor network, with only those connections present for which $G_{ij} > G_\mathrm{c}$, forms the first infinite cluster.[61] From there they can easily derive the field-effect mobility for temperatures $T \leq T_0$:

$$\mu = \frac{\sigma_0}{e}\left(\frac{\pi(\frac{T_0}{T})^3}{(2\gamma)^3 B_\mathrm{c}\Gamma(1-\frac{T_0}{T})\Gamma(1+\frac{T_0}{T})}\right)^{\frac{T_0}{T}} \cdot \left[\frac{(C_iV_\mathrm{g})^2}{2k_\mathrm{B}T_0\epsilon_\mathrm{s}}\right]^{\frac{T_0}{T}-1}, \tag{2.9}$$

with the Gamma function Γ, C_i the areal capacitance, V_g the gate voltage and ϵ_s the dielectric constant of the semiconductor.[61]
For the further discussion (see chapter 4) it is important to note the common features of these disorder-based transport models with respect to the macroscopic transport coefficients. The field-effect mobility mostly shows an Arrhenius-type temperature dependence ($\mu \sim \mu_0\exp(-\frac{E_\mathrm{a}}{k_\mathrm{B}T})$) with a characteristic activation energy E_a, as well as an increasingly strong temperature and charge density dependence with increasing disorder (e.g. in Eq. 2.9: $\mu \sim n^{\frac{2T_0}{T}-2}$). Furthermore, the dimensionality d of the

system influences the temperature dependence of the transport coefficients, e.g. the temperature dependence of the conductivity for variable-range hopping introduced by Mott has been shown to follow $\sigma \sim \sigma_0 \exp\left(-(\frac{T_0}{T})^{\frac{1}{d+1}}\right)$.[155,171]

2.1.2 Narrow-band transport in high-mobility conjugated copolymers

As outlined in section 1.2.2 tremendous progress in the performance of conjugated polymers has been made over the past decades, particularly with the development of high-mobility ($\mu > 1$ cm^2 V^{-1} s^{-1}) donor-acceptor copolymers in the past decade (Fig. 1.5c-g).[65–69] While the presented disorder-based transport models in the previous section have provided an acceptable framework for strongly disordered polymers ($\sigma \gg k_\mathrm{B} \cdot 300$ K ~ 26 meV, σ the standard deviation of the Gaussian DoS) with mobilities around $\mu \leq 10^{-2}$ cm^2 V^{-1} s^{-1}, they have been shown to be inappropriate for low-disorder conjugated copolymers.[54,135,172] This will be discussed in detail from a perspective of both charge and thermoelectric transport in chapter 4.[172] While static diagonal and off-diagonal disorder are still the transport limiting factors, one of the most striking features that all these high-mobility donor-acceptor conjugated copolymers have in common is their narrow bandwidth and low energetic disorder on the order of $\sigma \sim k_\mathrm{B} \cdot 300$ K ~ 26 meV.[54,135,172–175] It has been suggested from the study of a one-dimensional model Hamiltonian that the narrower bandwidth compared to homopolymers, originating from the copolymeric nature, results in higher resilience to disorder and that it promotes the electronic transitions between more localized states in the tail of the DoS to more delocalized states higher in the state distribution simply because they are energetically closer due to the narrowness of the band (Fig. 2.2a).[145,173,176] Furthermore, the origin of the low energetic disorder (σ) has been attributed to the extended rigid, fused-ring conjugated units that minimize variations of the dihedral angles in the polymer backbone and thereby allow for nearly planar, low-disorder conformations.[8,54] However to further qualitatively understand the transport in these systems, the transport processes at molecular, meso (10-100 nm) and large (0.1-1 µm) length scales need to be considered. Quantitatively these could be derived from multiscale theoretical simulations involving molecular dynamics simulation of a realistic morphology, partitioning into conjugation units (ϵ_j, Eq. 2.1, which might be extended over several monomers and π-π stacks), the calculation of transfer integrals (J_{ij}, Eq. 2.1) as well as transition rates (W_{ij}, e.g. Eq. 2.5) and the simulation of the transport dynamics via numerical solution of the Master equation (Eq. 2.6) or Monte

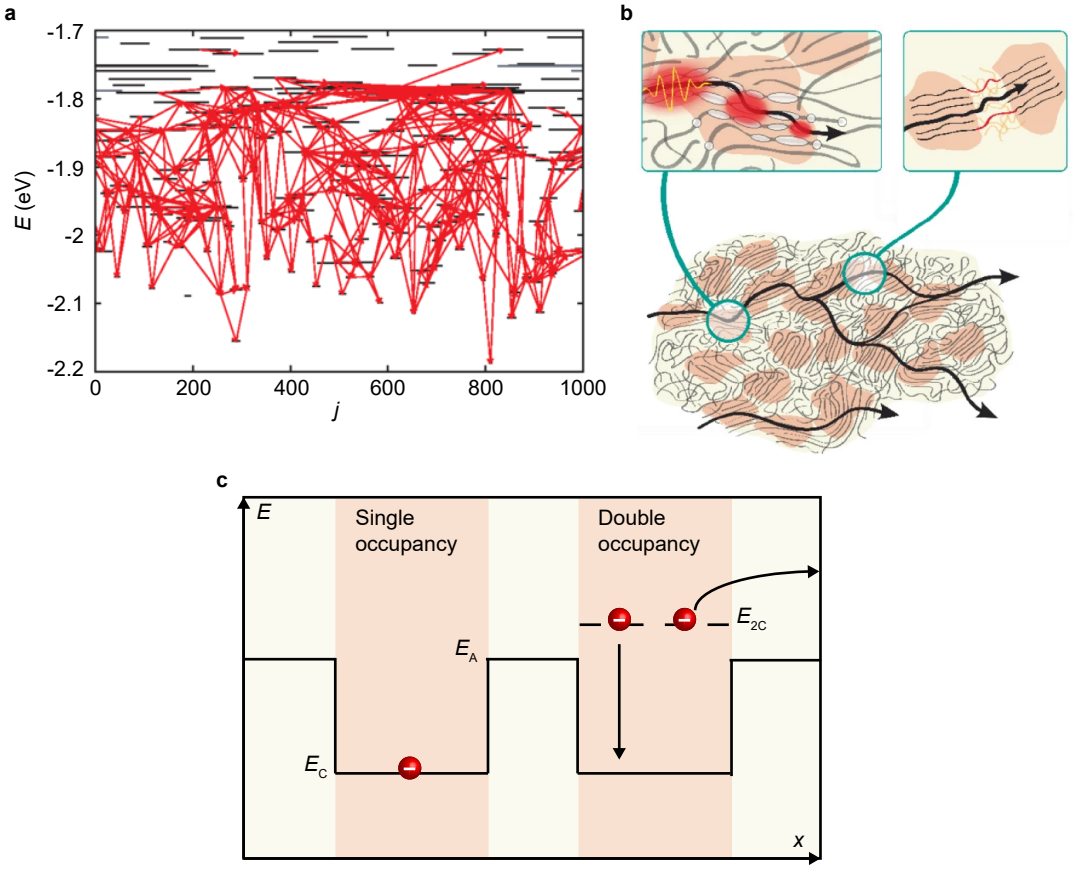

Figure 2.2. Electronic transitions, semicrystalline microstructure and electron-electron interactions. Panel (a) shows the eigenstates ($\psi_l^0 = \sum_j c_{j,l}|j\rangle$) and eigenenergies ($E_j$) computed from the diagonalization of a one-dimensional electronic Hamiltonian (H_{el}^0, Eq. 2.1) for a disordered polymer chain with 1000 monomers with ϵ_j set to 0 eV, electronic couplings $J = 1$ eV, diagonal disorder $\sigma = 100$ meV and off-diagonal disorder $\Sigma = 100$ meV. The eigenstates are represented by horizontal lines, centered on the sites where $c_{j,l}^2$ is maximum and with lengths according to the localization length defined as $2(\langle j^2\rangle - \langle j\rangle^2)^{1/2}$. The states at higher energy show larger delocalization and as evident from the most significant electronic transitions for the mobility (red lines) are of particular importance for charge transport and long range hops.[145,173] Panel (b) shows the semicrystalline microstructure with coexisting crystalline (light red) and amorphous (light yellow) domains. The top left inset highlights the transport in the crystalline domains showing conjugation units of different lengths (white ellipses) as well as wavefunctions (eigenstates) with different degrees of localization (red ellipses). Tie chains connecting the crystalline domains are highlighted in the top right inset. Panel (c) illustrates the electron-electron interactions in the crystalline domains of low-disorder, high-mobility semicrystalline conjugated polymers that have been proposed by Di Pietro *et al.* as a mechanism to overcome the barriers to the amorphous domains leading to Coulomb enhanced charge transport.[135] Detailed discussion of these is provided in chapter 4.[172] Panels (a) and (b) have been adapted from refs. [145] and [8] respectively.

Carlo simulations.[177,178] While on a molecular scale charge carrier mobilities of several hundred $\text{cm}^2\ \text{V}^{-1}\ \text{s}^{-1}$ have been measured,[8] the mesoscale arrangement and transport is particularly crucial in determining the performance of these conjugated polymers. With

typical device scales on the order of several to tens of μm, polymer chain lengths on the order of 100 nm and persistence lengths on the order of 10 nm, limiting inter-chain transport processes are inevitable. Furthermore, using grazing incidence wide-angle X-ray scattering (GIWAXS), optical absorption as well as electroluminescence measurements, it has been established that the mesoscale arrangement of most of these copolymers is characterized by a semicrystalline microstructure with the coexistence of crystalline and amorphous domains (Fig. 2.2b).[55] Due to the increased conjugation, energy levels are stabilized in the crystalline domains, leading to charge accumulation almost exclusively in these regions.[55,135] For efficient transport on the mesoscale, charge carriers need to be able to efficiently traverse the amorphous domains between these crystalline domains, which are on the order of 5-50 nm long.[8,55] Consequently, the importance of long bridging tie chains has been established and provides an explanation for the observed increasing field-effect mobilities with increasing molecular weight (M_W), saturating at around 100 kg mol^{-1}.[8,55,179] These insights further underline the importance of rigid backbones and high densities of crystalline domains enabling their efficient bridging via kink-free tie chains. On the large scale of carrier transport further long range order via aligned orientations of these crystalline domains and tie chains further improves charge transport.[72,75]

Considering the narrow bands and low energetic disorder on the order of $\sim k_\mathrm{B} \cdot 300$ K in these conjugated copolymers as well as the spatial confinement of accumulated charge carriers to the crystalline domains, it is worth to investigate whether the underlying assumption of negligible electron-electron interactions commonly assumed in charge transport modelling of these systems, e.g. on a basis of the Holstein-Peierls Hamiltonian (Eq. 2.1), is still justified. When Coulombic interactions (U) become comparable to $k_\mathrm{B}T$ and the electronic transfer integrals (J), such assumption breaks down. The simplest models that account for such electron-electron interactions are based on the Hubbard (only on-site Coulombic interactions) and extended Hubbard (also nearest-neighbour Coulombic interactions) Hamiltonians,[180,181] which have e.g. been employed to explain Mott metal-insulator transitions and will be further discussed in the context of thermoelectric transport in section 2.3.2. Di Pietro *et al.* have proposed that charge transport in semicrystalline conjugated polymers is enhanced by Coulombic interactions.[135] They have tuned the crystalline domain size in semicrystalline films of P(NDI2OD-T2) (Fig. 1.5g) via the choice of different solvents and the annealing temperature. Both vacuum dried as-cast and 200 °C annealed films displayed Urbach energies (E_u), characterizing the energetic width of the sub-bandgap absorption tail, in photothermal deflection spectroscopy (PDS) measurements on the order of 30 meV,

indicating low energetic disorder.[54,174] In contrast to disorder-based transport models the more crystalline films with larger crystalline domains (from GIWAXS measurements), showed a higher and more strongly charge density dependent field-effect mobility. Furthermore, charge accumulation spectroscopy (CAS), measuring the change in transmission ($\Delta T/T$) upon charge accumulation in an FET, revealed a direct correlation between the conjugation length and crystalline domain size (at comparable levels of paracrystallinity). For a given crystalline domain size the bleaching signal changes linearly with gate-voltage indicating essentially complete accumulation of charge carriers in the crystalline domains. Yet, the bleaching signal does not change its shape between gate voltages of 20-80 V, indicating that the average conjugation length explored by charge carriers with increasing charge density does not change significantly. This in turn suggests that the strong charge density dependence of the mobility in films of P(NDI2OD-T2) with large crystalline domains does not originate from a change in the extent of delocalization of electronic states with increasing energy, which is likely of significance for other, particularly more disordered systems.[173,176] Considering that the number of crystalline domains is comparable to the number of accumulated carriers in an FET ($\sim 10^{18}$-10^{19} cm^{-3}), multiple occupancy of crystalline domains is statistically likely. Therefore, Coulombic interactions of carriers in these domains, which scale with the crystalline domain size, is proposed as a mechanism for enhanced transport across the energetic barrier to the amorphous domains as well as the stronger charge density dependence of the mobility of films with larger crystalline domains (Fig. 2.2c).[135] These findings provide the basis for the further investigations of both charge and thermoelectric transport in these systems in chapter 4.

2.2 Charge transport in SWCNT networks

Similarly to the discussion of charge transport in conjugated polymer films, it is important to distinguish the transport processes at different length scales in SWCNT networks. For this purpose intra-SWCNT transport respectively transport in single SWCNTs as well as the disorder-based and heterogenous transport models reported for SWCNT networks focusing on the inter-SWCNT transport component are discussed.

2.2.1 Transport in single SWCNTs

As expected from the electronic structure of SWCNTs discussed in section 1.3.1, charge transport in single SWCNTs is dependent on their chirality respectively diameter (d), their length (L_t) as well as on the temperature, charge density and applied field

strength ($|\vec{F}|$). In the low field-regime (less than several volts per µm), for L_t on the order of several hundred nanometers and even at room temperature, transport in pure SWCNTs has been found to be ballistic.[17,18,79] In this scattering-free regime, with the mean free path of carriers much larger than the tube length ($l_\mathrm{mfp} \gg L_\mathrm{t}$) and in the absence of contact resistance, their conductance approaches the quantum conductance

$$G_\mathrm{q} = \frac{dI}{dV} = \frac{2e^2}{h} N_\mathrm{ch} = G_0 N_\mathrm{ch}, \tag{2.10}$$

with h being Planck's constant and N_ch the number of propagating modes. For metallic SWCNTs $N_\mathrm{ch} = 2$ due to the double degeneracy of the lowest subband and therefore the quantum resistance is given by $R_\mathrm{q} = \frac{h}{4e^2} \approx 6.45$ kΩ.[17,79] However, when the electronic mean free path becomes shorter than the tube length ($l_\mathrm{mfp} < L_\mathrm{t}$), transport becomes diffusive and the SWCNT resistance can be written as:[79]

$$R(L_\mathrm{t},\, T,\, |\vec{F}|) = R_\mathrm{res} + R_\mathrm{q} \left(1 + \frac{L_\mathrm{t}}{l_\mathrm{mfp}(T,\, |\vec{F}|)} \right) = R_\mathrm{c} + R_\mathrm{q} \frac{L_\mathrm{t}}{l_\mathrm{mfp}(T,\, |\vec{F}|)}, \tag{2.11}$$

with $R_\mathrm{c} = R_\mathrm{res} + R_\mathrm{q}$ being the total contact resistance and R_res a parasitic resistance for not fully (mode) transparent contacts to the SWCNT. For low fields and moderate temperature ($\lesssim 300$ K), the dominant source of electron scattering is from acoustic phonons with mean free paths on the order of 0.3-1 µm.[18,182–184] Consequently, resistances per unit length for SWCNTs ($\frac{R_\mathrm{q}}{l_\mathrm{mfp}}$) around 6-8 kΩ µm^{-1} have been found in this regime.[182,184] Considering the well-defined lattice structure in SWCNTs (section 1.3.1), their large transfer integrals and low disorder, Bloch-Boltzmann theory is well suited for the description of their macroscopic transport coefficients. Consequently, electron-phonon scattering is treated perturbatively and the transition rates ($W_{\vec{k},\,\vec{k}+\vec{q}}$) are obtained from Fermi's golden rule via the electron-phonon matrix elements based on e.g. a Su-Schrieffer-Heeger Hamiltonian with non-local dispersive electron-phonon couplings.[50,183,185,186] Subsequently, the steady-state multi-band Boltzmann transport equation (further discussion of the BTE in section 2.3.1) in the presence of an electric field is solved to calculate the mobility.[183,186] Both these theoretical considerations as well as experimental findings have shown that the field-effect mobility for low fields scales with the diameter squared and is anti-proportional to temperature ($\mu_0 \sim \frac{d^2}{T}$).[183,184] Room temperature mobilities are on the order of $10^3 - 10^4$ cm^2 V^{-1}s^{-1}, exceeding the mobilities of conjugated polymers discussed in the previous section even on the molecular scale by orders of magnitude.[184] For higher fields of several volts per µm (or in general higher energies, populated due to higher temperatures or charge densities), optical phonon scattering becomes the dominant scattering mechanism,

with significantly stronger electron-phonon coupling, reducing the mean free path to $\sim 10 - 100$ nm.[18,183,185,187] As a consequence only for very short devices (~ 10 nm) quasi-ballistic transport can be observed, while for longer tubes as well as high fields and also for low fields and high temperatures (> 300 K) transport is diffusive with strong optical phonon scattering of carriers.[18,183] In this regime the carrier velocity saturates and the mobility decreases with increasing electric field ($\mu^{-1} = \mu_0^{-1} + v_s^{-1} |\vec{F}|$, v_s the saturation velocity).[183] Furthermore, the strongly peaked DoS with several van Hove singularities (Fig. 1.8) inevitably leads to a strong charge density dependence of the mobility upon subband filling.[136,137,184]

2.2.2 Disorder-based and heterogeneous transport models for SWCNT networks

Compared to the well-established understanding of microscopic transport mechanisms and the dependence of macroscopic transport on charge density, temperature, electric field strength as well as SWCNT diameter and length in single SWCNTs, the respective understanding in SWCNT networks of controlled diameter composition is still in its infancy.[11] Before the development of SWCNT sorting techniques (discussed in section 1.3.2), modelling of transport in SWCNT networks was based on percolation theory (see also section 2.1.1), focusing on taking the metallic to semiconducting SWCNT ratio into account as well as to consider geometrical parameters of the network such as network density, SWCNT average length and distribution as well as their orientation.[188–192] Such approaches mostly employ the generation of random, typically 2D stacked networks composed of 1D sticks that represent the SWCNTs.[190,191] These random networks are subsequently translated into random resistor networks by assigning each SWCNT a length dependent resistance (Eq. 2.11) as well as each junction a constant resistance. From *I-V* and conductive atomic force microscopy (AFM) measurements junction resistances have been found to be larger for metallic-semiconducting SWCNT junctions than for metallic-metallic or semiconducting-semiconducting SWCNT junctions due to the formation of Schottky barriers, while the junction resistance has been found to decrease with increasing tube respectively bundle diameter and is on the order of 10s to 100s of kΩ.[193,194] Based on these resistor networks Kirchhoff's circuit laws are numerically solved and the network resistance has been found to decrease with increasing network density, partial alignment and increased SWCNT length due to the resulting fewer junctions that carriers experience along the transport paths.[189–191] However, these models offer little insight into the microscopic transport mechanisms and ignore the diameters of the SWCNTs composing the networks and the resulting

energetic landscape.[11] Already for mixed metallic and semiconducting SWCNT networks the temperature dependence of the conductivity was investigated and considering the much higher resistances of junctions compared to the SWCNTs, variable range hopping (VRH, see section 2.1.1) or fluctuation induced tunneling (FIT) between tubes have been proposed for the intertube transport process.[195–197] FIT describes the tunneling of charges across tunnel junctions between two large conducting regions due to voltage fluctuations across these junctions caused by the random thermal motion of carriers (Johnson noise). In a heterogeneous model proposed by Kaiser *et al.* for conducting conjugated polymers and SWCNT ropes and mats, the resistance consequently consists of a metallic intratube component to the resistivity as well as an intertube component of the form $\rho \sim \rho_0 \exp(\frac{T_B}{T+T_0})$, with T_B characterizing the temperature for which significant thermal excitation above the tunneling barrier is likely to occur and T_0 being the temperature above which thermal voltage fluctuations due to Johnson noise are relevant.[195,196,198] This model will be further discussed in extended form in chapter 5. In these early studies the lack of control over the metallic to semiconducting SWCNT ratio as well as the tube diameters prohibited more detailed insights into the microscopic transport mechanisms.

Subsequently, Yanagi *et al.* tuned the ratio of metallic to semiconducting SWCNTs in SWCNT buckypaper using density gradient ultracentrifugation and reported strong changes in the temperature dependence of the conductivity with changing metallic to semiconducting SWCNT ratio.[199] Purely metallic networks showed quantum transport phenomena such as weak localization, while with increasing ratio of semiconducting tubes, crossovers to Mott VRH (see section 2.1.1) with $d = 3$, then to $d = 2$ and for pure semiconducting SWCNT networks to Coulomb-gap-type conduction due to Coulomb interactions between localized electrons with $d = 1$ were reported. The origin for the strong disorder was hypothesized to be due to Schottky barriers between metallic and semiconducting tubes, and variations in the tube diameter and resulting bandgaps for pure semiconducting tubes.[199] However, the impact of the diameter composition and resulting energetic landscape on charge transport in SWCNT networks was only recently explored.[11,200–205] Using gate voltage dependent electroluminescence measurements it has been shown that in mixed diameter (0.8-1.1 nm) polymer-sorted semiconducting SWCNT networks the diameter composition has a strong impact on charge transport.[200] For low gate voltages (and hence charge densities) large diameter, small bandgap SWCNTs dominate the transport paths even if their relative ratio in the network is low. With increasing gate voltage smaller diameter, large bandgap SWCNTs start contributing to conduction, suggesting that narrow diameter distributions are beneficial for transport

and high on-currents in FETs. To understand the resulting charge density dependence of the mobility more quantitatively a random resistor model taking into account the diameter and length distribution of the SWCNTs as well as the diameter-dependent DoS of the individual SWCNTs composing the networks has been illustrative.[202] The model is based on a Master equation approach as discussed in section 2.1.1 and a resulting resistor network for low electric fields, in which the nodes represent the individual SWCNTs, while the bonds are the junction resistances (Fig. 2.3). However, these

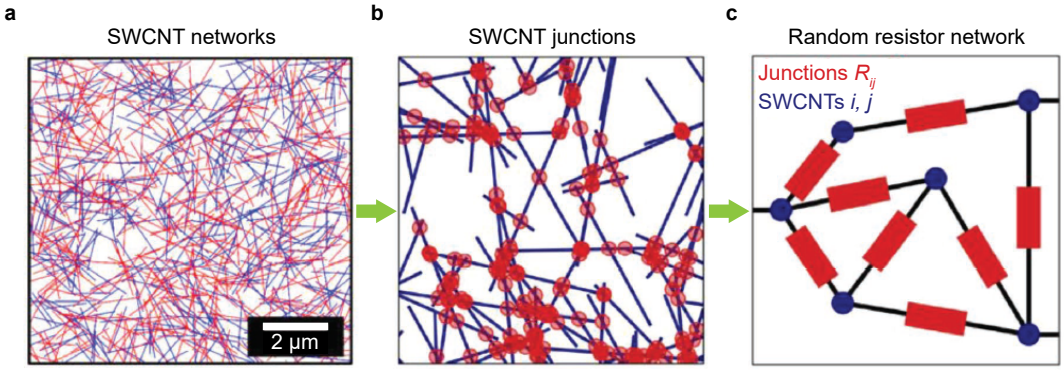

Figure 2.3. Illustration of random resistor networks for modelling of charge transport in SWCNT networks. The basic steps of random network generation ((a), different colours for different chiralities), SWCNT junction identification (b) and creation of the random resistor network with the SWCNTs representing the nodes and the junctions being the bonds with resistances R_{ij} between SWCNTs i and j (c) are shown. The figures have been adapted from ref. [11].

junction resistances are not taken as constants as in the percolation models discussed in the previous paragraph, but are instead calculated based on the Fermi level position (and hence charge density) via a Miller-Abrahams hopping rate between energy levels within the first subband DoS of the individual SWCNTs constituting the junction.[202] The resistances of the SWCNTs themselves are neglected since they have been shown to be much smaller than the junction resistances.[193,194,206] The predicted charge density dependence of the mobility of mixed diameter networks is in good agreement with experimental data and particularly the turnover from increasing to decreasing mobility with increasing charge density due to subband filling is found.[202] Nevertheless, recent measurements have shown a stronger charge density and temperature dependence of the mobility of polymer-sorted monochiral (6,5) SWCNT networks compared to mixed large diameter SWCNT networks, which cannot be explained within this random resistor model for which a narrower DoS distribution should lead to a weaker temperature dependence as in all disorder-based transport models.[203,204] This raises the question whether the intra-nanotube transport ($\mu \sim T^{-1}$) needs to be considered or whether

other scattering mechanisms and geometrical factors of the junctions are at play. Therefore, the charge density and temperature dependence of the field-effect mobility and field-effect-modulated Seebeck coefficient, which will be discussed in the next sections, of polymer-sorted semiconducting SWCNT networks with controlled diameter composition will be discussed in detail in chapter 5. Evidently, extrinsic factors to transport such as charge carrier trapping through the presence of residual oxygen and water or strong dipolar disorder due to an interface with a high-κ dielectric will be minimized to get insights into the intrinsic charge and thermoelectric transport of SWCNT networks.[207–209]

2.3 The Seebeck coefficient

As outlined in section 1.1, the Seebeck coefficient is defined as the ratio of the built-up thermal voltage to a temperature difference across a conducting system ($S = \frac{V_{\mathrm{th}}}{\Delta T}$). Thermoelectric effects such as the Seebeck, the Peltier as well as the Thomson effect are described by irreversible thermodynamics, which is based on the postulates of thermostatics and time reversal symmetry, meaning that the physical laws do not change upon replacing the time t with $-t$ and the magnetic field $\vec{B}$ with $-\vec{B}$.[210,211] While there are statistical-mechanical treatments of these irreversible thermodynamic processes such as the Kubo formalism,[212,213] which are particularly useful for the treatment of interacting many-body systems and will be briefly discussed in section 2.3.2, an introduction of the Seebeck coefficient based on the Onsager theorem should be given.[214,215] From a thermodynamic point of view the Seebeck coefficient is the entropy transported by a charge carrier divided by its charge, which will become more evident from the following considerations.[210,211]

For a system with electric and heat current flow in x-direction (considered without loss of generality) and in the absence of a magnetic field the linear dynamical equations can be written as:[210]

$$-J_{\mathrm{N}} = L_{11}\frac{1}{T}\nabla\mu + L_{12}\nabla\frac{1}{T}, \tag{2.12}$$

$$J_{\mathrm{Q}} = L_{12}\frac{1}{T}\nabla\mu + L_{22}\nabla\frac{1}{T}, \tag{2.13}$$

where J_{N} is the number of electrons current density, J_{Q} is the heat current density, μ is the electrochemical potential (per particle) of the electrons, T is the temperature and L_{ij} are the kinetic coefficients. Here the Onsager theorem $L_{ij}(\vec{B}) = L_{ji}(-\vec{B})$, stating that the kinetic coefficient L_{ij} measured in an external magnetic field $\vec{B}$ is identical to L_{ji} measured in the reverse magnetic field, has already been employed by equating

$L_{21} = L_{12}$ in the absence of a magnetic field.[210] From Eqs. 2.12 and 2.13 the electrical conductivity (σ), thermal conductivity in the absence of particle flow (κ_{T}) and Seebeck coefficient (S) can be easily written in terms of the kinetic coefficients. The electrical conductivity is defined as the electric current density (eJ_{N}) per unit potential gradient $\frac{1}{e}\nabla\mu$ in an isothermal system. Note that $\frac{1}{e}\nabla\mu = \vec{E} + \frac{1}{e}\nabla\mu_{\mathrm{c}}$, with $\vec{E}$ the electric field and $\frac{1}{e}\nabla\mu_{\mathrm{c}}$ an electric driving force due to a concentration gradient. Hence, the conductivity reads as:

$$\sigma \equiv \frac{-eJ_{\mathrm{N}}}{\frac{1}{e}\nabla\mu}, \qquad \text{for } \nabla T = 0 \tag{2.14}$$

and using Eq. 2.12 it follows that:

$$\sigma = \frac{e^2 L_{11}}{T}. \tag{2.15}$$

The thermal conductivity in the absence of particle flow (κ_{T}) is defined as the heat current density per unit temperature gradient for zero electric current:

$$\kappa_{\mathrm{T}} \equiv \frac{-J_{\mathrm{Q}}}{\nabla T}, \qquad \text{for } eJ_{\mathrm{N}} = 0 \tag{2.16}$$

and using Eqs. 2.12 and 2.13 it follows that:

$$\kappa_{\mathrm{T}} = \frac{L_{11}L_{22} - L_{12}^2}{T^2 L_{11}}. \tag{2.17}$$

Finally, the Seebeck coefficient is defined as the electromotive force per unit temperature gradient for zero electric current:

$$S \equiv \frac{-\frac{\nabla\mu}{e}}{\nabla T}, \qquad \text{for } eJ_{\mathrm{N}} = 0 \tag{2.18}$$

and using Eq. 2.12 it follows that:

$$S = -\frac{L_{12}}{eTL_{11}}. \tag{2.19}$$

Rewriting Eqs. 2.12 and 2.13 in terms of σ, κ_{T} and S and employing $J_{\mathrm{S}} = \frac{J_{\mathrm{Q}}}{T}$ for the current density of entropy:

$$J_{\mathrm{S}} = SeJ_{\mathrm{N}} + T\kappa_{\mathrm{T}}\nabla\frac{1}{T}, \tag{2.20}$$

the thermodynamic understanding of the Seebeck coefficient as the entropy tranported by a carrier divided by its charge is evident.[210,211] Subsequently, the central task of different formalisms is to compute the kinetic coefficients L_{ij} to obtain the transport coefficients. Amongst these are the solution of the widely employed Boltzmann transport equation for systems where the carriers obey the semiclassical transport equations

between collisions, which will be discussed in the following section, or the Kubo formalism which is particularly useful for strongly interacting systems and when a good approximation of the Hamiltonian of the system is known.[212,213,216]

Before presenting the Seebeck coefficient based on the solution of Boltzmann transport equation, a very versatile and illustrative approach based on thermodynamic considerations by Fritzsche, who developed a general expression for the conductivity and (electronic contribution to the) Seebeck coefficient in the absence of electron correlation effects, but without any assumptions concerning a specific conduction process, should be outlined.[217] Consequently, the conductivity is written as an integral over single electron states (while neglecting electron correlations):

$$\sigma = \int \sigma(E)dE = e \int g(E)\mu(E)f(E)[1 - f(E)]dE, \tag{2.21}$$

with $\sigma(E)$ the energy dependent conductivity, $g(E)$ the DoS, $\mu(E)$ the energy dependent mobility and $f(E)$ the Fermi-Dirac distribution.[217] It is worth noting that Cohen *et al.* have derived the expressions for the electrical conductivity and Seebeck coefficient more rigorously using the Kubo formalism and outlined that $\mu(E)$ as defined by Fritzsche is not strictly the microscopic mobility for electron states of energy E ($\mu_{\mathrm{E}}(E)$, $v(E) = \mu_{\mathrm{E}}(E) \cdot F$, where $v(E)$ is the average velocity induced in electrons at energy E by the electric field F).[218] Comparing the definition of $\mu(E)$ by Fritzsche to the rigorous derivation from the Kubo formalism, the microscopic mobility and energy dependent mobility are related via $\mu_{\mathrm{E}}(E) = -\mu(E)[1 - f(E)]$ (see further discussion in chapter 6).[217,218] Another consequence of the Onsager theorem is the relation of the Seebeck coefficient (S) and the Peltier coefficient (Π), which is defined as the heat current density per unit electric current density in an isothermal system:

$$\Pi \equiv \frac{J_{\mathrm{Q}}}{eJ_{\mathrm{N}}}, \qquad \text{for } \nabla T = 0 \tag{2.22}$$

and using Eqs. 2.12 and 2.13 it follows that:

$$\Pi = -\frac{L_{12}}{eL_{11}} = S \cdot T. \tag{2.23}$$

Therefore, the Peltier coefficient describes the heat energy transported by a carrier divided by its charge.[217] Considering that the transported energy is measured relative to the Fermi level E_{F} and that each carrier contributes to Π in proportion to its relative contribution to the total conduction, the (electronic contribution to the) Peltier and Seebeck coefficient can generally be expressed as:[217]

$$\Pi = -\frac{1}{e} \int (E - E_{\mathrm{F}}) \frac{\sigma(E)}{\sigma} dE \tag{2.24}$$

and

$$S = -\frac{k_\mathrm{B}}{e}\int\left(\frac{E-E_\mathrm{F}}{k_\mathrm{B}T}\right)\frac{\sigma(E)}{\sigma}dE, \tag{2.25}$$

with k_B the Boltzmann constant and $\sigma(E)$ as well as σ given by Eq. 2.21. The Seebeck coefficient is $S<0$ for predominant electron conduction and $S>0$ for majority hole conduction. Defining the transport energy $E_\mathrm{T}=\frac{1}{eT}\int E\frac{\sigma(E)}{\sigma}dE$, the Seebeck coefficient can be written as:

$$S = -\frac{E_\mathrm{T}-E_\mathrm{F}}{eT}, \tag{2.26}$$

further emphasizing its thermodynamic interpretation as the entropy transported by a carrier divided by its charge. From Eq. 2.25 the established expressions for the Seebeck coefficient for single band conduction in semiconductors and metals can be derived. If charge carriers are only mobile above (below) a conduction (valence) band or mobility edge (see e.g. Fig. 2.1b), the Seebeck coefficient of semiconductors for electron conduction can be written as:[217]

$$S = -\frac{k_\mathrm{B}}{e}\left[\frac{E_\mathrm{C}-E_\mathrm{F}}{k_\mathrm{B}T}+A_\mathrm{C}\right], \qquad \text{for } E>E_\mathrm{C}, \tag{2.27}$$

as well as for hole conduction respectively:

$$S = \frac{k_\mathrm{B}}{e}\left[\frac{E_\mathrm{F}-E_\mathrm{V}}{k_\mathrm{B}T}+A_\mathrm{V}\right], \qquad \text{for } E<E_\mathrm{V}, \tag{2.28}$$

with E_C the conduction band edge, E_V the valence band edge and A_C as well as A_V given by:

$$\begin{aligned} A_\mathrm{C} &= \frac{\int_0^\infty \frac{\epsilon}{k_\mathrm{B}T}\sigma(\epsilon)d\epsilon}{\int_0^\infty \sigma(\epsilon)d\epsilon}, \qquad \text{with } \epsilon = E-E_\mathrm{C}, \\ A_\mathrm{V} &= \frac{\int_{-\infty}^0 \frac{\epsilon}{k_\mathrm{B}T}\sigma(\epsilon)d\epsilon}{\int_{-\infty}^0 \sigma(\epsilon)d\epsilon}, \qquad \text{with } \epsilon = E_\mathrm{V}-E. \end{aligned} \tag{2.29}$$

A_C and A_V account for the fact that conduction does not take place at a single energy and therefore incorporate the energetic landscape and interaction of carriers with their environment (scattering processes). However, in conventional inorganic crystalline semiconductors, for which the motion of carriers is well described by the semiclassical transport equations between collisions, these coefficients are typically found to be constants on the order of 2-4 and therefore also referred to as heat-of-transport constants.[211,217,219] For instance if $g(E)$ and $\mu(E)$ increase linearly in E for $E>E_\mathrm{C}$, then $A=3$, while if they are constant, then $A=1$.[217] For field-effect gated Seebeck coefficients of rubrene and pentacene single crystals A has been found to be on the order

of 2-3 and interpreted as a manifestation of band-like transport.[219] From the solution of Boltzmann transport equation under the relaxation time approximation, which will be discussed in the following section, a direct relationship between the scattering physics ($\tau \sim E^r$, τ the relaxation time and r characterizing the scattering mechanism) and $A = \frac{5}{2} + r$ can be established in the non-degenerate regime, where the Fermi level is far away from the band edge ($\frac{E_\mathrm{C}-E_\mathrm{F}}{k_\mathrm{B}T} \gg 1$).[220,221]
Similarly for conventional metals with wide bands, where the Fermi level E_F is deep inside the band and transport is dominated by carriers with energies $E = E_\mathrm{F} \pm k_\mathrm{B}T$, $\sigma'(E) = eg(E)\mu(E)k_\mathrm{B}T$ can be expanded by a Taylor series around $E = E_\mathrm{F}$ in Eq. 2.25 and from the first non-vanishing term Mott's formula for metals is obtained:[164,217,222]

$$S = -\frac{\pi^2}{3}\frac{k_\mathrm{B}}{e}k_\mathrm{B}T\left[\frac{d\ln(\sigma'(E))}{dE}\right]_{E=E_\mathrm{F}}. \tag{2.30}$$

Considering that $\frac{k_\mathrm{B}}{e} \sim 86\ \frac{\mu\mathrm{V}}{\mathrm{K}}$, it is evident from Eqs. 2.27, 2.28 and 2.30 that semiconductors (particularly in the non-degenerate regime) typically show Seebeck coefficients on the order of several hundred $\frac{\mu\mathrm{V}}{\mathrm{K}}$, while metals display Seebeck coefficients only on the order of a few $\frac{\mu\mathrm{V}}{\mathrm{K}}$ since transport takes place very close to the Fermi level. Furthermore, the linear temperature dependence of the Seebeck coefficient of metals as well as the decrease of the Seebeck coefficient of crystalline inorganic semiconductors with increasing temperature for sufficiently high temperatures ($S \sim T^{-1}$) is evident.[211] This introduction has revealed that the Seebeck coefficient is an effective tool to study the DoS as well as transport and scattering physics of systems and provides additional insights beyond those solely obtained from a study of the field-effect mobility.

2.3.1 The Seebeck coefficient from Boltzmann transport equation

Carriers in a perfect periodic (lattice) potential can be described as Bloch waves ($\psi_{n,\vec{k}}(\vec{r}) = u_{n,\vec{k}}(\vec{r})\exp(i\vec{k}\vec{r})$, with n the band index, $\vec{k}$ the wave vector and $u_{n,\vec{k}}(\vec{r}) = u_{n,\vec{k}}(\vec{r}+\vec{R})$) with energies $\epsilon_n(\vec{k})$ and mean velocity $\vec{v}_n(\vec{k}) = \frac{1}{\hbar}\frac{\partial\epsilon_n(\vec{k})}{\partial\vec{k}}$. In the semiclassical transport model their motion in the presence of electric ($\vec{E}(\vec{r},t)$) and magnetic ($\vec{H}(\vec{r},t)$) fields follows the semiclassical equations of motion between collisions:[216]

$$\begin{aligned}\frac{d}{dt}\vec{r} &= \vec{v}_n(\vec{k}) = \frac{1}{\hbar}\frac{\partial\epsilon_n(\vec{k})}{\partial\vec{k}},\\ \hbar\frac{d}{dt}\vec{k} &= -e\left[\vec{E}(\vec{r},t) + \frac{1}{c}\vec{v}_n(\vec{k})\times\vec{H}(\vec{r},t)\right] = \vec{F}(\vec{r},\vec{k},t),\end{aligned} \tag{2.31}$$

with c being the speed of light. In thermal equilibrium the occupation probability of the energy $\epsilon_n(\vec{k})$ is given by the Fermi-Dirac distribution function:

$$h(\vec{r},\vec{k},t) = f(\epsilon_n(\vec{k})) = \frac{1}{1+\exp\left(\frac{\epsilon_n(\vec{k})-\mu}{k_\mathrm{B}T}\right)}, \tag{2.32}$$

with μ being the electrochemical potential. However, in the presence of applied fields or temperature gradients the non-equilibrium probability distribution function $h(\vec{r},\vec{k},t)$ of finding a carrier in the phase space volume $d\vec{r}\,d\vec{k}$ at time t deviates from the Fermi-Dirac distribution function due to diffusion, collisions and the motion of carriers due to the external forces. The non-equilibrium distribution function $h(\vec{r},\vec{k},t)$ is described by Boltzmann transport equation (BTE) which describes the non-equilibrium statistical behaviour of thermodynamic systems (not restricted to electron gases):[216]

$$\frac{\partial}{\partial t}h(\vec{r},\vec{k},t) + \vec{v}_n(\vec{k})\cdot\frac{\partial}{\partial\vec{r}}h(\vec{r},\vec{k},t) + \vec{F}(\vec{r},\vec{k},t)\cdot\frac{1}{\hbar}\frac{\partial}{\partial\vec{k}}h(\vec{r},\vec{k},t) = \left(\frac{\partial}{\partial t}h(\vec{r},\vec{k},t)\right)_\mathrm{coll}, \tag{2.33}$$

where the term on the right hand side is the change of the distribution function due to collisions. In order to derive a closed form of the transport coefficients introduced in the previous section, the relaxation time approximation (RTA) is frequently made. It assumes that the distribution of electrons emerging from collisions at any time does not depend on the non-equilibrium distribution before the collision and that the collisions are responsible for restoring thermodynamic equilibrium. Under the RTA the collision term can be approximated as:

$$\left(\frac{\partial}{\partial t}h(\vec{k})\right)_\mathrm{coll} = -\frac{h(\vec{k})-f(\vec{k})}{\tau(\vec{k})}, \tag{2.34}$$

with the relaxation time $\tau(\vec{k})$. Further considering weak, spatially uniform and static electric fields and temperature gradients as well as the relaxation time to be independent of $\vec{r}$ and only energy dependent, the non-equilibrium distribution function in the absence of magnetic fields can be expressed as:[216]

$$h(\vec{k}) = f(\vec{k}) - \tau(\epsilon(\vec{k}))\left(-\frac{\partial f}{\partial\epsilon}\right)\vec{v}(\vec{k})\cdot\left[e\vec{\mathcal{E}} + \frac{\epsilon(\vec{k})-\mu}{T}\nabla T\right], \tag{2.35}$$

with $\vec{\mathcal{E}} = \vec{E} + \frac{\nabla\mu}{e}$ and μ the electrochemical potential. Similar to Eqs. 2.12 and 2.13, omitting the summation over several bands, the electric current density $\vec{j} = -\frac{e}{4\pi^3}\int\vec{v}(\vec{k})\cdot h(\vec{k})g(\vec{k})d\vec{k}$ ($g(\vec{k})$ the DoS for wavevector $\vec{k}$, for metals $g(\vec{k})=1$) and thermal current

density $\vec{j}_{\mathrm{Q}} = \frac{1}{4\pi^3}\int[\epsilon(\vec{k})-\mu]\vec{v}(\vec{k})h(\vec{k})g(\vec{k})d\vec{k}$ can be written as:

$$\vec{j} = \boldsymbol{L}^{11}\vec{\mathcal{E}} + \boldsymbol{L}^{12}(-\nabla T), \tag{2.36}$$

$$\vec{j}_{\mathrm{Q}} = \boldsymbol{L}^{21}\vec{\mathcal{E}} + \boldsymbol{L}^{22}(-\nabla T), \tag{2.37}$$

where the matrices $\boldsymbol{L}^{ij}$ are expressed in terms of:

$$\boldsymbol{\mathcal{L}}^{\alpha} = \frac{e^2}{4\pi^3}\int\left(-\frac{\partial f}{\partial\epsilon}\right)\tau(\epsilon(\vec{k}))g(\vec{k})\vec{v}(\vec{k})\vec{v}(\vec{k})(\epsilon(\vec{k})-\mu)^{\alpha}d\vec{k} \tag{2.38}$$

and consequently read as:

$$\begin{aligned}\boldsymbol{L}^{11} &= \boldsymbol{\mathcal{L}}^{0},\\ \boldsymbol{L}^{21} &= T\boldsymbol{L}^{12} = -\frac{1}{e}\boldsymbol{\mathcal{L}}^{1},\\ \boldsymbol{L}^{22} &= \frac{1}{e^2T}\boldsymbol{\mathcal{L}}^{2}.\end{aligned} \tag{2.39}$$

It is further common to define the energy dependent conductivity tensor as:

$$\boldsymbol{\sigma}(\epsilon) = \frac{e^2}{4\pi^3}\tau(\epsilon)\int\delta(\epsilon-\epsilon(\vec{k}))g(\vec{k})\vec{v}(\vec{k})\vec{v}(\vec{k})d\vec{k}, \tag{2.40}$$

leading to:

$$\boldsymbol{\mathcal{L}}^{\alpha} = \int\left(-\frac{\partial f}{\partial\epsilon}\right)(\epsilon(\vec{k})-\mu)^{\alpha}\boldsymbol{\sigma}(\epsilon)d\epsilon. \tag{2.41}$$

Consequently, following the definition of the electrical conductivity (Eq. 2.14) and Seebeck coefficient (Eq. 2.18) these can be written as:

$$\boldsymbol{\sigma} = \boldsymbol{L}^{11} = \int\boldsymbol{\sigma}(\epsilon)\left(-\frac{\partial f}{\partial\epsilon}\right)d\epsilon = \frac{e^2}{4\pi^3}\int\left(-\frac{\partial f}{\partial\epsilon}\right)\tau(\epsilon(\vec{k}))g(\vec{k})\vec{v}(\vec{k})\vec{v}(\vec{k})d\vec{k}, \tag{2.42}$$

$$\boldsymbol{S} = (\boldsymbol{L}^{11})^{-1}\boldsymbol{L}^{12} = -\frac{1}{eT}\left(\int\boldsymbol{\sigma}(\epsilon)\left(-\frac{\partial f}{\partial\epsilon}\right)d\epsilon\right)^{-1}\int\boldsymbol{\sigma}(\epsilon)(\epsilon(\vec{k})-\mu)\left(-\frac{\partial f}{\partial\epsilon}\right)d\epsilon. \tag{2.43}$$

When restricting these expressions to one dimension, the agreement with the general expressions for the conductivity and Seebeck coefficient by Fritzsche purely from thermodynamic considerations (Eqs. 2.21 and 2.25) are evident. In contrast to the general expressions by Fritzsche, the solution of BTE under the RTA provides an explicit form to calculate the transport coefficients since $g(\vec{k})$, $v(\vec{k})$ and $\tau(\epsilon(\vec{k}))$ are governed by the bandstructure of the conventional metal or crystalline inorganic semiconductor. This approach will be useful for the discussion of thermoelectric transport in SWCNTs in chapter 5. However, due to positional and energetic disorder in organic semiconductors the applicability of the derived expressions from BTE for these systems is

questionable.[223] Therefore, the limiting case of narrow-band conduction relevant for high-mobility conjugated polymers starting from the general expressions by Fritzsche will be discussed in the following section.

2.3.2 The Seebeck coefficient in organic semiconductors

In contrast to the comparatively well-established formalism for the description of thermoelectric transport coefficients in conventional metals and crystalline inorganic semiconductors, there is currently no corresponding unified description of thermoelectric transport coefficients in organic semiconductors.[223] Controlled and systematic measurements of the Seebeck coefficient in dependence of temperature and charge density in organic semiconductors are scarce.[54,172,219,224–227] The most common approach to tune the charge density and thereby the Seebeck coefficient in organic semiconductors is via molecular doping. While this approach allows to modify the charge density and conductivity over orders of magnitude, it is less suitable for the study of intrinsic charge transport in organic semiconductors, considering that the presence of molecular dopants typically introduces additional positional disorder as well as an additional electrostatic background potential due to anions or cations in the organic semiconductor thin film.[41,221,228,229] For molecularly doped conjugated polymers phenomenological relationships between the Seebeck coefficient and the electrical conductivity of $S \sim \sigma^{-\frac{1}{4}}$ or in terms of a phenomenological transport function have been reported:

$$\sigma(E,T) = \begin{cases} \sigma_0(T) \cdot \left(\frac{E-E_\mathrm{t}}{k_\mathrm{B}T}\right)^s \left(-\frac{\partial f(E)}{\partial E}\right), & E > E_\mathrm{t} \\ 0, & E < E_\mathrm{t}, \end{cases} \tag{2.44}$$

with the transport edge E_t, a temperature-dependent transport coefficient $\sigma_0(T)$ and a constant transport parameter s, which is found to be $s = 3$ for many polythiophene-based conjugated polymers and $s = 1$ for PEDOT-based polymers.[221,229] The latter transport model will be discussed in more detail in chapter 4. However, the majority of this thesis has focused on the characterization of the intrinsic charge and thermoelectric transport of conjugated polymer semiconductors as well as SWCNT networks and therefore field-effect modulated Seebeck coefficients have been investigated. Thermoelectric transport models of disordered organic semiconductors are mostly based on the disorder-based charge transport models introduced in section 2.1.1 (illustrated in Fig. 2.1). Typically electron correlations are neglected and the general expressions for the conductivity and Seebeck coefficient by Fritzsche (Eqs. 2.21 and 2.25) are assumed for further derivations.[223] Subsequently, the transport function $\sigma(E) = -eg(E)\mu_\mathrm{E}(E)f(E)$ is found, typically by

assuming a Gaussian DoS ($g(E)$) and calculating $\mu_{\mathrm{E}}(E)$ from a differential form of a generalized Einstein relation:[223,230–232]

$$\mu_{\mathrm{E}}(E) = \eta \frac{e}{k_{\mathrm{B}}T} R(E)^2 \nu_{\mathrm{esc}}(E)[1 - f(E)], \tag{2.45}$$

with η a dimensionless fit parameter, $R(E)$ the mean jump distance of a carrier located in a state of energy E and $\nu_{\mathrm{esc}}(E)$ the total escape rate. Similar to the charge transport models presented in section 2.1.1 there are many variants for the calculations of $\nu_{\mathrm{esc}}(E)$ and $R(E)$. However, the Miller-Abrahams rate (Eq. 2.4) or extended Marcus rate (Eq. 2.5) are typically used to calculate $\nu_{\mathrm{esc}}(E)$,[223,231] while a percolation argument of the form:[161]

$$\frac{4\pi}{3B_{\mathrm{c}}} R(E)^3 \int_{-\infty}^{E} g(\epsilon)(1 - f(\epsilon, \epsilon_{\mathrm{F}}))d\epsilon \cong 1, \tag{2.46}$$

with the critical bond number $B_{\mathrm{c}} \approx 2.7 - 2.8$ defined by percolation criteria,[61,161,223] is made to determine $R(E)$ as:[161,223]

$$R(E) \cong \left[\frac{4\pi}{3B_{\mathrm{c}}} \int_{-\infty}^{E} g(\epsilon)(1 - f(\epsilon, \epsilon_{\mathrm{F}}))d\epsilon \right]^{-\frac{1}{3}}. \tag{2.47}$$

Further percolation theory and Monte Carlo simulation-based approaches to describe the Seebeck coefficient in disordered organic semiconductors are reviewed in ref. [223].[223,233,234] Similar to the disorder-based charge transport models, these disorder-based thermoelectric transport models have the commonality that the predicted charge density and temperature dependence of the Seebeck coefficient increases with increasing disorder (width of the Gaussian DoS (σ)).[172,233,234] Yet, as already outlined in section 2.1.2, high-mobility conjugated copolymer semiconductors have been shown to display disorders on the order of $\sigma \sim k_{\mathrm{B}} \cdot 300$ K ~ 26 meV.[54,174] For such low-disorder systems these disorder-based models have been shown to be inappropriate and at least within a temperature range of approx. 180-300 K the narrow-band approximation has been found to provide an adequate description of the thermoelectric transport (see chapter 4).[54,135,172] In the limit of zero energetic disorder, respectively in the high-temperature narrow-band limit when the bandwidth (W) and transfer integrals (J) are much smaller than $k_{\mathrm{B}}T$ ($J, W \ll k_{\mathrm{B}}T$), the DoS can be approximated by $N = 2 \cdot N_{\mathrm{sites}}$ iso-energetic states (accounting for spin degeneracy) with energy E_{C}:

$$g(E) = N\delta(E - E_{\mathrm{C}}). \tag{2.48}$$

Consequently, in this regime the charge density is given by:[211]

$$n = \int g(E)f(E)dE = Nf(E_{\mathrm{C}}) = \frac{N}{1 + \exp\left(\frac{E_{\mathrm{C}} - E_{\mathrm{F}}}{k_{\mathrm{B}}T}\right)} \tag{2.49}$$

and the fraction of occupied sites can be expressed as $c = \frac{n}{N_{\text{sites}}} = 2 \cdot f(E_{\text{C}})$ (site occupancy ratio). Furthermore, inserting the DoS (Eq. 2.48) into the general expressions for the conductivity and Seebeck coefficient by Fritzsche (Eqs. 2.21 and 2.25, neglecting electron correlations) as well as employing Eq. 2.49, the conductivity and Seebeck coefficient in the narrow-band limit can be expressed as:

$$\sigma = e\mu_{\text{C}} f(E_{\text{C}}) \left[1 - f(E_{\text{C}})\right] = e\mu_{\text{C}} \frac{n}{N} \cdot \left[1 - \frac{n}{N}\right] = e\mu_{\text{C}} \frac{c}{2} \cdot [1 - \frac{c}{2}], \tag{2.50}$$

$$S = -\frac{E_{\text{C}} - E_{\text{F}}}{eT} = -\frac{k_{\text{B}}}{e} \ln\left(\frac{N-n}{n}\right) = -\frac{k_{\text{B}}}{e} \ln\left(\frac{2-c}{c}\right). \tag{2.51}$$

The expression for the Seebeck coefficient in Eq. 2.51 is Heikes formula for fermions with spin,[181,235] henceforth simply referred to as Heikes formula in this thesis. It predicts a temperature independent Seebeck coefficient in this high temperature regime (with all states in the band being thermally accessible) as well as a decreasing Seebeck coefficient with increasing charge density of approximately 198 $\frac{\mu\text{V}}{\text{K}\cdot\text{dec}}$ ($\frac{\partial S}{\partial \log(n)} = -\frac{k_{\text{B}}}{e}\ln(10)$). Furthermore, it is worth to note that all expressions given for the Seebeck coefficients so far have referred to the electronic contribution (change of the entropy of mixing due to the addition of a charge carrier) as well as the spin degree of freedom to the transported entropy.[211] In principle in the presence of strong electron-phonon interactions and localized states, the addition of a charge carrier can further lead to changes in the stiffness constants that govern the vibrations of the surrounding atoms of the carrier, which in turn causes two further contributions to the Seebeck coefficient. The first additional contribution is a carrier-induced increase of the vibrational entropy of the atoms leading to S_{vib}, which is temperature independent in the high temperature regime, while the second additional contribution is the vibrational energy transport that accompanies the hop of a carrier, which vanishes for high temperatures.[149,211,236] In contrast to the entropy of mixing respectively the electronic contribution to transported entropy, S_{vib} is charge density independent. While these vibrational entropy contributions have been found to be on the order of 200 $\frac{\mu\text{V}}{\text{K}}$ in pentacene thin films,[237] a surprisingly low gate-voltage dependence of the Seebeck coefficient was reported in these measurements. Considering the small polaron binding energies of high-mobility conjugated polymers,[144] as well as the recently reported field-effect-modulated Seebeck coefficient measurements of IDTBT and DPP-based copolymers,[54,227] these vibrational entropy contributions to the Seebeck coefficient of high-mobility conjugated copolymers are presumed to be negligibly small and are therefore not further considered in this thesis.[227] Venkateshvaran *et al.* have extended Heikes formula via the consideration of a certain fraction of trapped carriers ($f = \frac{n_{\text{trap}}}{n}$, due to shallow traps), consequently replacing n with $n \cdot (1 - f)$ in Eq. 2.51.

Considering that N is on the order of the monomer density ($N \sim 10^{20} - 10^{21}$ cm^{-3}) and the charge density $n \sim 10^{18} - 10^{19}$ cm^{-3} in field-effect transistors, they assumed $n \ll N$ and found $S = -\frac{k_\mathrm{B}}{e} \ln\left(\frac{2N_\mathrm{sites}}{n \cdot (1-f)}\right)$, in good agreement with their temperature-independent Seebeck coefficients of IDTBT and PBTTT in the temperature range of 200-300 K.[54] For the further discussion in chapter 4, the inclusion of electron-electron interactions in the narrow-band limit as discussed for a Hubbard model Hamiltonian by Chaikin and Beni should be briefly discussed.[180,181] As discussed, both the general expressions for the electrical conductivity and Seebeck coefficient by Fritzsche (Eqs. 2.21 and 2.25), as well as those obtained from the solution of BTE under the RTA (Eqs. 2.42 and 2.43) are concerned with one electron states in the absence of electron correlations. A basic model system to take such electron-electron interactions into account is to consider the Hubbard Hamiltonian with on-site Coulomb repulsion U:[180,181]

$$H = J \sum_{i,\sigma} (a^\dagger_{i,\sigma} a_{i+1,\sigma} + a^\dagger_{i+1,\sigma} a_{i,\sigma}) + U \sum_i n_{i,\uparrow} n_{i,\downarrow}, \tag{2.52}$$

where J is the transfer integral, $a^\dagger_{i,\sigma}$ and $a_{i,\sigma}$ denote the creation and annihilation operators of an electron at site i with spin σ respectively and $n_{i,\uparrow} = a^\dagger_{i,\uparrow} a_{i,\uparrow}$ as well as $n_{i,\downarrow} = a^\dagger_{i,\downarrow} a_{i,\downarrow}$ are the number operators for spin-up and spin-down electrons at site i respectively. Using the Kubo formalism to compute the Seebeck coefficients of systems with large many-body interactions, they express the Seebeck coefficient as:[180,181,213]

$$S = \frac{-\frac{S^{(2)}}{S^{(1)}} + \frac{\mu}{e}}{T}, \tag{2.53}$$

with the chemical potential μ and the correlation functions:

$$S^{(1)} = \frac{1}{2} \frac{e^2}{k_\mathrm{B} T} \int_0^\infty \langle v v(\tau) + v(\tau) v \rangle d\tau, \tag{2.54}$$

$$S^{(2)} = \frac{1}{2} \frac{e}{k_\mathrm{B} T} \int_0^\infty \langle Q v(\tau) + v(\tau) Q \rangle d\tau, \tag{2.55}$$

with $v(\tau) = \exp(\tau H) v \exp(-\tau H)$, $\langle \cdots \rangle$ denoting thermal averaging, v is the velocity operator and Q the energy flux operator.[180] The important outcome for the further discussion in chapter 4, is that in the limiting case of $k_\mathrm{B}T \gg U$ (non-interacting regime) Heikes formula in Eq. 2.51 is recovered and in the opposite regime $U \gg k_\mathrm{B}T$ (regime of strong Coulomb interactions) the Seebeck coefficient is given by:

$$S = -\frac{k_\mathrm{B}}{e} \ln\left(\frac{2 \cdot (1-c)}{c}\right) = -\frac{k_\mathrm{B}}{e} \ln\left(\frac{N-2n}{n}\right), \tag{2.56}$$

with c the site occupancy ratio.[180,181] This is essentially a modified Heikes formula forbidding double occupancy of a site i due to the strong on-site Coulomb interaction.

The relevance of electron-electron interactions for charge and thermoelectric transport in semicrystalline conjugated copolymers with low energetic disorder will be further discussed in chapter 4.

2.3.3 The Seebeck coefficient in SWCNT networks

The fundamental understanding of the intrinsic thermoelectric transport of single SWCNTs as well as diameter-selected SWCNT networks is comparatively (if not more) limited compared to that of organic semiconductors.[24,47] This is partly due to the fact that control over specific diameters of SWCNTs via the sorting methods discussed in section 1.3.2 have only recently emerged.[118,120,125] Before the broad accessibility of SWCNT purification techniques, studies have focused on SWCNT ropes and mats with statistically distributed mixtures of metallic (approx. one third) and semiconducting (approx. two thirds) SWCNTs.[195,238,239] These have mainly focused on phenomenologically explaining the temperature dependence of the Seebeck coefficient based on linear or quasi-1D metallic contributions from the metallic SWCNTs, phonon-drag contributions at low temperatures, as well as temperature-activated contributions from the semiconducting SWCNTs.[195,238,239] Yet, these studies are still of relevance for diameter-selected SWCNT networks, e.g. in terms of the development of heterogeneous transport models.[195,198,239] It is typically considered that the SWCNT themselves rather than the SWCNT junctions dominate the thermoelectric transport due to their much longer extensions (factor $> 10^3$) and presumed larger thermal resistance over which most of the temperature difference drops (see further discussion in chapter 5).[47,198,239] Charge density and temperature-dependent measurements of the Seebeck coefficient of both single SWCNTs as well as diameter-selected SWCNT networks are scarce.[24,240,241] For single metallic SWCNTs Mott's formula (Eq. 2.30) has been found to provide an adequate description of the Seebeck coefficient below 100 K.[240] However, it has been pointed out that for short channel devices with 1D mesoscopic conduction channels, the Landauer expression for the electrical conductance $G = \frac{2e^2}{h}t$, with t the electron transmission coefficient, should be incorporated in Mott's formula.[240,242] Landauer theory for electronic transport in combination with the non-equilibrium Green's function formalism and extended Hückel theory has recently also been considered for the calculation of the intrinsic contribution of SWCNTs in SWCNT networks, based on the assumption that the ballistic contribution to transport dominates.[243,244] It is important to point out that such treatment implicitly assumes no inelastic scattering in the SWCNTs (no Joule heating) and that each tube is connected to two electron and heat reservoirs.[242] Instead Hung *et al.* proposed to employ Boltzmann transport formalism under the

relaxation time approximation to describe the Seebeck coefficient of single SWCNTs (Eq. 2.43 reduced to one dimension).[245] Considering that SWCNTs in networks are often longer than the mean-free path of carriers as well as that overlapping SWCNTs could lead to additional scattering,[18,194,206] renders the application of Boltzmann transport formalism to describe the intrinsic contribution of SWCNTs in SWCNT networks to the Seebeck coefficient as an adequate approach (further discussion in chapter 5). In case of the presence of strong disorder potentials, e.g. when the charge density is not field-effect-modulated but rather tuned through substitution of carbon atoms with nitrogen impurities, Yamamoto and Fukuyama have recently proposed to describe the Seebeck coefficient based on the Kubo formalism (see previous section) as well as the non-equilibrium Green's function formalism to compute the spectral conductivity function.[246,247] However, the most widely employed routine to tune the charge density in SWCNT thermoelectrics is via molecular doping through the interactions of dopant molecules with the SWCNT π-electron system.[24,46,47,241] Based on both field-effect modulated and molecularly doped studies of the Seebeck coefficient as well as the theoretical description based on Boltzmann transport formalism, the Seebeck coefficient of SWCNTs is expected to be strongly dependent on diameter and charge density.[24,47,137,245] It has been found to be decreasing with increasing diameter respectively decreasing bandgap.[24,47,245] While in the low charge density regime, Seebeck coefficients of several hundred $\frac{\mu V}{K}$ have been reported, it strongly reduces with increasing charge density due to subband filling.[24,47,136,137] Substantial amount of studies have focused on the optimization of the thermoelectric power factor $\sigma \cdot S^2$ of SWCNT networks.[24,46,47] These have established that it is beneficial to remove extrinsic factors to transport such as the excess wrapping polymer in the SWCNT network and that minimizing the SWCNT bundle diameter strongly promotes high power factors.[24,46,241]

In order to improve the fundamental understanding of the charge and thermoelectric transport in polymer-sorted SWCNT networks, charge density and temperature-dependent field-effect mobility and gated Seebeck coefficient measurements of monochiral small diameter (6,5) (0.76 nm) and mixed large diameter SWCNT (1.17-1.55 nm) networks with different network densities and length distributions are discussed in chapter 5.

Chapter 3

Experimental methods

This chapter provides an overview of the materials and dispersions, thermoelectric device fabrication as well as electric, thermoelectric, structural and optical characterization employed for the investigations of the charge and thermoelectric transport in semicrystalline conjugated polymers (chapter 4), polymer-sorted semiconducting SWCNT networks (chapter 5) and aligned, molecularly doped conjugated polymers (chapter 6).

3.1 Materials and dispersions

3.1.1 Conjuated polymers, small molecules and SWCNTs

For the study of charge and thermoelectric transport in low-disorder, semicrystalline conjugated polymers in chapter 4, the widely investigated n-type copolymer poly([*N,N'*-bis(2-octyldodecyl)-naphthalene-1,4,5,8-bis(dicarboximide)-2,6-diyl]-*alt*-5,5'-(2,2'-bithiophene)) (P(NDI2OD-T2), molecular structure shown in Figs. 1.5g and 4.1a)[69] has been employed as a model system. P(NDI2OD-T2) was purchased from Polyera (Polyera N2200, number average molecular weight $M_\mathrm{N} = 29.3$ kg mol^{-1}, weight average molecular weight $M_\mathrm{W} = 101.7$ kg mol^{-1} and polydispersity index $PDI = \frac{M_\mathrm{W}}{M_\mathrm{N}} \sim 3.5$). From cyclic voltammetry and optical absorption spectroscopy the HOMO (E_H) and LUMO (E_L) energies have been reported to be approximately $E_\mathrm{H} \sim -5.36$ eV and $E_\mathrm{L} \sim -3.91$ eV with an optical bandgap of $E_\mathrm{g} \sim 1.45$ eV.[248] Field-effect mobilities of P(NDI2OD-T2) are typically on the order of 0.1 cm^2 V^{-1} s^{-1}, its crystallinity can be easily tuned via the choice of solvent as well as post-deposition annealing treatments without affecting positional and energetic disorder and its energetic disorder is low, with an Urbach energy from photothermal deflection spectroscopy around $E_\mathrm{u} \sim 30$ meV.[69,73,135] Further relevant reported considerations on its charge transport have been outlined in section 2.1.2 and further structural characterization is provided together with the charge and thermoelectric transport studies in chapter 4.

For the investigations of charge and thermoelectric transport in polymer-sorted SWCNT networks in chapter 5, semiconducting SWCNTs were selected from CoMoCAT (CHASM Advanced Materials Inc., SG65i-L58, diameter 0.7-1.0 nm) and plasma torch (Raymor Industries Inc., RN-220, diameter 0.9-1.6 nm, batch RNB739-220-A329) raw material by polymer wrapping in toluene (analytical grade, VWR Chemicals) using poly[(9,9-dioctylfluorenyl-2,7-diyl)-*alt*-(6,6')-(2,2'-bipyridine)] (PFO-BPy, American Dye Source Inc., ADS153UV, $M_W = 40\,\mathrm{kg\,mol^{-1}}$, molecular structure shown in Fig. 5.1a), as described previously in detail and outlined briefly in the next section.[113,204] As emphasized at the beginning of chapter 5 the SWCNT network device fabrication as well as optical and structural characterization was performed by the PhD students Severin Schneider and Felix Berger from Prof. Zaumseil's group at the University of Heidelberg. For the same study 1,2,4,5-tetrakis(tetramethylguanidino)benzene (ttmgb, molecular structure shown in inset of Fig. 5.6a) was synthesized and purified as described previously and the colourless crystals were subsequently stored in dry nitrogen.[249,250] Solutions of ttmgb in anhydrous toluene were prepared directly prior to use. As outlined at the beginning of chapter 5, Simone Leingang, technical employee in Prof. Hans-Jörg Himmel's group at the University of Heidelberg and Prof. Hans-Jörg Himmel synthesized the ttmgb molecules.

The study of the impact of polymer chain alignment on the temperature-dependent charge and thermoelectric transport in the high charge density limit in chapter 6 has focused on the semicrystalline polymer poly(2,5-bis(3-tetradecylthiophen-2-yl)thieno[3,2-*b*]thiophene) (PBTTT) with C_{12} (*n*-dodecyl) alkyl side chains for solubility.[63] PBTTT-C_{12} (batch FZP852; $M_N = 45$ kg mol^{-1}, $M_W = 67$ kg mol^{-1}, $PDI = 1.49$, molecular structure shown in Fig. 1.5b) was synthesized by the Heeney group as described previously.[251] The crystallinity of PBTTT can be easily tuned via post-deposition annealing treatments, it displays field-effect mobilities of up to 1 cm^2 V^{-1} s^{-1} and the HOMO and LUMO energies are $E_H \sim -5.1$ eV and $E_L \sim -3.2$ eV respectively.[64,251,252] Furthermore, PBTTT-C_{12} has recently attracted interest considering its ability to host high densities of dopant molecules in its lamellar stacks as well as its remarkably high reported electrical conductivities on the order of 10^5 S cm^{-1}, which is almost comparable to conventional metals such as copper, when aligned via high-temperature rubbing (see further discussion in chapter 6).[253,254] As emphasized at the beginning of chapter 6, the thermoelectric device fabrication and optical characterization for this study was performed by Yuxuan Huang and Dr. Ian Jacobs, PhD student and postdoctoral researcher in Prof. Henning Sirringhaus's group at the University of Cambridge respectively. For the ion-exchange doping of PBTTT-C_{12}, BMP-TFSI (1-Butyl-1-methylpyrrolidinium

bis(trifluoromethanesulfonyl)imide, 99.9 %, < 20 ppm water, < 1 ppm total halides) was purchased from Solvionic, while $FeCl_3$ (anhydrous, > 99.99 % trace metals basis) was purchased from Sigma Aldrich. Anhydrous acetonitrile (Romil Hi-Dry, < 20 ppm water) was used to prepare all doping solutions, while anhydrous dichlorobenzene (DCB, Romil Hi-Dry, < 20 ppm water) was used for the polymer solution preparation (further details in section 3.2.3 and chapter 6).

3.1.2 SWCNT dispersions

(6,5) SWCNT dispersions were prepared by adding CoMoCAT (0.38 mg mL^{-1}) raw material to a solution of PFO-BPy (0.5 mg mL^{-1}) in toluene, and shear-force-mixing (Silverson L2/Air, 10230 rpm) for 72 h at 20 °C with two subsequent centrifugation steps at 60000 g (Beckman Coulter Avanti J-26XP) for 45 min. The supernatant containing the wrapped (6,5) SWCNTs was collected after each step. Mixed SWCNTs were selected by adding plasma torch raw material (1.5 mg mL^{-1}) to a PFO-BPy/toluene solution (0.5 mg mL^{-1}) and bath sonication for 60 min at 20 °C followed by centrifugation as described above. All dispersions were passed through PTFE membrane filters (Merck Millipore, JVWP, 0.1 µm pore size) and the resulting (6,5) and mixed SWCNT filter cakes were washed with toluene (80 °C, three times). The filter cake was redispersed in pure toluene (1 mL) by bath sonication for 30 min at 20 °C, leading to the (6,5) and mixed large diameter plasma torch (RN) SWCNT dispersions employed for the device fabrication. The charge transport of (6,5) SWCNT (diameter 1.27 nm and optical bandgap $E_g = 1.27$ eV) as well as RN (diameters of 1.17-1.55 nm and optical bandgaps of $E_g = 0.7 - 0.88$ eV) networks has been previously investigated and their high purity (absence of metallic SWCNTs) as well as different diameter range provided ideal model systems to gain further insights into the charge and thermoelectric transport of polymer-sorted semiconducting SWCNT networks (further discussion in chapter 5).[203,204]

3.1.3 Dielectrics

For the thermoelectric devices employed for the measurements of the field-effect mobility and gated Seebeck coefficient in chapter 4 and 5 poly(methyl methacrylate) (PMMA) and hybrid PMMA/HfO_x dielectric layers have been applied (further details in the following sections). PMMA was purchased from Polymer Source (syndiotactic, M_N = 318 kg mol^{-1} in chapter 4 and M_W = 315 kg mol^{-1} with $PDI = 1.05$ in chapter 5). Tetrakis(dimethylamino)hafnium (Strem Chemicals Inc.) has been used as a precursor for the atomic layer deposition of HfO_x (further details in section 3.2.2). Cytop (Asahi

Glass) has been employed in the patterning process of P(NDI2OD-T2) and PBTTT (and subsequently removed as outlined in ref. [255], see sections 3.2.1 and 3.2.3). PMMA has been shown to provide a smooth interface with low trap density and low dipolar disorder, while the hybrid PMMA/HfO_x dielectric further allows for low voltage operation and encapsulation for the SWCNT networks.[209,256]

3.2 Fabrication of thermoelectric devices

3.2.1 Conjugated polymer-based gated Seebeck devices

The device structure, a bottom-contact top-gate field-effect transistor structure with an on-chip heater, used to measure the charge carrier density and temperature-dependent saturation mobility and Seebeck coefficient of the semicrystalline polymer P(NDI2OD-T2)[69,248] is shown in Fig. 3.1 (a 3D illustration of the device architecture is shown in Fig. 4.1a) and was adopted from refs. [54] and [257]. The eight contact pads (h1-h4 and c1-c4) used for the four-point-probe (4pp) sensor resistance calibrations as well as the two pads for the on-chip heater (pads 1 and 2) are shown in golden colour, the patterned semiconductor in green and the gate electrode in dark grey. The dimensions of the active layer of the device are a width of one millimetre ($W = 1$ mm), a channel length of fifty micrometre ($L = 50$ µm) and a spacing between the heater stripe (width of 20 µm close to the active area) and the hot sensor of twenty micrometre (15 µm spacing to the organic layer). Chromium/Gold (3 nm/12 nm) contacts are used for the sensors and heater (plus a second double layer of 3 nm/50 nm of chromium/gold for the contact pads to improve contact), while the active layer is an approx. 35 nm thick film of the semiconducting polymer P(NDI2OD-T2). A layer of approx. 300 nm of PMMA is used as the dielectric layer and a 25 nm thick layer of Aluminium is employed for the gate contact. The devices were fabricated as follows: glass slides (Corning 1737, 700 µm thick) have been cut to approx. 1.7 cm times 1.7 cm substrates, which subsequently were cleaned in four ultrasonication steps in Decon 90 diluted in deionized (DI) water, DI water, acetone and 2-propanol for ten minutes each, followed by microwave plasma cleaning (250 W for ten minutes). The bottom contacts were fabricated via photolithography (double-layer photoresist LOR5B/S1813) and thermal evaporation of chromium/gold. P(NDI2OD-T2) (Polyera N2200, $M_N = 29.3$ kg mol^{-1}, $M_W = 101.7$ kg mol^{-1}, $PDI = 3.5$) was dissolved in toluene with 5 mg mL^{-1} concentration, heated for six hours at 90 °C and spin-coated at 2000 rpm for 60 s. Depending on the desired condition the device was either annealed at 200 °C for 15 min (ann.) and slowly cooled to room temperature or dried in vacuum (as-cast). After the patterning of P(NDI2OD-T2) according to

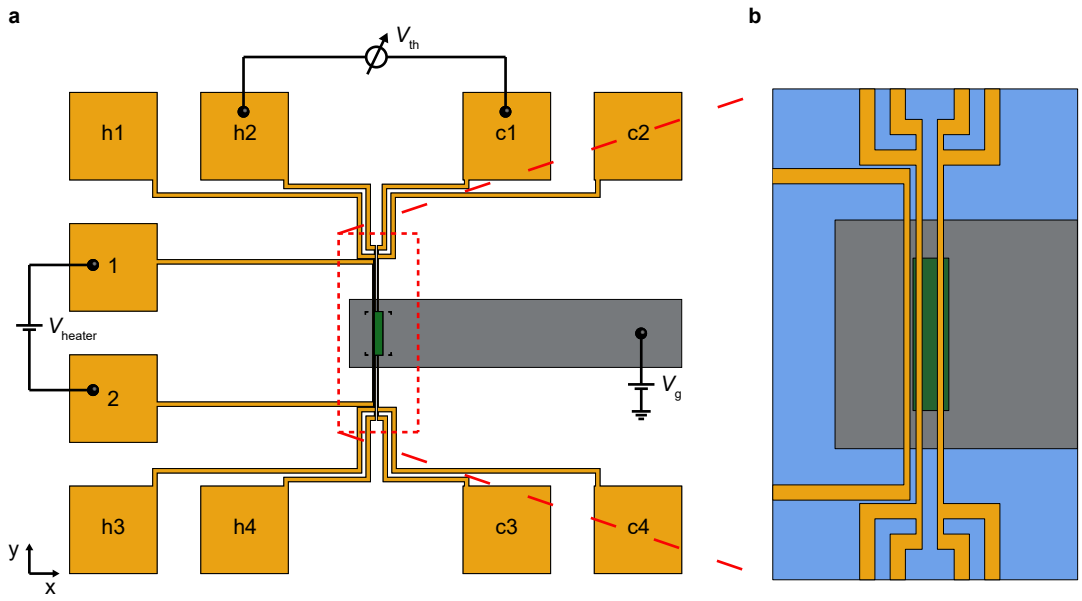

Figure 3.1. Device architecture of conjugated polymer-based gated Seebeck devices. The top view (a) as well as close-up of the active area (b, vertical dimensions of the electrodes outside the active area adjusted and PMMA as well as gate electrode shown behind the active layer and electrode structure for visual clarity) of the thermoelectric device architecture employed for the measurements of the field-effect mobility and gated Seebeck coefficient of conjugated polymers is shown. The electrode structure is shown in golden, the patterned semicrystalline polymer P(NDI2OD-T2) in green, the gate electrode in grey and the PMMA dielectric (not shown in (a)) in blue colour respectively. Pads 1 and 2 are connected to the on-chip heater, pads h1-h4 are connected to the source of the transistor structure and simultaneously the four-point-probe (4pp) hot resistance sensor for the Seebeck coefficient measurements, while pads c1-c4 are connected to the drain of the transistor structure and concurrently to the 4pp cold resistance sensor respectively. The gate voltage (V_g) is applied with respect to the grounded source and the thermal voltage (V_{th}) is measured from the cold to the hot resistance sensor (positive for p-type conduction). This device design was adopted from refs. [54] and [257].

ref. [255], PMMA (M_N = 318 kg mol^{-1}) from Polymer Source was dissolved in n-butyl acetate with 45 mg mL^{-1} concentration and spin-coated at 1000 rpm for 120 s. Finally, a 25 nm thick Aluminium gate electrode was evaporated using a shadow mask.

3.2.2 SWCNT network-based gated Seebeck devices

For the field-effect mobility and gated Seebeck coefficient measurements of the polymer-sorted SWCNT networks (chapter 5), the device architecture introduced in the previous section has been further improved (further discussion in section 3.3.1). A bottom-contact top-gate field-effect transistor structure with 4pp voltage probes and two on-chip heaters has been employed and is shown in Fig. 3.2 (a 3D illustration of the device architecture is shown in Fig. 5.5a). The active area dimensions were the same as for the structure

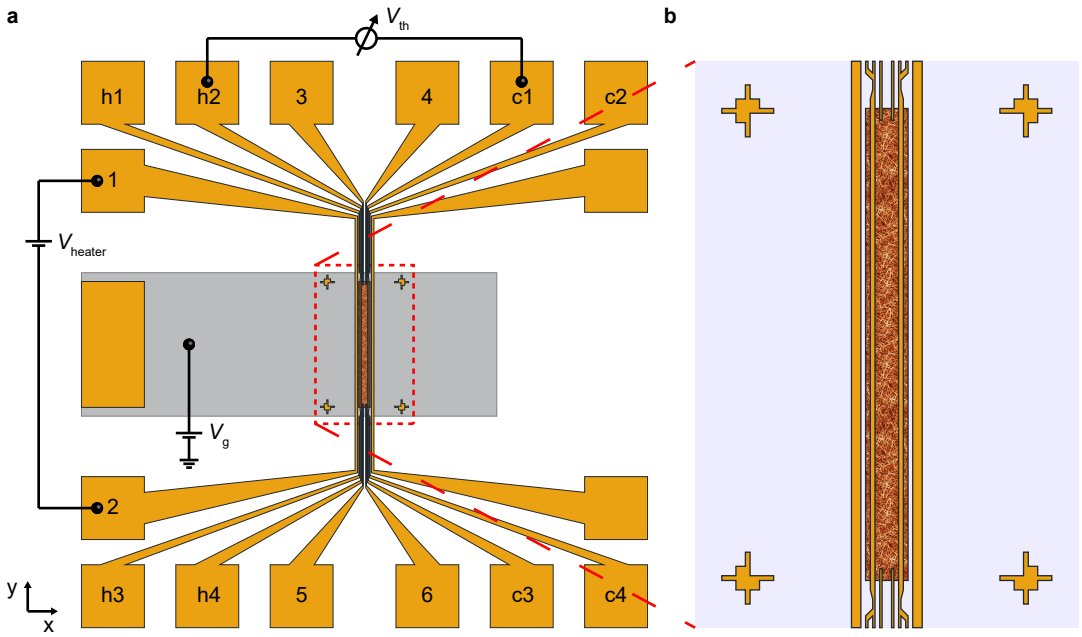

Figure 3.2. Device architecture of polymer-sorted SWCNT network-based gated Seebeck devices. The top view (a) as well as close-up of the active area (b) of the thermoelectric device architecture employed for the measurements of the field-effect mobility and gated Seebeck coefficient of the polymer-sorted SWCNT networks is shown. The electrode structure is shown in golden, the patterned SWCNT network in brown, the hybrid PMMA/HfO_x dielectric in light blue (only in (b) and for visual clarity behind the other layers) and the gate electrode in light grey colour (only in (a) and for visual clarity behind the other layers). Pads 1 and 2 are connected to the left on-chip heater, pads h1-h4 are connected to the source of the transistor structure and simultaneously the four-point-probe (4pp) hot resistance sensor for the Seebeck coefficient measurements, while pads c1-c4 are connected to the drain of the transistor structure and concurrently to the 4pp cold resistance sensor respectively. Pads 3-6 are connected to 4pp voltage probes that allow for 4pp linear mobility measurements. The gate voltage (V_g) is applied with respect to the grounded source and the thermal voltage (V_{th}) is measured from the cold to the hot resistance sensor (positive for p-type conduction).

introduced in the previous section (channel width $W = 1000$ µm and length $L = 50$ µm, as well as 20 µm spacing between heater and hot sensor). The spacing between heater and SWCNT networks was 10 µm and the 5 µm wide 4pp voltage probes were centred at positions $L_{P1} = 12.5$ µm and $L_{P2} = 37.5$ µm in the channel. The electrode design was patterned on AF 32 eco glass (Schott AG, 300 µm thick, 6 devices on 2 cm times 3 cm substrates) by standard photolithography (see previous section) in combination with electron-beam evaporation of titanium (3 nm) and gold (12 nm) with subsequent lift-off in *N*-methyl-2-pyrrolidone (HPLC grade, Sigma). SWCNT dispersions were spin-coated at 2000 rpm for 30 s and annealed at 100 °C for 20 min (this process was repeated three times). The network density was controlled via correlation with the absorbance peaks $E_{11,(6,5)}$ and $E_{22,RN,max}$ of the (6,5) and RN SWCNT dispersions respectively

(see Fig. 5.1b).[258] After thorough rinsing with tetrahydrofuran and isopropyl alcohol to remove residual excess polymer, the films were patterned with standard photolithography (double-layer photoresist LOR5B/S1813) and oxygen plasma etching. The substrates were annealed at 300 °C for 30 min in dry nitrogen to remove any residual solvent and water in the SWCNT networks. Ttmgb (2.5 mg mL^{-1}) was applied to selected samples by dip-coating in a solution in anhydrous toluene for 20 min and subsequent annealing at 150 °C for 30 min. Spin-coating of PMMA (Polymer Source, $M_W = 315$ kg mol^{-1}) in n-butyl acetate (6 mg mL^{-1}) at 4000 rpm for 60 s and atomic layer deposition of HfO_x (Ultratech Savannah S100) at 100 °C with water as the oxygen source and tetrakis(dimethylamino)hafnium (Strem Chemicals Inc.) as the precursor formed the hybrid dielectric (PMMA (11 nm), HfO_x (60 nm)).[209] The devices were completed by thermal evaporation of silver gate electrodes (30 nm).

3.2.3 Multifunctional devices for conducting material systems

For the temperature-dependent conductivity and Seebeck coefficient measurements of molecularly doped PBTTT another device architecture with a similar bottom electrode pattern to the one introduced in the previous section was designed. The device architecture is essentially a Hall bar architecture with two on-chip heaters, where source and drain electrodes are simultaneously 4pp resistance thermometers for the Seebeck coefficient measurements (Fig. 3.3, see further discussion in section 3.3.1). The active layer has a channel width of $W = 105$ µm and channel length of 420 µm, with 5 µm wide 4pp voltage probes centred at $L_{P1} = 140$ µm and $L_{P2} = 280$ µm in the channel. Close to the active area the heater is 20 µm wide and is 20 µm and 40 µm separated from the organic layer as well as the hot sensor respectively. The electrode design was patterned onto 1.5 cm times 1.5 cm glass substrates (Schott Eagle XG, 700 µm thick) via double-resist LOR5B/S1813 photolithography as discussed in section 3.2.1. The chromium/gold (5 nm/25 nm) electrodes were thermally evaporated. The solutions of 10 mg/ml PBTTT-C_{12} ($M_W = 67$ kg mol^{-1}, synthesized by the Heeney group) in DCB, glass pipettes and the substrates were preheated to 80 °C. Subsequently, the solutions were spin-coated using the preheated glass pipettes onto the substrates at 1000 rpm for 60 s, followed by 5000 rpm for 5 s to remove any excess solution from the substrates. Consequently, the PBTTT film was patterned according to ref. [255]. For the unaligned PBTTT-based thermoelectric devices, the substrates were subsequently annealed at 180 °C for 20 min and slowly cooled to room temperature. For the aligned PBTTT-based thermoelectric devices, the patterned PBTTT active layer was rubbed at 155 °C (as all other spin coating and annealing steps in an N_2 glovebox) using an RM-50

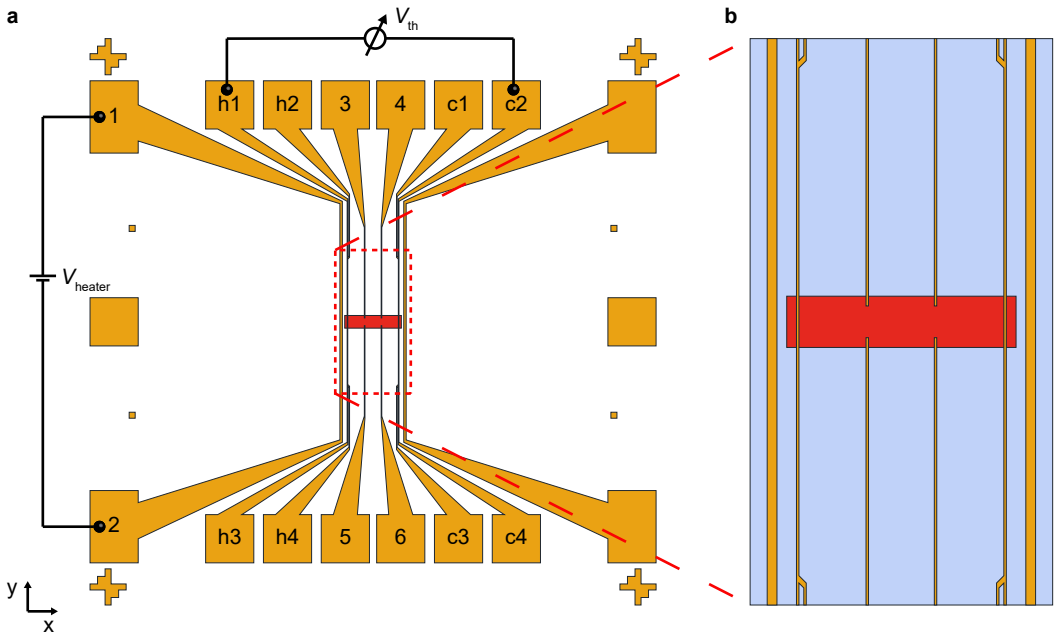

Figure 3.3. Device architecture for thermoelectric measurements of molecularly doped PBTTT. The top view (a) as well as close-up of the active area (b) of the thermoelectric device architecture employed for the measurements of the temperature-dependent conductivity and Seebeck coefficient of molecularly doped PBTTT is shown. The electrode structure is shown in golden, the patterned molecularly doped PBTTT in red and the Cytop encapsulation layer in light blue colour (only in (b), for visual clarity the electrode structure is shown on top of PBTTT and the encapsulation layer). Pads 1 and 2 are connected to the left on-chip heater, pads h1-h4 are connected to the source of the Hall bar structure and simultaneously the four-point-probe (4pp) hot resistance sensor for the Seebeck coefficient measurements, while pads c1-c4 are connected to the drain of the Hall bar and concurrently to the 4pp cold resistance sensor respectively. Pads 3-6 are connected to 4pp voltage probes that allow for 4pp conductivity and Hall voltage measurements. The thermal voltage (V_{th}) is measured from the cold to the hot resistance sensor (positive for p-type conduction).

rubbing machine (EHC Co.) to align the polymer chains of PBTTT. The rubbing roller was covered with a microfiber cloth and while it was rotating at 1400 rpm, the sample stage transfer speed during rubbing was set to 1 cm s^{-1}. After rubbing the samples were annealed at 190 °C for 20 min and slowly cooled to room temperature. The ion-exchange doping solutions were prepared just prior to use, considering the low stability of the oxidizing agents in the presence of dilute water impurities. The 100:1 mM electrolyte:oxidizer doping solution was obtained by mixing 1 M BMP-TFSI in acetonitrile electrolyte stock solution with 10 mM $FeCl_3$ in acetonitrile oxidizing agent stock solution and acetonitrile at 1:1:8 volume ratio respectively. The active PBTTT layer was sequentially doped by covering the substrate with 150 µL doping solution, waiting for 100 s and subsequently spinning off the excess solution at 8000 rpm,

while washing the devices with 1 mL acetonitrile to remove any excess oxidizing agent and electrolyte from the surface. For the multifunctional devices the conductivity could be varied by the concentration of the doping solution (the doping process of the small Hall bar pattern was already complete after a few seconds of waiting time). Finally, a 500 nm Cytop encapsulation layer was employed via spin-coating of 3:1 Cytop:solvent at 2000 rpm for 90 s on top of all films and devices.

3.3 Electric and thermoelectric characterization

3.3.1 Measurement routines

Conjugated polymer-based gated Seebeck devices

The transistor transfer curves, the sensor resistance measurements as well as the thermal voltage measurements were performed within a cryogenic testing chamber BCT-43 MDC Nagase & Co., LTD. with six probes controlled by an Agilent 4156B Semiconductor Parameter Analyser (SPA). The transfer curves (Fig. 3.4) were measured in a condition $V_{gs} = V_{ds} + V_{on}$ (V_{on} the onset voltage) at each gate voltage in order to ensure that the transistor is operated in the saturation regime during the entire measurement. V_{on} was determined by taking several transfer measurements with

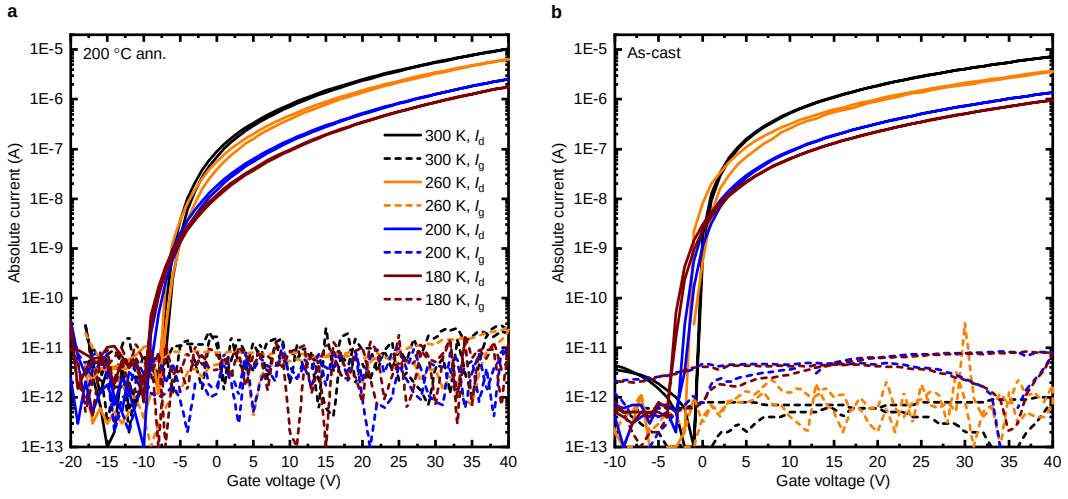

Figure 3.4. Transistor transfer curves of P(NDI2OD-T2)-based devices. Transistor transfer curves of the 200 °C annealed (200 °C ann., (a)) and as-cast P(NDI2OD-T2)-based device (b) at various temperatures are shown. Due to the patterning of P(NDI2OD-T2) the gate leakage current is very low and on the order of 10 pA. It is evident that both preparation conditions show temperature-activated transport, while the charge density dependence of the saturation mobility differs strongly between the two conditions.

different values for V_{on} and choosing the value which lead to a clear onset in the transfer measurement and a drain current on the order of the noise level for voltages $V_{gs} < V_{on}$ (at 300 K $V_{on} = -8$ V for the annealed sample and $V_{on} = -1$ V for the as-cast sample). Consequently, the saturation mobilities were extracted according to ref. [138] (see section 1.4, Eq. 1.25). The gate voltages were used to calculate the accumulated charge density via the relationship: $n = \frac{\epsilon_0 \cdot \epsilon_r}{d \cdot h} \cdot (V_{gs} - V_{on})$, where $\epsilon_r = 3.6$ for PMMA, $d = 300$ nm for the dielectric layer thickness and the height of the accumulation layer was assumed to be $h = 2$ nm.[174] In principle the thermal voltages as well as the temperature differences between the sensors and hence the Seebeck coefficients were measured according to refs. [54] and [257]. 4-point-probe (4pp) resistance measurements were used for the calibration of the sensors in order to get accurate values for the temperature coefficients of the sensor resistances. It is evident from the device structure shown in Fig. 3.1 that these 4pp measurements of the resistance sensors are crucial to get accurate values of the temperatures of the hot and cold sensor in the active area region. For two-point-probe measurements the temperature coefficients of the sensor resistances would be significantly overestimated, leading to an underestimation of the temperature difference and an overestimation of the Seebeck coefficient (see further discussion of the measurement routine below).

In the following the procedure of the Seebeck coefficient measurements shall be presented for the 200 °C annealed preparation condition (the procedure was exactly the same for the as-cast condition). The temperature difference (ΔT) between the hot and cold sensor at a given temperature (T) and heater power (W) has been measured indirectly via the change of the sensor resistances with temperature (and therefore with heater power) and is determined according to:[259]

$$\Delta T = W \cdot \left(\frac{\frac{dR_{hot}}{dW}}{\frac{dR_{hot}}{dT}} - \frac{\frac{dR_{cold}}{dW}}{\frac{dR_{cold}}{dT}} \right). \tag{3.1}$$

The sensor resistances were measured at a given temperature (Fig. 3.5a: 300 K, Fig. 3.5b: 260 K, Fig. 3.5c: 200 K, Fig. 3.5d: 180 K, hot sensor (solid circles) and cold sensor (open circles)) by applying a current of 10^{-4} A through two of the four sensor contact pads and simultaneously measuring the voltage across the other two contact pads during the application of a heater power corresponding to an applied heater voltage of $0 - 10$ V in steps of 2 V to the two heater contact pads. After applying the heater voltage, before measuring the sensor resistances at each heater power, a 5 s hold time was used to allow the chip to get to a thermal steady state. Such short hold times were enabled by the large thermal mass of the sample stage of the BCT-43 MDC Nagase

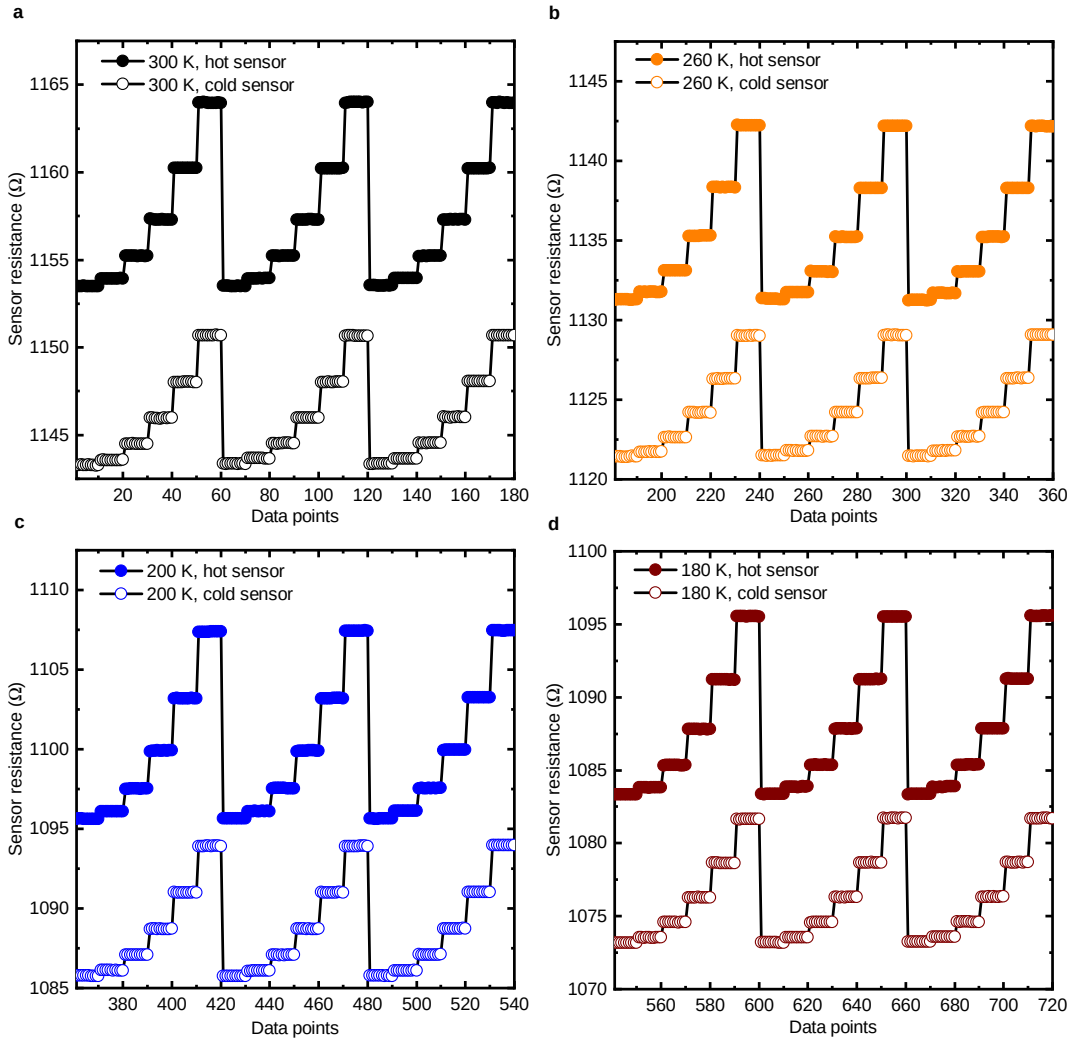

Figure 3.5. Sensor calibration of 200 °C annealed P(NDI2OD-T2)-based device. Sweep of the heater power at a given temperature ((a): 300 K, (b): 260 K, (c): 200 K, (d): 180 K) and corresponding change of the hot (solid circles) and cold (open circles) sensor resistances are shown. The applied heater powers correspond to an applied heater voltage of $0 - 10$ V in steps of 2 V. Three sweeps in the heater power with ten data points at each heater power were taken in order to improve the level of confidence of the measurement. The first 60 data points of each panel correspond to the first heater power sweep, the next 60 to the second sweep and the last 60 to the third sweep.

& Co., LTD. testing chamber (as well as good thermal contact between sample stage and substrate enabled by the thermal grease Apiezon N). However, as discussed in the next section the large thermal mass of the sample stage of this cryogenic chamber concomitantly lead to very long stabilization times to reach thermal equilibrium of the sample stage of at least 6 hours upon changing the temperature of the stage. Three

sweeps in the heater power with ten data points at each heater power were taken in order to improve the level of confidence of the measurement. Based on these raw data (Fig. 3.5) the average heater powers and the corresponding average sensor resistances (averaged over the 30 data points taken) at each temperature were calculated and from linear regression fits to these data the coefficients $\frac{dR_{\mathrm{hot/cold}}}{dW}$ (Fig. 3.6) as well as $\frac{dR_{\mathrm{hot/cold}}}{dT}$ (Fig. 3.7) were determined. For the $\frac{dR_{\mathrm{hot/cold}}}{dT}$ coefficients the resistances at zero applied heater power were used. Further to these calibration measurements, the thermal voltage was measured at different temperatures, heater powers and gate voltages (Fig. 3.8). The heater power during the thermal voltage measurement was measured and used in Eq. 3.1 to calculate the corresponding temperature difference ΔT. As for the calibration measurements, 5 s hold time were used to allow the chip to get to a thermal steady state before measuring the thermal voltage at each heater power and each gate voltage. After each gate voltage step, 20 s hold time were employed before measuring the thermal voltage to allow for the charge carriers to accumulate at the semiconductor-dielectric interface. At each temperature as for the calibration measurements, the heater power was swept by sweeping the heater voltage from $0 - 10$ V in steps of 2 V. This sweep was repeated for each gate voltage, which was swept from $0 - 50$ V in steps of 2.5 V in order to vary the accumulated charge density. The thermal voltage was correspondingly measured at each heater power and gate voltage via a current devoid measurement, grounding one of the sensors and leaving the other floating (measuring the potential and forcing the current to zero with the corresponding SMU). Long integration times of 200 ms (respectively 10 power line cycles) have been employed for the thermal voltage measurements throughout this thesis. It is worth to note that the patterning process of the semiconducting layer not only avoids any stray current contributions for an accurate determination of the field-effect mobility, but also ensures the absence of current leakage from the heater as well as low gate leakage currents on the order of 10 pA. If either leakage currents from the heater due to insufficient alignment of the active layer or gate leakage currents due to an insufficiently homogeneous dielectric layer, exceed approximately 1 nA (also dependent on the resistances of the pathways), the thermal voltage measurement cannot be performed reliably any more, since the current devoid condition of the measurement would not be ensured in this case. In order to improve the level of confidence of the measurement two ramps in the gate voltage were performed: for the ramp-up the hot sensor was grounded and the cold one was left floating, hence the polarity of the measured thermal voltage for the n-type semicrystalline polymer semiconductor P(NDI2OD-T2) was negative, while for the ramp-down the hot sensor was left floating and the cold one was grounded, which results in a positive polarity

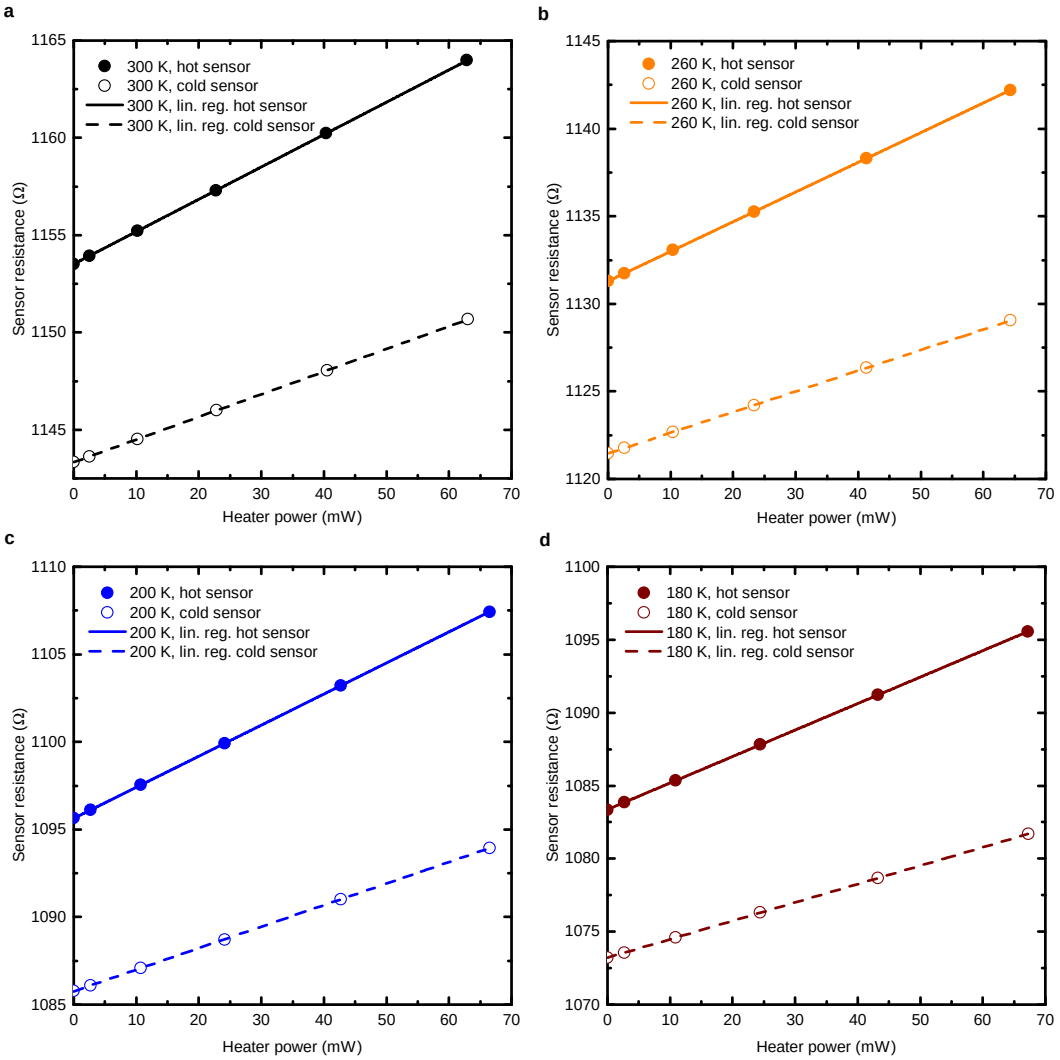

Figure 3.6. Average sensor resistance versus average heater power of 200 °C annealed P(NDI2OD-T2)-based device. Average sensor resistance (hot sensor: solid circles, cold sensor: open circles) at a given temperature ((a): 300 K, (b): 260 K, (c): 200 K, (d): 180 K) versus the corresponding average heater powers as well as the linear regression fits (hot sensor: solid lines, cold sensor: dashed lines) to extract $\frac{dR_{\mathrm{hot/cold}}}{dW}$ are shown.

of the thermal voltage. This procedure is illustrated for each temperature in Fig. 3.8. At each gate voltage the measured thermal voltage follows the parabolic sweep of the heater power. In order to obtain the Seebeck coefficient at each temperature and gate voltage, the thermal voltage average $V_{\mathrm{th}} = \frac{V_{\mathrm{th1}} - V_{\mathrm{th2}}}{2}$ of the two sweeps at each temperature, gate voltage and heater power was calculated. Here V_{th1} denotes the thermal voltage that is measured during the ramp-up and V_{th2} is the corresponding

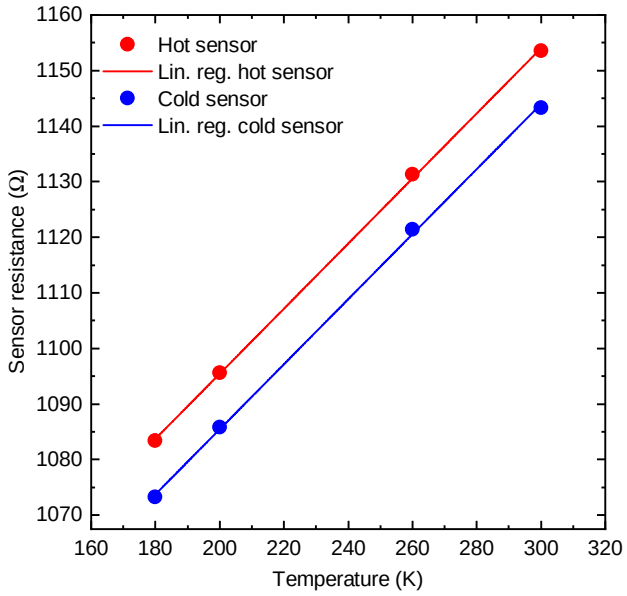

Figure 3.7. Average sensor resistance versus temperature of 200 °C annealed P(NDI2OD-T2)-based device. Average sensor resistance at zero applied heater power at each temperature as well as the linear regression fits used to extract $\frac{dR_{\mathrm{hot/cold}}}{dT}$ are shown.

(same temperature, heater power and gate voltage) thermal voltage of the ramp-down in gate voltage. These thermal voltages were plotted against the corresponding average temperature difference $\Delta T = \frac{\Delta T_1 + \Delta T_2}{2}$ and consequently the Seebeck coefficient was obtained from the slope of the linear regression fit at each gate voltage and temperature. This procedure is illustrated in Fig. 3.9 for the 300 K measurements. In order to obtain Fig. 4.4, the charge densities were obtained according to $n = \frac{\epsilon_0 \cdot \epsilon_\mathrm{r}}{d \cdot h} \cdot (V_\mathrm{gs} - V_\mathrm{on})$. In addition to the great advantage of easily and accurately tuning the charge density during the measurement, the on-chip measurement of the Seebeck coefficient further offers very high measurement accuracy and precision with relative errors in the Seebeck coefficient discussed in chapter 4 of around 7 % (as analysed in section 3.3.2). Further improvements of the measurement accuracy and precision of the Seebeck coefficient in this thesis with relative errors down to 2 % will be discussed in the following sections.

SWCNT network-based gated Seebeck devices

Transistor transfer and output, sensor resistance calibration and thermal voltage measurements were performed under vacuum ($< 10^{-6}$ mbar) in a six-probe closed-cycle cryogenic probe station (Lake Shore Cryotronics Inc., CRX-4K) with two Keithley 2612B

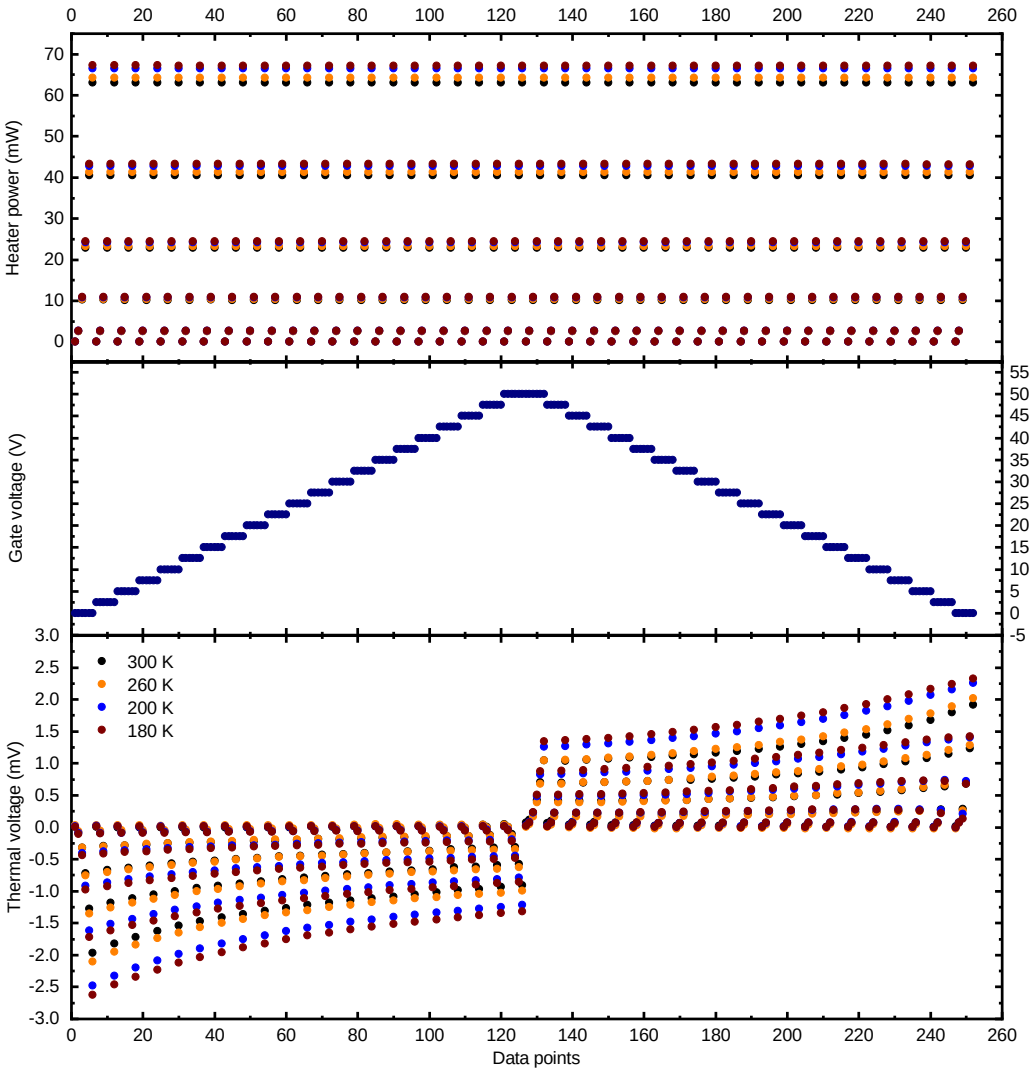

Figure 3.8. Temperature and gate voltage dependent thermal voltage measurement of 200 °C annealed P(NDI2OD-T2)-based device. The bottom panel shows the measured thermal voltages at each temperature, gate voltage (swept according to the center panel) and heater power (swept according to the top panel). Six data points correspond to one heater power sweep (heater voltage swept from $0 - 10$ V in steps of 2 V) at a specific gate voltage. For the first 126 data points (21 gate voltages) the hot sensor is grounded for the thermal voltage measurement, while the cold one is left floating. For the last 126 data points the polarity is swapped to improve the level of confidence of the measurement.

Dual Channel SourceMeters and one Keithley 6430 Sub-Femtoamp Remote SourceMeter including Remote PreAmp. While the principle of the sensor resistance calibration and thermal voltage measurements is the same as in the previous section,[54,172] the range of feasible charge densities and temperatures has been further extended and the

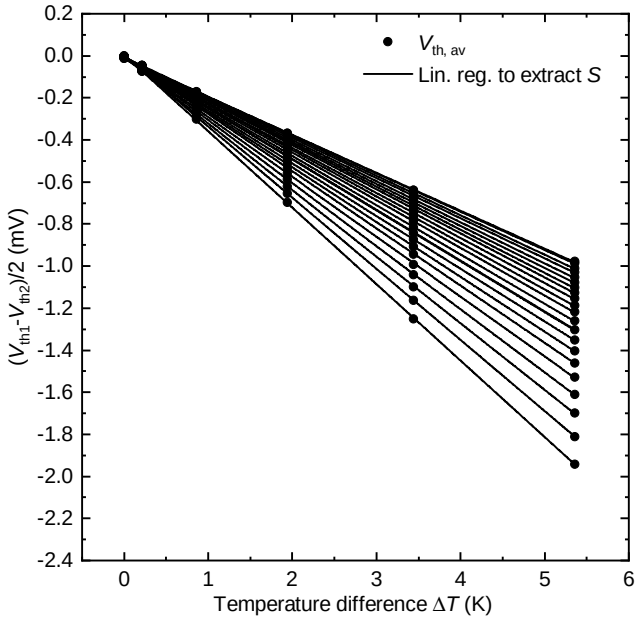

Figure 3.9. Average thermal voltage versus temperature difference at 300 K of 200 °C annealed P(NDI2OD-T2)-based device. Average thermal voltage ($V_{\mathrm{th}} = \frac{V_{\mathrm{th1}}-V_{\mathrm{th2}}}{2}$) from the two sweeps measured at 300 K and each gate voltage ($0 - 50$ V in steps of 2.5 V) versus the corresponding averaged temperature differences ($\Delta T = \frac{\Delta T_1+\Delta T_2}{2}$) are shown. Furthermore, the linear regression fits to extract the Seebeck coefficient from the slope of the fit at each gate voltage are presented.

unidirectionality of the temperature gradient as well as the accuracy of the on-chip resistive thermometers have been further improved. Significant effort has been devoted to the setup of the newly installed six-probe closed-cycle cryogenic probe station (Lake Shore Cryotronics Inc., CRX-4K) for these measurements. The details of the new measurement configuration are presented below.

Firstly, details concerning the electrical characterization of the SWCNT networks presented in chapter 5 are provided. The device capacitance (Fig. 5.7 and Table 5.2) of the SWCNT network-based gated Seebeck devices was determined using an impedance spectrometer (ModuLab XM MTS System, Solartron Analytical). Measurements were conducted at 1.0 kHz, and the maximum capacitance C_{m} was extracted in the on-state ($V_{\mathrm{gs}} = \pm 5$ V, for electron and hole transport respectively). Consequently, the areal capacitance $C_{\mathrm{i}} = \frac{C_{\mathrm{m}}}{W \cdot L_{\mathrm{pattern}}}$ ($L_{\mathrm{pattern}} = 90$ µm being the entire length of the SWCNT patterned area) was obtained. Both four-point-probe (4pp) linear (μ_{4pp}) as well as saturation mobilities (μ_{sat}) were determined. The 4pp linear mobilities and contact resistances were obtained at $V_{\mathrm{ds}} = -0.1$ V (apart from $V_{\mathrm{ds}} = +0.1$ V for the n-type (6,5)-s-ttmgb device) using two 5 µm wide voltage probes located at $L_{\mathrm{P1}} = 12.5$ µm and

$L_{P2} = 37.5$ µm in the 50 µm long channel (Eq. 1.23, Fig. 3.2).[130,134,203] The saturation transfer curves were measured in the condition $V_{ds} = V_{gs} - V_{on}$ (with V_{on} being the onset voltage) to ensure a unipolar saturation regime throughout the entire gate voltage range.[138] The onset voltages ($V_{on,h}$ and $V_{on,e}$) were extracted from the linear transfer curves as the voltages for which the source-drain current rises above the background noise and gate-leakage current level for hole and electron transport respectively (Figs. 5.7a and 5.10). The charge densities were obtained as $n = \frac{C_i}{h} \cdot (V_{gs} - V_{on})$, assuming the height of the accumulation layer to be $h = 2$ nm.[174]

In order to measure the charge density and temperature dependence of the Seebeck coefficient ($S = \frac{V_{th}}{\Delta T}$) of the SWCNT networks, both the thermal voltage ($V_{th}(T, V_{gs}, W)$) as a function of temperature (T), gate voltage (V_{gs}) and heater power (W) as well as the temperature difference ($\Delta T(T, W)$) between the hot and cold four-point-probe (4pp) resistance sensor (Figs. 3.2 and 5.5) as a function of temperature and heater power were measured. At each temperature of interest (typically 50 K to 300 K in steps of 50 K), the thermal voltage was measured via the following procedure: the source respectively hot sensor was grounded and a gate-source potential was established with a source measure unit (SMU) of a Keithley 2612B Dual Channel SourceMeter. A hold time of 20 s was employed to allow for carrier accumulation at the SWCNT network/dielectric interface and the applied gate voltages were typically varied from -7 V to 0 V and 7 V to 0 V (in steps of ±0.5 V) for electron and hole transport respectively. Subsequently, a second SMU of a Keithley 2612B Dual Channel SourceMeter was used to set the heater voltage (V_{heater} and hence heater power ($W = V_{heater} \cdot I_{heater}$)), typically from 0 V to 5 V in steps of 0.5 V across the left on-chip heater of the device. After a hold time of 60 s (100 K to 300 K) respectively 120 s at lower temperatures (< 100 K) to establish a steady temperature profile across the device, the thermal voltage was measured with the SMU of a Keithley 6430 Sub-Femtoamp Remote SourceMeter including its Remote PreAmp, from the cold to the grounded hot sensor (lowest voltage measurement range (200 mV), forcing zero current flow, with a current output range of 10 pA). This measurement unit allowed for a very high input impedance ($R_{in} > 10^{16}$ Ω), enabling reliable thermal voltage measurements of highly resistive samples and hence enabling measurements down to low temperatures and small overdrive voltages ($V_{ov} = V_{gs} - V_{on} < 1$ V, with V_{on} the onset voltage).

It is worth to note that the hold time of the heater voltage was chosen to be substantially longer than for the devices presented in the previous section that were measured in the BCT-43 MDC Nagase & Co., LTD. testing chamber. It is presumed that the significantly longer thermalization time of the substrate for a given heater power in the Lake Shore

Cryotronics Inc., CRX-4K probe station is due to the much smaller thermal mass of the sample stage. However, the advantage of the smaller thermal mass of the CRX-4K sample stage is a much faster stabilization time upon resetting the stage temperature of around $20-30$ min. To further improve thermal contact particularly at low temperatures VGE-7031 varnish instead of Apiezon N has been employed as a thin thermal contact layer between the sample holder and the substrates. VGE-7031 varnish offers much higher thermal conductivities (κ) at low temperatures compared to Apiezon N (e.g. at 4.2 K $\kappa = 0.062$ W m^{-1} K^{-1} for VGE-7031 varnish versus $\kappa = 0.005$ W m^{-1} K^{-1} for Apiezon N), which in turn improves out-of-plane heat conduction, leading to more efficient cooling. This allows for larger temperature differences at a given heater power and thereby reduces the relative errors in the Seebeck coefficient measurement (as will be further discussed in section 3.3.2). Furthermore, VGE-7031 varnish did not undergo any phase transitions within the investigated range of temperatures ($50 - 300$ K), while Apiezon N has typically been found to crystallize at temperatures < 180 K and in this phase the out-of-plane heat conduction was significantly hampered.
The sequence of gate and heater voltage application and subsequent thermal voltage measurement was repeated at each temperature for 11 heater powers and 15 gate voltages in the range given above. Representative thermal voltage measurements of the RN dense short-tube (RN-d-st) networks between 50 K and 300 K as well as the corresponding gate voltages and heater powers are shown in Fig. 3.10. At each temperature, after measuring the thermal voltages, the hot and cold 4pp sensor resistances (R_{hot} and R_{cold}) were measured in dependence of heater power (same range as for the thermal voltage measurements and three sweeps of ten data points per heater power) using both SMUs of a Keithley 2612B Dual Channel SourceMeter, in order to establish the temperature differences during the thermal voltage measurement according to Eq. 3.1. For the temperature coefficient of resistance of the hot and cold sensor ($\frac{dR_{\mathrm{hot}}}{dT}$ respectively $\frac{dR_{\mathrm{cold}}}{dT}$), the averaged 4pp resistances at zero heater power at each temperature were considered. For the analysis of the Seebeck coefficient only those heater powers were considered that caused a maximum rise in temperature of the hot sensor of approximately 15 K, in order to keep the average sample temperature close to the set sample stage temperature. Representative measurements of the hot and cold 4pp sensor resistances of the RN-d-st devices for different temperatures at zero heater power and in dependence of heater power (representatively at 300 K and 200 K) are shown in Fig. 3.11. Finally, the Seebeck coefficients were obtained as the slopes of the linear regression fits of the thermal voltage versus the temperature difference. Representative fits to obtain the Seebeck coefficients of the RN-d-st networks at 300 K

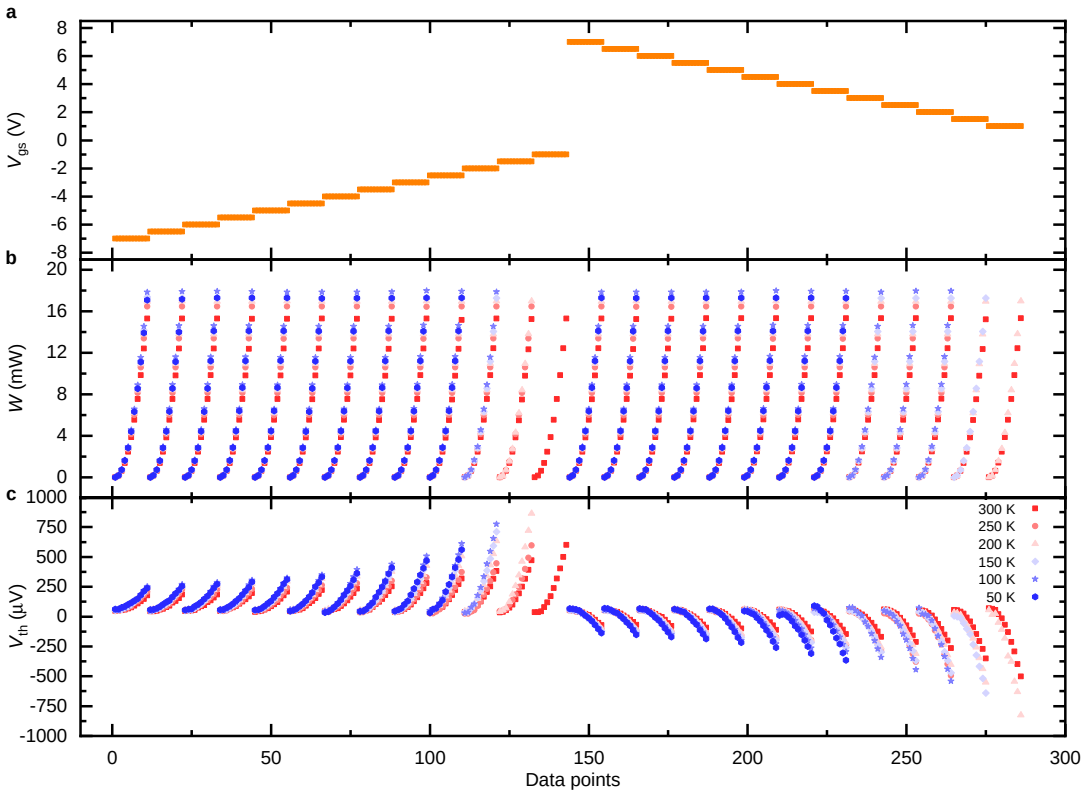

Figure 3.10. Thermal voltage measurements of SWCNT networks. Representative thermal voltage measurements of the RN dense short-tube networks (RN-d-st) in dependence of temperature (50 K to 300 K), gate voltage (a) and heater power (b) are shown (c). A strong modulation of the thermal voltage with carrier density is evident. In order to obtain the charge density and temperature-dependent Seebeck coefficients, a calibration of the temperature difference between the resistance sensors for a specific heater power and temperature based on Eq. 3.1 is necessary.

for hole ($V_{gs} = -7$ V to -1 V in steps of 0.5 V) and electron ($V_{gs} = 7$ V to 1 V in steps of -0.5 V) transport are shown in Fig. 3.12.

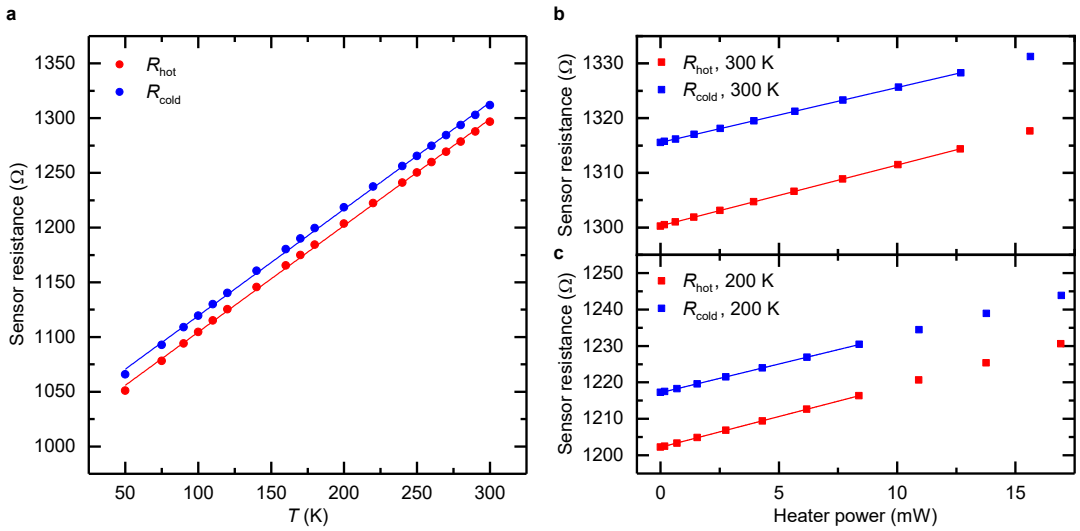

Figure 3.11. Sensor resistance measurements of SWCNT network-based thermoelectric devices. Representative 4pp resistance measurements of the hot and cold sensor (R_{hot} respectively R_{cold}) of the RN dense short-tube (RN-d-st) network device versus temperature at zero heater power (a) as well as versus heater power at 300 K (b) and 200 K (c) are shown. For lower temperatures the heater power had to be restricted more strongly (to keep the maximum rise in temperature of the hot sensor less than approximately 15 K), as the reduced out-of-plane heat extraction lead to strong heating effects even for small heater powers.

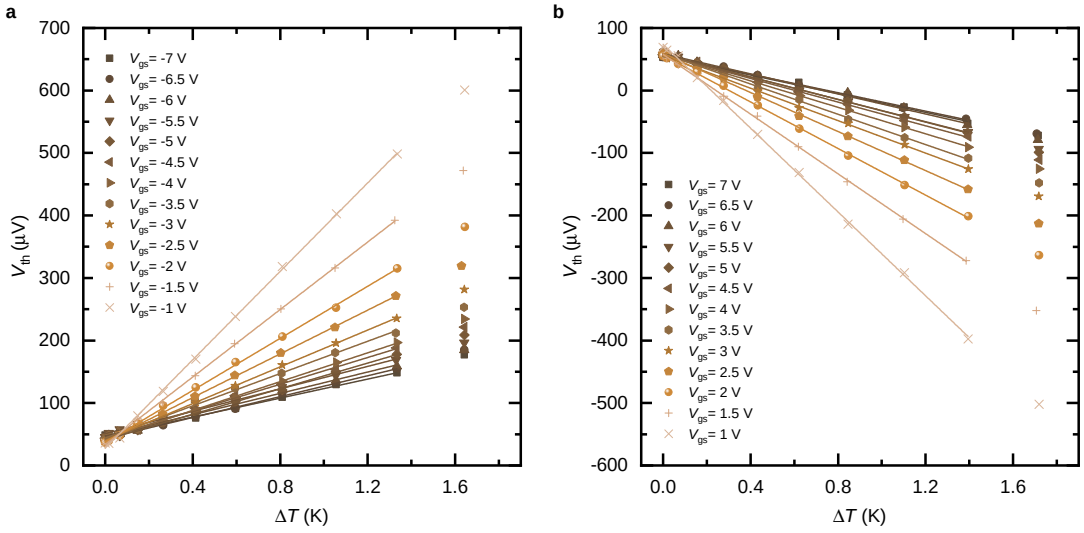

Figure 3.12. Seebeck coefficient extraction of SWCNT networks. Representatively, the thermal voltages of the RN dense short-tube networks at 300 K for hole ($V_{\mathrm{gs}} = -7$ V to -1 V in steps of 0.5 V, (a)) and electron ($V_{\mathrm{gs}} = 7$ V to 1 V in steps of -0.5 V, (b)) transport versus the temperature difference between the resistance sensors are shown. The Seebeck coefficient was obtained as the slope of the linear regression fit at each gate voltage. The Seebeck coefficient extraction was limited to those data points that maintained the rise in temperature of the hot sensor to less than approximately 15 K.

Multifunctional devices for conducting material systems

The multifunctional devices shown in Fig. 3.3 have been designed to measure the 4pp conductivity, Hall and Seebeck coefficient of conducting respectively molecularly doped material systems on the same chip. Similar to the further improved gated Seebeck devices (Fig. 3.2) the branching points of the 4pp resistance thermometers have been moved close to the active area. This allows for more accurate measurements of the temperature at the hot and cold resistance sensor within the active area region of interest and therefore more accurate measurements of the Seebeck coefficient. COMSOL simulations of the temperature profile across the devices by William Wood, PhD student in Prof. Sirringhaus's group, have further confirmed that a single strip line heater as employed in all devices presented in this thesis, causes negligibly small temperature gradients along the vertical (y-) direction of the resistance sensors (seen from the centre position of the resistance sensors), particularly when the branching points are close to the active area. Serpentine heaters instead can cause significant temperature distributions along the y-direction, which can lead to inaccurate measurements of the temperature at the resistance sensors in the active area region of interest. Compared to the gated Seebeck devices (Fig. 3.2), as discussed in sections 3.2.2 and 3.2.3, substantially different dimensions for the active area have been chosen, due to the following two considerations: for reliable Hall voltage measurements the device length L should be much longer than the device width W ($L \gg W$) to avoid field-line distortions along the y-axis within the active area at the Hall probe positions due to the fixed potential of the source and drain electrodes.[260] L should be at least four times as long as W ($L \geq 4 \cdot W$) and therefore $L = 4 \cdot W$ has been employed for the presented devices (see section 3.2.3).[260] Both AC and DC Hall measurements have been performed with the designed devices in Prof. Sirringhaus's group, but will not be further discussed here. Further devices, with $L = 6 \cdot W$, $L = 8 \cdot W$ and $L = 10 \cdot W$ have been designed but not employed for the thermoelectric transport measurements to minimize the effect of inhomogeneous weighing of contributions to the thermal voltage from different regions along the x-axis of the active area (due to non-linear temperature gradients along the x-axis), which is inevitable when moving the resistance sensors further apart. Whether devices with such long channels are in fact detrimental to measurements of the Seebeck coefficient needs to be established in future experiments. As long as the thermal voltage is a linear function of the temperature difference, meaning that it is a linear response to this temperature difference ($\Delta T \ll T$), even such non-linear temperature profiles should be acceptable for Seebeck coefficient measurements of homogeneous samples. The second reason for the chosen device dimensions, is related to the fact that the relative error in

the Seebeck coefficient measurement (see further discussion in the following section) can be reduced by increasing the spacing between the resistance sensors. Considering that molecularly doped material systems are highly conducting, with device resistances on the order of kΩ to MΩ depending on doping level and temperature, they are much less restrictive on the W/L ratio. For gated thermoelectric devices this ratio needs to be high in order to keep the device resistance low, allowing to extend the range of temperatures and charge densities before the load resistance becomes considerably large compared to the input impedance of the thermal voltage measurement unit (SMU). Since the resistance of conducting material systems is inherently low, ratios as low as $W/L = 0.1$ can be employed without concern, reducing the relative error in the Seebeck coefficient measurements.

Temperature-dependent 4pp electrical conductivity and Seebeck coefficient measurements of ion-exchange doped PBTTT were performed under vacuum ($< 10^{-6}$ mbar) in a six-probe closed-cycle cryogenic probe station (Lake Shore Cryotronics Inc., CRX-4K) with a Keithley 2612B Dual Channel SourceMeter and a Keithley 6430 Sub-Femtoamp Remote SourceMeter including Remote PreAmp. The principle measurement routine was identical to the one introduced for the field-effect-modulated Seebeck coefficient measurements of the polymer-sorted SWCNT networks (apart from the loop over the gate voltage). For the 4pp conductivity measurements one SMU of the Keithley 2612B was used to sweep the source-drain voltage (V_{ds}) from -0.1 V to 0.1 V. The other SMU of the Keithley 2612B was used to measure the potential between the upper right Hall probe (closer to the drain) and the source (V_{P1}, between pads 4 and h2), while the SMU of the Keithley K6430 including pre-amplifier was used to measure the potential between the upper left Hall probe and the source (V_{P2}, between pads 3 and h2). Hence, the 4pp conductivity was obtained according to:

$$\sigma_{\mathrm{4pp}} = \frac{D}{W \cdot h} \left| \frac{\partial I_{\mathrm{ds}}}{\partial (V_{\mathrm{P1}} - V_{\mathrm{P2}})} \right|, \tag{3.2}$$

with $D = 140$ µm the distance between the Hall voltage probes, $W = 105$ µm the channel width, $h \sim$ 60-100 nm the PBTTT film thickness determined by atomic force microscopy (AFM) and I_{ds} the source-drain current. Once again one SMU of the Keithley 2612B has been employed to vary the heater power by changing the heater voltage from $0 - 3$ V in steps of 0.3 V for the sensor resistance and thermal voltage measurements, while the thermal voltage was measured again with the SMU and pre-amplifier of the Keithley K6430 from the cold to the grounded hot sensor. Further details are discussed in chapter 6.

3.3.2 Error analysis and accurate Seebeck coefficient measurements

In the following the relative errors of the Seebeck coefficient measurements shall be analysed. The analysis is presented for the field-effect-modulated Seebeck coefficient measurements of the semicrystalline polymer P(NDI2OD-T2). The respective modifications in the analysis due to the modified device designs and employed measurement units for the SWCNT network-based gated Seebeck as well as multifunctional devices are outlined at the end of this section. Recalling the definition of the Seebeck coefficient:

$$S = \frac{V_{\mathrm{th}}}{\Delta T} \tag{3.3}$$

and substituting ΔT with Eq. 3.1, the Seebeck coefficient can be expressed as:

$$S = \frac{V_{\mathrm{th}}}{W \cdot \left(\frac{\frac{dR_{\mathrm{hot}}}{dW}}{\frac{dR_{\mathrm{hot}}}{dT}} - \frac{\frac{dR_{\mathrm{cold}}}{dW}}{\frac{dR_{\mathrm{cold}}}{dT}} \right)}. \tag{3.4}$$

Defining the 'bracket value' B as

$$B \equiv \left(\frac{\frac{dR_{\mathrm{hot}}}{dW}}{\frac{dR_{\mathrm{hot}}}{dT}} - \frac{\frac{dR_{\mathrm{cold}}}{dW}}{\frac{dR_{\mathrm{cold}}}{dT}} \right), \tag{3.5}$$

and $x \equiv S \cdot B$, the relative error in the Seebeck coefficient can be expressed as:

$$\left(\frac{\Delta S}{S} \right) = \sqrt{\left(\frac{\Delta x}{x} \right)^2 + \left(\frac{\Delta B}{B} \right)^2}. \tag{3.6}$$

These two contributions originate from the fact that x is first obtained from a linear fit of the thermal voltage versus heater power (times B), which causes a fitting error Δx and then x is divided by B, which has an error ΔB itself, to obtain S.
The measurement errors in the thermal voltage and the heater power are negligible as explained in the following, but are also contained in the fitting error Δx. The relative fitting error Δx is usually <1 %.
Since the measured thermal voltages are in a range of 0 to 2 V, the resolution in the thermal voltage measurement ΔV_{th} according to the data sheet of the Agilent SPA 4156B is around 2 µV. In principle the relative error in the measured thermal voltage could be quite large, however since the extracted Seebeck coefficient does not change when only the three data points with the highest heater powers are considered for the linear fit of the (ΔT, V_{th}) data points (compared to all data points), it is justified to consider the measured thermal voltages to be on the order of 0.2 to 2 mV. Therefore, the relative error in the thermal voltage measurement is in the worst case around 1 %:

$$\frac{\Delta V_{\mathrm{th}}}{V_{\mathrm{th}}} \approx \frac{2 \cdot 10^{-6}\,\mathrm{V}}{2 \cdot 10^{-4}\,\mathrm{V}} \approx 0.01. \tag{3.7}$$

The error in the heater power $W = V_{\text{heater}} \cdot I_{\text{heater}}$ can be written as:

$$\begin{aligned} \Delta W &= \sqrt{(\frac{\partial W}{\partial V_{\text{heater}}} \cdot \Delta V_{\text{heater}})^2 + (\frac{\partial W}{\partial I_{\text{heater}}} \cdot \Delta I_{\text{heater}})^2} \\ &= \sqrt{(I_{\text{heater}} \cdot \Delta V_{\text{heater}})^2 + (V_{\text{heater}} \cdot \Delta I_{\text{heater}})^2}. \end{aligned} \tag{3.8}$$

According to the data sheet of the SPA, the resolution in the output voltage in a voltage range of 0 to 20 V is $\Delta V_{\text{heater}} = 100$ mV. The resolution in the current measurement in a current range from 0 to 10 mA, is $\Delta I_{\text{heater}} = 10$ nA. The highest error occurs when the heater current I_{heater} and heater voltage V_{heater} are the highest, which means for the highest applied heater powers. In that case the heater current is around 7 mA and the heater voltage around 10 V, which means that the error in the heater power in the worst case scenario reads as:

$$\begin{aligned} \Delta W &= \sqrt{(7 \cdot 10^{-3}\,\text{A} \cdot 10^{-1}\,\text{V})^2 + (10\,\text{V} \cdot 10 \cdot 10^{-9}\,\text{A})^2} \\ &\approx 7 \cdot 10^{-4}\,\text{W}. \end{aligned} \tag{3.9}$$

Therefore, the relative error in the worst case scenario is around 1 %:

$$\frac{\Delta W}{W} = \frac{7 \cdot 10^{-4}\,\text{W}}{70 \cdot 10^{-3}\,\text{W}} \approx 0.01. \tag{3.10}$$

The relative error in the bracket value B can be significantly larger. Defining $\alpha \equiv \frac{dR_{\text{hot}}}{dW}$, $\beta \equiv \frac{dR_{\text{hot}}}{dT}$, $\gamma \equiv \frac{dR_{\text{cold}}}{dW}$, $\theta \equiv \frac{dR_{\text{cold}}}{dT}$, $a \equiv \frac{\alpha}{\beta}$ and $b \equiv \frac{\gamma}{\theta}$ and considering that:

$$\begin{aligned} \frac{\Delta B}{B} &= \frac{1}{B}\sqrt{(\Delta a)^2 + (\Delta b)^2}, \\ \Delta a &= a \cdot \sqrt{\left(\frac{\Delta\alpha}{\alpha}\right)^2 + \left(\frac{\Delta\beta}{\beta}\right)^2}, \\ \Delta b &= b \cdot \sqrt{\left(\frac{\Delta\gamma}{\gamma}\right)^2 + \left(\frac{\Delta\theta}{\theta}\right)^2}, \end{aligned} \tag{3.11}$$

the relative error in the bracket value ($\frac{\Delta B}{B}$) can be written as:

$$\left(\frac{\Delta B}{B}\right) = \frac{1}{B}\sqrt{a^2\left[\left(\frac{\Delta\alpha}{\alpha}\right)^2 + \left(\frac{\Delta\beta}{\beta}\right)^2\right] + b^2\left[\left(\frac{\Delta\gamma}{\gamma}\right)^2 + \left(\frac{\Delta\theta}{\theta}\right)^2\right]}. \tag{3.12}$$

The relative errors in the measured resistances are smaller than 1 % as explained below, but are contained in the fitting error ΔB. With $R_{\text{sens}} = \frac{V_{\text{sens}}}{I_{\text{sens}}}$ and

$$\frac{\Delta R_{\text{sens}}}{R_{\text{sens}}} = \sqrt{\left(\frac{\Delta V_{\text{sens}}}{V_{\text{sens}}}\right)^2 + \left(\frac{\Delta I_{\text{sens}}}{I_{\text{sens}}}\right)^2}, \tag{3.13}$$

where $I_{\text{sens}} = 10^{-4}$ A, $\Delta I_{\text{sens}} = 10^{-8}$ A according to the Agilent SPA handbook for the current output range from 0 to 100 µA, $V_{\text{sens}} \approx 0.1$ V and $\Delta V_{\text{sens}} = 2$ µV according to the voltage measurement resolution of the SPA for the voltage range from 0 to 2 V, the relative error in the resistance measurement is approximately:

$$\begin{aligned} \frac{\Delta R_{\text{sens}}}{R_{\text{sens}}} &= \sqrt{\left(\frac{2 \cdot 10^{-6}\,\text{V}}{10^{-1}\,\text{V}}\right)^2 + \left(\frac{10^{-8}\,\text{A}}{10^{-4}\,\text{A}}\right)^2} \\ &\approx 10^{-4}. \end{aligned} \tag{3.14}$$

Considering this analysis, the total relative error in the Seebeck measurement is dominated by the relative error in the bracket value $\frac{\Delta B}{B}$, which is caused by the several fitting errors during the linear regression fits to extract the change of the sensor resistances with heater power and temperature. $\frac{\Delta B}{B}$ has been reduced to approx. 6 % (compared to previous > 10 %) using 4pp resistance calibration measurements (for the device structure in Fig. 3.1).

With respect to the modification of the measurement unit to the Keithley K2612B and K6430, the presented analysis is still valid, meaning that $\frac{\Delta V_{\text{th}}}{V_{\text{th}}}$, $\frac{\Delta W}{W}$ and $\frac{\Delta R_{\text{sens}}}{R_{\text{sens}}}$ are still < 1 % and negligible compared to $\frac{\Delta B}{B}$, considering that the resolution of these units is generally higher than that of the Agilent SPA 4156B. For instance the voltage measurement resolution in the relevant lowest voltage range is 0.1 µV and 1 µV for the Keithley K2612B and K6340 respectively (compared to 2 µV for the SPA).

Aside from the added 4pp voltage probes the advantage of the device structure employed for the SWCNT networks (Fig. 3.2) over the one employed for the gated Seebeck coefficient measurements of P(NDI2OD-T2) (Fig. 3.1) is predominantly an improved measurement accuracy. Moving the branching points of the resistance sensors closer to the active area and establishing a more one-dimensional temperature gradient via the modified heater design, improves the accuracy of the local temperature and thereby the Seebeck coefficient measurements (as also discussed in the previous section for the multifunctional devices). The relative errors in the Seebeck coefficients were comparable to the previous design and on the order of 5 %.

Concerning the further reduction of the relative errors in the Seebeck coefficient, it is worth to note that the relative errors of the resistance change with temperature typically exceed those of the resistance change with heater power ($\frac{\Delta\beta}{\beta} > \frac{\Delta\alpha}{\alpha}$ and $\frac{\Delta\theta}{\theta} > \frac{\Delta\gamma}{\gamma}$) and are typically on the order of 1 %. It is therefore obvious that the relative error in the Seebeck coefficient can be further reduced with more temperature calibration data points. Furthermore, from Eq. 3.12 it is also evident that higher bracket values B lead to a reduction in the relative error of the Seebeck coefficient. Higher bracket values can

be achieved by moving the resistance sensors further apart and thereby improving the cooling of the cold sensor (increasing B). It is presumed that the lower relative errors in the Seebeck coefficients of ~ 2 % (for only 3-7 temperature data points) measured with the multifunctional devices is predominantly enabled by this larger spacing between the resistance sensors.

3.4 Structural characterization

3.4.1 Atomic force microscopy

Atomic force microscopy (AFM) images of the SWCNT networks were collected using a Bruker corp. Dimension Icon atomic force microscope in ScanAsyst mode. The images are reported in section 5.2.

3.4.2 Grazing incidence wide-angle X-ray scattering

As emphasized at the beginning of chapter 4 and 6, the grazing incidence wide-angle X-ray scattering (GIWAXS) measurements were performed by Dr. Xuechen Jiao and Prof. Chris McNeill from the Monash University in Australia. GIWAXS measurements of the P(NDI2OD-T2) films were performed at the SAXS/WAXS beamline at the Australian Synchrotron.[261] 15 keV photons were used with 2-dimensional scattering patterns recorded on a Dectris Pilatus 1M detector. Images shown in section 4.3 were acquired at an incident angle close to the critical angle. Such images were chosen from a series of images taken with incident X-ray angle varying from 0.02° to 0.15° in steps of 0.01° with the chosen image showing the highest scattering intensity. The X-ray exposure time was 1 s such that no film damage was identified. The sample-to-detector distance was calibrated using a silver behenate sample. The results were analysed by an altered version of the NIKA 2D[262] based in IgorPro. A similar procedure was employed for the GIWAXS measurements of the PBTTT films in section 6.2.

3.5 Optical characterization

3.5.1 Absorbance measurements

The absorption spectra of the SWCNT dispersions (section 5.2) and PBTTT films (section 6.2) were obtained with a Cary 6000i absorption spectrometer (Varian Inc.). An additional Glan-Taylor polarizer was used for the polarized UV-Vis measurements of aligned PBTTT films in section 6.2.

3.5.2 Raman spectroscopy

Raman spectra of the deposited SWCNT networks were recorded with a Renishaw plc inVia Reflex confocal Raman microscope with a 50x objective (Leica, NA = 0.75). Maps consisting of approximately 1600 spectra over an area of 100 x 100 μm^2 were collected in StreamLine mode with three different lasers (532 nm, 633 nm and 785 nm). For each sample, the spectra were averaged and baseline-corrected. The spectra are reported in section 5.2.

3.5.3 Photothermal deflection spectroscopy

As emphasized at the beginning of chapter 5, the photothermal deflection spectroscopy (PDS) measurements were performed by Dr. Mojtaba Abdi-Jalebi, visiting researcher of the Optoelectronics Group at the University of Cambridge and University Lecturer at the University College London. PDS measurements of the SWCNT networks were performed with a custom setup similar to the one presented by Jackson and coworkers.[54,263] Apart from using Heraeus Spectrosil 2000 substrates, the SWCNT networks were prepared as for the thermoelectric devices. The samples were held in a hermetically sealed Suprasil quartz cuvette (Hellma GmbH & Co. KG) filled with an inert liquid (3M Fluorinert Electronic Liquid FC-72), excited with a modulated monochromated light beam produced by a 100 W Xenon arc lamp (Osram GmbH) and a CVI Digikrom DK240 monochromator and probed with a 670 nm fibre-coupled diode laser (iFLEX2000, Qioptiq Ltd.). The beam deflections were measured using a quadrant photodiode and a lock-in amplifier (Stanford Research Systems SR830). The data and extracted Urbach energies are presented in section 5.2.

Chapter 4

Charge and thermoelectric transport in low-disorder, semicrystalline conjugated polymers

Substantial parts of this chapter were published in *Communications Physics* as Statz, M. *et al.* On the manifestation of electron-electron interactions in the thermoelectric response of semicrystalline conjugated polymers with low energetic disorder. *Commun. Phys.* **1,** 16 (2018).[172]

The device architecture employed for the work presented in this chapter was designed by Dr. Deepak Venkateshvaran, postdoctoral member of Prof. Henning Sirringhaus's group at the University of Cambridge. The presented grazing incidence wide-angle X-ray scattering (GIWAXS) measurements of samples prepared by Dr. Sam Schott, postdoctoral member of Prof. Henning Sirringhaus's group, were performed by Dr. Xuechen Jiao and Prof. Chris McNeill from the Monash University in Australia at the Australian Synchrotron. The theoretical model was developed in collaboration with Dr. Riccardo Di Pietro, at the time senior research scientist at the Hitachi Cambridge Laboratory, and with support from Adj. Prof. David Emin from the University of New Mexico in the USA.

4.1 Motivation and outline

As outlined in section 1.2.2, in the past decade semicrystalline donor-acceptor copolymer semiconductors with field-effect mobilities comparable to or even exceeding those of amorphous silicon have been developed. While leading to significant advances in flexible electronic applications, this evolution has exposed limitations of describing charge transport in these materials with disorder-based models developed originally for more disordered, lower mobility polymers. Here we show that the charge density and temperature dependence of the field-effect electron mobility and gated Seebeck coefficient in the semicrystalline polymer P(NDI2OD-T2) with varying degrees of crystallinity are incompatible with a description of charge transport being limited by energetic disorder effects. We provide instead direct evidence of low-disorder, narrow-band conduction. A spatially inhomogeneous density of states (DoS) and the inclusion of short range electron-electron interactions allow to consistently explain both the measured mobility and Seebeck coefficient. These results provide a rationale for improving the thermoelectric efficiency of polymer semiconductors via increasing the extension of crystalline domains.

The charge transport properties of conjugated polymers have experienced tremendous progress in the past decade with the development of low-disorder amorphous as well as semicrystalline polymers with charge carrier mobilities that outperform those of amorphous silicon and make these materials suitable candidates for a variety of electronic applications.[12,54,67] Most theoretical models of charge transport in conjugated polymers assume transport to be dominated by energetic disorder effects and describe the transport properties in terms of hopping between localized states or delocalized transport above a mobility edge (ME).[61,144,159] These models were initially developed by Mott for transport in strongly disordered inorganic semiconductors and provided an accurate prediction of the temperature and charge density dependence of the conductivity, the most prominent feature of amorphous inorganic semiconductors.[164] They have been extensively refined by considering a Gaussian, exponential or more complex DoS in order to better describe organic semiconductors.[158] Several types of hopping mechanisms have been considered, most notably those developed by Miller and Abrahams as well as those for polaron transport.[153,161,167] Nevertheless, it has to be stressed that some of these models have been employed outside their range of validity. Emin showed, for example, that for both acoustic and optical phonons the Miller-Abrahams hopping rates only emerge at very low temperatures, yet they are used frequently outside this range.[149,168]

Different approaches were developed to calculate the macroscopic transport coefficients. Among those are numerically solving the Master equation or applying a percolation theory approach.[61,154,159]

While such energetic disorder-based models describe the transport properties of low-mobility conjugated polymers very well,[159] it has recently been shown that they are not applicable to some high-mobility systems: for nearly amorphous polymers with well-defined near-planar chain conformation the energetic disorder broadening of the DoS can become so low that nearly all repeat units along the polymer chain become thermally accessible for transport and that the charge carrier mobility becomes independent of carrier concentration.[54,256] In high-mobility polymers with strong aggregation and semicrystalline microstructure the description of transport is even more challenging:[55,67,69,264] one has to consider the heterogeneity of the electronic structure due to the coexistence of crystalline and amorphous domains. There is clear experimental evidence for such inhomogeneities in the DoS but these are usually not considered within disorder-based transport models.[55,265,266] It was shown recently that energetic disorder models are not consistent with the measured microstructure of semicrystalline polymers.[135] In particular, a common prediction of such models is a stronger charge density dependence of the mobility with stronger energetic disorder. This is in contradiction with observations that a stronger charge density dependence of the mobility is unambiguously tied to an increase in average crystallite size, i.e., a higher degree of structural order.[135]

A better understanding of the transport properties of these polymers is urgently required in order to make further progress on materials and device performance. For this a more powerful, experimental methodology is needed as measurements of the charge carrier mobility and its carrier concentration and temperature dependence alone can often be fitted well by different transport models and different sets of parameters.[135] Therefore, we extend such measurements to include simultaneous determination of the thermoelectric Seebeck coefficient and its carrier concentration and temperature dependence which allows us to constrain the possible transport models. We investigate the more complex case of a semicrystalline, high-mobility polymer, in which the DoS cannot be assumed to be uniform. We show that, although common disorder-based transport models can reproduce the temperature and charge density dependence of the mobility correctly, they fail to explain the temperature and charge density dependence of the Seebeck coefficient simultaneously. We measure a temperature-independent Seebeck coefficient which exhibits a $\frac{k_B}{e}\ln(10)$-slope indicative of narrow-band transport in a non-degenerate semiconductor. We show that in order to explain the full set of experimental mobility and Seebeck data on such semicrystalline polymers consistently

it is necessary to consider a spatially inhomogeneous DoS and include electron-electron interactions through an explicitly charge density-dependent DoS.

4.2 Thermoelectric transport in the non-degenerate regime

The Seebeck coefficient represents the entropy transported by a charge carrier divided by its charge.[210] It allows to directly probe the DoS as well as the relative contribution to charge transport of different conduction channels within the DoS.
The general expression for the Seebeck coefficient in an independent-electron model with a spatially homogeneous DoS can be derived from the Boltzmann transport equation (see section 2.3.1)[216,217] and reads:

$$S = -\frac{1}{eT}\left[\frac{\int (E - E_{\mathrm{F}})\sigma(E)dE}{\int \sigma(E)dE}\right], \tag{4.1}$$

where $\sigma(E)$ is the energy dependent conductivity function in the expression for the conductivity:

$$\begin{aligned}\sigma &= \int \sigma(E)dE \\ &= \int e\mu(E)g(E)k_{\mathrm{B}}T\left(-\frac{\partial f(E)}{\partial E}\right)dE,\end{aligned} \tag{4.2}$$

with $f(E)$ representing the Fermi-Dirac distribution function and $g(E)$ the DoS. In Eq. 4.1 each charge contributes to the transported energy according to its excess energy with respect to the chemical potential $(E - E_{\mathrm{F}})$, weighted by the relative contribution of the conduction channel $\frac{\sigma(E)}{\sigma}$ to the total conductivity.
It can be shown that if the state occupancy is low, i.e. $\frac{n}{\overline{N}} \ll 1$, where n is the field-induced charge density and $\overline{N}$ is the total number of states per unit volume (in semicrystalline systems, like the one investigated here, this includes states in both the amorphous as well as the crystalline domains as well as spin degeneracy), the difference in S between two carrier concentrations n_1 and n_2 with $n_2 > n_1$ just depends on the logarithm of the ratio of the two carrier concentrations. In this low-occupancy, non-degenerate limit ($\frac{n}{\overline{N}} \ll 1, |E - E_{\mathrm{F}}| \gg k_{\mathrm{B}}T$) the Seebeck coefficient S assumes the characteristic $\frac{k_{\mathrm{B}}}{e}\ln(10)$-slope when plotted against the logarithm of the charge density and can be expressed in terms of $\widetilde{N}$, the effective DoS that is thermally accessible to

charge carriers contributing to transport:

$$\begin{aligned} S(n_2) - S(n_1) &= \frac{k_\mathrm{B}}{e} \ln\left(\frac{n_2}{n_1}\right) \\ \Rightarrow S(n) &= -\frac{k_\mathrm{B}}{e} \ln\left(\frac{\widetilde{N}}{n}\right). \end{aligned} \tag{4.3}$$

This can be easily derived from the general expression for the Seebeck coefficient (within a spatially homogeneous DoS) from Boltzmann transport equation (Eq. 4.1).
In the low-occupancy, non-degenerate regime the Fermi-Dirac distribution function ($f(E)$) can be approximated with the Boltzmann distribution function and hence it holds:

$$\left(-\frac{\partial f(E)}{\partial E}\right) \approx \frac{1}{k_\mathrm{B}T} \exp\left(-\frac{E - E_\mathrm{F}}{k_\mathrm{B}T}\right). \tag{4.4}$$

Therefore, if the Seebeck coefficient for a certain charge density n_1 respectively Fermi energy E_F is:

$$S(E_\mathrm{F}) = -\frac{1}{eT}\left[\frac{\int (E - E_\mathrm{F}) g(E)\mu(E) \exp\left(-\frac{E-E_\mathrm{F}}{k_\mathrm{B}T}\right) dE}{\int g(E)\mu(E) \exp\left(-\frac{E-E_\mathrm{F}}{k_\mathrm{B}T}\right) dE}\right], \tag{4.5}$$

then the Seebeck coefficient for n_2 respectively $\bar{E}_\mathrm{F} = E_\mathrm{F} + \Delta E$ is:

$$\begin{aligned} S(\bar{E}_\mathrm{F}) &= -\frac{1}{eT}\left[\frac{\int (E - \bar{E}_\mathrm{F}) g(E)\mu(E) \exp\left(-\frac{E-\bar{E}_\mathrm{F}}{k_\mathrm{B}T}\right) dE}{\int g(E)\mu(E) \exp\left(-\frac{E-\bar{E}_\mathrm{F}}{k_\mathrm{B}T}\right) dE}\right], \\ &= S(E_\mathrm{F}) + \frac{\Delta E}{eT}. \end{aligned} \tag{4.6}$$

ΔE can be expressed in terms of the charge densities n_1 and n_2 by considering:

$$\begin{aligned} n_1 = n(E_\mathrm{F}) &= \int g(E) \exp\left(-\frac{E - E_\mathrm{F}}{k_\mathrm{B}T}\right) dE, \\ n_2 = n(E_\mathrm{F} + \Delta E) &= n_1 \exp\left(\frac{\Delta E}{k_\mathrm{B}T}\right). \end{aligned} \tag{4.7}$$

Hence $\Delta E = k_\mathrm{B}T \ln\left(\frac{n_2}{n_1}\right)$ holds and therefore we arrive at Eq. 4.3:

$$S(n_2) = S(n_1) + \frac{k_\mathrm{B}}{e} \ln\left(\frac{n_2}{n_1}\right). \tag{4.8}$$

Furthermore, the observation of a $\frac{k_\mathrm{B}}{e}\ln(10)$-slope of the Seebeck coefficient when plotted against the logarithm of the charge density necessitates the low-occupancy,

non-degenerate regime ('if and only if'- relationship). This can be easily shown as follows:
If we observe a $\frac{k_B}{e}\ln(10)$-slope of the Seebeck coefficient when plotted against the logarithm of the charge density, the following holds according to Eq. 4.3:

$$\frac{k_B}{e} = \frac{S(n_2) - S(n_1)}{\ln(n_2) - \ln(n_1)}, \forall\, n_1,\, n_2. \tag{4.9}$$

Let us consider an arbitrary n_1, with $\xi = \frac{n_2}{n_1}$ and an arbitrary n_1', with $\xi = \frac{n_2'}{n_1'}$, then it follows from Eq. 4.9 that:

$$S(\xi n_1) - S(n_1) = S(\xi n_1') - S(n_1'), \forall\, n_1,\, n_1'. \tag{4.10}$$

Nevertheless, it is evident that when employing Eqs. 4.1 and 4.2 to express the Seebeck coefficients in Eq. 4.10, the equation only holds for all n_1 and n_1' if the Fermi-Dirac distribution function is approximated with the Boltzmann distribution function. Hence, we can follow: if we observe a $\frac{k_B}{e}\ln(10)$-slope of the Seebeck coefficient when plotted against the logarithm of the charge density, then we are in the low-occupancy, non-degenerate regime ($\frac{n}{\widetilde{N}} \ll 1$, E_F outside the band) which is governed by Boltzmann statistics.
Equation 4.3 describes the entropy-of-mixing contribution to the Seebeck coefficient, which is the change of the entropy-of-mixing upon adding a charge carrier.[211,267] In this way measurements of the Seebeck coefficient provide direct and powerful insight into the DoS. It has been reported for several high mobility polymer systems such as indacenodithiophene-benzothiadiazole (IDTBT), with a very well defined planar polymer chain conformation that is maintained uniformly despite a nearly amorphous microstructure, that $\widetilde{N}$ is approximately temperature independent via the observation of a temperature-independent Seebeck coefficient in the low-occupancy regime.[54] Furthermore, it has been shown that the slope extracted from a plot of the field-effect gated Seebeck coefficient against the logarithm of the carrier concentration exhibits a value close to $\frac{k_B}{e}\ln(10)$.[54]

4.3 Structural characterization

We investigate P(NDI2OD-T2), a widely studied n-type conjugated polymer with a relatively high electron mobility on the order of 0.1 $cm^2\ V^{-1}\ s^{-1}$.[69] We have fabricated top-gate, field-effect transistors with an on-chip heater (Fig. 4.1a, b, see section 3.2.1 for further details) to characterize both charge carrier mobility and the Seebeck coefficient

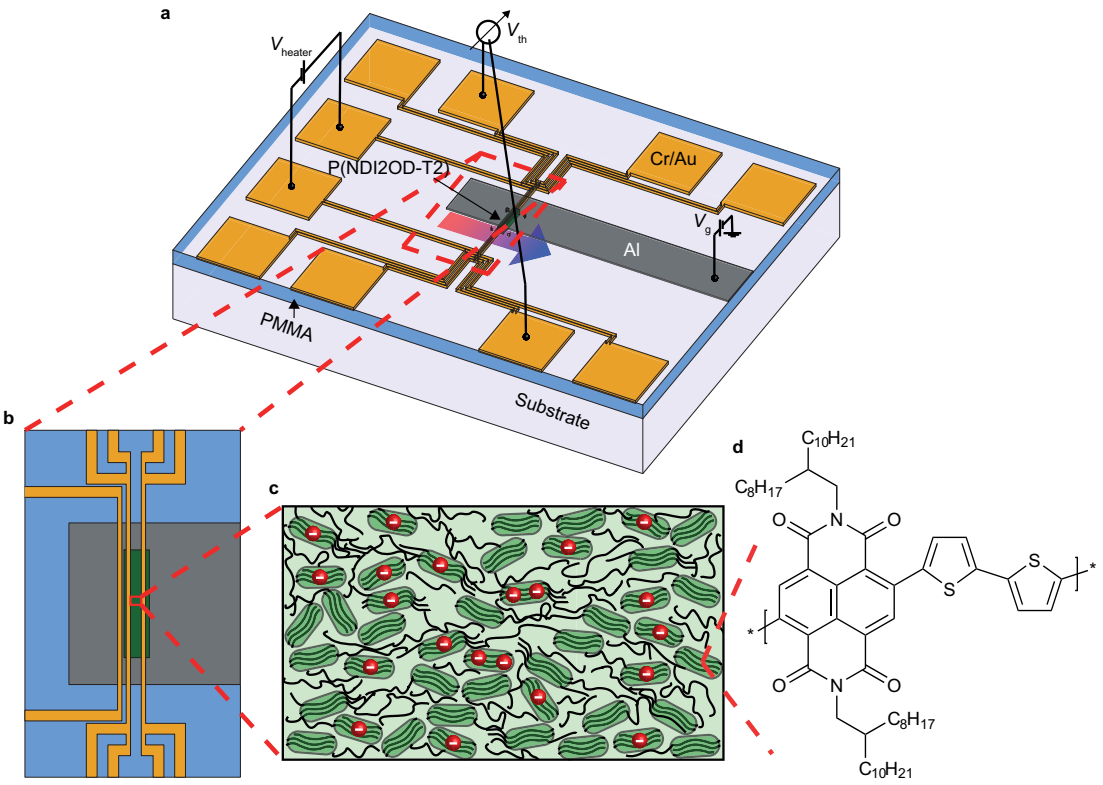

Figure 4.1. Device architecture and model illustration. Schematic of the device structure of the thin film transistors with an on-chip heater element (a, b: modified dimensions for illustration) as well as the microstructure of the semicrystalline polymer semiconductors (c) and the molecular structure of P(NDI2OD-T2) (d) are shown.

in the same device.[54,257] P(NDI2OD-T2) was spin-coated from a 5 g L^{-1} solution in toluene and the gate dielectric was PMMA (see sections 3.1 and 3.2.1 for further details). It has already been shown how by controlling the processing conditions it is possible to selectively tune the size of the crystalline domains in these films while keeping other properties such as cumulative positional disorder, energetic disorder and polymer chain orientation in the crystalline domains unaffected (microstructure illustrated in Fig. 4.1c, molecular structure shown in Fig. 4.1d).[135] Here we focus on films annealed at 200 °C and films dried in a vacuum oven (as-cast).

We characterised the microstructure of each polymer film by 2D grazing incidence wide-angle X-ray scattering (GIWAXS) (Fig. 4.2, see section 3.4.2 for further experimental details). 1D GIWAXS in-plane (IP) and out-of-plane (OOP) intensity profiles are shown in Fig. 4.3a and Fig. 4.3b. Coherence length and lattice parameters are extracted from these datasets and summarized in Table 4.1. Upon annealing we observe an increase in coherence length from 2.1 nm to 3.5 nm along the π-π stacking direction, from 16.5 nm

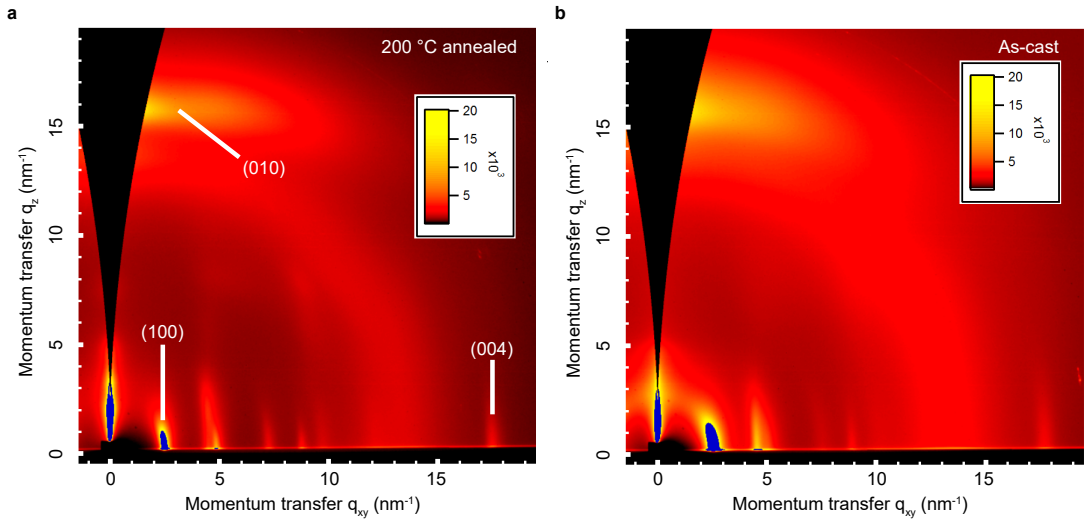

Figure 4.2. 2D grazing incidence scattering patterns of P(NDI2OD-T2) polymer films. The GIWAXS patterns for the 200 °C annealed film (a) and the as-cast film (b) are shown. The peak assignments are based on previous reports.[268,269] From the diffraction peaks an increase in coherence length in all directions upon annealing is evident. This indicates an increase in the average volume of crystalline domains by a factor of 4 and the average lamellar area (relevant for charge transport in OFETs) by a factor of 2. The measurements have been performed by Dr. Xuechen Jiao and Prof. Chris McNeill.

to 20.7 nm along the backbone direction and from 20.1 nm to 38.1 nm along the lamellar stacking direction, indicating an increase in the average volume of crystalline domains by a factor of 4 and the average lamellar area (relevant for charge transport in organic field-effect transistors (OFETs)) by a factor of 2 (Table 4.1). D-spacings along the three crystallographic directions are not appreciably altered by the annealing (Table 4.1).

4.4 Electric and thermoelectric characterization

Both charge carrier mobility and Seebeck coefficient have been measured as a function of temperature and charge density, according to the procedure reported in section 3.3.1. The temperature calibration of the source and drain contacts was performed with a 4-point-probe calibration (Fig. 4.1b). The temperature-dependent saturation mobilities for the annealed and as-cast device were extracted from saturation transfer curves (section 3.3.1, Figure 3.4) according to ref. [138] and are presented in Fig. 4.4a and Fig. 4.4b respectively. The extracted mobility is thermally activated for both films with large and small crystalline domains. In contrast to nearly amorphous polymers like IDTBT the annealed sample, with large crystalline domains shows a pronounced

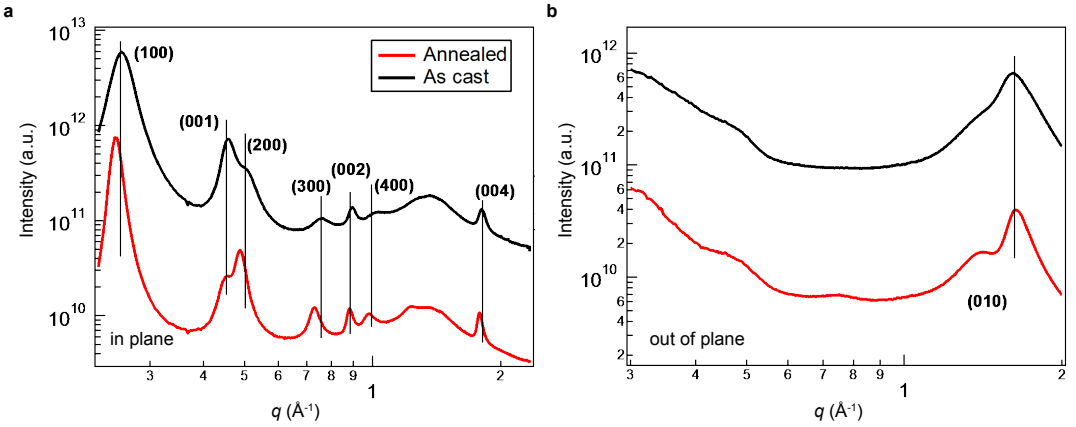

Figure 4.3. 1D GIWAXS profiles. In plane (a) and out of plane (b) 1D GIWAXS profiles are shown. The peak assignments are based on previous reports.[268,269] From the sharper diffraction peaks, the (100) lamellar stacking peak, the (010) π-π stacking peak and the (002) backbone stacking peak, an increase in coherence length in all directions upon annealing is evident (black line: as-cast condition, red line: 200 °C annealed condition). The measurements have been performed by Dr. Xuechen Jiao and Prof. Chris McNeill.

Table 4.1. Lattice parameters and coherence lengths from 2D GIWAXS measurements.

	q (Å^{-1}) IP (100)	Lamellar stacking (Å) IP (100)	FWHM (Å^{-1}) IP (100)	Coherence length (Å) IP (100)
P(NDI2OD-T2) 200 °C	0.248	25.32	0.0165	380.61
P(NDI2OD-T2) as-cast	0.256	24.51	0.0312	201.28
	q (Å^{-1}) IP (002)	Backbone stacking (Å) IP (002)	FWHM (Å^{-1}) IP (002)	Coherence length (Å) IP (002)
P(NDI2OD-T2) 200 °C	0.883	14.22	0.0303	207.26
P(NDI2OD-T2) as-cast	0.896	14.02	0.0381	164.83
	q (Å^{-1}) OOP (010)	π-π stacking (Å) OOP (010)	FWHM (Å^{-1}) OOP (010)	Coherence length (Å) OOP (010)
P(NDI2OD-T2) 200 °C	1.644	3.82	0.1799	34.91
P(NDI2OD-T2) as-cast	1.624	3.87	0.2969	21.15

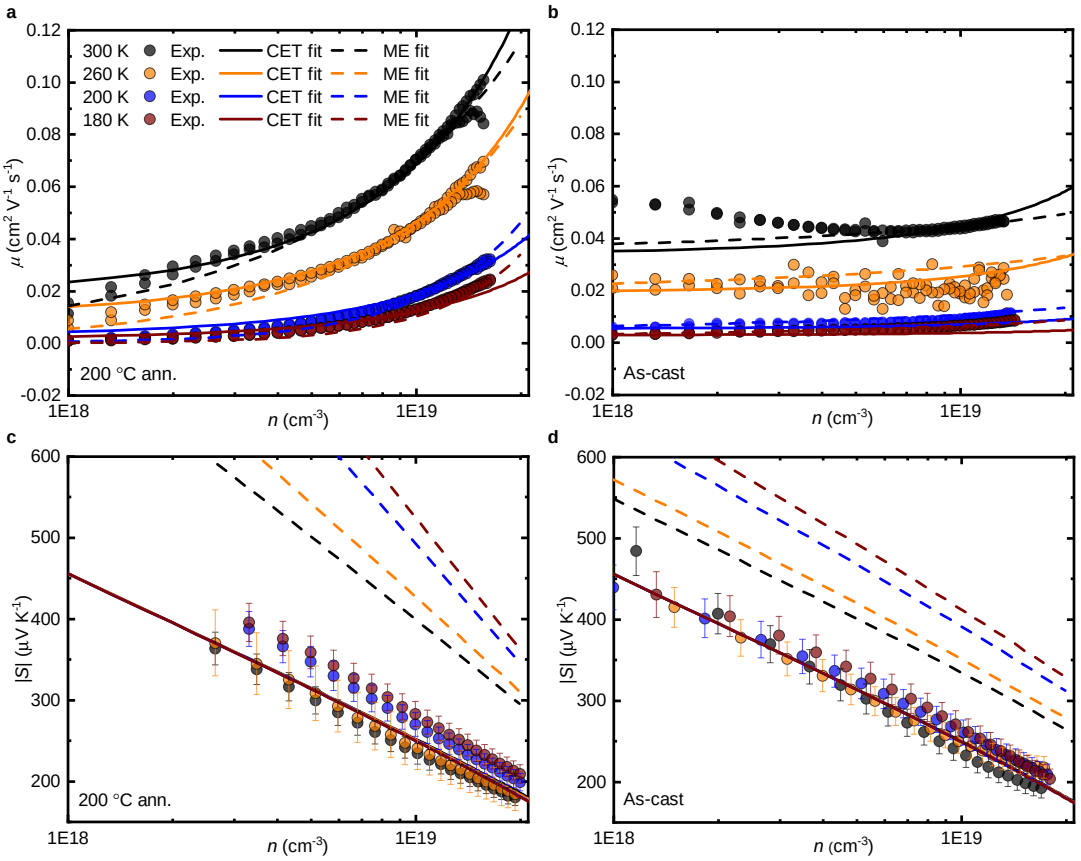

Figure 4.4. Saturation mobility (μ) and Seebeck coefficient (S) versus charge density (n). Charge density and temperature-dependent saturation mobility as well as Seebeck coefficient measurements of the 200 °C annealed (a, c) and as-cast device (b, d) are shown. The fits of the Coulomb enhanced charge transport (CET) model[135] (solid lines) and the ME model[144] (dashed lines) are presented as well. The fitting parameters for the CET fits are $E_{\mathrm{barr}} = 95$ meV, $\mu_{02\mathrm{C}} = 20 \cdot \frac{300\,\mathrm{K}}{T}$ cm^2 V^{-1} s^{-1}, $N = 2 \cdot 10^{20}$ cm^{-3} (a-d) and $G \approx 80$ meV, $\mu_0 = 0.75$ cm^2 V^{-1} s^{-1} (a, c) respectively $G \approx 120$ meV, $\mu_0 = 1.35$ cm^2 V^{-1} s^{-1} (b, d). The fitting parameters for the ME fits are $E_{\mathrm{deep}} = -8$ eV, $W_{\mathrm{deep}} = 0.01$ eV, $E_0 = -4$ eV, $E_{\mathrm{C}} = 0.037$ eV, $N_{\mathrm{tot}} = 2 \cdot 10^{20}$ cm^{-3} (a-d) and $\mu_0 = 0.7$ cm^2 V^{-1} s^{-1}, $N_{\mathrm{tail}} = 5 \cdot 10^{19}$ cm^{-3}, $W_{\mathrm{tail}} = 0.042$ eV, $E_{\mathrm{a}} = 0$ eV (a, c) respectively $\mu_0 = 5.2$ cm^2 V^{-1} s^{-1}, $N_{\mathrm{tail}} = 1.8 \cdot 10^{20}$ cm^{-3}, $W_{\mathrm{tail}} = 0.018$ eV, $E_{\mathrm{a}} = 0.04$ eV (b, d). The relative error in the Seebeck coefficient is approx. 7 %, calculated from the intrinsic current and voltage measurement errors of the Agilent SPA 4156B as well as the linear regression fit errors from the sensor resistance calibration and the thermal voltage versus temperature difference plots (shown as error bars on the data points).

charge density dependence of the mobility and an overall higher mobility than the as-cast sample (with small crystalline domains). In the as-cast sample the mobility is independent of the carrier concentration. This behaviour is fully consistent with previous mobility measurements on the same system which used normal FET device architectures without integrated heaters.[135]

In addition to these saturation mobility measurements, the charge density and temperature-

dependent Seebeck coefficient measurements of the annealed and as-cast device are presented in Fig. 4.4c and Fig. 4.4d respectively. Within the uncertainty of the measurement (approx. 7 %, the full error estimation is reported in section 3.3.2), we measured a very similar Seebeck coefficient for the two different samples. We observe a slight increase in the Seebeck coefficient with decreasing temperature, however such increase is within the precision of our measurement: the variation of the Seebeck is less than 14 % in the range 180 K - 300 K, and can consequently be considered to be constant in this temperature range. The slope of the Seebeck coefficient versus charge density of 220 μV K^{-1} $decade^{-1}$ is close to the ideal slope of $\frac{k_B}{e}\ln(10)$ (corresponding to 198 μV K^{-1} $decade^{-1}$) and a total DoS of $\widetilde{N} = 2 \cdot 10^{20}$ cm^{-3} is extracted from a fit to the Seebeck data for both annealed and as-cast films, despite the average crystallite size increasing by a factor of 2 upon annealing. If the increase in crystallite size was connected to a reduction of the amorphous states and an increase of the crystalline ones, it would cause an increase in the Seebeck coefficient of $\frac{k_B}{e}\ln(2) \approx 60$ μV, which we do not observe in our measurements. The fact that $\widetilde{N}$ stays constant indicates that a smaller number of larger crystalline domains are formed upon annealing so that the total number of electronic states is not changed significantly. This is in agreement with the results of UV-Vis spectroscopy, which show that the density of aggregates in the films does not change upon annealing.[73] The density calculated from the Seebeck coefficient is lower than the one estimated from UV-Vis (approx. $4 \cdot 10^{20}$ cm^{-3}) but there are several factors that can contribute to such difference. The monomer density is estimated from the lattice spacing of the crystalline fraction, and might lead to an overestimation of the total (crystalline + amorphous) monomer density. UV-Vis spectroscopy probes the bulk of the film, while the transport measurements probe the top surface, and the ratio between crystalline and amorphous domains can be different among the two. A more fundamental issue that will require further analysis is that the estimate from UV-Vis is obtained by probing the neutral molecules and neglects effects related to polaron formation that are instead captured by the Seebeck coefficient measurements.[264]

4.5 Evidence of low-disorder narrow-band conduction

From the experimental results we can draw some important general conclusions that do not rely on specific modeling. The observation of a $\frac{k_B}{e}\ln(10)$-slope and the temperature independence of S is direct evidence that the band in the DoS that contributes to transport is narrow with negligible disorder and that we are in the non-degenerate limit (E_F outside the band). The Seebeck coefficient follows a modified Heikes formula[235] in

which $\widetilde{N}$ is not equal to the total DoS $\overline{N} = 10^{21}$ cm^{-3} that can be estimated from the density of repeat units of the polymer, but is 5 times smaller. This result is consistent with the semicrystalline microstructure of P(NDI2OD-T2). Our interpretation is that in this system $\widetilde{N}$ reflects the DoS in the crystalline domains N_{C}, which is the band where most of the charges accumulate.[135] The temperature independence of S indicates that these states are not significantly disorder-broadened. The contribution to the DoS from the amorphous domains is expected to be energetically offset by more than 100 meV from the crystalline states due to the difference in bandgap between crystalline domains and amorphous regions and does not directly contribute to transport and to S.[135]
This raises the question how the strong gate voltage dependence of the mobility in the films annealed at 200 °C can be explained. It is straightforward to show generally that in the independent-electron approximation no charge density dependence of the mobility can be observed for a semiconductor in the non-degenerate limit:
In the low-occupancy, non-degenerate regime the Fermi-Dirac distribution can be approximated with the Boltzmann distribution function and hence two arbitrary charge densities n_1 and n_2 obey:

$$\xi = \frac{n_2}{n_1} = \exp\left(\frac{\Delta E}{k_{\mathrm{B}}T}\right), \tag{4.11}$$

according to Eq. 4.7. Following Eq. 4.2 the corresponding conductivities can be written as:

$$\begin{aligned} \sigma_1 &= \int e\mu(E)g(E)k_{\mathrm{B}}T\left(-\frac{\partial f(E, E_{\mathrm{F},1})}{\partial E}\right)dE, \\ \sigma_2 &= \int e\mu(E)g(E)k_{\mathrm{B}}T\left(-\frac{\partial f(E, E_{\mathrm{F},2})}{\partial E}\right)dE. \end{aligned} \tag{4.12}$$

By approximating the Fermi-Dirac distribution with the Boltzmann distribution and consequently considering Eqs. 4.4 and 4.7, Eq. 4.12 can be written as:

$$\sigma_2 = \sigma_1 \exp\left(\frac{\Delta E}{k_{\mathrm{B}}T}\right) = \sigma_1 \frac{n_2}{n_1}. \tag{4.13}$$

Substituting $\sigma_2 = en_2\mu_2$ and $\sigma_1 = en_1\mu_1$ into Eq. 4.13 immediately leads to:

$$\mu_2 = \mu_1, \forall n_1, n_2, \tag{4.14}$$

in the low-occupancy, non-degenerate regime within the independent-electron approximation.
The observation of a $\frac{k_{\mathrm{B}}}{e}\ln(10)$-slope in the plot of the Seebeck coefficient versus the logarithm of the charge density is therefore not compatible with a charge density-dependent

mobility in the independent-electron approximation. We would like to emphasize that these conclusions are general, are not obtained from a specific charge transport model and are made possible by the high accuracy with which the Seebeck measurements have been performed. The results rule out the possibility of describing transport using any type of model which is based on the effect of disorder on the DoS, since they rely on the semiconductor being treated as a degenerate system.

This is evident when fitting our results with a mobility edge (ME) model, as we did in Fig. 4.4.[144] We present the shortcomings of a ME model[144] in order to exemplify and emphasize the necessity for the consideration of the inhomogeneity of the DoS as well as electron-electron interactions.

The key concept of all ME models is a DoS that has trap or strongly localized low-mobility states at energies below a ME at energy E_0, while high-mobility extended states are considered above this ME. Within such a model a stronger charge density dependence of the mobility can be modeled by an increase in disorder and a broadening of the DoS: with increasing charge density, the chemical potential (E_F) moves higher in the band modifying the trapped (or low mobility) to high mobility charge carrier ratio. Such change is stronger for more disordered systems. In the ME model considered by Chang *et al.*[144] two exponentially decaying contributions of localized states (shallow and deep states) with zero contribution to the total mobility as well as a density of extended states in the form of a free electron gas ($g(E) \propto \sqrt{E}$) above the ME are considered. These three contributions can be expressed as:

$$g(E) = \begin{cases} g_\mathrm{deep}(E) = \dfrac{N_\mathrm{tail}}{W_\mathrm{tail}} \exp\left(\dfrac{E_\mathrm{deep}}{W_\mathrm{tail}}\right) \exp\left(\dfrac{E - E_0 - E_\mathrm{deep}}{W_\mathrm{deep}}\right), & E < E_\mathrm{deep} + E_0, \\ g_\mathrm{tail}(E) = \dfrac{N_\mathrm{tail}}{W_\mathrm{tail}} \exp\left(\dfrac{E - E_0}{W_\mathrm{tail}}\right), & E_\mathrm{deep} + E_0 \leq E < E_0, \\ g_\mathrm{mob}(E) = \dfrac{N_\mathrm{tail}}{W_\mathrm{tail}\sqrt{E_\mathrm{C}}} \sqrt{E_\mathrm{C} + E - E_0}, & E_0 \leq E \leq E_0 + E_\mathrm{max}, \end{cases} \tag{4.15}$$

where N_tail is the concentration of tail states, W_tail is the width of the exponential shallow trap distribution, W_deep is the width of the exponential deep trap distribution, E_0 is the energy of the mobility edge, which is set to $E_0 = -4$ eV corresponding to the LUMO energy of P(NDI2OD-T2) and E_C is a parameter used to tailor the width of the density of mobile states which is set to $E_\mathrm{C} = 0.037$ eV according to ref. [144]. For all fits in Fig. 4.4 the energy of the deep traps was chosen as $E_\mathrm{deep} = -8$ eV in order to avoid the contribution from deep traps because we have no experimental evidence suggesting that deep traps should be considered in the description of charge transport in P(NDI2OD-T2). In order to obtain a physical meaningful DoS we fix the total

DoS (N_{tot}) and hence limit the width of the mobile band to E_{max}. E_{max} is obtained according to:

$$N_{\mathrm{tot}} = \int_{-\infty}^{E_{\mathrm{deep}}+E_0} g_{\mathrm{deep}}(E)dE + \int_{E_{\mathrm{deep}}+E_0}^{E_0} g_{\mathrm{tail}}(E)dE + \int_{E_0}^{E_0+E_{\mathrm{max}}} g_{\mathrm{mob}}(E)dE. \quad (4.16)$$

Since we did not consider any contribution from deep traps ($E_{\mathrm{deep}} = -8$ eV), the choice of W_{deep} is irrelevant. The total DoS (N_{tot}) was set to $N_{\mathrm{tot}} = 2 \cdot 10^{20}$ cm^{-3} according to a fit of the Seebeck coefficient data with Heikes formula for both preparation conditions (see section 4.4).[235] The Fermi-energy (E_{F}) for each gate voltage respectively charge density is found according to:

$$\begin{aligned} n_{\mathrm{tot}} &= \int_{-\infty}^{E_{\mathrm{deep}}+E_0} g_{\mathrm{deep}}(E)f(E,E_{\mathrm{F}})dE + \int_{E_{\mathrm{deep}}+E_0}^{E_0} g_{\mathrm{tail}}(E)f(E,E_{\mathrm{F}})dE \\ &+ \int_{E_0}^{E_0+E_{\mathrm{max}}} g_{\mathrm{mob}}(E)f(E,E_{\mathrm{F}})dE \\ &= \frac{\epsilon_0 \cdot \epsilon_{\mathrm{r}}}{d \cdot h} \cdot (V_{\mathrm{gs}} - V_{\mathrm{on}}), \end{aligned} \quad (4.17)$$

where $\epsilon_{\mathrm{r}} = 3.6$ for PMMA, $d = 300$ nm for the dielectric layer thickness and the thickness of the accumulation layer was assumed to be $h = 2$ nm.[174] At 300 K the onset voltage (V_{on}) is $V_{\mathrm{on}} = -8$ V for the annealed sample and $V_{\mathrm{on}} = -1$ V for the as-cast sample. The density of mobile charge carriers (n_{mob}) is obtained using the obtained Fermi-energy (E_{F}):

$$n_{\mathrm{mob}}(V_{\mathrm{gs}},T) = \int_{E_0}^{E_0+E_{\mathrm{max}}} g_{\mathrm{mob}}(E)f(E,E_{\mathrm{F}})dE. \quad (4.18)$$

Consequently, the mobility is calculated from the ratio between the mobile and total charge density:

$$\mu = \mu_0 \exp\left(-\frac{E_{\mathrm{a}}}{k_{\mathrm{B}}T}\right) \frac{n_{\mathrm{mob}}(V_{\mathrm{gs}},T)}{n_{\mathrm{tot}}}, \quad (4.19)$$

where E_{a} is the polaron activation energy and μ_0 is the mobility of a free carrier with zero polaron activation energy. Since the mobilities of the annealed device are fairly high (~ 0.1 cm^2 V^{-1} s^{-1}) the polaron activation energy was set to zero ($E_{\mathrm{a}} = 0$ eV), while for the lower mobilities of the as-cast device the polaron activation energy was set to $E_{\mathrm{a}} = 40$ meV.[144] The other resulting fitting parameters $\mu_0 = 0.7$ cm^2 V^{-1} s^{-1}, $N_{\mathrm{tail}} = 5 \cdot 10^{19}$ cm^{-3} and $W_{\mathrm{tail}} = 42$ meV for the annealed condition (Fig. 4.4a, c) as well as $\mu_0 = 5.2$ cm^2 V^{-1} s^{-1}, $N_{\mathrm{tail}} = 1.8 \cdot 10^{20}$ cm^{-3} and $W_{\mathrm{tail}} = 18$ meV for the as-cast condition (Fig. 4.4b, d), nicely illustrate the general feature of disorder-based transport models, showing a more pronounced charge density dependence of the mobility for a more

strongly disordered DoS ($W_{\text{tail}} = 42$ meV for the annealed condition with large charge density dependence versus $W_{\text{tail}} = 18$ meV for the as-cast condition with small charge density dependence). It was already argued earlier that these values of W_{tail} are not consistent with microstructure and spectroscopic characterisation, including GIWAXS and photothermal deflection spectroscopy measurements, in which both samples have similar energetic and positional disorder.[135] It is worth to note that despite the fact that the total DoS was set to $N_{\text{tot}} = 2 \cdot 10^{20}$ cm^{-3} for both preparation conditions, the ratio of mobile to trap states was significantly different for the two conditions: 75 % mobile states, $N_{\text{mob}} = 1.5 \cdot 10^{20}$ cm^{-3} and $N_{\text{trap}} = 0.5 \cdot 10^{20}$ cm^{-3} ($E_{\text{max}} \approx 86.63$ meV) for the annealed and 10 % mobile states, $N_{\text{mob}} = 0.2 \cdot 10^{20}$ cm^{-3} and $N_{\text{trap}} = 1.8 \cdot 10^{20}$ cm^{-3} ($E_{\text{max}} \approx 1.97$ meV) for the as-cast condition. Such massive change in the ratio of mobile to trapped carriers upon annealing underlines the inappropriateness of this model. Furthermore, despite the fact that the tail widths are in contradiction to previous structural characterization of P(NDI2OD-T2),[135] another key shortcoming of the ME model is the large amount of fitting parameters allowing non-unique fitting parameter sets. The DoS employed for fitting the charge density and temperature-dependent mobility and Seebeck coefficient data of the two different fabrication conditions are shown in Fig. 4.5. Clearly, this illustration underlines the non-physical result that the microstructurally more disordered as-cast preparation condition has a less disordered DoS according to the transport coefficient fits. This shortcoming is a general feature of disorder-based charge transport models that tie the extent of the charge density dependence of the mobility to the extent of disorder.

We can now show more convincingly that these DoS parameters required to fit the mobility data are also not consistent with the measured Seebeck coefficient. The modeled Seebeck coefficient calculated according to Eq. 4.1 has a much higher value than observed in the experiments, a stronger charge density dependence with a slope significantly higher than $\frac{k_{\text{B}}}{e} \ln(10)$ and predicts a temperature dependence of the Seebeck coefficient which is much stronger than what could be consistent within the error of our Seebeck measurements (Fig. 4.4c, d). This shows that the agreement observed between fit and experimental mobility curve is just coincidental. The fit to the Seebeck data is closer to the $\frac{k_{\text{B}}}{e} \ln(10)$-slope for the as-cast sample. Here the measured charge density dependence of the mobility is much weaker, hence the data can be fit with the ME model using a tail density of $N_{\text{tail}} = 1.8 \cdot 10^{20}$ cm^{-3}. But the accuracy of the fit is still too poor (the model predicts a too large temperature dependence of the Seebeck coefficient) and the reason is that when the band tails extend in the forbidden energy gap the system cannot be considered as a non-degenerate semiconductor at the charge

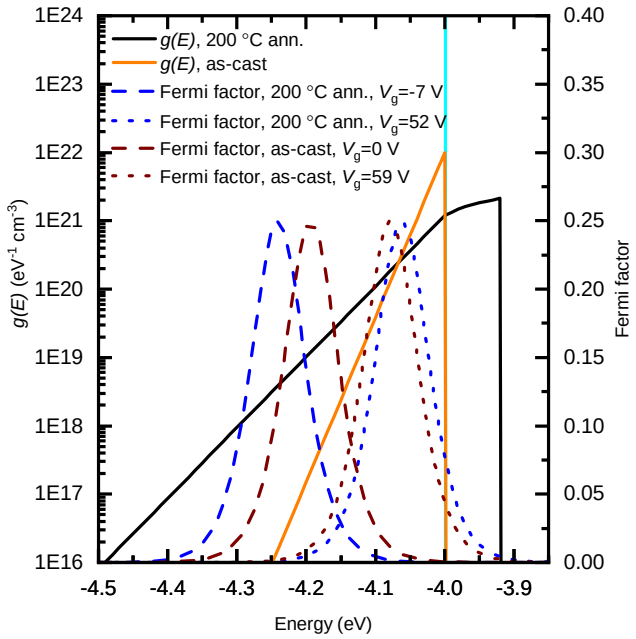

Figure 4.5. Density of states used for the mobility edge model fits presented in Fig. 4.4. The solid black and orange curves show the DoS that were used for the ME model fits of the mobility and Seebeck coefficient of the 200 °C annealed and as-cast preparation condition presented in Fig. 4.4. The blue dashed and dotted lines are the Fermi factor at 300 K ($k_{\mathrm{B}}T\left(-\frac{\partial f(E)}{\partial E}\right)$) for the annealed condition at $n \approx 3.32 \cdot 10^{17}$ cm^{-3} and $n \approx 1.99 \cdot 10^{19}$ cm^{-3}. The dark red dashed and dotted lines are the Fermi factor for the as-cast condition at $n \approx 3.32 \cdot 10^{17}$ cm^{-3} and $n \approx 1.99 \cdot 10^{19}$ cm^{-3}. The vertical turquoise line represents the ME energy $E_0 = -4$ eV respectively the LUMO energy of P(NDI2OD-T2).

densities we are considering here. Hence, it is impossible for the model to predict the $\frac{k_{\mathrm{B}}}{e}\ln(10)$-slope we measure or the lack of temperature dependence, regardless of the specific choice for the DoS.

To show that this is a general issue and not specific to the model we chose, we have extended our comparison in Fig. 4.6a to other disorder-based models which are commonly employed to describe charge transport in semicrystalline polymers including the one investigated here (P(NDI2OD-T2)).[135,155,164,221] In particular, we have extended our analysis to the variable-range hopping (VRH) and mobility edge (ME) model by Mott as well as to the transport model that was recently developed by Snyder and coworkers for conducting polymers (Fig. 4.6a).[155,164,171,221,229] The graph in Fig. 4.6 shows the measured Seebeck coefficient of the 200 °C annealed device versus conductivity at 300 K and 200 K, as well as the fits with the different transport models. To convert the mobility into conductivity ($\sigma = \frac{\epsilon_0 \cdot \epsilon_{\mathrm{r}}}{d \cdot h} \int_{V_{\mathrm{on}}}^{V_{\mathrm{gs}}} \mu(V_{\mathrm{gs}}^{'}) dV_{\mathrm{gs}}^{'}$) we estimated a channel thickness of 2 nm.[174] A slightly different value would lead to a small rigid horizontal shift of the

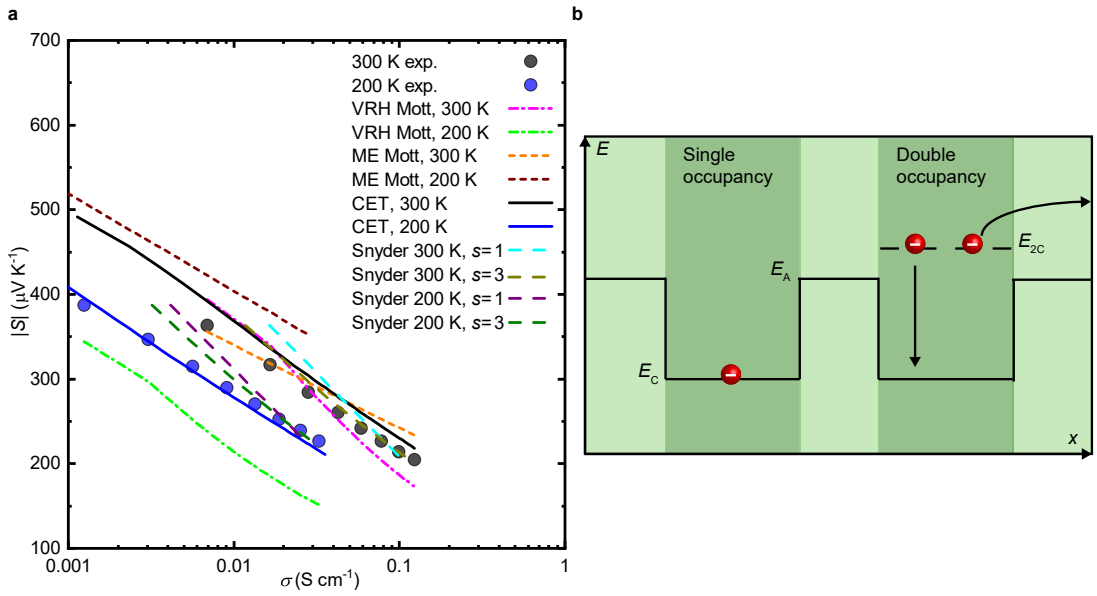

Figure 4.6. Seebeck coefficient (S) versus conductivity (σ) as well as Coulomb enhanced charge transport (CET) model illustration. The measured Seebeck coefficient versus conductivity of the 200 °C annealed device at 300 K and 200 K, as well as the fits of different transport models are shown in panel (a).[135,155,164,221] For the fits with the VRH Mott model the following parameters were used: $\gamma = 1/3$ and $\xi_\mathrm{d} = 6.15387$ nV K^{-2} (pink and green dashed dotted lines). $A = 0$ has been used for the ME Mott fits (orange and dark red dashed lines). The fitting parameters for the CET model (solid black and solid blue line)[135] are the same as in Fig. 4.4. For the fits with Snyder and coworkers' model the following conductivity prefactors were used: $\sigma_0 = 0.151$ S cm^{-1} ($s = 1$, 300 K, turquoise dashed line), $\sigma_0 = 2.2$ mS cm^{-1} ($s = 3$, 300 K, olive dashed line), $\sigma_0 = 0.051$ S cm^{-1} ($s = 1$, 200 K, purple dashed line) and $\sigma_0 = 0.82$ mS cm^{-1} ($s = 3$, 200 K, dark green dashed line). Panel (b) illustrates the two key processes of the CET model. The first process is exemplified as having single independent electrons in a crystalline domain and the second process of two charges in a crystalline domain raised in energy due to their Coulomb interaction.

data which would not affect any of the conclusions obtained from the analysis.

The original ME model by Mott was evaluated following a similar procedure as presented by Glaudell *et al.*, i.e. fitting the temperature dependence of the conductivity at each charge density in an Arrhenius plot in order to extract the charge density-dependent activation energy $E_\mathrm{A} = B\ln(\sigma) + C$ (which was assumed to be temperature independent).[155,229] The Arrhenius plots ($\ln(\sigma)$ versus $1/T$) for the annealed preparation condition at eight different charge densities (corresponding to the gate voltages $V_\mathrm{g} = 0$ V for $n_1 \approx 2.65 \cdot 10^{18}$ cm^{-3} in steps of 5 V up to $V_\mathrm{g} = 35$ V for $n_8 \approx 1.43 \cdot 10^{19}$ cm^{-3}) as well as the corresponding charge density-dependent activation energy are shown in Fig. 4.7. Using these extracted activation energies the Seebeck coefficient data of the 200 °C annealed preparation condition at 200 K and 300 K was fit according to $S = \frac{k_\mathrm{B}}{e}\left(\frac{B\ln(\sigma)+C}{k_\mathrm{B}T}\right) + A$, with $A \geq 0$ as a free fitting parameter (where the activation en-

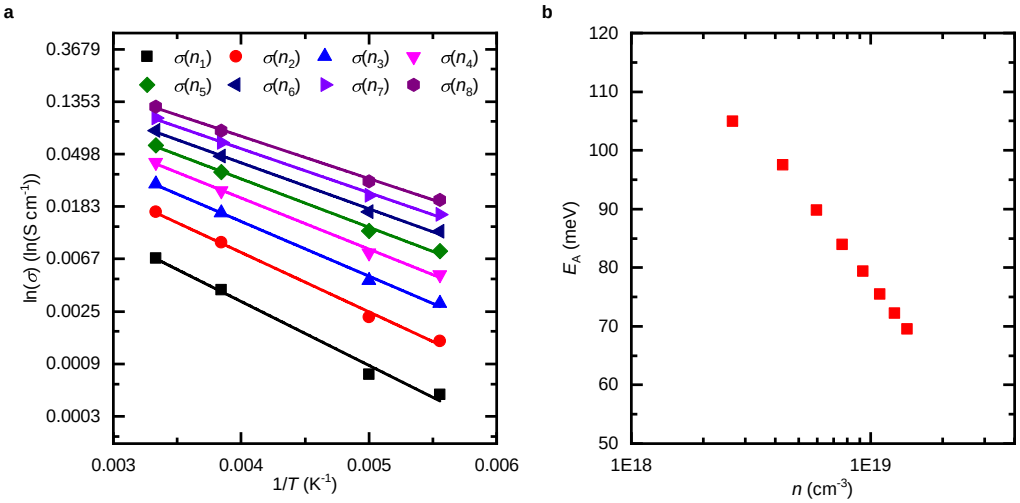

Figure 4.7. Activation energy extraction for the analysis with the mobility edge Mott model. The natural logarithm of the conductivity of the 200 °C annealed preparation condition for eight different charge densities (corresponding to the gate voltages $V_g = 0$ V for $n_1 \approx 2.65 \cdot 10^{18}$ cm^{-3} in steps of 5 V up to $V_g = 35$ V for $n_8 \approx 1.43 \cdot 10^{19}$ cm^{-3}) is plotted against $1/T$ (a) in order to extract the charge density-dependent activation energy E_A (b) for the ME Mott analysis. The solid lines in panel (a) represent the linear regression fits used to extract the activation energies from the slopes of these fits.

ergy for the Seebeck coefficient was estimated to be equal to the activation energy of the conductivity and assumed to be temperature independent, $A = 0$ obtained).[155,229] The fit fails to follow the temperature dependence because of the predicted $1/T$-temperature dependence of the Seebeck coefficient, which is in contrast to the measured values that are temperature independent.

The VRH model by Mott was evaluated by fixing $\gamma = \frac{1}{d+1} = \frac{1}{3}$ according to 2D-variable-range hopping, given our essentially 2D-charge density profile, in $\sigma = \sigma_0 \exp\left[-\left(\frac{T_0}{T}\right)^{\gamma}\right]$ and the T_0 values of the 200 °C annealed preparation condition for eight different charge densities were extracted (Fig. 4.8).[155,171] Using these T_0 values the Seebeck coefficient data of the 200 °C annealed preparation condition for eight different charge densities at 200 K and 300 K was fit with $S = \xi_d T_0^{\frac{2}{d+1}} T^{\frac{d-1}{d+1}}$, where ξ_d, a temperature-independent factor that depends on the dimension of VRH considered and obeys the proportionality $\xi_d \propto \left[\frac{\partial \ln \overline{N}(E)}{\partial E}\right]_{E=E_F}$, was used as a free fitting parameter ($\xi_d \approx 6.15387$ nV K^{-2} was obtained).[155,171,270] The variable-range hopping model fails to explain our experimental data as the Seebeck coefficient is predicted to depend on temperature according to $S \propto T^{\frac{1}{3}}$, while the experimental data show a temperature-independent Seebeck coefficient. Furthermore, the predicted slope of the Seebeck coefficient with respect to

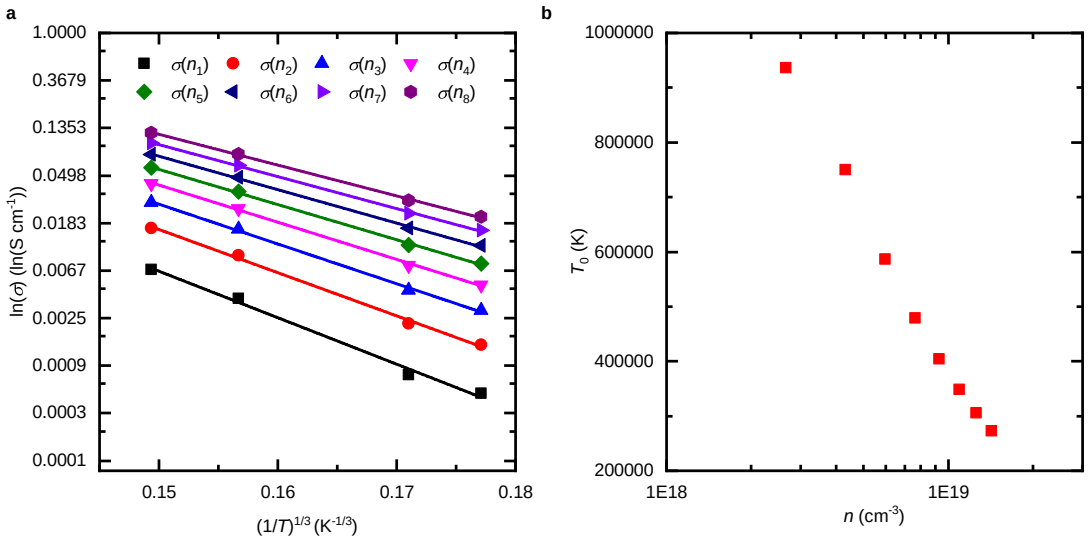

Figure 4.8. T_0 extraction for the analysis with the VRH Mott model. The natural logarithm of the conductivity of the 200 °C annealed preparation condition for eight different charge densities (corresponding to the gate voltages $V_g = 0$ V for $n_1 \approx 2.65 \cdot 10^{18}$ cm^{-3} in steps of 5 V up to $V_g = 35$ V for $n_8 \approx 1.43 \cdot 10^{19}$ cm^{-3}) is plotted against $(1/T)^{1/3}$ in order to extract the charge density-dependent T_0 parameter for the VRH Mott model analysis (a). The solid lines represent the linear regression fits used to extract the T_0 values from the slopes of these fits. The obtained T_0 values are shown in panel (b).

conductivity is too high to resemble the data (Fig. 4.6a).

Finally, the data has been fit with the model Snyder and coworkers developed for doped conducting polymers.[221] By inserting their expression for the energy-dependent conductivity:

$$\sigma(E,T) = \begin{cases} \sigma_0(T) \cdot \left(\frac{E-E_t}{k_B T}\right)^s \left(-\frac{\partial f(E)}{\partial E}\right), & E > E_t \\ 0, & E < E_t, \end{cases} \tag{4.20}$$

into the expression from the Boltzmann transport equation (Eq. 4.2):

$$\sigma = \int \sigma(E,T) dE, \tag{4.21}$$

and introducing the reduced chemical potential $\eta(T) = \frac{E_F - E_t}{k_B T}$ (with E_t being the transport energy), they arrive at the simplified expression:

$$\sigma = \sigma_0(T) \cdot s F_{s-1}(\eta), \tag{4.22}$$

where $F_i(\eta) = \int_0^\infty \frac{\epsilon^i}{1+\exp(\epsilon-\eta)} d\epsilon$ is the non-normalized complete Fermi-Dirac integral. Furthermore, they express the Seebeck coefficient from Boltzmann transport equation

(Eq. 4.1):

$$S = \frac{1}{\sigma}\left(\frac{k_B}{e}\right)\int\left(\frac{E - E_F}{k_B T}\right)\sigma(E,T)dE, \tag{4.23}$$

in dependence of η:

$$S = \frac{k_B}{e}\left[\frac{(s+1)F_s(\eta)}{sF_{s-1}(\eta)} - \eta\right]. \tag{4.24}$$

Firstly, $\eta(T,n)$ is obtained from $S(T,n)$ for each fixed value of s ($s = 1$ and $s = 3$) by numerically solving Eq. 4.24 for η at each charge density, temperature and s-value. The values of $\eta(T)$ versus $S(T)$ for the 200 °C annealed preparation condition are shown for eight different charge densities (corresponding to the gate voltages $V_g = 0$ V to $V_g = 35$ V in steps of 5 V) at 300 K and 200 K for $s = 1$ and $s = 3$ in Fig. 4.9a. Subsequently,

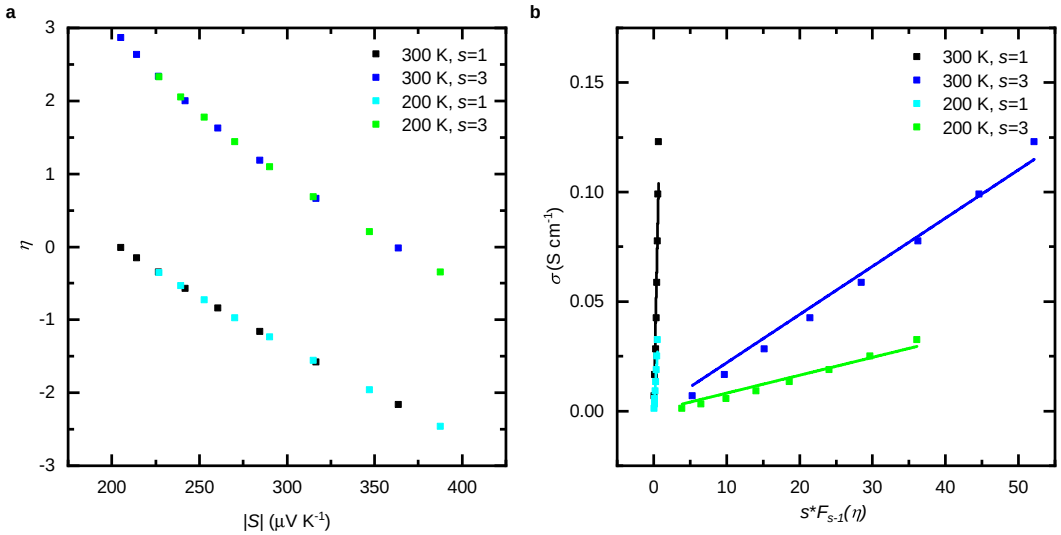

Figure 4.9. σ_0 extraction for the analysis with the model by Snyder and coworkers. Panel (a) shows the values of $\eta(T)$ versus $S(T)$ for the 200 °C annealed preparation condition for eight different charge densities (corresponding to the gate voltages $V_g = 0$ V for n_1 in steps of 5 V up to $V_g = 35$ V for n_8) at 300 K and 200 K for $s = 1$ and $s = 3$ obtained from numerically solving Eq. 4.24 for η. Panel (b) shows the corresponding $s \cdot F_{s-1}(\eta)$ versus σ plots as well as the linear regression fits (solid lines) to extract the conductivity prefactors σ_0 for each temperature and value of s. The obtained σ_0 values are $\sigma_0 = 0.151$ S cm^{-1} ($s = 1$, 300 K, black solid line), $\sigma_0 = 2.2$ mS cm^{-1} ($s = 3$, 300 K, blue solid line), $\sigma_0 = 0.051$ S cm^{-1} ($s = 1$, 200 K, turquoise solid line) and $\sigma_0 = 0.82$ mS cm^{-1} ($s = 3$, 200 K, green solid line).

these $\eta(T,n)$ values were used to calculate $s \cdot F_{s-1}(\eta)$ and the conductivity prefactors σ_0 for each value of s and each temperature have been obtained from linear regression fits of σ versus $s \cdot F_{s-1}(\eta)$ (Fig. 4.9b). Using the obtained conductivity prefactors σ_0, the conductivity σ and Seebeck coefficient S have been calculated according to Eqs. 4.22 and 4.24. In this case the slope of the Seebeck coefficient versus conductivity curve

is far too steep (Fig. 4.6a), regardless of the type of conduction considered ($s = 1$ for acoustic-phonon scattering, $s = 3$ for ionized-impurity scattering), particularly visible for the 200 K data. Although the model has been shown to work for chemically doped polymer films, we argue that the presence of counterions in molecularly doped polymer films leads to a strong broadening of the DoS, which is not the case for the electrostatically doped semiconductors in this study for which no broadening is observed upon introduction of additional charge carriers (also in consideration of the much lower charge density achievable in an FET geometry).[228]

Similar limitations and shortcomings appear also when using more complex models: Lu *et al.* have developed a thermoelectric transport model using percolation theory in a disorder-broadened Gaussian DoS which shows that in disordered systems the Seebeck coefficient is strongly enhanced with increasing disorder.[234] Our Seebeck coefficient data (Fig. 4.4c, d) would indicate negligible disorder ($< 0.5\ k_{\mathrm{B}}T$) for both annealed and as-cast films. For such low disorder the model would predict a very low charge density dependence of the mobility for both preparation conditions, in clear contrast with our results (Fig. 4.4a).[234] A similar treatment which also takes into account the charge carrier delocalisation fails to describe our results as well, since it is not able to simultaneously describe the charge density and temperature dependence of Seebeck coefficient and mobility.[159,232] The general issue that becomes evident in all these models is that the strong gate voltage dependence of the mobility that is observed experimentally in the annealed sample can be modelled only in the degenerate limit for strong disorder. This is incompatible with the (lack of) temperature dependence and the charge density dependence of the Seebeck coefficient which we experimentally measure.

4.6 Modelling transport with the inclusion of electron-electron interactions

Having shown that no disorder-based model can explain our results and having demonstrated from basic principles that in an independent-electron approximation the non-degenerate limit and the charge density dependence of the mobility are incompatible, we need to revisit the main assumptions behind Eqs. 4.1 and 4.2. Two aspects that are so far neglected in our analysis are (a) the non-homogeneous nature of the DoS and (b) that electrons confined within nanoscale crystalline domains can experience strong local electron-electron interactions. In our system the surface density of crystalline domains is approximately $10^{12} - 10^{13}$ cm^{-2} (from the GIWAXS measurements (section 4.3) with

spectroscopic estimates of the total volume fraction between crystalline and amorphous domains (about 1:1)[135]). In our transport regime also the surface electron density is around 10^{12} cm^{-2}. This suggests indeed that multiple occupancy of crystallites cannot be neglected.

We have recently introduced a simple transport model that lifts these two assumptions by incorporating both a non-uniform DoS and taking into account electron-electron interactions due to multiple occupancy of crystallites, which we have further improved here. This Coulomb enhanced charge transport (CET) model is able to consistently explain the mobility data as well as microstructrual and spectroscopic characterisation of P(NDI2OD-T2).[135] It assumes charges to be confined to nanoscale crystalline domains, separated by amorphous regions (Fig. 4.1c). These regions act as potential barriers for charges moving from a crystallite to an adjacent one. The value for the potential barrier will depend on the local configuration of the molecules at the interface, but is considered as an average value E_{barr} for our macroscopic electrical measurements. The local Coulomb repulsion between multiple charge carriers accumulated in the same crystalline domain provides additional energy to overcome this energy barrier E_{barr} and allows a small fraction of the accumulated charges to be transported with much higher mobility. The two processes are illustrated in Fig. 4.6b, where we exemplify the process as having single independent electrons in a crystalline domain for the first process and two electrons next to each other for the charges experiencing Coulomb interaction. We ignore energetic disorder within the crystalline domains and assume that there are in total N_{C} isoenergetic states per unit volume within the crystalline domains. N_{C} can be estimated from the temperature-independent value of $\widetilde{N}$ extracted from the experimental Seebeck data above (section 4.4, Fig. 4.4c, d). We then consider two populations of charges, one for non-interacting electrons for which Coulomb interaction can be neglected ($n_{1\mathrm{C}}$) and a second one ($n_{2\mathrm{C}}$) for charges which experience a strong Coulomb interaction increasing the electron energy by a charging energy $U_{\mathrm{C}} > E_{\mathrm{barr}}$. This effect is modelled by mapping non-interacting and electrostatically interacting electrons into a charge density-dependent single-electron density of states (DoS) where we assume that each charge that accumulates in the crystalline domains lifts ν states in energy by U_{C}, which are available to accommodate a second electron which can then travel with much higher mobility. The total DoS is split into two narrow bands: one band of states at energy E_{C} with density $N_{\mathrm{C}} - \nu n_{1\mathrm{C}}$ for low mobility charges and the other band of states at $E_{2\mathrm{C}} = E_{\mathrm{C}} + U_{\mathrm{C}}$ and density $N_{2\mathrm{C}} = \nu n_{1\mathrm{C}}$ for high mobility charges. The total number of states N_{C} is fixed but the number of states $N_{2\mathrm{C}}$ increases with increasing charge density, and the two populations can be determined according to

the following equation:

$$\begin{aligned} g(E) &= \left[N_{\mathrm{C}} - \nu n_{1\mathrm{C}}\right] \delta(E - E_{\mathrm{C}}) + \nu n_{1\mathrm{C}} \delta(E - E_{2\mathrm{C}}) \\ &= N_{\mathrm{C}} \cdot \left(1 - \frac{\nu f(E_{\mathrm{C}})}{1 + \nu f(E_{\mathrm{C}})}\right) \delta(E - E_{\mathrm{C}}) + \frac{N_{\mathrm{C}} \nu f(E_{\mathrm{C}})}{1 + \nu f(E_{\mathrm{C}})} \delta(E - E_{2\mathrm{C}}), \end{aligned} \tag{4.25}$$

where $n_{1\mathrm{C}}$ and $n_{2\mathrm{C}} = \nu n_{1\mathrm{C}} f(E_{2\mathrm{C}})$ are the charge densities of low and high mobility electrons and $f(E)$ is the Fermi-Dirac distribution function. Equation 4.25 leads to the following occupancy ratio (in the non-degenerate limit):

$$\frac{n_{2\mathrm{C}}}{n_{1\mathrm{C}}} = f(E_{\mathrm{C}}, E_{\mathrm{F}}) e^{ln(\nu) - \frac{U_{\mathrm{C}}}{k_{\mathrm{B}}T}} \cong \frac{n}{N_{\mathrm{C}}} e^{-\frac{G}{k_{\mathrm{B}}T}}, \tag{4.26}$$

where $G = U_{\mathrm{C}} - k_{\mathrm{B}} T ln(\nu)$ is the free energy associated with the interacting charge pair, and $n = n_{1\mathrm{C}} + n_{2\mathrm{C}}$. The right-hand side shows the main qualitative features of this approach. The population ratio increases with increasing charge density, the feature responsible for the observed charge density dependence of the mobility. An increase in crystallite size results in a decrease in the free energy by both reducing the Coulomb repulsion experienced by the two electrons (hence reducing U_{C}) and increasing the available states (ν) for the formation of such charge pair.

The two populations of charges can be used to obtain the macroscopic electron mobility from a charge density average considering that high mobility electrons represent the electron of an interacting charge pair which can overcome the energy barrier and travel with a higher mobility, following the same approach used by Emin in ref. [271]:

$$\mu = \frac{n_{1\mathrm{C}} \mu_{1\mathrm{C}} + n_{2\mathrm{C}} \mu_{2\mathrm{C}}}{n_{1\mathrm{C}} + n_{2\mathrm{C}}}. \tag{4.27}$$

Here $\mu_{1\mathrm{C}} = \mu_0 \exp\left(-\frac{E_{\mathrm{barr}}}{k_{\mathrm{B}}T}\right)$ is the mobility of low mobility electrons (representative of non-interacting electrons), which is limited by thermal activation across the energy barrier and $\mu_{2\mathrm{C}} = \mu_{02\mathrm{C}} \cdot \frac{300\,\mathrm{K}}{T}$ is the mobility of high mobility charges (representative of the electron-electron pairs experiencing sufficient Coulomb repulsion), which is assumed to be scattering limited and significantly higher than $\mu_{1\mathrm{C}}$. The mobility pre-factors μ_0 and $\mu_{02\mathrm{C}}$ are determined by the microscopic properties of the material. In this model the spatial inhomogeneity is responsible for the temperature-activated dependence of the mobility, but the amorphous region is not explicitly included in the DoS as a further parallel conduction channel for simplicity. It would in fact not change any of the fits appreciably. As shown previously, the amount of charges in the high energy amorphous band would always be below 5 % of the total charge density, as confirmed experimentally through charge accumulation spectroscopy (CAS) measurements, and would therefore

be well within the uncertainty of the experimentally measured charge density.[135] The changes due to the different charge densities upon inclusion of the amorphous band are therefore negligible compared to our experimental sensitivity. Combined with the much lower mobility charges have in the amorphous phase the contribution such charges would give to both mobility and Seebeck calculations would be even less relevant.
In order to calculate the Seebeck coefficient it is paramount to take into account that the two energy bands that form our DoS are not present at the same point in space: if charges are electrostatically interacting only the high energy band is present, if they do not interact only the lower band is present. We cannot plug the DoS in Eq. 4.25 directly into Eq. 4.1 as doing so is equivalent to considering the two bands as present in parallel everywhere in space and leads to a large overestimation of the Seebeck coefficient (see further details in the next paragraph). The contribution to the Seebeck coefficient of the two charge populations can instead be readily calculated by considering the entropy of such a system and exploiting the definition of the Seebeck coefficient as entropy transported per unit charge, an approach already detailed in ref. [271]. Following the reported procedure[271] we consider the entropy of the system of interacting electrons (which we denote here as S_{ent} to avoid confusion with the Seebeck coefficient S):

$$S_{\text{ent}} = k_{\text{B}} \left[c_2^+ \ln(c_2^+) + c_2^- \ln(c_2^-) + c_1^+ \ln(c_1^+) + c_1^- \ln(c_1^-) + c_{\text{v}} \ln(c_{\text{v}}) \right], \tag{4.28}$$

where $c_{1,2}^{+,-}$ is the concentration of low mobility charges (1) and high mobility charges (2) with spin up (+) and down (-) and c_{v} is the concentration of vacant sites. The Seebeck coefficient is by definition $S = \frac{1}{q}\frac{dS_{\text{ent}}}{dc}$, where c is the total charge concentration $c = c_2^+ + c_2^- + c_1^+ + c_1^- = c_2 + c_1$, $c_i^+ = c_i^- = \frac{c_i}{2}$ (for $i = 1, 2$) and q is the charge carried by each charge carrier. Taking into account that $c_2^+ + c_2^- + c_1^+ + c_1^- + c_{\text{v}} = 1$, the Seebeck coefficient reads as:

$$S = \frac{1}{q}\frac{dS_{\text{ent}}}{dc} = \frac{k_{\text{B}}}{q}\left[\ln\left(\frac{c_2}{2}\right)\frac{dc_2}{dc} + \ln\left(\frac{c_1}{2}\right)\frac{dc_1}{dc} + \ln\left(c_{\text{v}}\right)\frac{dc_{\text{v}}}{dc} \right]. \tag{4.29}$$

Since $\frac{dc_{\text{v}}}{dc} = -1$ and $\frac{dc_1}{dc} = 1 - \frac{dc_2}{dc}$, we can rewrite the Seebeck coefficient as:

$$S = \frac{k_{\text{B}}}{q}\left[\ln\left(\frac{c_1}{2c_{\text{v}}}\right) + \ln\left(\frac{c_2}{c_1}\right)\frac{dc_2}{dc} \right]. \tag{4.30}$$

By considering that $\frac{c_2}{c_1} \approx 10^{-2}$, we can approximate $c_{\text{v}} = 1 - c_1$. Given that $c_i = \frac{n_i}{N_{\text{sites}}}$ (for $i = 1, 2$), where $N_{\text{sites}} = \frac{N}{2}$ denotes the total number of thermally accessible sites, we can finally rewrite the Seebeck coefficient as:[271]

$$S = \frac{k_{\text{B}}}{q}\left[\ln\left(\frac{n_1}{2(N_{\text{sites}} - n_1)}\right) + \ln\left(\frac{n_2}{n_1}\right)\frac{dn_2}{dn} \right]. \tag{4.31}$$

Therefore, by identifying $n_1 = n_{1C}$, $n_2 = n_{2C}$ and $N_C = 2 \cdot N_{sites}$, the macroscopic Seebeck coefficient is given by:

$$S = -\frac{k_B}{q}\left\{ \ln\left[\frac{(N_C - 2n_{1C})}{n_{1C}}\right] - \frac{\partial n_{2C}}{\partial n}\ln\left(\frac{n_{2C}}{n_{1C}}\right)\right\}. \tag{4.32}$$

Considering that the number of doubly occupied crystalline domains is predicted to be always below 5 % of the total accumulated charge density ($\frac{\partial n_{2C}}{\partial n} \cong \frac{n_{2C}}{n_{1C}} \approx 10^{-2}$) it is readily seen that the inclusion of short range electron-electron interactions has a negligible effect on the Seebeck coefficient. Equation 4.32 is effectively equal to Heikes formula for a system of fermions with forbidden occupancy of the same site (i.e. no bipolaron formation), regardless of the extension of the crystalline domains.[181] It is important to note that the Seebeck coefficient in Eq. 4.32 is not explicitly dependent on the mobility of the two charge populations, since the mobility enhancement is a local effect caused by Coulomb interactions rather than due to different channels present in parallel for charge transport (further details in the following paragraph). The fits to the data (based on Eqs. 4.27 and 4.32) are reported as solid lines in Fig. 4.4 and Fig. 4.6a and show the agreement of the Seebeck coefficient with a slightly modified Heikes formula with a $\frac{k_B}{e}\ln(10)$-slope and no temperature dependence. On the other hand, the impact of sufficiently strong Coulomb interacting electrons on the macroscopic electron mobility is much stronger due to the much higher mobility of this small charge population ($\mu_{2C} \gg \mu_{1C}$). The close fit of both datasets is summarized in Fig. 4.6a where it is shown how the presented model finally allows us to accurately fit the data both in terms of slope and temperature dependence, in agreement with the structural characterisation. Figure 4.10 displaying the Seebeck coefficient versus conductivity for both the annealed and as-cast device, provides additional support for the exceptionally well fit of the CET model compared to disorder-based transport models. It is important to note that when fitting mobility and Seebeck data at the same time, only 4 parameters are available to fit the mobility data (E_{barr}, μ_{02C}, μ_0 and G), of which only 2, the free energy associated with an interacting charge pair G and the mobility prefactor μ_0 are different between the different preparation conditions. We did not attempt to determine ν from the fits, as we do not have an independent estimate of U_C. However, the Seebeck coefficient provides a direct estimation of the total number of states in the conduction band within the crystalline domains ($N_C = 2 \cdot 10^{20}$ cm^{-3}). We note that this value is approx. one order of magnitude higher than the effective DoS at room-temperature for crystalline silicon ($N_C = 2.86 \cdot 10^{19}$ cm^{-3} and $N_V = 3.10 \cdot 10^{19}$ cm^{-3}),[272] highlighting the suitability of narrow-band polymer semiconductors for thermoelectric applications. Together with the observation that crystallinity can be used to selectively increase the

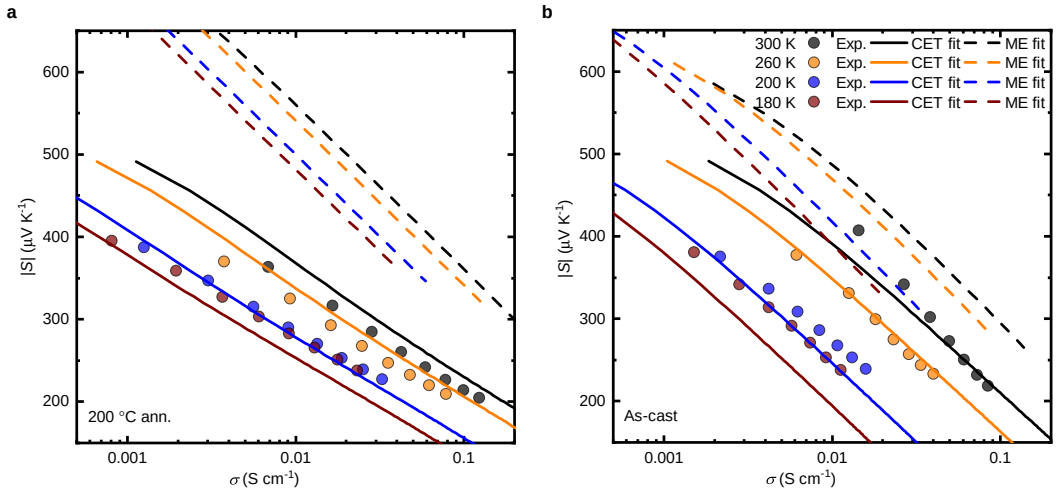

Figure 4.10. Seebeck coefficient versus electrical conductivity. Seebeck coefficient versus electrical conductivity for the 200 °C annealed (a) as well as the as-cast condition (b) at various temperatures. The predictions by the CET and ME model[144] with the parameters used for the fits in Fig. 4.4c, d are shown as well.

electrical conductivity without affecting the Seebeck coefficient, increasing crystallinity provides a method to improve the power factor of organic semiconductor-based thermoelectric generators.[23] Our theoretical model shows the importance of introducing a more realistic inhomogeneous DoS and the presence of local electron-electron interactions which are necessary to fully explain the experimental data.

As outlined in the previous paragraph we have also investigated a simple two-band, independent-electron model with adjustable energy gap between the two states and adjustable total number of states in both bands. A few illustrative simulations emphasizing the necessity to take both the inhomogeneity of the DoS as well as local electron-electron interactions into account to simultaneously explain the mobility and Seebeck coefficient are shown in Fig. 4.11. If the inhomogeneity of the DoS is not considered and electrons are approximated to be independent, the Boltzmann transport formalism applies and the mobility and Seebeck coefficient can be calculated according to Eqs. 4.1 and 4.2. Applying this formalism to the CET DoS (Eq. 4.25) however will result in a large anomalous increase in the Seebeck coefficient at high charge density. This is evident by comparing mobility and Seebeck coefficient calculated according to Eqs. 4.27 and 4.32 (solid black line in Fig. 4.11) and the black dashed line (CET parameters, mobility and Seebeck coefficient calculated according to the Boltzmann transport formalism, Eqs. 4.1 and 4.2). It is apparent that the consideration of two parallel conduction channels that are homogeneously accessible across the whole sample

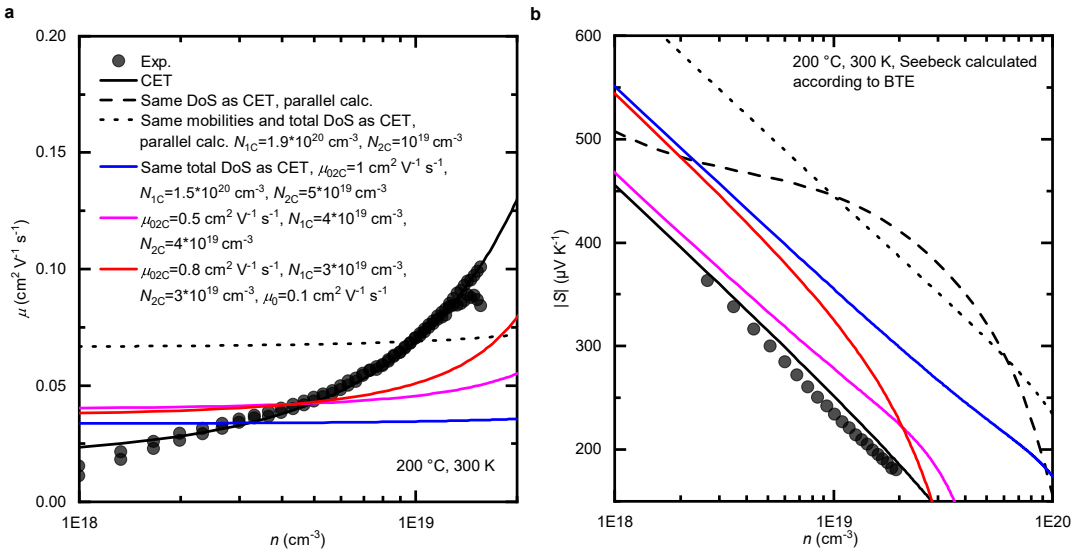

Figure 4.11. Parallel conduction simulations of mobility and Seebeck coefficient versus charge density. Dotted symbols are the data of the 200 °C annealed device at 300 K. The black solid line is the calculation of the CET model as presented in Fig. 4.4. The black dashed line is a calculation with identical parameters as for the CET model but using Eq. 4.1 for the Seebeck coefficient calculation. The black dotted line is a calculation with the same mobilities as for the CET model but a fixed DoS of $N_{1C} = 1.9 \cdot 10^{20}$ cm^{-3} and $N_{2C} = 10^{19}$ cm^{-3} separated in energy by $U_C \approx 80$ meV. The solid blue line is a calculation with the same total DoS as the CET model, but $\mu_{02C} = 1$ cm^2 V^{-1} s^{-1} as well as $N_{1C} = 1.5 \cdot 10^{20}$ cm^{-3} and $N_{2C} = 5 \cdot 10^{19}$ cm^{-3}. The solid pink line is a calculation with discrete levels, with the same parameters as the CET model but $\mu_{02C} = 0.5$ cm^2 V^{-1} s^{-1} as well as $N_{1C} = 4 \cdot 10^{19}$ cm^{-3} and $N_{2C} = 4 \cdot 10^{19}$ cm^{-3}. The solid red line is a calculation with discrete levels, with the same parameters as for the CET model but $\mu_{02C} = 0.8$ cm^2 V^{-1} s^{-1}, $\mu_0 = 0.1$ cm^2 V^{-1} s^{-1} as well as $N_{1C} = 3 \cdot 10^{19}$ cm^{-3} and $N_{2C} = 3 \cdot 10^{19}$ cm^{-3}.

(Eqs. 4.1 and 4.2), causes the Seebeck coefficient to strongly deviate from Heikes formula (black dashed line, note that the mobilities of the black dashed and solid lines are exactly overlapping since they are calculated in exactly the same manner, Eq. 4.27). The origin of this strong deviation is the assumption of Boltzmann transport formalism that the high mobility band is present everywhere in our film, even where no charges are present, contradicting our starting assumption that such levels are formed only when two charges are sufficiently close together. The other simulations shown in Fig. 4.11 further illustrate the failure of the Boltzmann transport formalism (Eqs. 4.1 and 4.2) for the description of charge and thermoelectric transport in P(NDI2OD-T2) at charge densities around 10^{18} cm^{-3} to 10^{19} cm^{-3}. The black dotted line represents a two narrow-band system employing the same mobility parameters as the CET model, but a DoS independent of charge density ($N_{1C} = 1.9 \cdot 10^{20}$ cm^{-3} and $N_{2C} = 10^{19}$ cm^{-3} separated in energy by $U_C \approx 80$ meV). Neglecting local electron-electron interactions and the inhomogeneity of the DoS leads to an almost charge density-independent mobility (black dotted line in

Fig. 4.11a), since the system is in the non-degenerate regime, as proven in Eqs. 4.11-4.14. Furthermore, as outlined in the previous section, the Seebeck coefficient follows Heikes formula in this low-occupancy, low-disorder independent-electron regime (black dotted line in Fig. 4.11b). In order to attempt getting a more reasonable fit to the data within the Boltzmann transport formalism (Eqs. 4.1 and 4.2), the DoS in each band has been changed to $N_{1C} = 1.5 \cdot 10^{20}$ cm^{-3} and $N_{2C} = 5 \cdot 10^{19}$ cm^{-3} to allow more carriers to occupy the higher conductivity channel. In line with this increase in occupancy of the higher conductivity conduction channel, the mobility prefactor of this channel had to be decreased from $\mu_{02C} = 20$ cm^2 V^{-1} s^{-1} to $\mu_{02C} = 1$ cm^2 V^{-1} s^{-1} in order to get a reasonable fit for low charge densities ($n \sim 10^{18}$ cm^{-3}). Nevertheless, the transport in this case is still governed by the lower conductivity channel and the mobility is as proven in Eqs. 4.11-4.14 essentially charge density independent. Therefore, the DoS was significantly reduced ($N_{1C} = 4 \cdot 10^{19}$ cm^{-3} and $N_{2C} = 4 \cdot 10^{19}$ cm^{-3}) in order to reach the degenerate limit that is more strongly governed by the high conductivity channel (pink solid line). Once again the mobility prefactor had to be further reduced to $\mu_{02C} = 0.5$ cm^2 V^{-1} s^{-1} in order to fit the data at low charge densities as well. Nevertheless, it can be seen that in this regime the Seebeck coefficient deviates already strongly from Heikes formula. The last simulation (red solid line) is performed with an even lower DoS ($N_{1C} = 3 \cdot 10^{19}$ cm^{-3} and $N_{2C} = 3 \cdot 10^{19}$ cm^{-3}) and $\mu_0 = 0.1$ cm^2 V^{-1} s^{-1} in order to fit the data at low charge densities. This provides further evidence of the shortcomings of the description with the Boltzmann transport formalism: the even stronger degenerate case does allow a stronger charge density dependence of the mobility (still not sufficient) but also causes the Seebeck coefficient to deviate even more from Heikes formula. Furthermore, the assumption of a total DoS within the crystalline domains as small as $N = 6 \cdot 10^{19}$ cm^{-3} has no physical meaning. As proven in section 4.2 and Eqs. 4.11-4.14 it is impossible to observe a strongly charge density-dependent mobility in the low-occupancy regime in the independent-electron approximation while simultaneously observing a $\frac{k_B}{e}$ ln(10)-slope of the Seebeck coefficient (black dotted, blue, pink and red line). The mathematical considerations in section 4.2 and Eqs. 4.11-4.14 as well as the considerations and illustrative simulations of this paragraph once again underline that the inhomogeneity of the DoS as well as local electron-electron interactions need to be taken into account to explain a strongly charge density-dependent mobility and a Seebeck coefficient following a $\frac{k_B}{e}$ ln(10)-slope in the low-occupancy, low-disorder regime as observed in our measurements on P(NDI2OD-T2).

Finally, we point out that the concept of the inclusion of electron-electron interactions in narrow-band transport as in our CET model, was also explored in the limit of infinite

temperature in the theoretical work by Beni for charge transport in the correlated electron regime in a narrow-band Hubbard chain at arbitrary electron density.[180] Both approaches predict a Seebeck coefficient resembling a slightly modified Heikes formula with the characteristic $\frac{k_B}{e}\ln(10)$-slope in the low-occupancy limit: the Seebeck coefficients versus charge density of the 200 °C annealed and as-cast device at 300 K and 180 K are shown in Fig. 4.12. The predictions of our CET model using the same fitting

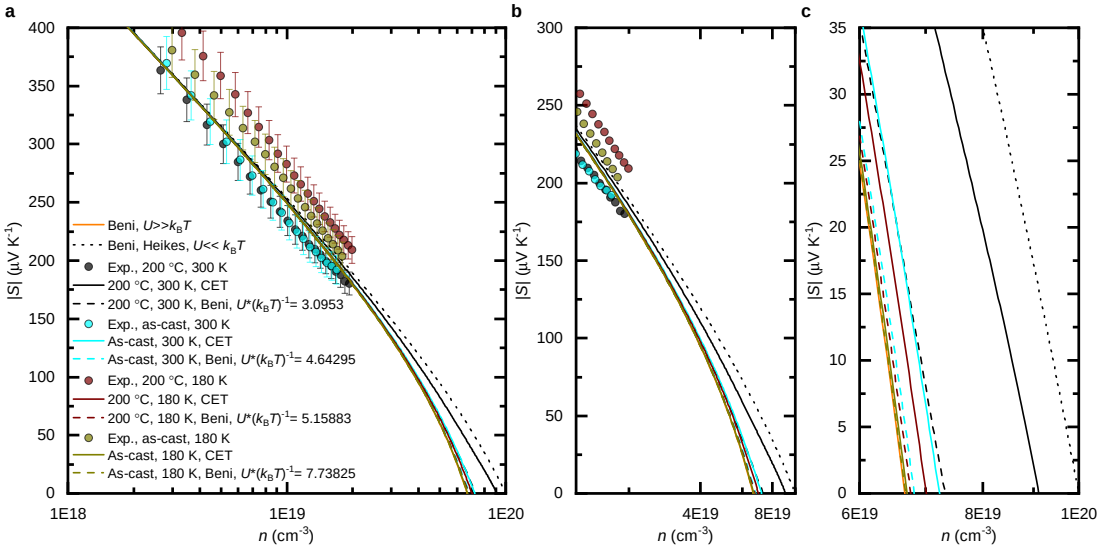

Figure 4.12. Comparison of CET and Hubbard chain model. Seebeck coefficient versus charge density of the 200 °C annealed and as-cast device at 300 K and 180 K. The predicitions of our CET model as well as the theoretical considerations for charge transport in a narrow-band Hubbard chain by Beni[180] are shown as well. A density of thermally accessible sites of $N_{\text{sites}} = 10^{20}$ cm^{-3} respectively a total thermally accessible DoS of $\widetilde{N} = 2 \cdot 10^{20}$ cm^{-3} has been used for all calculations, the fitting parameters for the CET model are the same as in all other figures. The relative error in the Seebeck coefficient is approx. 7 %, calculated from the intrinsic current and voltage measurement errors of the Agilent SPA 4156B as well as the linear regression fit errors from the sensor resistance calibration and the thermal voltage versus temperature difference plots (shown as error bars on the data points, further details in section 3.3.2).

parameters as in all other figures ($N_{\text{sites}} = 10^{20}$ cm^{-3}, solid lines) as well as the theoretical considerations for charge transport in a narrow-band Hubbard chain by Beni[180] (dashed lines) are shown as well. The Seebeck coefficient in the two limiting cases $U \ll k_B T$ (on-site Coulomb repulsion much smaller than thermal energy, corresponding to Heikes formula) as well as $U \gg k_B T$ is shown. The predictions for charge transport in the narrow-band Hubbard chain (dashed lines) were obtained by evaluating Beni's equation 12:

$$S = -\frac{k_B}{e}\left(\frac{\beta U x^2}{\exp(\beta U) + x^2} - \ln(x)\right), \tag{4.33}$$

where $\beta = \frac{1}{k_B T}$ and $x = \exp(\beta U)$, using his equation 15:

$$x = \frac{-(1-\rho) + \left[(1-\rho)^2 + \rho(2-\rho)\exp(-\beta U)\right]^{1/2}}{\exp(-\beta U)(2-\rho)} \tag{4.34}$$

and approximating the on-site Coulomb repulsion with the free energy associated with an interacting charge pair G used for the CET fits ($U = G$, solid lines). The predictions of both models for the Seebeck coefficient are remarkably similar and qualitatively the same. Most importantly both predict a Seebeck coefficient resembling a slightly modified Heikes formula, approximately:

$$S \approx -\frac{k_B}{e} \ln\left(\frac{2 \cdot |(1 - \frac{n}{N_{\text{sites}}})|}{\frac{n}{N_{\text{sites}}}}\right), \tag{4.35}$$

since $U \approx 3$ to $7\ k_B T$ ($U \gg k_B T$) for all fits. In addition, an important feature of the Seebeck coefficient in a correlated electron system is a sign change of the Seebeck coefficient at a charge density $n < N_{\text{sites}}$ (for the charging energy $U \gg k_B T$), which is also expected in our treatment (Fig. 4.12c). In order to reach such regime however a higher charge density regime needs to be attained and further improvements on the accuracy of the measurement are required.

4.7 Conclusions

In conclusion, we have demonstrated that charge transport within and between crystalline domains in high-mobility, semicrystalline polymer semiconductors is not determined by energetic disorder effects, but involves a relatively narrow DoS, that manifests itself in a temperature-independent Seebeck coefficient approximately following a modified Heikes formula. To explain a pronounced carrier concentration dependence of the mobility in this transport regime we have shown that electron-electron interactions between the carriers in the small crystalline domains need to be considered. We have constructed a charge transport model that is able to consistently explain mobility and Seebeck measurements as a function of carrier concentration and temperature. The model is simplistic, in particular, in the way that it takes into account the complex energy spectrum of crystalline domains that are occupied by multiple, Coulomb-interacting charges but it nevertheless provides important insight into how electron-electron interactions affect the structure-property relationships and provides a foundation for further improvements in the carrier mobilities and thermoelectric performance of this important class of conjugated polymers.

Chapter 5

Charge and thermoelectric transport in polymer-sorted semiconducting SWCNT networks

Substantial parts of this chapter were published in *ACS Nano* as Statz, M. *et al.* Charge and thermoelectric transport in polymer-sorted semiconducting single-walled carbon nanotube networks. *ACS Nano* **14,** 15552-15565 (2020).[273]

Severin Schneider and Felix J. Berger, both PhD students in Prof. Jana Zaumseil's group at the University of Heidelberg in Germany, have fabricated all devices and performed all atomic force microscopy (AFM) and Raman measurements, presented in this chapter. William A. Wood, PhD student in Prof. Henning Sirringhaus's group at the University of Cambridge, has written the drivers for the measurement electronics employed for the electric and thermoelectric characterization and provided support with the implementation of the Java code for the measurement routines. Dr. Mojtaba Abdi-Jalebi, visiting researcher of the Optoelectronics Group at the University of Cambridge and University Lecturer at the University College London, performed the photothermal deflection spectroscopy measurements. Simone Leingang, technical employee in Prof. Hans-Jörg Himmel's group at the University of Heidelberg and Prof. Hans-Jörg Himmel synthesized the 1,2,4,5-tetrakis(tetramethylguanidino)benzene (ttmgb) molecules.

5.1 Motivation and outline

In the previous chapter it has been established that the simultaneous study of both charge density and temperature-dependent field-effect mobility as well as on-chip gated Seebeck coefficient is a powerful tool to discern between different transport mechanisms and can offer insights into the prevailing transport regime as well as the interaction of carriers with their environment. As introduced in section 1.1, single-walled carbon nanotube (SWCNT) networks display a very promising material system for both flexible electronics and flexible thermoelectric generators. Understanding the charge transport mechanisms in chirality-selected SWCNT networks and the influence of network parameters is essential for further advances of their optoelectronic and thermoelectric applications. Here, we report on charge density and temperature-dependent field-effect mobility and on-chip field-effect-modulated Seebeck coefficient measurements of polymer-sorted monochiral small diameter (6,5) (0.76 nm) and mixed large diameter SWCNT (1.17-1.55 nm) networks (plasma torch nanotubes, RN) with different network densities and length distributions. All untreated networks display balanced ambipolar transport and electron-hole symmetric Seebeck coefficients. We show that charge and thermoelectric transport in SWCNT networks can be modelled by the Boltzmann transport formalism, incorporating transport in heterogeneous media and fluctuation-induced tunneling. Considering the diameter-dependent one-dimensional density of states (DoS) of the SWCNTs composing the network, we can simulate the charge density and temperature-dependent Seebeck coefficients. Our simulations suggest that scattering in these networks cannot be described as simple one-dimensional acoustic and optical phonon scattering as for single SWCNTs. Instead the relaxation time is inversely proportional to energy ($\tau \propto (E - E_C)^s$, $s = -1$, E_C being the energy of the first van Hove singularity), presumably pointing towards the more two-dimensional character of scattering events and the necessity to include scattering at SWCNT junctions. Finally, our observation of higher power factors in trap-free, 1,2,4,5-tetrakis(tetramethylguanidino)benzene (ttmgb)-treated (6,5) networks than in the RN networks, emphasizes the importance of chirality selection to tune the width of the DoS. In order to benefit from both higher intrinsic mobilities and a large thermally accessible DoS, we propose trap-free, narrow DoS distribution, large diameter SWCNT networks for both electronic and thermoelectric applications.

Semiconducting single-walled carbon nanotube (SWCNT) networks are excellent candidates for next generation electronic devices due to their stability, flexibility, solution-processability as well as high carrier mobilities and Seebeck coefficients.[11,24,274,275] Recently, the ability to tune the diameter distribution in these networks using selective dispersion with conjugated polymers and other separation methods (see section 1.3.2) has led to significant advances in electronic circuits and other applications.[15,21,118,120] As these highly selective sorting methods have only emerged lately, a complete understanding of the charge transport mechanisms in these networks is urgently desired to further improve device performance.[203,241] Most existing transport models for SWCNT networks were developed before the advent of ultra-pure semiconducting networks without any metallic nanotubes. Those studies have focused on explaining transport in terms of fluctuation-induced tunneling, variable-range hopping and percolation theory (section 2.2.2).[196,197,239,276] They mainly consider energetic disorder and sample heterogeneity effects, without explicitly considering the diameter distribution composing the networks.[197,238,239] Nevertheless, studies on chirality-selected SWCNT networks have shown that the consideration of the relative contribution of different chiralities to charge transport is essential.[200,202,203,245] A random resistor model of SWCNT junctions, considering the density of states (DoS) of individual SWCNTs but ignoring their resistance, and hence neglecting any intra-nanotube contributions, has been able to explain many qualitative features of the charge density dependence of the field-effect mobilities of mixed chirality SWCNT networks. This approach is rooted in percolation theory with variable-range hopping as a transport process and correctly predicts how with increasing charge density the filling of the first subband of the SWCNTs leads to a pronounced charge density dependence of the mobility in SWCNT networks.[136,137,202] Furthermore, it demonstrates how small bandgap, large diameter SWCNTs dominate transport, particularly in the low charge density regime, in mixed chirality networks which has also been shown spectroscopically.[200,202,205] However, we recently established that contrary to the expectation from this random resistor model, the temperature dependence of the mobility of large diameter mixed SWCNT (1.17-1.55 nm) networks, with a larger energetic disorder due to the bandgap distribution, is smaller than in monochiral (6,5) SWCNT (0.76 nm) networks.[203] This raises the question of potential phonon scattering-limited intra-nanotube transport contributions leading to the well-established dependence of carrier mobility on diameter ($\propto d^2$) and temperature ($\propto T^{-1}$, section 2.2.1).[183,184] Hence, these findings necessitate further investigations of the influence of network parameters on the presumed transport mechanisms.

To establish the transport mechanisms in SWCNT networks with certain diameter

distributions and to elucidate the influence of network parameters on charge and thermoelectric transport, we study the charge density and temperature-dependent field-effect mobility and on-chip field-effect-modulated Seebeck coefficient of polymer-sorted small diameter (6,5) SWCNT (0.76 nm) networks as well as large diameter mixed SWCNT (1.17-1.55 nm) networks with different network densities and length distributions. We also establish the impact of trap states on transport by studying (6,5) SWCNT networks that were treated with 1,2,4,5-tetrakis(tetramethylguanidino)benzene (ttmgb), which leads to pure electron transport.[277] As the Seebeck coefficient is the entropy transported by a charge carrier divided by its charge, it provides unique insights into the transport energetics and mechanisms (section 2.3).[172,217] While the electrical conductivity has been shown to be predominantly limited by the highly resistive tunneling junctions, the Seebeck coefficient is expected to be much more sensitive to the energetics within the SWCNTs in the network, where most of the applied temperature drops.[198,239] By using field-induced charge density-modulated measurements of the Seebeck coefficient we can eliminate the influence of the Coulombic interaction with counterions that would be present if carriers were introduced by molecular doping,[228] These measurements allow us to establish a direct relationship between the DoS of the SWCNT networks and their Seebeck coefficients. Considering the diameter-dependent one-dimensional DoS of the network-composing SWCNTs from tight-binding nearest-neighbour calculations including trigonal warping effects (see section 1.3.1),[84,85] scaled with the network density and length distribution, as well as dipolar disorder-broadened ($\delta_{\text{dipole}} = 5$ meV, width of the Gaussian distribution), we can simulate the measured charge density and temperature-dependent electron-hole symmetric Seebeck coefficients within the Boltzmann transport formalism. As the transport energetics are strongly affected by the energy-dependent relaxation time, the Seebeck coefficient offers further insights into the carrier scattering mechanisms. Consequently, we can establish whether scattering in these networks can still be described as simple one-dimensional acoustic and optical phonon scattering as for single SWCNTs and discern the energy dependence of the relaxation time.[183,278,279] The improved understanding of charge transport and energetics in SWCNT networks and their dependence on network parameters, allows us to provide design guidelines for both electronic and thermoelectric applications.

5.2 SWCNT network characterization

In order to study the impact of the chirality distribution on charge and thermoelectric transport in SWCNT networks, we selectively dispersed semiconducting SWCNTs

from different growth processes in toluene using polymer wrapping with poly[(9,9-dioctylfluorenyl-2,7-diyl)-*alt*-(6,6')-(2,2'-bipyridine)] (PFO-BPy, molecular structure shown in Fig. 5.1a).[107,125] While using CoMoCAT raw nanotube material yielded

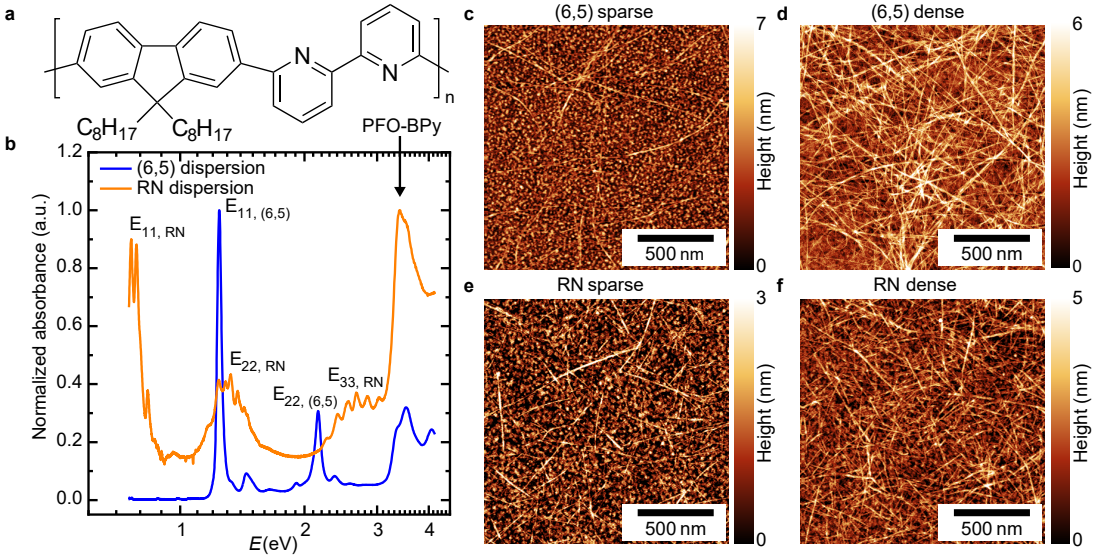

Figure 5.1. SWCNT network characterization. The molecular structure of the wrapping polymer PFO-BPy (a), the normalized absorption spectra of the (6,5) and RN dispersions (b) as well as the AFM images of the (6,5) sparse (c), (6,5) dense (d), RN sparse (e) and RN dense (f) networks are shown. The measurements have been performed by Severin Schneider and Felix Berger.

an essentially monochiral dispersion of (6,5) SWCNTs with a diameter of 0.76 nm and bandgap of 1.27 eV, using plasma torch grown SWCNTs resulted in a dispersion of a broader chirality distribution of large diameter (1.17-1.55 nm), small bandgap (0.70-0.88 eV) SWCNTs (RN SWCNTs).[113,203] The diameter and bandgap range were determined from the E_{11} and E_{22} transitions in the UV-vis-NIR absorption spectra (Fig. 5.1b). Via repeated washing of the SWCNT filter cakes with toluene (80 °C, see section 3.2.2 for further details) the amount of residual wrapping polymer in the SWCNTs networks became negligible (Fig. 5.1b-f). Furthermore, the SWCNT networks were free of metallic nanotubes as evident from Raman spectroscopy (see section 3.5.2 for further experimental details). The Raman spectra of the (6,5) and RN SWCNT networks in the radial breathing mode (RBM) and G-mode region are shown in Fig. 5.2. The Raman spectra on the RN SWCNT networks were recorded with incident wavelengths of 633 nm and 785 nm and similar laser power. Excitation at 785 nm is resonant with small-diameter semiconducting minority chiralities and near-resonant with some of the main semiconducting chiralities in the RN networks, thus leading to strong RBM signals. By contrast, excitation at 633 nm is primarily resonant with metallic SWCNTs and

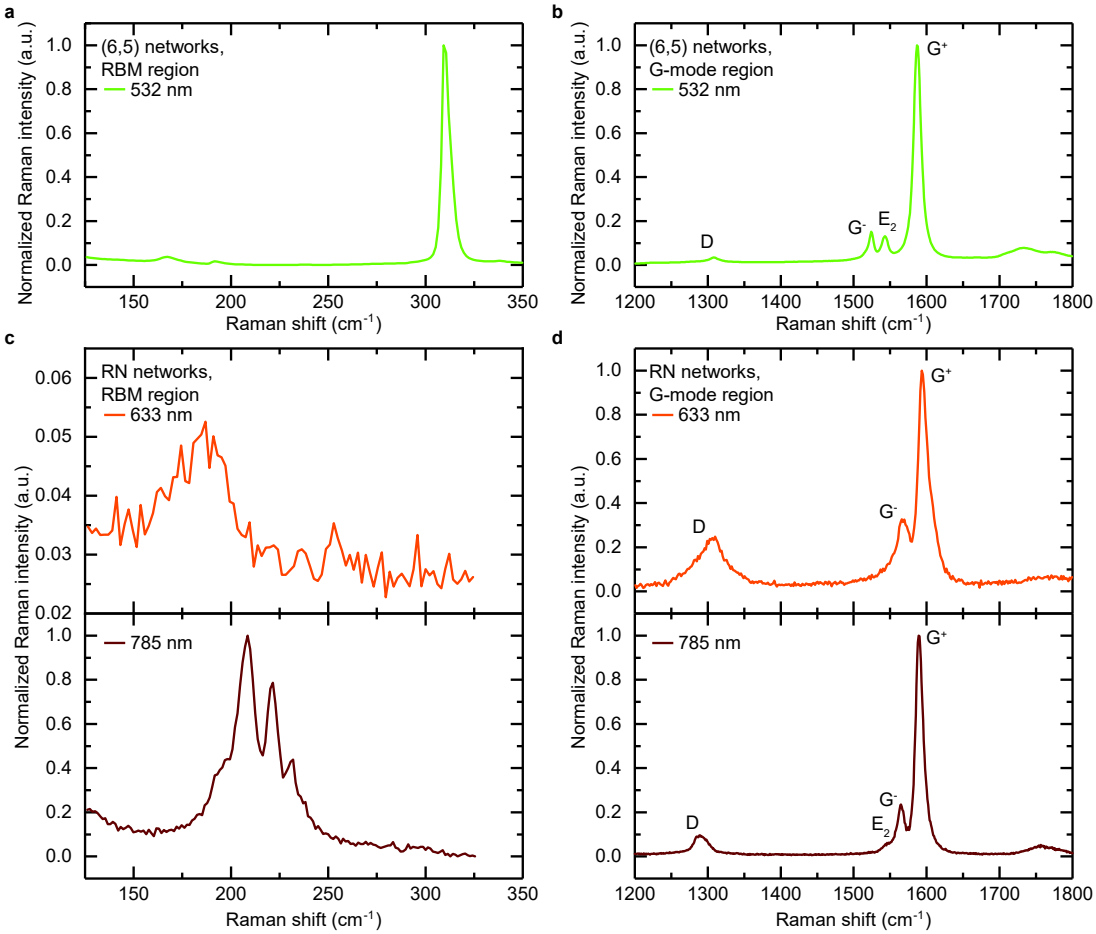

Figure 5.2. Raman spectra of SWCNT networks. The Raman spectra in the radial breathing mode (RBM) and G-mode region of the deposited (6,5) (panel (a) respectively (b), 532 nm excitation) as well as RN networks (panel (c) respectively (d), 633 nm and 785 nm excitation) are shown. An intense RBM mode of the (6,5) networks at 309 cm^{-1} and sharp Lorentzian peaks in the G-mode region for both networks are observed, indicating purely semiconducting SWCNTs. Furthermore, both networks show weak defect-related D-mode peaks. The measurements have been performed by Severin Schneider and Felix Berger.

off-resonant with the majority of semiconducting SWCNTs. Hence, the negligible signal in the RBM region upon 633 nm excitation supports the very low content of metallic SWCNTs in the RN networks. Consequently, based on RBM assignments via Sivarajan chart following the results from Weisman *et al.* and Maultzsch *et al.*,[94,95] as well as the absence of a broad Breit-Wigner-Fano lineshape of the G^- mode,[96] all SWCNT networks show no detectable amount of metallic nanotubes.

Both network density and length distribution of the networks were determined by atomic force microscopy (AFM) images (Figs. 5.1c-f and 5.3, section 3.4.1). The length

distribution depends on the raw material, the exfoliation method used for the polymer wrapping process as well as the re-dispersion method and conditions.[113,280] The length distribution of the SWCNT networks was determined from AFM images of sparse SWCNT networks with well-separated tubes on polished silicon wafers. The SWCNT networks were thoroughly rinsed with tetrahydrofuran and isopropyl alcohol to remove any residual excess polymer. Representative AFM images used to determine the length distribution of the (6,5), short-tube RN and long-tube RN networks are presented in Fig. 5.3a-c. More than 100 SWCNTs per sample were counted and the SWCNT length was found to follow a log-normal distribution. Remaining bundles were excluded from the analysis. The length distribution and average length ($\tilde{l}$) of the (6,5), short-tube RN and long-tube RN networks are shown in Fig. 5.3d-f. The monochiral (6,5)

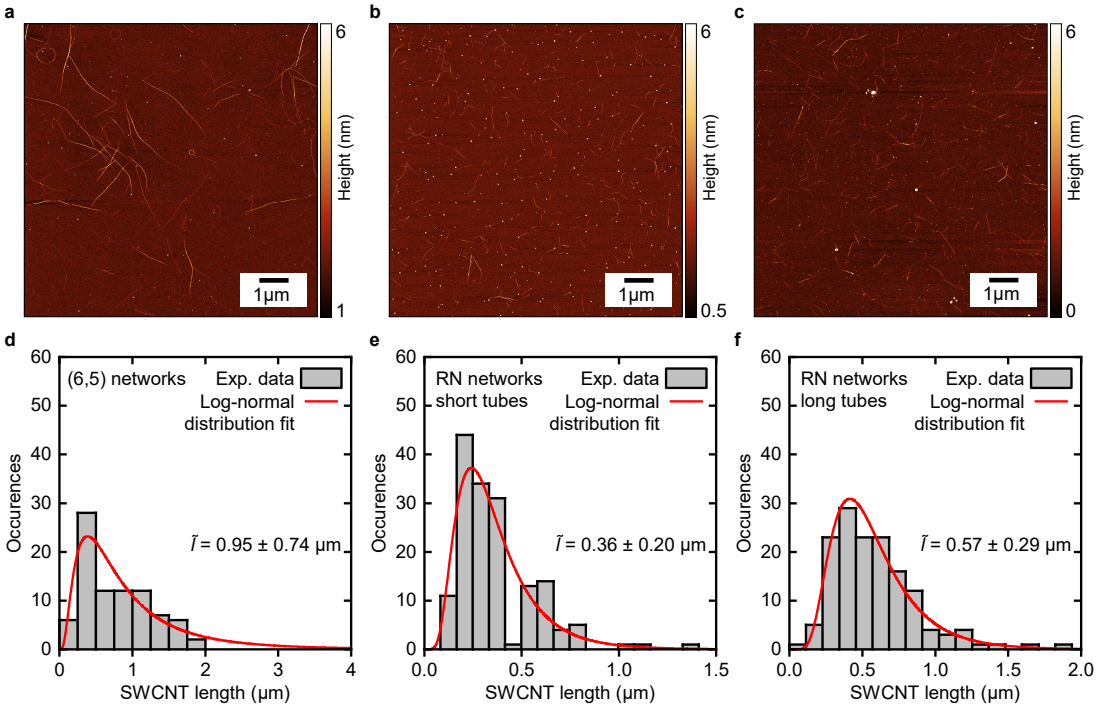

Figure 5.3. SWCNT length determination. Representative atomic force microscopy images used to determine the length distribution of the (6,5) (a), short-tube RN (b) and long-tube RN (c) networks, and their corresponding length distribution and average length ($\tilde{l}$, panels (d)-(f)) are shown. The measurements have been performed by Severin Schneider and Felix Berger.

SWCNT networks have slightly longer tubes (0.95 ± 0.74 µm) than the RN networks (0.57 ± 0.29 µm). For a study of the intrinsic charge and thermoelectric transport properties of SWCNT networks it is important to consider relatively high network densities to reduce the impact of water or hydroxyl groups on polar surfaces that cause

charge carrier trapping and hysteresis in transistor curves.[207,208,258] Therefore, the impact of the network density on thermoelectric transport was investigated well above the percolation threshold and in the regime of mobility saturation (approx. > 13 μm^{-1}) by choosing a sparse network condition at the threshold of this regime and a dense network condition with at least twice the density.[258] Representative AFM images used to extract the network density of the (6,5) and RN networks are shown in Fig. 5.1c-f and the extracted network parameters are displayed in Table 5.1. To probe the effect

Table 5.1. SWCNT network parameters.

Network	Abbreviation	Network density (λ) (μm^{-1})	Average SWCNT length (μm)
(6,5) sparse (Fig. 5.1c)	(6,5)-s	12.6 ± 2.8	0.95 ± 0.74
(6,5) sparse, ttmgb-treated	(6,5)-s-ttmgb		
(6,5) dense (Fig. 5.1d)	(6,5)-d	31.7 ± 3.1	
RN sparse, long tubes (Fig. 5.1e)	RN-s-lt	19.2 ± 2.5	0.57 ± 0.29
RN dense, long tubes (Fig. 5.1f)	RN-d-lt	37.9 ± 3.1	
RN dense, short tubes	RN-d-st	36.5 ± 3.8	0.36 ± 0.20

of small length variations we also investigated dense RN networks with shorter tubes (RN-d-st, obtained from 60 min of re-dispersion, see section 3.1.2 for further details). Since the (6,5) networks showed a non-negligible trap density even for high network densities (evident from their stronger hysteresis in transistor transfer curves, larger onset voltages and stronger modulation of the Seebeck coefficient with charge density, see next section for further details), we also studied (6,5) sparse networks treated with the strongly reducing ttmgb ((6,5)-s-ttmgb), which blocks hole transport and removes residual water from the SWCNT network via protonation of ttmgb.[277]

To characterize the energetic disorder of the combined DoS and compare it with the thermoelectric transport energetics, photothermal deflection spectroscopy (PDS) measurements of the (6,5) and RN networks were performed. PDS is a sensitive absorption measurement technique that detects heating due to non-radiative relaxation of the absorbed light (see section 3.5.3 for further details). Due to its high sensitivity it is suitable for the detection of sub-bandgap tail states and the extraction of the Urbach energy E_u, which is the characteristic energy of the exponential absorption tail in solid state absorption due to energetic disorder.[54,174,281] The PDS measurements of the (6,5) sparse ((6,5)-s), long-tube RN sparse (RN-s-lt) and long-tube RN dense

(RN-d-lt) networks are presented in Fig. 5.4. For both the sparse and dense RN

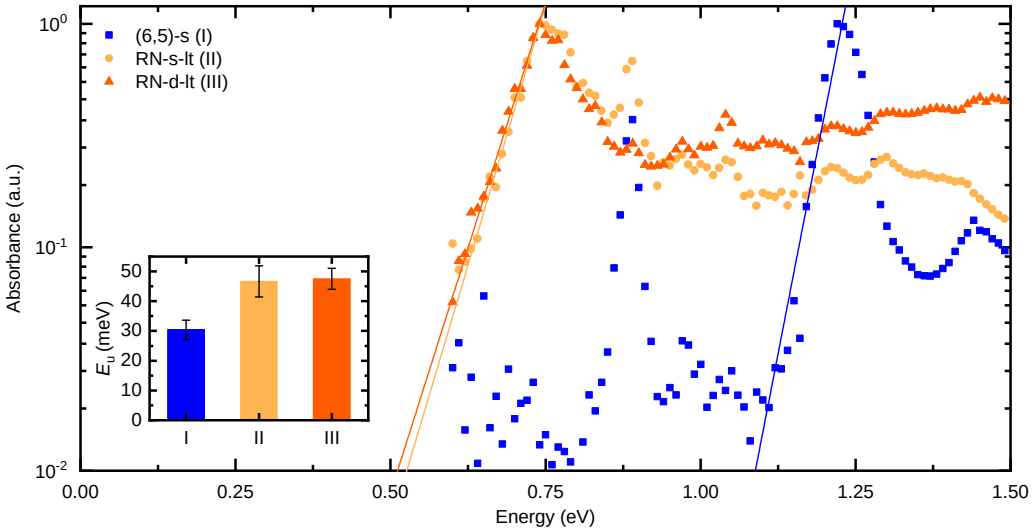

Figure 5.4. Photothermal deflection spectroscopy measurements of SWCNT networks. The PDS measurements of the (6,5) sparse, long-tube RN sparse and long-tube RN dense networks are shown. The solid lines are the exponential fits to the absorption tail to extract the characteristic Urbach energies (E_u), which are displayed in the inset. The error bar of approximately 10 % represents the fitting error. The measurements have been performed by Dr. Mojtaba Abdi-Jalebi.

networks the extracted Urbach energy from the exponential absorption tail is $E_{u,\,RN} \approx 47 \pm 5$ meV, independent of the network density in the high network density regime (> 13 µm^{-1}). In agreement with the tight-binding nearest-neighbour calculations and our thermoelectric transport measurements, the Urbach energy of the monochiral (6,5) networks is substantially smaller ($E_{u,\,(6,5)} \approx 30 \pm 3$ meV). The larger energetic disorder of the bandtail of the RN networks originates from the close proximity in energy of the first van Hove singularities of representative chiralities ((16,2), (10,9) and (12,7)).[84,85,94]

5.3 Electric and thermoelectric characterization at 300 K

Four-point-probe (4pp) linear mobility (μ_{4pp}), contact resistance (R_c), saturation mobility (μ_{sat}) as well as hole and electron Seebeck coefficient (S_h and S_e) of the six network conditions ((6,5)-s, (6,5)-d, (6,5)-s-ttmgb, RN-s-lt, RN-d-lt and RN-d-st) were characterized depending on temperature and charge density using a bottom-contact top-gate field-effect transistor architecture with 4pp voltage probes and two on-chip heaters (channel width $W = 1000$ µm and length $L = 50$ µm, Figs. 5.5 and 5.6). The hybrid

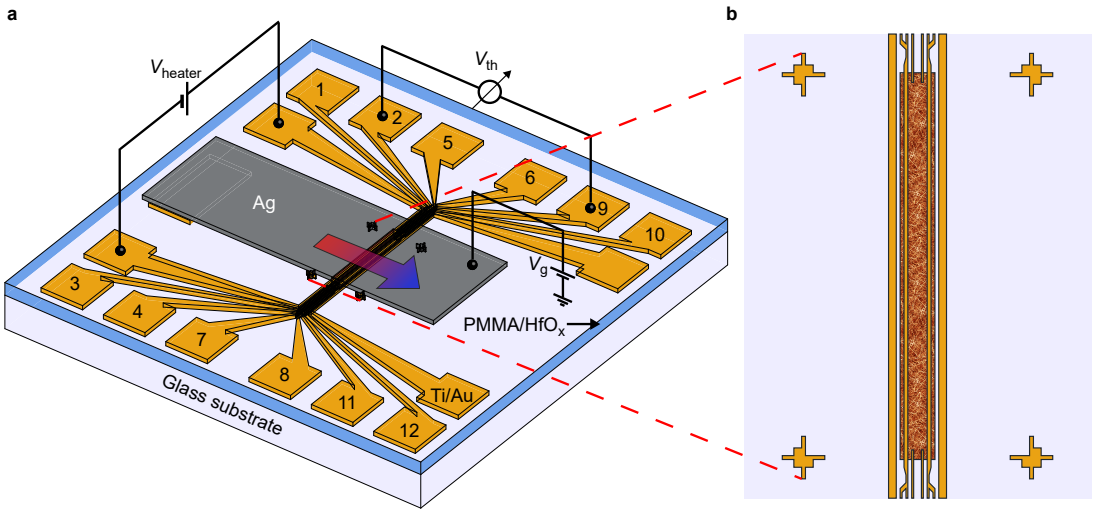

Figure 5.5. Thermoelectric device architecture. The bottom-contact top-gate field-effect transistor architecture with four-point-probe (4pp) contacts and two on-chip heaters ((a), close-up of the active area in (b)) for the thermoelectric transport measurements is shown. In panel (a) pads 1-4 denote the source of the FET structure and the hot resistance sensor, pads 5-8 are 4pp voltage probes and pads 9-12 are the drain of the FET structure as well as the cold resistance sensor.

dielectric (60 nm high-κ HfO_x on top of 11 nm poly(methyl methacrylate) (PMMA), see section 3.1.3) facilitated reduced dipolar disorder and low-voltage operation with low gate leakage currents ($<$ 100 pA, Figs. 5.6a, b and 5.7a).[209] Further details on the fabrication of the thermoelectric devices is reported in section 3.2.2. Source and drain electrodes were used as on-chip 4pp resistance thermometers for the temperature calibration of the Seebeck coefficient measurements (pads 1-4 and 9-12 in Fig. 5.5a respectively, see section 3.3.1 for further details).[54,172] All untreated networks show balanced ambipolar transport characteristics with low hysteresis (onset voltage (V_{on}) difference between forward and reverse sweep) and onset voltages $|V_{on}| \leq 2$ V at 300 K. The onset voltages are the voltages for which the drain-source current (I_{ds}) rises above the background noise and gate-leakage current level extracted from the linear transfer curves. The extraction of the hole and electron onset voltage at 300 K for the long-tube RN dense networks ($V_{on,h} = -0.7$ V and $V_{on,e} = 0.4$ V) is representatively shown in Fig. 5.7a. In addition, Fig. 5.7b shows the extraction of the maximum capacitance (C_m) in the on-state ($V_{gs} = \pm 5$ V, for electron and hole transport respectively), exemplarily for the long-tube RN dense networks. The maximum on-state capacitances for hole and electron transport of the six network conditions are summarized in Table 5.2. The charge density was consequently obtained using the relationship $n = \frac{C_i}{h} \cdot (V_{gs} - V_{on})$, with $C_i = \frac{C_m}{W \cdot L_{pattern}}$ ($W = 1000$ µm the width and $L_{pattern} = 90$ µm the length of

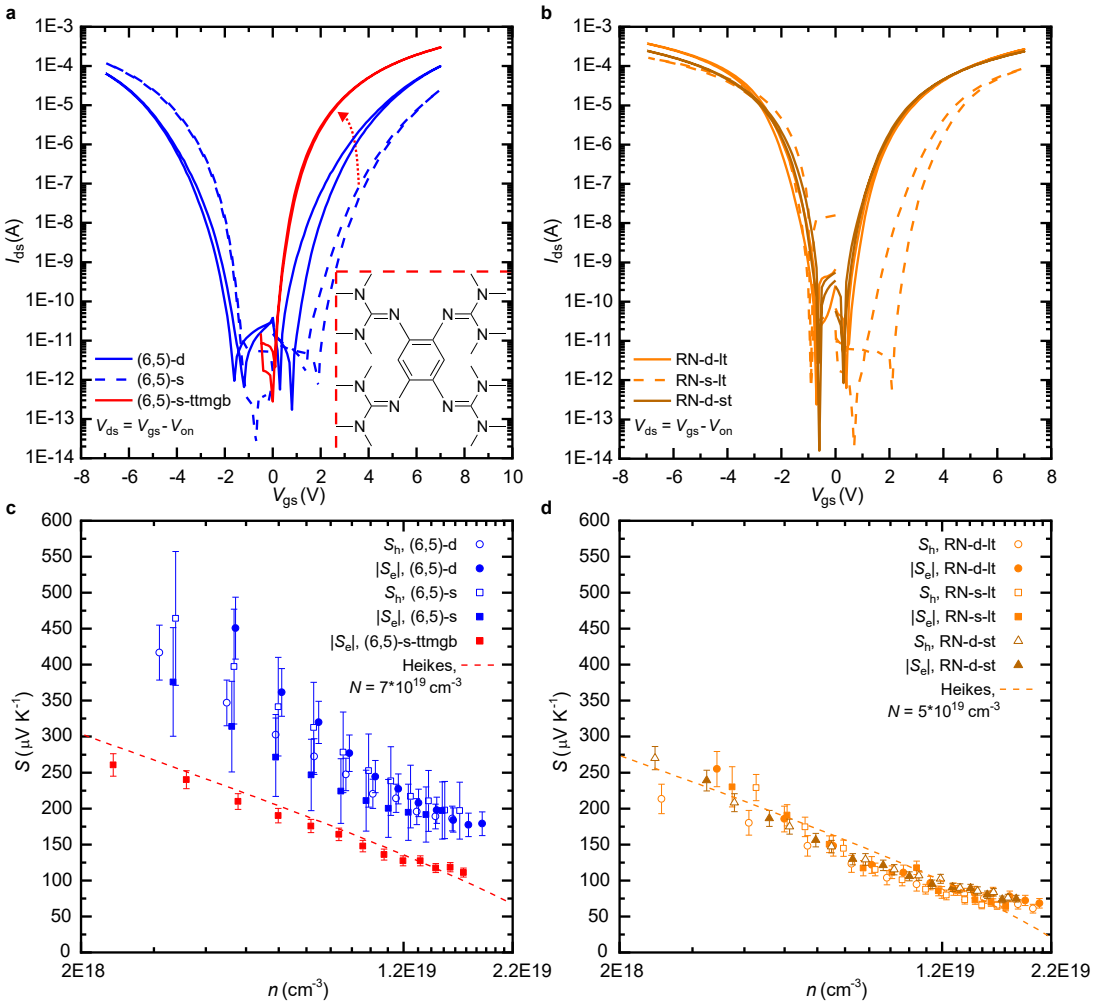

Figure 5.6. Charge and thermoelectric transport at 300 K. Saturation transfer curves (with $V_{ds} = V_{gs} - V_{on}$) as well as hole and absolute electron Seebeck coefficients (S_h and $|S_e|$) versus charge density of the (6,5) dense ((6,5)-d), (6,5) sparse ((6,5)-s) and (6,5) sparse ttmgb-treated ((6,5)-s-ttmgb) networks ((a) respectively (c)) as well as the long-tube RN dense (RN-d-lt), long-tube RN sparse (RN-s-lt) and short-tube RN dense (RN-d-st) networks ((b) respectively (d) are shown (network parameters in Table 5.1). The red arrow in (a) indicates the ttmgb treatment (molecular structure shown in inset of (a)). The red and orange dashed lines in (c) and (d) display Heikes formula with $N = 7 \cdot 10^{19}$ cm^{-3} and $N = 5 \cdot 10^{19}$ cm^{-3}.[235] The relative error in the Seebeck coefficient is $5 - 10$ % (except 20 % for the (6,5)-s network), while the error analysis was performed according to ref. [172].

the SWCNT patterned area) being the areal capacitance and $h = 2$ nm the assumed height of the accumulation layer.[174] The saturation transfer curves were measured in the condition $V_{ds} = V_{gs} - V_{on}$ to ensure a unipolar saturation regime throughout the entire gate voltage range (300 K measurements shown in Fig. 5.6a, b).[138] 4pp linear and saturation mobilities have been found to be in good agreement. A representative

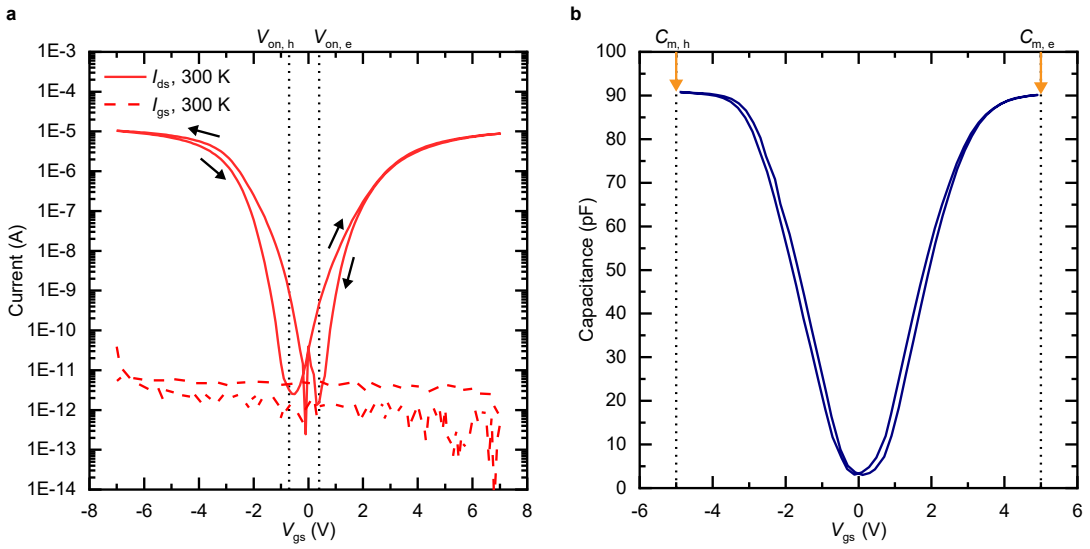

Figure 5.7. Onset voltage and device capacitance extraction. The extraction of the hole and electron onset voltage ($V_{\mathrm{on,\,h}} = -0.7$ V and $V_{\mathrm{on,\,e}} = 0.4$ V, black dotted lines) at 300 K from the linear transfer measurements ($V_{\mathrm{ds}} = -0.1$ V, (a)) as well as hole and electron on-state capacitance ($C_{\mathrm{m,\,h}} = 91$ pF and $C_{\mathrm{m,\,e}} = 90$ pF, black dotted lines and orange arrows, (b)) for the long-tube RN dense networks are representatively shown.

Table 5.2. SWCNT network on-state capacitances.

Network	Abbreviation	Hole on-state capacitance ($C_{\mathrm{m,\,h}}$) (pF)	Electron on-state capacitance ($C_{\mathrm{m,\,e}}$) (pF)
(6,5) sparse	(6,5)-s	75	74
(6,5) sparse, ttmgb-treated	(6,5)-s-ttmgb	-	69
(6,5) dense	(6,5)-d	81	80
RN sparse, long tubes	RN-s-lt	77	77
RN dense, long tubes	RN-d-lt	91	90
RN dense, short tubes	RN-d-st	78	78

comparison of the hole and electron saturation ($\mu_{\mathrm{h,\,sat}}$ and $\mu_{\mathrm{e,\,sat}}$) as well as 4pp linear ($\mu_{\mathrm{h,\,4pp}}$ and $\mu_{\mathrm{e,\,4pp}}$) mobilities of the short-tube RN dense networks at 300 K is shown in Fig. 5.8. Since the noise level of the saturation mobilities was generally lower than that of the 4pp linear mobilities, they have been employed for the presented electrical analysis.

In the high network density regime (approx. > 13 µm^{-1}) both electric and thermoelectric transport are, within our measurement error of 5-10 %, independent of the

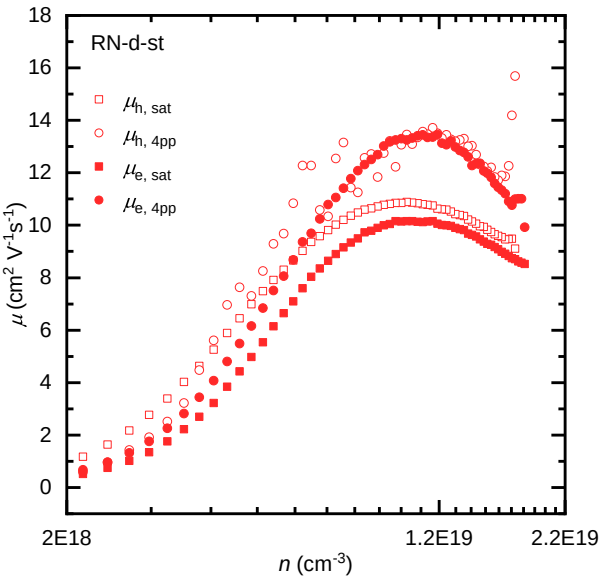

Figure 5.8. Comparison of 4pp linear and saturation mobilities. The hole and electron saturation ($\mu_{h,\,sat}$ and $\mu_{e,\,sat}$) as well as 4pp linear ($\mu_{h,\,4pp}$ and $\mu_{e,\,4pp}$) mobilities of the short-tube RN dense networks at 300 K are representatively shown and found to be in good agreement.

network density (compare RN-s-lt and RN-d-lt in Fig. 5.6b, d) and small SWCNT length variations (compare RN-d-lt and RN-d-st in Fig. 5.6b, d).[258] Thermoelectric transport is electron-hole symmetric ($|S_e| \approx S_h$) as expected from the electron-hole symmetric DoS for low energies in single SWCNTs (Fig. 5.6c, d).[84] Due to the absence of any metallic SWCNTs and the only moderately high charge densities, the magnitude of the Seebeck coefficient of all networks is several hundreds of $\frac{\mu V}{K}$ and decreases with increasing charge density. Particularly at high charge densities ($n > 10^{19}$ cm^{-3}), the Seebeck coefficient of the monochiral (6,5)-s-ttmgb networks exceeds that of the mixed large diameter RN networks. The differences in the saturation transfer curves between the (6,5)-d and (6,5)-s networks originate from different trap state densities. Treatment with the electron-donating and highly alkaline ttmgb blocks hole transport and neutralizes electron trap states via protonation of ttmgb (molecular structure shown in inset of Fig. 5.6a).[277] The reduced trap density manifests itself through reduced hysteresis and onset voltage ($V_{on,\,(6,5)\text{-}s,\,e} = 1.2$ V to $V_{on,\,(6,5)\text{-}s\text{-}ttmgb,\,e} = 0.0$ V) as well as a decrease of the slope of the absolute electron Seebeck coefficient versus charge density (from approx. 251 $\frac{\mu V}{K \cdot dec}$ for the (6,5)-s networks to approx. 185 $\frac{\mu V}{K \cdot dec}$ for the (6,5)-s-ttmgb networks) due to reduced Fermi-level pinning by trap states.[172] Heikes formula ($S = \frac{k_B}{e} \ln\left(\frac{N-n}{n}\right)$) for iso-energetic narrow-band conduction (N being the total thermally accessible DoS,

k_B the Boltzmann constant and e the electron charge) with $N = 7 \cdot 10^{19}$ cm^{-3} and $N = 5 \cdot 10^{19}$ cm^{-3} is shown in Fig. 5.6c, d.[235] At low charge densities Heikes formula describes the data well suggesting that in this regime ($n \ll N$) the SWCNT networks behave as low-disorder systems due to the sharp DoS around the first van Hove singularity and the low dipolar disorder. As a result configurational entropy governs the Seebeck coefficient. However, for high charge densities the Seebeck coefficient of the SWCNT networks deviates from Heikes formula and the dependence of the Seebeck coefficient on carrier concentration becomes weaker. This also manifests itself in the slope of the Seebeck coefficient plotted versus the logarithm of carrier concentration and calculated over the whole range of data being slightly smaller than what is expected from Heikes formula (198 $\frac{\mu V}{K \cdot dec}$). The values are 185 $\frac{\mu V}{K \cdot dec}$ for the (6,5)-s-ttmgb and 188 $\frac{\mu V}{K \cdot dec}$ for the RN networks. The reduced carrier concentration dependence of the Seebeck coefficient is a manifestation of Boltzmann statistics becoming insufficient due to the Fermi-level (E_F) approaching the state distribution ($n \ll N$ does not hold). In this regime a narrow-band description is inappropriate and the actual DoS of the networks needs to be considered (further details in section temperature-dependent thermoelectric transport in SWCNT networks).[172]

5.4 Fluctuation-induced tunneling in SWCNT networks

Electrical transport is thermally activated for all accessible charge densities (approx. $n \leq 2.2 \cdot 10^{19}$ cm^{-3}) for both the (6,5)-s-ttmgb-treated and as previously reported for all untreated networks (Fig. 5.9a, b).[203] The temperature-dependent onset voltages for hole and electron transport ($V_{on,\,h}$ and $V_{on,\,e}$) of the six network conditions, used to obtain the charge densities ($n = \frac{C_i}{h} \cdot (V_{gs} - V_{on})$, as outlined in the previous section) are shown in Fig. 5.10. Representative saturation electron mobilities ($\mu_{e,\,sat}$) of the (6,5)-s-ttmgb and saturation hole mobilities ($\mu_{h,\,sat}$) of the RN-d-st networks are shown in Fig. 5.9a, b. 4pp linear and saturation mobilities are in good agreement (Fig. 5.8) and all show a distinct maximum at 300 K within the charge density range of $n = 1 \cdot 10^{18}$ cm^{-3} – $2 \cdot 10^{19}$ cm^{-3} due to progressive filling of the first subband of the dipolar disorder-broadened one-dimensional DoS of the SWCNT networks with increasing charge density (Fig. 5.9a, b).[136,137,202] Due to the larger SWCNT diameters and the broader DoS originating from the presence of multiple chiralities in the RN networks, this filling effect occurs at lower charge densities than for the (6,5) networks. The normalized saturation mobilities $\frac{\mu_{sat}}{\mu_{sat,\,300\,K}}$ extracted for six (RN-d-st) respectively seven ((6,5)-s-ttmgb) different overdrive voltages $V_{ov} = V_{gs} - V_{on}$ (2 V – 4.5 V respectively 2 V –

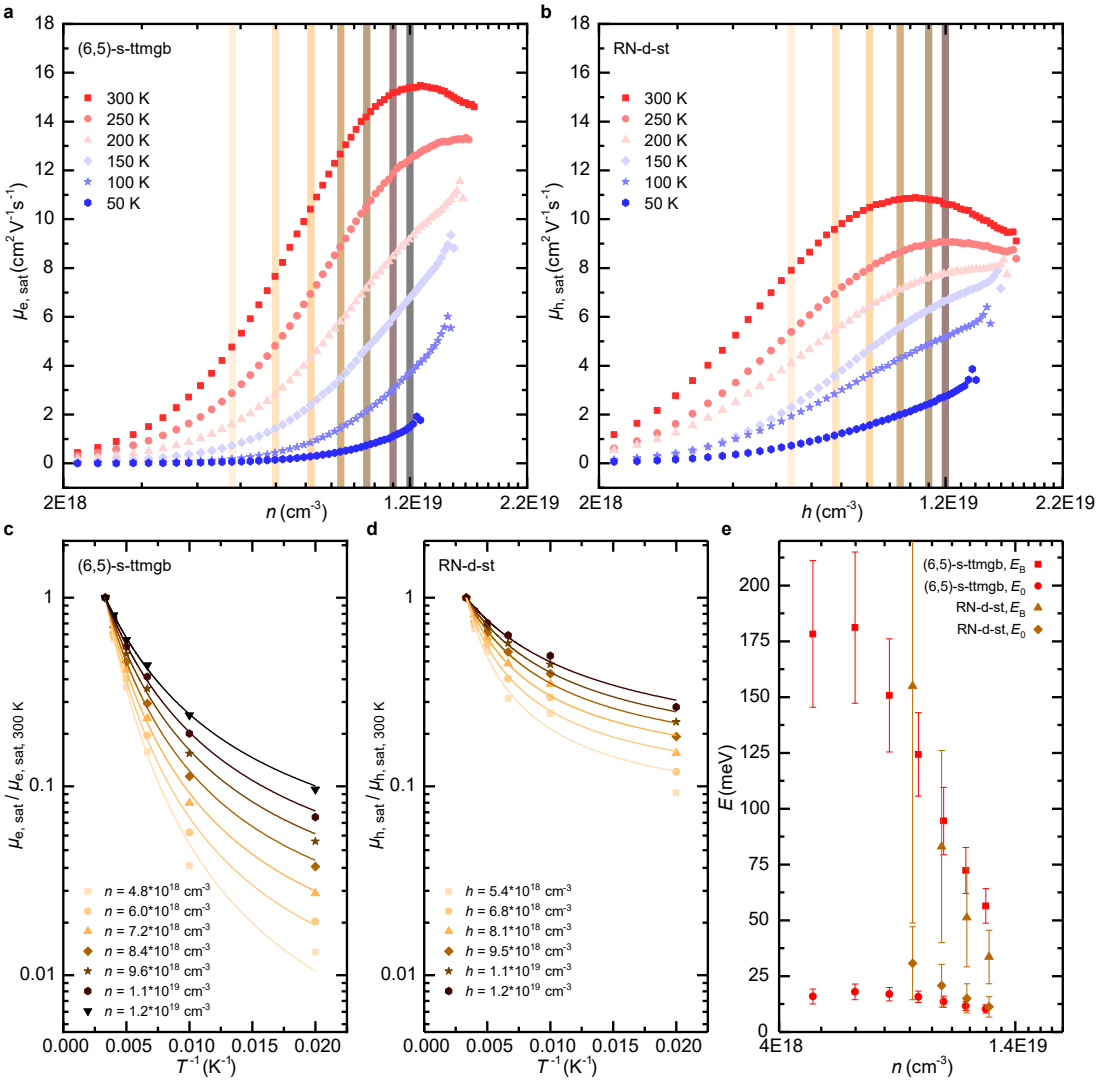

Figure 5.9. Fluctuation-induced tunneling (FIT) in SWCNT networks. The temperature and charge density-dependent electron respectively hole saturation mobility ($\mu_{\mathrm{e,\,sat}}$ and $\mu_{\mathrm{h,\,sat}}$) of the (6,5)-s-ttmgb (a, c) and RN-d-st (b, d) networks are shown. The normalized saturation mobilities $\frac{\mu_{\mathrm{sat}}}{\mu_{\mathrm{sat,\,300\,K}}}$ at several charge densities (line-cuts in (a) and (b)), and the FIT fits using the mobility analogue to Eq. 5.1 are shown in (c) and (d). The extracted characteristic energies E_{B} and E_0 are presented in (e). Error bars display the standard deviation of the fitting parameters.

5 V in steps of 0.5 V) and hence charge densities ($4.8 \cdot 10^{18}$ cm^{-3} – $1.2 \cdot 10^{19}$ cm^{-3} and $5.4 \cdot 10^{18}$ cm^{-3} – $1.2 \cdot 10^{19}$ cm^{-3}, respectively, line-cuts in Fig. 5.9a, b) are plotted versus the inverse temperature in Fig. 5.9c, d. Despite the smaller energetic disorder experienced by carriers in the monochiral (6,5) networks (see temperature-dependent thermoelectric transport data in the following section) the charge density and temperature dependence

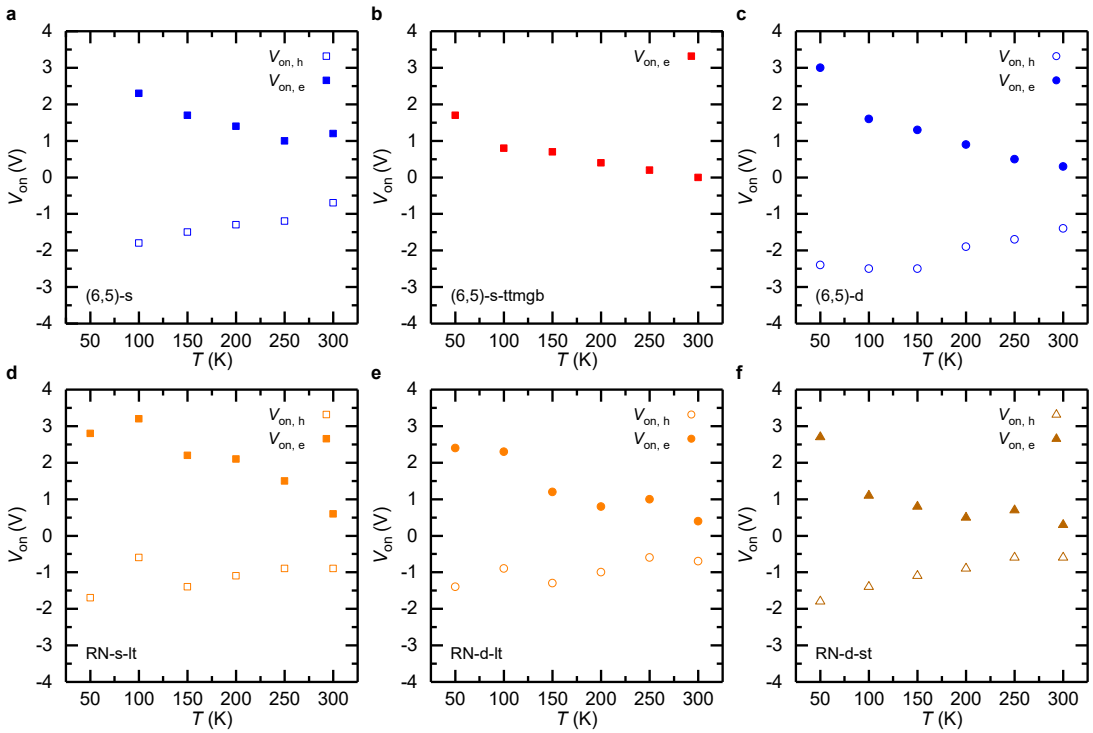

Figure 5.10. Temperature-dependent onset voltages. The temperature-dependent onset voltages for hole and electron transport ($V_{on,h}$ and $V_{on,e}$) of the (6,5) sparse ((6,5)-s, (a)), (6,5) sparse ttmgb-treated ((6,5)-s-ttmgb, (b)), (6,5) dense ((6,5)-d, (c)), long-tube RN sparse (RN-s-lt, (d)), long-tube RN dense (RN-d-lt, (e)) and short-tube RN dense (RN-d-st, (f)) networks are shown.

of the saturation mobility for a fixed charge density (e.g. $n_0 = 1.2 \cdot 10^{19}$ cm^{-3}) and most notably for comparable DoS filling levels (e.g. $n_0 = 1.2 \cdot 10^{19}$ cm^{-3} for (6,5)-s-ttmgb and $h_0 = 9.5 \cdot 10^{18}$ cm^{-3} for RN-d-st) of the (6,5) networks is stronger than that of the RN networks as previously observed (Fig. 5.9c, d).[204] This observation is not expected within a framework of a homogeneous medium and disorder-based transport rooted in variable-range or Miller-Abrahams hopping for which a lower disorder inevitably leads to a smaller charge density and temperature dependence of the field-effect mobility.[61,135,172] We find that charge transport within semiconducting SWCNT networks can be described by the notions of transport in heterogeneous media and fluctuation-induced tunneling.[196,198,203,282,283] We extend these general notions and emphasize that the heterogeneous medium for SWCNT networks consists of two main segments, the SWCNTs themselves with a Gaussian disorder-broadened, one-dimensional DoS that depends on the diameter distribution and the junctions with a distribution of tunnel barrier heights that depend on both the charge density, i.e. the position of the Fermi-level, as well as the diameter distribution of the constituting junctions. Transport along the SWCNTs is

ballistic for short segments and even for long segments (longer than the mean free path due to acoustic phonon scattering) without SWCNT crossings, mobilities of $> 1000\ \frac{\mathrm{cm}^2}{\mathrm{V{\cdot}s}}$ can be achieved (further details have been introduced in section 2.2.1).[183,184] While it has been shown that SWCNT crossings can lead to substantial reductions of the single SWCNT mobility, presumably due to enhanced scattering at these crossings, the conductivities of SWCNT segments will nevertheless be significantly larger than those of the tunnel barrier segments ($\sigma_{\mathrm{SWCNT}} \gg \sigma_{\mathrm{B}}$).[194,284] Within effective-medium theory the conductivity of each transport path (σ_j) in the percolating network (with N_{path} number of transport paths) can therefore be approximated with the conductivity of a single junction along this path for a peaked distribution of tunnel barrier heights.[170,196,285] Transport through these tunnel barriers connecting two large conducting regions occurs through thermal activation across the tunnel barrier and fluctuation-induced tunneling, a thermally activated tunneling process due to voltage fluctuations across the junction capacitance caused by the random thermal motion of carriers (Johnson noise). Within this framework and the approximations of a parallel plate capacitance for the junction capacitance, a parabolic barrier approximation and the Wentzel-Kramers-Brillouin (WKB) approximation, the conductivity of SWCNT networks (σ) can be written as:[196]

$$\sigma \approx N_{\mathrm{path}} \cdot \sigma_B = \sigma_0(E_{\mathrm{F}}) \cdot \exp\left(-\frac{T_{\mathrm{B}}(E_{\mathrm{F}})}{T + T_0(E_{\mathrm{F}})}\right). \tag{5.1}$$

Here $T_{\mathrm{B}}(E_{\mathrm{F}}) = \frac{C{\cdot}(V_{\mathrm{B}}(E_{\mathrm{F}}))^2}{2{\cdot}k_{\mathrm{B}}{\cdot}e^2}$ and $T_0(E_{\mathrm{F}}) = \frac{T_{\mathrm{B}}(E_{\mathrm{F}})}{2{\cdot}\chi{\cdot}w{\cdot}\xi(0)}$, while C is the junction capacitance within the parallel plate approximation, $V_{\mathrm{B}}(E_{\mathrm{F}})$ is the Fermi-level-dependent barrier height of the tunnel barrier, k_{B} is the Boltzmann constant, e is the electron charge, $\chi = \left(\frac{2{\cdot}m{\cdot}V_{\mathrm{B}}(E_{\mathrm{F}})}{\hbar^2}\right)^{\frac{1}{2}}$ is the Fermi-level-dependent tunneling constant, m is the effective carrier mass, w is the width of the tunneling junction and $\xi(0) = \int_0^1 (u{\cdot}(1{-}u))^{\frac{1}{2}}du = \frac{\pi}{8}$ is a scaling factor that originates from the Taylor expansion of the transmission coefficient around the Fermi-level within the WKB approximation and depends on the parabolic shape of the tunnel barrier. $\sigma_0(E_{\mathrm{F}})$ is a weakly temperature-dependent conductivity pre-factor that takes the number of conduction paths N_{path} as well as the initial and final DoS on each side of the junction at the Fermi level ($g_i(E_{\mathrm{F}})$ and $g_f(E_{\mathrm{F}})$) into account. $T_{\mathrm{B}}(E_{\mathrm{F}})$ characterizes the temperature for which significant thermal excitation across the tunnel barrier is likely to occur and $T_0(E_{\mathrm{F}})$ is the temperature above which thermal voltage fluctuations due to Johnson noise are relevant. For temperatures $T < T_0(E_{\mathrm{F}})$ the expression becomes temperature-independent (elastic tunneling). The fact that there has not been any experimental evidence for an attainable charge density regime for which the conductivity in semiconducting SWCNT networks decreases with increasing

temperature, further supports the validity of Eq. 5.1.[241] The diameter dependence of the conductivity of the semiconducting SWCNT network within this framework is crucial. Firstly, the diameter distribution influences the energetic landscape (DoS) and thereby the position of the Fermi-level for a given charge density and temperature. The diameter distribution also influences the junction capacitance, since larger diameter SWCNTs are expected to have larger contact areas and therefore larger capacitances in the parallel plate approximation. Furthermore, smaller diameter tubes have been found to exhibit higher contact resistances, which has been attributed to higher tunnel barriers $V_{\mathrm{B}}(E_{\mathrm{F}})$.[194]

Due to the existence of tunnel barriers for all charge densities, the temperature-activated behaviour of the saturation mobilities ($\sigma = \frac{C_{\mathrm{i}}}{h} \cdot \int_{V_{\mathrm{on}}}^{V_{\mathrm{gs}}} \mu_{\mathrm{sat}}(V_{\mathrm{gs}}^{'})\, dV_{\mathrm{gs}}^{'}$) within the framework of a heterogenous medium and fluctuation-induced tunneling is expected (Eq. 5.1). The prefactor $\sigma_0(E_{\mathrm{F}})$ accounts for the DoS filling effect and the existence of a mobility maximum caused by an eventual decrease of the initial and final DoS at the Fermi-level on each side of the junction ($\sigma_0(E_{\mathrm{F}}) \propto g_i(E_{\mathrm{F}})$, $g_f(E_{\mathrm{F}})$)), which outweighs the slight reduction in the tunnel barrier height $V_{\mathrm{B}}(E_{\mathrm{F}})$ in this charge density regime. Considering the proportionalities $T_{\mathrm{B}}(E_{\mathrm{F}}) \propto C \cdot (V_{\mathrm{B}}(E_{\mathrm{F}}))^2$ and $T_0(E_{\mathrm{F}}) \propto C \cdot (V_{\mathrm{B}}(E_{\mathrm{F}}))^{\frac{3}{2}} \cdot m^{-\frac{1}{2}}$, the expected proportionality between junction capacitance and diameter as well as the anti-proportionality between tunnel barrier height and diameter,[194] the stronger charge density and temperature dependence of the saturation mobility of the (6,5) compared to the RN networks (Fig. 5.9a-d) may be rationalized, not as a manifestation of different degrees of disorder, but in terms of the dependence of the tunneling junctions between tubes on tube diameter: The smaller diameter of the (6,5) SWCNTs is expected to lead to both higher tunnel barriers at any fixed charge density (n_0) in the (6,5) networks ($V_{\mathrm{B},\,(6,5)}(E_{\mathrm{F}}(n_0)) > V_{\mathrm{B,\,RN}}(E_{\mathrm{F}}(n_0))$) as well as smaller SWCNT overlap areas resulting in smaller junction capacitances compared to the RN networks ($C_{(6,5)} < C_{\mathrm{RN}}$).[194] The characteristic energies of the saturation mobilities, $E_{\mathrm{B}} = k_{\mathrm{B}}T_{\mathrm{B}}$ and $E_0 = k_{\mathrm{B}}T_0$, of the (6,5)-s-ttmgb and RN-d-st networks at various charge densities were obtained from fits of the normalized saturation mobilities $\frac{\mu_{\mathrm{sat}}}{\mu_{\mathrm{sat,\,300\,K}}}$ with an analogue to Eq. 5.1 (substituting σ with μ_{sat}, Fig. 5.9e). Consistent with expectations we find higher characteristic barrier energies for the (6,5) compared to the RN networks ($E_{\mathrm{B},\,(6,5)}(E_{\mathrm{F}}) > E_{\mathrm{B,\,RN}}(E_{\mathrm{F}})$, Fig. 5.9e). The characteristic energy of significant voltage fluctuations is larger for the RN networks ($E_{0,\,\mathrm{RN}}(E_{\mathrm{F}}) > E_{0,\,(6,5)}(E_{\mathrm{F}})$, Fig. 5.9e). This may reflect a smaller carrier effective mass and larger junction capacitance induced by the larger diameter of the RN tubes. Our experimental findings also confirm the expected slightly weaker charge density and Fermi-level dependence of $E_{\mathrm{B}}(E_{\mathrm{F}})$ of the (6,5) networks due to its narrower

DoS (Fig. 5.9e). We note that our assumption of a weakly temperature-dependent Fermi-level for the extraction of the characteristic energies can be justified by the observation of a temperature-independent Seebeck coefficient of the two networks within the temperature range of 150 K to 300 K and a weak temperature dependence below 150 K (within the measurement error of 5-10 %) due to the sharp DoS distribution of the networks (see following section).

5.5 Temperature-dependent thermoelectric transport in SWCNT networks

Based on the established independence of the Seebeck coefficient on network density and small SWCNT tube length variations in the high network density regime (approx. $> 13\ \mu m^{-1}$) as well as its electron-hole symmetry (Fig. 5.6c, d), we focus our temperature-dependent thermoelectric transport analysis on the absolute electron Seebeck coefficient ($|S_e|$) of the representative (6,5)-s-ttmgb and RN-d-st networks (Fig. 5.11). The full temperature dependence of the hole and absolute electron Seebeck coefficient (S_h and $|S_e|$) of all six network conditions (Table 5.2) is presented in Figure 5.12. The error analysis was performed as previously reported[172] and the measurement errors were approximately 5-10 % (except 10-20 % for the (6,5)-s device). The Seebeck coefficients of the (6,5)-s-ttmgb and dense RN networks are temperature-independent between 150 K and 300 K but show an increasing temperature dependence for lower temperatures (within the measurement error of 5-10 %, Fig. 5.11b, d). The Seebeck coefficients of all untreated (6,5) SWCNT networks and the sparse RN networks show a stronger and more gradual temperature dependence as well as a stronger charge density dependence due to higher trap densities and the resulting Fermi-level pinning (Figs. 5.6c, 5.11b, d and 5.12).[172]

We find that thermoelectric transport in semiconducting SWCNT networks can be modelled within the notions of transport in heterogeneous media and Boltzmann transport formalism.[198,245] The relative orientation of transport path segments (SWCNTs and tunnel barriers) with respect to the temperature gradient has to be considered for the evaluation of the Seebeck coefficient. Kaiser pointed out that the tunnel barriers are likely to impact the thermal transport less than the electrical transport.[198,239] Furthermore, in the percolating dense network density regime considered here, most tunnel barriers will be orthogonal to the temperature gradient and hence their contribution to the Seebeck coefficient is negligible. Therefore, the Seebeck coefficient of the SWCNT networks (S)

can be approximated as:

$$S = \frac{\Delta T_{\mathrm{SWCNTs}}}{\Delta T} \cdot S_{\mathrm{SWCNTs}} + \frac{\Delta T_{\mathrm{B}}}{\Delta T} \cdot S_{\mathrm{B}} \approx S_{\mathrm{SWCNTs}}, \tag{5.2}$$

with $\Delta T_{\mathrm{SWCNT}}$ and S_{SWCNTs} being the temperature drop across the SWCNTs and their Seebeck coefficient, while ΔT_{B} and S_{B} are the temperature drop across the tunnel barriers and their Seebeck coefficient, respectively.

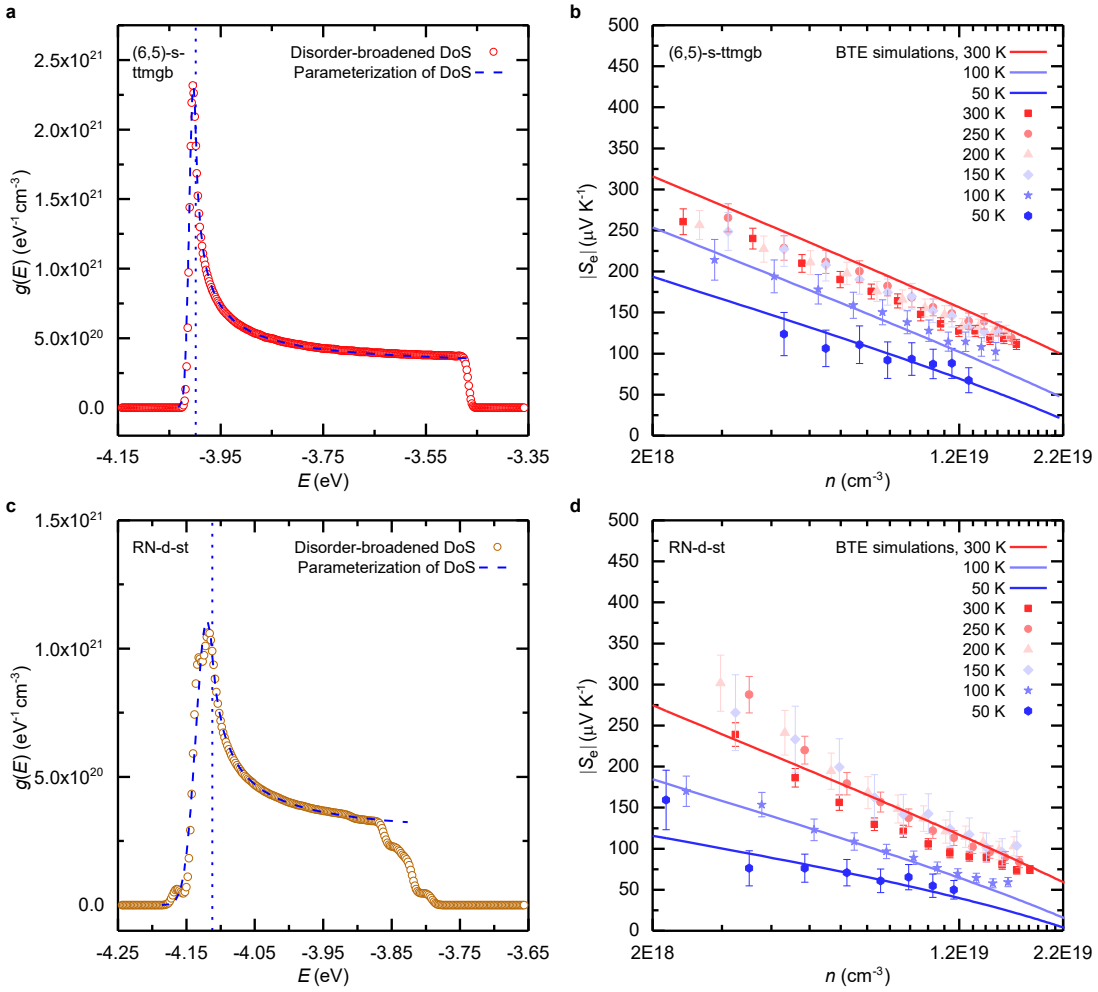

Figure 5.11. Temperature-dependent thermoelectric transport in SWCNT networks. The dipolar disorder-broadened ($\delta_{\mathrm{dipole}} = 5$ meV) DoS of the (6,5) (a) and RN (c) networks from tight-binding nearest-neighbour calculations including trigonal warping effects,[84,85] scaled according to the network density and length distribution (Table 5.1) as well as the charge density and temperature-dependent absolute electron Seebeck coefficient ($|S_{\mathrm{e}}|$) of the (6,5)-s-ttmgb (b) and RN-d-st (d) networks are shown. The blue dashed lines in panel (a) and (c) are the DoS parameterizations (Table 5.3) used for the BTE simulations of the Seebeck coefficients in panel (b) and (d). The vertical dotted blue lines in panel (a) and (c) indicate the transition energies from the disorder-based to the SWCNT-based parameterization. The relative error in the Seebeck coefficient is $5-10$ % (error analysis performed according to ref. [172]).

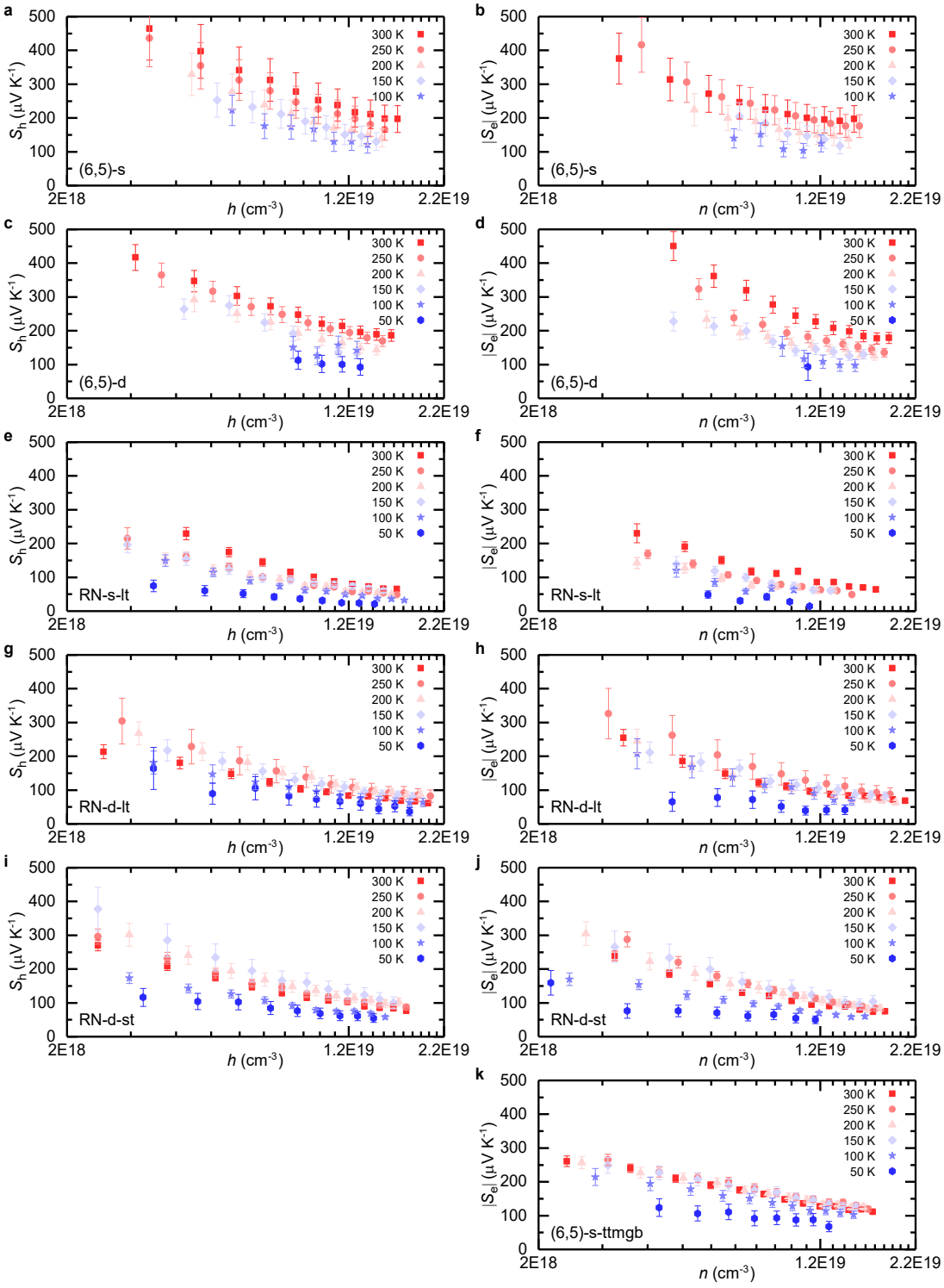

Figure 5.12. Temperature- and charge density-dependent hole and absolute electron Seebeck coefficient (S_h and $|S_e|$) of all six network conditions (Table 5.2).

For the DoS of the SWCNT network ($g(E)$) we consider the convolution of the superposition of the DoS of the individual chiralities of the network ($g_{\mathrm{c},\,i}(E)$), weighted according to their relative fraction in the network (w_i) and scaled according to the network density and length distribution (Table 5.1), with a normalized Gaussian dipolar disorder distribution ($g_{\mathrm{dipole}}(E) = \exp(-\frac{E^2}{2\cdot\delta^2_{\mathrm{dipole}}})$). For $g_{\mathrm{c},\,i}(E)$ we consider reported tight-binding nearest-neighbour (TBNN) calculations including trigonal warping effects.[84,85] Given our charge density regime ($n \leq 2.2\cdot10^{19}$ cm^{-3}) and temperature range of 50 K to 300 K (low energies), it is sufficient to consider the first subband of the TBNN DoS of each chirality (further supported by the electrical data in Fig. 5.9a, b). Therefore, the DoS of the SWCNT network can be expressed as:

$$g(E) = N_{\mathrm{SWCNTs}} \cdot \frac{g_{\mathrm{dipole}}(E) \circledast \sum_i w_i \cdot g_{\mathrm{c},\,i}(E)}{\int g_{\mathrm{dipole}}(E) \circledast \sum_i w_i \cdot g_{\mathrm{c},\,i}(E)dE}, \tag{5.3}$$

where $N_{\mathrm{SWCNTs}} = \rho_{\mathrm{SWCNTs}} \cdot \bar{N}_{\mathrm{single,\,SWCNT}}$ is the total first subband DoS of the SWCNTs in the network, $\rho_{\mathrm{SWCNTs}} = \beta \cdot \frac{\pi\cdot\lambda_{\mathrm{th}}}{2\cdot\tilde{l}\cdot\tilde{d}}$ is the volumetric SWCNT density (interrelation assumes uniform random orientation of SWCNTs, see next paragraph),[202] λ_{th} the linear threshold network density for which the Seebeck coefficient becomes approximately independent of network density ($\sim$ 13 µm^{-1}, as established in section 5.3), $\tilde{l}$ and $\tilde{d}$ are the average SWCNT length and diameter of the SWCNTs in the network respectively, β is a constant factor considering bundling of SWCNTs and $\bar{N}_{\mathrm{single,\,SWCNT}} = \int \sum_i w_i \cdot g_{\mathrm{c},\,i}(E)dE$ is the average total DoS per single SWCNT.
For the expression of the volumetric SWCNT density (ρ_{SWCNT}) in Eq. 5.3, we assume a uniform random orientation of SWCNTs. As previously employed,[202] under this assumption the areal network density ($\sigma_{\mathrm{d,\,SWCNT}}$) can be obtained as the ratio of the linear network density (λ) to the average length of SWCNTs in x-direction ($\tilde{l_{\mathrm{x}}}$, respectively y-direction, for randomly oriented SWCNTs). Consequently, the following relationship, which we have confirmed by random network simulations, is obtained for randomly oriented SWCNT networks:

$$\sigma_{\mathrm{d,\,SWCNT}} = \frac{\lambda}{\tilde{l_{\mathrm{x}}}} = \frac{\lambda}{\tilde{l}} \cdot \frac{1}{\frac{1}{\frac{\pi}{2}}\int_0^{\frac{\pi}{2}}\cos(x)dx} = \frac{\pi\cdot\lambda}{2\cdot\tilde{l}}, \tag{5.4}$$

with $\tilde{l}$ being the average length of SWCNTs in the network. Considering the effect of bundling, we therefore obtain the employed expression for the volumetric SWCNT density in the high network density regime relevant for the BTE simulations of the Seebeck coefficient ($\rho_{\mathrm{SWCNTs}} = \beta \cdot \frac{\sigma_{\mathrm{d,\,SWCNT}}}{\tilde{d}} = \beta \cdot \frac{\pi\cdot\lambda_{\mathrm{th}}}{2\cdot\tilde{l}\cdot\tilde{d}}$).
As outlined in section 2.3.1, within the independent electron and relaxation time

approximation the Seebeck coefficient can be derived from Boltzmann transport equation (BTE) and expressed as:[216,217,245]

$$S = -\frac{\langle E - E_\mathrm{F} \rangle_\sigma}{eT} = -\frac{1}{eT}\left[\frac{\int (E - E_\mathrm{F})\sigma(E)dE}{\int \sigma(E)dE}\right], \tag{5.5}$$

where $\sigma(E)$ is the energy-dependent conductivity function in the expression for the conductivity:

$$\begin{aligned} \sigma &= \int \sigma(E)dE = \int \sigma'(E)\left(-\frac{\partial f(E)}{\partial E}\right)dE \\ &= \int e^2 \upsilon(E)\tau(E)\upsilon(E)g(E)\left(-\frac{\partial f(E)}{\partial E}\right)dE, \end{aligned} \tag{5.6}$$

with $f(E)$ representing the Fermi-Dirac distribution function, $g(E)$ the DoS, $\upsilon(E)$ the carrier velocity and $\tau(E)$ the carrier relaxation time. As outlined in sections 2.3.1 and 4.2, Eq. 5.5 emphasizes the physical meaning of the Seebeck coefficient as the entropy transported by a carrier divided by its charge and illustrates that each charge carrier contributes to the transported energy according to its excess energy with respect to the Fermi-level ($E - E_\mathrm{F}$), weighted by the relative contribution of the conduction channel $\frac{\sigma(E)}{\sigma}$ to the total conductivity.[172,217] With the same reasoning as for the DoS we can express the conductivity function without the occupancy factors of the SWCNT network ($\sigma'(E)$) as

$$\sigma'(E) = g_\mathrm{dipole}(E) \circledast \sum_i w_i \cdot \sigma'_{\mathrm{c},\,i}(E), \tag{5.7}$$

with $\sigma'_{\mathrm{c},\,i}(E) = \upsilon_{\mathrm{c},\,i}(E)^2 \tau_{\mathrm{c},\,i}(E) g_{\mathrm{c},\,i}(E)$. The carrier velocity within each SWCNT is determined by its dispersion relation $\upsilon_{\mathrm{c},\,i}(E) = \frac{1}{\hbar}\left(\frac{\partial E}{\partial k}\right) \propto g_{\mathrm{c},\,i}(E)^{-1}$.[79] For the carrier relaxation time we investigate one-dimensional acoustic and optical phonon scattering $\tau_{\mathrm{c},\,i}(E) \propto g_{\mathrm{c},\,i}(E)^{-1}$ which is dominant in single SWCNTs as well as a more general power law relationship $\tau_{\mathrm{c},\,i}(E) \propto (E - E_{\mathrm{C},\,i})^s$, with $E_{\mathrm{C},\,i}$ being the first van Hove singularity of the i-th chirality in the network and s the scattering parameter characterizing the type of scattering.[183,221,278,279]

In order to simulate the Seebeck coefficient of the SWCNT networks using BTE, we parameterize both the TBNN DoS (Eq. 5.3) shown in Fig. 5.11a, c for the (6,5) and RN networks as well as the conductivity function without occupancy factors ($\sigma'(E)$, next paragraph). The absolute energy scale in Fig. 5.11a, c is based on the TBNN calculations as well as the redox potentials of the SWCNTs ($E_{\mathrm{F}_0,\,(6,5)} = -4.55$ eV for the (6,5) networks and we assume $E_{\mathrm{F}_0,\,\mathrm{RN}} \approx -4.45$ eV for all chiralities in the RN network).[94,286] For the RN network DoS we estimate a plausible chirality assignment

based on an analysis of the absorption peaks in the E_{22} region (Fig. 5.13, $w_{(17,3)} = 0.04$, $w_{(16,2)} = 0.28$, $w_{(10,9)} = 0.2$, $w_{(12,7)} = 0.12$, $w_{(13,5)} = 0.22$, $w_{(10,8)} = 0.14$). Each E_{22}

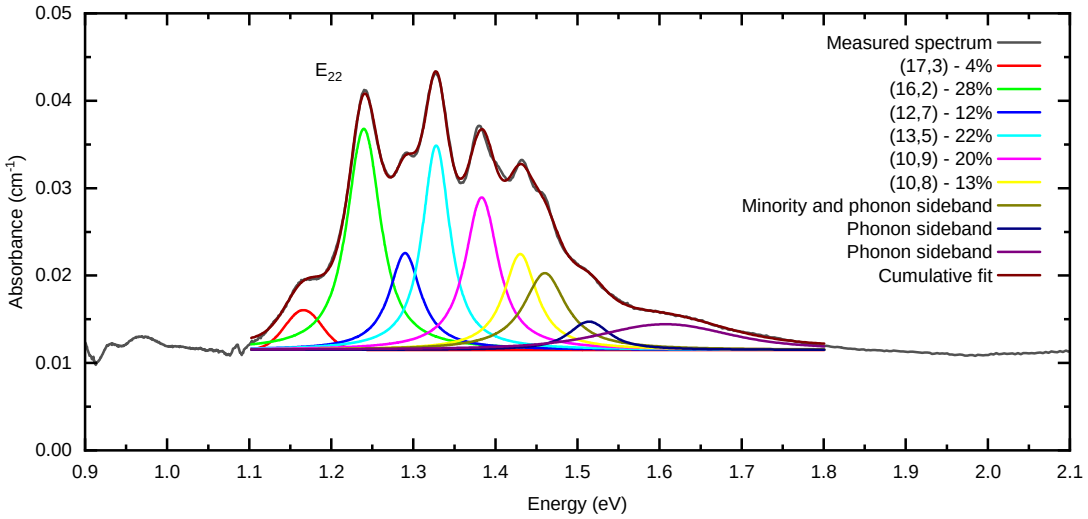

Figure 5.13. Estimation of RN network composition. The absorption spectrum of the RN networks in the E_{22} region is shown. In order to estimate the network composition each E_{22} absorption band was fitted with a Voigt function and the blue-shifted phonon sidebands were collectively fitted using three separate Voigt functions. The measurements have been performed by Severin Schneider and Felix Berger.

absorption band was fitted with a Voigt function and the blue-shifted phonon sidebands were collectively fitted using three separate Voigt functions.[94] For the BTE simulations the fraction (integral of the E_{22} absorption band of a specific chirality divided by the integral of the network E_{22} absorption band excluding phonon side bands) of the (10,8) tubes has been rounded to 14 %. The network DoS is parameterized (Fig. 5.11a, c) with a disorder-dominated DoS for low energies ($E < E_{\mathrm{trans}}$, E_{trans} being the transition energy, Fig. 5.11a, c)

$$g_{\mathrm{LE}}(E) = \frac{N_{\mathrm{C}}}{\sqrt{2\pi}\delta_{\mathrm{C}}} \cdot \exp\left(-\frac{(E - E_{\mathrm{C}})^2}{2\delta_{\mathrm{C}}^2}\right), \tag{5.8}$$

with N_{C} being the total DoS, δ_{C} the width and E_{C} the center of the low energy DoS parameterization. For high energies ($E_{\mathrm{trans}} < E < E_{\mathrm{co}}$, with E_{co} being the cut-off energy of the parameterization) the network DoS is parameterized with a one-dimensional SWCNT DoS

$$g_{\mathrm{HE}}(E) = N_{\mathrm{HE}} \cdot \frac{\left|E + \left|E_{\mathrm{F}_0}\right|\right|}{\sqrt{\left(\left|E + \left|E_{\mathrm{F}_0}\right|\right|\right)^2 - \left(\left|E_{\mathrm{C,\,HE}} + \left|E_{\mathrm{F}_0}\right|\right|\right)^2}}, \tag{5.9}$$

with N_{HE} characterizing the magnitude of the DoS and $E_{\mathrm{C,\,HE}}$ the energy of the first van Hove singularity of the high energy DoS parameterization. The parameters used for the parameterization of the TBNN network DoS that is employed for the Seebeck coefficient simulations in Fig. 5.11b, d (solid lines) are summarized in Table 5.3. The

Table 5.3. Tight-binding nearest-neighbour DoS parameterization for simulation of Seebeck coefficients in SWCNT networks.

Network	Total DoS of the first subband of the SWCNT network (N_{SWCNTs})	Total DoS of the low energy DoS (N_{C})	Width of the low energy DoS (δ_{C})	Center of the low energy DoS (E_{C})	Transition energy (E_{trans})	Magnitude of the high energy DoS (N_{HE})	First van Hove singularity of the high energy DoS (E_{HE})	Cut-off energy (E_{co})
(6,5)-s-ttmgb (Fig. 5.11a)	$2.94 \cdot 10^{20}$ cm^{-3}	$4.66 \cdot 10^{19}$ cm^{-3}	8.1 meV	−4.003 eV	−3.998 eV	$3.080 \cdot 10^{20}$ cm^{-3}eV^{-1}	−4.005 eV	−3.467 eV
RN-d-st (Fig. 5.11c)	$1.50 \cdot 10^{20}$ cm^{-3}	$4.49 \cdot 10^{19}$ cm^{-3}	16.2 meV	−4.120 eV	−4.112 eV	$2.760 \cdot 10^{20}$ cm^{-3}eV^{-1}	−4.126 eV	−3.826 eV

only parameters in the BTE simulations of the Seebeck coefficients of the (6,5)-s-ttmgb and RN-d-st networks (Fig. 5.11b, d) that are not a direct consequence of the network parameters and the TBNN DoS of the SWCNTs, are the width of the disorder distribution ($\delta_{\mathrm{dipole}} = 5$ meV) and the scattering parameter $s = -1$, which are identical for the two networks, as well as the bundling factor β that accounts for bundling of SWCNTs in the network ($\beta_{(6,5)} \approx 2.9$ and $\beta_{\mathrm{RN}} \approx 4.3$).

The parameterization of the conductivity function without occupancy factors ($\sigma'(E)$, Eq. 5.7, Fig. 5.14), is performed similarly to the parameterization of the TBNN DoS. For low energies ($E < E_{\mathrm{trans}}$, E_{trans} being the transition energy, identical to the DoS parameterization) a disorder-dominated function is used

$$\sigma'_{\mathrm{LE}}(E) = \frac{\sigma_{\mathrm{C}}}{\sqrt{2\pi}\delta_{\mathrm{LE}}} \cdot \exp\left(-\frac{(E - E_{\mathrm{C}})^2}{2\delta_{\mathrm{LE}}^2}\right), \tag{5.10}$$

with σ_{C} characterizing the magnitude, δ_{LE} the width and E_{C} (being the same as for the DoS parameterization) the center of the low energy parameterization. For the high energy parameterization we consider that the carrier velocity within each SWCNT is determined by its dispersion relation $v_{\mathrm{c},\,i}(E) = \frac{1}{\hbar}\left(\frac{\partial E}{\partial k}\right) \propto g_{\mathrm{c},\,i}(E)^{-1}$ (and hence $v_{\mathrm{c},\,i}(E) \propto \left[1 - (\frac{E_{\mathrm{C},\,i}}{E})^2\right]^{\frac{1}{2}}$, with $E_{\mathrm{C},\,i}$ being the first van Hove singularity of the i-th chirality in the network).[79] Furthermore, for the carrier relaxation time we already

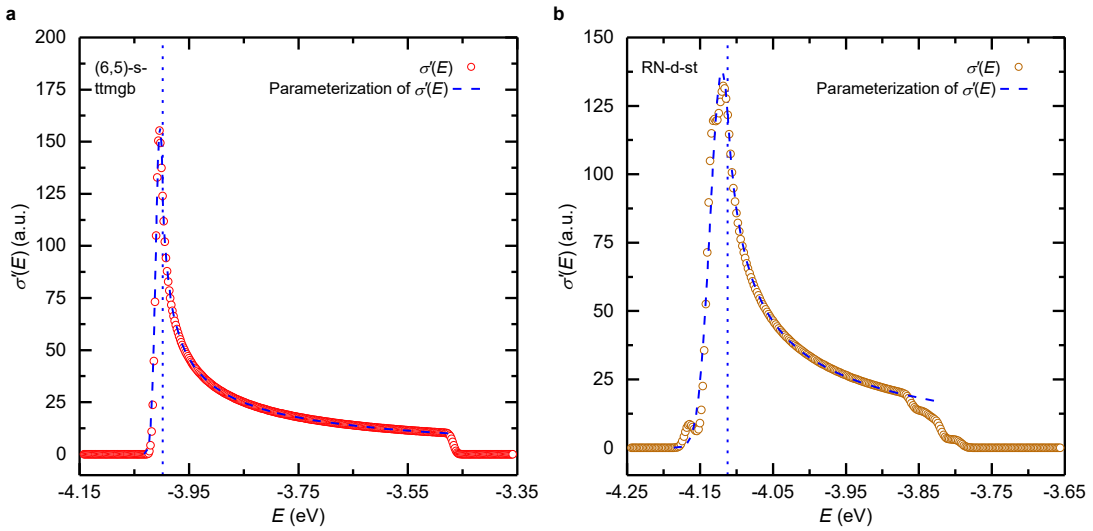

Figure 5.14. Conductivity function without occupancy factors used for BTE simulations of the Seebeck coefficient presented in Fig. 5.11. The conductivity function without occupancy factors ($\sigma'(E)$) as well as its parameterization (dashed blue lines, parameters shown in Table 5.4) for the (6,5) sparse ttmgb-treated ((6,5)-s-ttmgb, (a)) and short-tube RN dense (RN-d-st, (b)) networks used for the BTE simulations of the Seebeck coefficients presented in Fig. 5.11b, d are shown. The blue dotted lines indicate the transition energies from the low energy disorder-dominated parameterization to the high energy parameterization.

emphasized that we investigate both one-dimensional acoustic and optical phonon scattering as well as the more general power law relationship $\tau_{\mathrm{c},\,i}(E) \propto (E - E_{\mathrm{C},\,i})^s$. We first refer to the BTE simulations of the absolute electron Seebeck coefficients of the (6,5) and RN networks in Fig. 5.11b, d, that provide a good fit to our data and for which we need to consider s to be approximately -1 (and $\delta_{\mathrm{dipole}} = 5$ meV). The conductivity function without occupancy factors for each chirality then shows the proportionality $\sigma'_{\mathrm{c},\,i}(E) = \upsilon_{\mathrm{c},\,i}(E)^2 \tau_{\mathrm{c},\,i}(E) g_{\mathrm{c},\,i}(E) \propto \left[1 - (\frac{E_{\mathrm{C},\,i}}{E})^2\right]^{\frac{1}{2}} \cdot (E - E_{\mathrm{C},\,i})^{-1}$. Therefore, for high energies ($E_{\mathrm{trans}} < E < E_{\mathrm{co}}$, with E_{co} being the cut-off energy of the parameterization and the same as for the DoS parameterization) the network conductivity function without occupancy factors is parameterized by

$$\sigma'_{\mathrm{HE}}(E) = \sigma_{\mathrm{HE},\,0} \cdot \left[1 - \left(\frac{E_{\mathrm{C,\,HE}} + |E_{\mathrm{F}_0}|}{E + |E_{\mathrm{F}_0}|}\right)^2\right]^{\frac{1}{2}} \cdot (E - E_{\mathrm{C,\,HE}})^{-1}, \tag{5.11}$$

with $\sigma_{\mathrm{HE},\,0}$ characterizing the magnitude of network conductivity function without occupancy factors, $E_{\mathrm{C,\,HE}}$ the energy of the first van Hove singularity of the high energy parameterization and E_{F_0} the redox potential of the SWCNTs (as for the DoS parameterization).[94,286] The parameters used for the parameterization of the network

conductivity function without occupancy factors ($\sigma'(E)$) that is employed for the Seebeck coefficient simulations in Fig. 5.11b, d are summarized in Table 5.4. Both $\sigma'(E)$ and

Table 5.4. Parameterization of conductivity function without occupancy factors for simulation of Seebeck coefficients in SWCNT networks.

Network	Magnitude of low energy conductivity function (σ_{C})	Width of low energy conductivity function (δ_{LE})	Center of low energy conductivity function (E_{C})	Transition energy (E_{trans})	Magnitude of high energy conductivity function ($\sigma_{\mathrm{HE},\,0}$)	First van Hove singularity of high energy conductivity function ($E_{\mathrm{C,\,HE}}$)	Cut-off energy (E_{co})
(6,5)-s-ttmgb	3.08 (a.u.)	7.8 meV	−4.003 eV	−3.998 eV	6.172 (a.u.)	−4.007 eV	−3.467 eV
RN-d-st	5.54 (a.u.)	16.1 meV	−4.120 eV	−4.112 eV	5.997 (a.u.)	−4.126 eV	−3.826 eV

its parameterization for the electron Seebeck coefficient simulations of the (6,5)-s-ttmgb and RN-d-st networks in Fig. 5.11b, d are shown in Fig. 5.14.

We now show that one-dimensional acoustic and optical phonon scattering with $\tau_{\mathrm{c},\,i}(E) \propto g_{\mathrm{c},\,i}(E)^{-1} \propto \left[1-(\frac{E_{\mathrm{C},\,i}}{E})^2\right]^{\frac{1}{2}}$ cannot explain the charge density and temperature dependence of the Seebeck coefficient of the SWCNT networks. As presented in Fig. 5.15 for the (6,5)-s-ttmgb networks (for both no dipolar disorder and $\delta_{\mathrm{dipole}} = 8$ meV), this form of scattering would give too much weight to the high energy conduction channels, resulting in a strongly temperature-dependent thermally accessible DoS which would lead to a much stronger temperature dependence of the Seebeck coefficient between 100 K and 300 K than observed experimentally.

Our BTE simulations based on the dipolar disorder-broadened TBNN DoS allow insights into the microscopic transport mechanisms as well as the origins of the charge density and temperature dependence of the Seebeck coefficients of the SWCNT networks. The magnitude of the Seebeck coefficient primarily depends on the magnitude and sharpness of the DoS within the energy window $f(E)\cdot[1-f(E)]$ which determines the states participating in transport. Since the (6,5) SWCNTs have more states in the vicinity of the first van Hove singularity than the large diameter SWCNTs present in the RN networks, the low energy DoS of the (6,5) networks, which dominates transport in our charge density regime, is higher than that of the RN networks ($N_{\mathrm{C},\,(6,5)} > N_{\mathrm{C,\,RN}}$, see Table 5.3). The latter is the dominant factor for the observed higher Seebeck coefficients of the (6,5) compared to the RN networks (Fig. 5.11b, d). As expected from the mono-chirality of the (6,5) network and in agreement with our PDS measurements ($E_{\mathrm{u},\,(6,5)} \approx 30 \pm 3$ meV and $E_{\mathrm{u,\,RN}} \approx 47 \pm 5$ meV), the low energy (6,5)

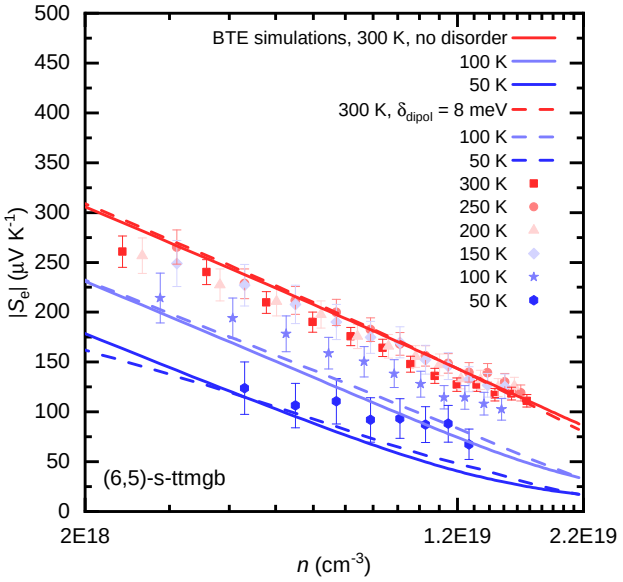

Figure 5.15. BTE simulations of Seebeck coefficient considering one-dimensional acoustic and optical phonon scattering. The charge density and temperature-dependent absolute electron Seebeck coefficient of the (6,5)-s-ttmgb network is shown. From the BTE simulations of the Seebeck coefficient it is evident that one-dimensional acoustic and optical phonon scattering (solid lines for no dipolar disorder and dashed lines for $\delta_{\mathrm{dipole}} = 8$ meV) cannot explain the experimentally observed temperature dependence of the Seebeck coefficient.

DoS is effectively much sharper than that of the RN networks ($\delta_{\mathrm{C},(6,5)} \approx 8.1$ meV versus $\delta_{\mathrm{C,RN}} \approx 16.2$ meV). This in turn leads to the weaker temperature dependence of the Seebeck coefficient of the (6,5) compared to the RN networks (Fig. 5.11b, d). In addition, the sharper DoS in combination with the energy dependence of the relaxation time ($\tau_{\mathrm{c},i}(E) \propto (E - E_{\mathrm{C},i})^s$), $s = -1$, leads to a stronger charge density dependence of the Seebeck coefficient in the (6,5) networks at lower temperatures, because the dominant transport energies are pinned energetically closer to the van Hove singularity (Fig. 5.11b, d). The energy dependence of the relaxation time with $s = -1$ is different from that of individual SWCNTs. This is likely to reflect energy-dependent relaxation processes associated with the tube junctions or it might be a manifestation that the effective dimensionality of the SWCNT networks is not one-, but two-dimensional. We note that the energy dependence of the relaxation time due to acoustic phonon scattering in graphene is also characterized by $s = -1$.[287,288] This observation may warrant a detailed theoretical study that takes into account an appropriate deformation potential and scattering at the SWCNT junctions.

5.6 Implications for SWCNT network FETs and thermoelectrics

Based on our electrical transport data (Fig. 5.9 and inset of Fig. 5.16), two important, general guidelines for SWCNT network FETs are evident in our measurements. Firstly,

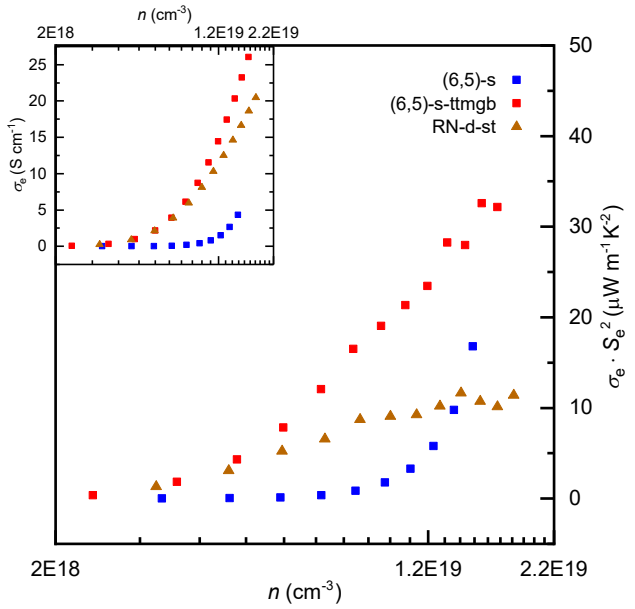

Figure 5.16. Thermoelectric performance at 300 K. The charge density-dependent electron power factors ($\sigma_e \cdot S_e^2$) and conductivities (inset) of the (6,5)-s, (6,5)-s-ttmgb and RN-d-st networks are shown. The monochiral (6,5)-s-ttmgb networks strongly outperform the broad diameter distribution RN networks due to their higher Seebeck coefficients (Fig. 5.6c, d), emphasizing both the importance of trap state minimization as well as chirality selection to narrow and increase the thermally accessible DoS.

even SWCNT networks with ambipolar transport character and moderate hysteresis can still exhibit significant amount of trap states ((6,5) networks, Fig. 5.6a). Minimizing this trap state density by treatments such as the ttmgb-treatment used here is essential for further performance optimization of FETs based on SWCNT networks.[277] Secondly, large diameter (1.2-1.6 nm) SWCNT networks show higher carrier mobilites at comparable trap densities probably due to lower tunnel barriers. Chirality selection towards monochiral networks enables enhanced mobilities due to reduced energetic disorder via a narrower thermally accessible DoS.[194,204] The upper diameter limit is given by the on/off current ratio requirements of the electronic application. Consequently, we suggest trap density-minimized monochiral SWCNTs of large diameter in the range of 1.2-1.6 nm, such as the recently demonstrated (14,6) networks, for high on/off current

ratio, high-mobility SWCNT network FETs.[204,289]

As introduced in section 1.1, the conversion efficiency of waste heat to electricity by thermoelectric materials is governed by the figure of merit $zT = \frac{PF}{\kappa} \cdot T = \frac{\sigma \cdot S^2}{\kappa} \cdot T$, with the power factor $PF = \sigma \cdot S^2$, σ the electrical conductivity, S the Seebeck coefficient and κ the thermal conductivity.[25] Furthermore, it has been emphasized that highly doped SWCNT networks have displayed ambipolar power factors in excess of 500 $\frac{\mu W}{m \cdot K^2}$ and are therefore promising candidates for next generation flexible thermoelectric generators (see section 1.1 for further details).[46] For further improvements in device performance the optimal chirality distribution of the SWCNT networks needs to be established.[24,47] We therefore present the charge density-dependent electron power factors ($\sigma_e \cdot S_e^2$) of the (6,5)-s, (6,5)-s-ttmgb and RN-d-st networks at 300 K in Fig. 5.16. Despite the significantly lower conductivities of the (6,5) networks (inset of Fig. 5.16), the power factors of the (6,5) networks exceed those of the RN networks, particularly for high charge densities relevant for applications. The power factors of the trap-free ttmgb-treated (6,5) networks exceed those of the RN networks for almost all investigated charge densities. As revealed by our BTE simulations, this is caused by the higher Seebeck coefficients primarily due to the larger DoS of the (6,5) SWCNTs in the vicinity of the first van Hove singularity ($N_{C,(6,5)} > N_{C,RN}$, see Table 5.3). For practical applications the charge density needs to be tuned to higher levels on the order of several times 10^{20} cm^{-3}, allowing the Fermi-level to be in the vicinity of the second van Hove singularity.[46,47,137] This will be the optimal Fermi-level position, as it allows for both high conductivities (due to the high charge densities) as well as a large thermally accessible DoS within the transport window $f(E) \cdot [1 - f(E)]$ leading to high Seebeck coefficients. In terms of the Seebeck coefficient multiple chiralities in the network are acceptable if the effective width of the network DoS around the second van Hove singularities is still narrower than the transport window ($\sim 4\, k_B T$), as it would allow for a comparable thermally accessible DoS (with only slightly reduced Seebeck coefficient due to the Fermi-level being closer to the van Hove singularity). Nevertheless, given that the conductivities of monochiral networks are expected to be higher, as well as the fact that molecular doping introduces additional energetic disorder, monochiral networks are still preferable. Our simulations also indicate that the effect of smaller diameter tubes having a larger thermally accessible DoS in the vicinity of the van Hove singularities will still prevail, meaning that the optimal diameter for SWCNT network based thermoelectric devices will likely be smaller than that for FETs, where the reduced Seebeck coefficient of larger diameter tubes is no constraint. The precise optimal diameter can only be predicted once more data on trap-free monochiral networks is available. Therefore, in order

to benefit from both lower tunnel barriers and higher conductivities, as well as high Seebeck coefficients, we propose to investigate a series of moderately large (1.0-1.4 nm) monochiral networks, such as the recently demonstrated (14,6) networks.[289]

5.7 Conclusions

In summary, we have shown that charge and thermoelectric transport in polymer-sorted SWCNT networks with selected diameters and different network densities as well as length distributions, can be modelled by the Boltzmann transport formalism, incorporating transport in heterogeneous media and fluctuation-induced tunneling. We directly relate the charge density and temperature dependence of the Seebeck coefficient in these networks to their dipolar disorder-broadened and network parameter-scaled TBNN DoS. Furthermore, our BTE simulations of the Seebeck coefficients point towards a more two-dimensional character of carrier scattering and the necessity to consider scattering at SWCNT junctions as the relaxation time is found to be anti-proportional to the energy in these SWCNT networks, as opposed to simple one-dimensional acoustic and optical phonon scattering found in single SWCNTs. Based on our fundamental insights on charge and thermoelectric transport, we propose narrow DoS distribution (ideally monochiral), large diameter SWCNT networks, that enable a large thermally accessible DoS leading to high Seebeck coefficients as well as low tunnel barriers and high conductivities for both electronic and thermoelectric applications. While for electronic applications the on/off current ratio poses an upper limit for the SWCNT diameter (1.2-1.6 nm), the additional requirement of high Seebeck coefficients in thermoelectric devices is likely to be a stronger constraint on the SWCNT diameter (1.0-1.4 nm).

Chapter 6

Charge and thermoelectric transport in molecularly doped, aligned conducting polymers

The optical characterization as well as the fabrication of the thermoelectric devices presented in this chapter was performed by Yuxuan Huang and Dr. Ian Jacobs, PhD student and postdoctoral researcher in Prof. Henning Sirringhaus's group respectively. The presented grazing incidence wide-angle X-ray scattering (GIWAXS) measurements of samples prepared by Yuxuan Huang and Dr. Ian Jacobs, were performed by Dr. Xuechen Jiao and Prof. Chris McNeill from the Monash University in Australia at the Australian Synchrotron.

6.1 Motivation and outline

While the previous two chapters have focused on an improved understanding of charge and thermoelectric transport in semicrystalline conjugated polymers and polymer-sorted SWCNT networks via charge density and temperature-dependent field-effect mobility and gated Seebeck coefficient measurements, this chapter is concerned with the study of the impact of polymer-chain alignment on charge and thermoelectric transport in the molecularly doped semicrystalline polymer PBTTT. Field-effect modulation of the charge density in an FET architecture is particularly useful for minimizing extrinsic contributions to charge and thermoelectric transport, providing an excellent platform for an understanding of intrinsic transport at moderate charge densities for further advances of electronic applications. However, charge densities are typically limited to a range of approximately $10^{18} - 10^{19}$ cm^{-3}, rendering a direct relation to the transport regime relevant for conjugated polymer and SWCNT network-based thermoelectric device applications with charge densities on the order of $10^{20} - 10^{21}$ cm^{-3} difficult.[23,24]

Considering the low thermal conductivities on the order of 0.2 W m^{-1} K^{-1} in van der Waals-bonded conjugated polymers, optimization of the figure of merit zT (see section 1.1) for their thermoelectric applications typically focuses on the optimization of the power factor ($PF = \sigma \cdot S^2$, σ the electrical conductivity and S the Seebeck coefficient) via tuning the charge density by molecular doping.[23] In the past decade significant advances in controlling and understanding molecular doping of conjugated polymers have been made and attaining charge densities in molecularly doped conjugated polymers in excess of 10^{20} cm^{-3} has become feasible.[290–296] Upon molecular doping, the fundamental processes of ion-pair formation (integer charge transfer) and charge-transfer complex formation via hybridization of the frontier orbitals of the conjugated polymer and small molecule are distinguished. The formation of charge transfer complexes has been found to be detrimental to the doping efficiency, due to higher ionization energies required to create free charge carriers.[291] In contrast to the more conventional solution-mixing doping routine (pre-deposition mixing of conjugated polymer and doping solutions), sequential doping processes with the preparation of the active conjugated polymer layer and subsequent doping from the solution or vapour phase have recently been found to be more efficient.[41,292,293] Particularly high electrical conductivities on the order of $200 - 700$ S cm^{-1} and power factors around $50 - 120$ μW m^{-1} K^{-2} have been obtained by sequentially doping the semicrystalline polymer PBTTT from the vapour phase (solid state diffusion doping) with the small molecule 2,3,5,6-tetrafluoro-7,7,8,8-tetracyanoquinodimethane (F4TCNQ).[41,293,296] This high performance has been ascribed to the non-destructive nature of the doping process that largely retains the microstructure of the undoped PBTTT films. An increase of the out-of-plane lamellar *d*-spacing from approximately 21.5 Å to 23.4 Å upon doping, combined with a small decrease of the in-plane π-π stacking distance from approximately 3.6 Å to 3.47 Å (for PBTTT-C_{14}) has been interpreted as the incorporation of the F4TCNQ molecules into the free volume of the PBTTT lamellar stacks.[293,296,297] Facilitated by this non-disruptive doping routine, coherent transport phenomena such as a nearly ideal Hall effect as well as a positive magnetoconductance due to weak localization have been observed in molecularly doped PBTTT.[293] More recently, even higher charge densities on the order of 10^{21} cm^{-3} (extracted from Hall effect measurements) have been realized by F4TCNQ and Li-TFSI-based ion-exchange doping, leading to conductivities of around 600 S cm^{-1} as well as the observation of weak localization.[42] Even higher conductivities and power factors have been achieved via additional polymer chain alignment of PBTTT via high-temperature rubbing.[254,298] Recently, conductivities as high as $2 \cdot 10^5$ S cm^{-1} (approaching those of conventional metals) and power factors of 2 mW m^{-1} K^{-2} (exceeding those of

state-of-the-art unaligned, polymer-sorted SWCNT networks by a factor of $2-3$)[46] have been reported for $FeCl_3$-doped, aligned PBTTT-C_{12}.[254] Such high power factors, render molecularly doped, aligned conducting polymers as promising candidates for flexible thermoelectric device applications, provided that the thermal conductivity is not significantly higher than in the undoped state.

In order to further improve the material performance an improved understanding of the charge and thermoelectric transport of these molecularly doped, aligned conducting polymers in this high charge density limit is of paramount importance. However, even the fundamental understanding of transport in unaligned molecularly doped conjugated polymers is still in its infancy. As outlined in section 2.3.2, Glaudell *et al.* have reported an empirical relationship between the Seebeck coefficient and electrical conductivity of molecularly doped polythiophene-based conjugated polymers ($S \sim \sigma^{-\frac{1}{4}}$), while Snyder and coworkers have proposed a phenomenological transport function (Eq. 2.44 in section 2.3.2) and found good agreement with the Seebeck coefficient versus electrical conductivity relationship (see also Eqs. 4.20-4.24 in section 4.5) for several (mostly polythiophene-based) conjugated polymers, when assuming $s = 3$ for the transport parameter, determining the energy dependence of the transport function $\sigma(E)$.[221,229] It remains to be investigated how this transport parameter relates to the microstructure, DoS and transport processes within the conjugated polymers. In addition, further justification needs to be provided for the assumption of a rigid transport function for describing systems in which the conductivity changes over seven orders of magnitude upon molecular doping (spanning non-degenerate as well as highly degenerate regimes),[296,299] while it has been shown that the DoS of the conjugated polymers is modified in the presence of dopants.[228,290,291,299,300] Careful control of the Fermi-level and hence charge density via molecular doping and concomitant measurements of both electrical conductivity and Seebeck coefficient in dependence of charge density and temperature allows a detailed characterization of the energy dependent conductivity. Cohen *et al.* have derived the (macroscopic) conductivity and Seebeck coefficient within the independent electron approximation via the Kubo formalism:[213,218]

$$\sigma = \int \sigma_{\mathrm{E}}(E) \left(-\frac{\partial f}{\partial E}\right) dE, \tag{6.1}$$

$$S = -\frac{k_{\mathrm{B}}}{e} \int \frac{\sigma_{\mathrm{E}}(E)}{\sigma} \frac{E - E_{\mathrm{F}}}{k_{\mathrm{B}}T} \left(-\frac{\partial f}{\partial E}\right) dE, \tag{6.2}$$

with $\sigma_{\mathrm{E}}(E)$ the microscopic conductivity and $f(E)$ the Fermi-Dirac distribution function. Equations 6.1 and 6.2 are structurally similar to those presented by Fritzsche (Eqs. 2.21 and 2.25 in section 2.3) from thermodynamic arguments, however the microscopic

conductivity ($\sigma_{\mathrm{E}}(E)$) as presented by Cohen *et al.* excludes the occupancy factors. From the Kubo formalism Cohen *et al.* derive a relationship between the microscopic conductivity ($\sigma_{\mathrm{E}}(E)$) and the microscopic mobility for electron states of energy E ($\mu_{\mathrm{E}}(E)$, $v(E) = \mu_{\mathrm{E}}(E) \cdot F$, where $v(E)$ is the average velocity induced in electrons at energy E by the electric field F):[218]

$$\frac{d\sigma_{\mathrm{E}}(E)}{dE} = -eg(E)\mu_{\mathrm{E}}(E), \tag{6.3}$$

with $g(E)$ the DoS. The charge density and temperature dependence of conductivity and Seebeck coefficient combined with a detailed structural characterization has therefore the potential to disentangle the contributions of the DoS ($g(E)$) and microscopic mobility ($\mu_{\mathrm{E}}(E)$) and can therefore establish a link between microstructure and transport as well as scattering mechanisms. This disentanglement is further supported by independent measurements of the charge density via electron spin resonance measurements or a Mott-Schottky analysis as well as Hall effect mobility measurements.[296,301–304] Recent attempts to disentangle the contributions to the microscopic conductivity ($\sigma_{\mathrm{E}}(E)$) were based on Eq. 6.3 and have found a good agreement for the Seebeck coefficient versus conductivity relationship of molecularly doped PBTTT when considering the transport function by Snyder and coworkers (Eq. 2.44 in section 2.3.2), with an exponential tail state distribution below and a constant DoS above the transport edge (E_{t}) as well as a microscopic mobility with fully localized carriers below and $\mu_{\mathrm{E}}(E) \sim (E - E_{\mathrm{t}})^2$ above the transport edge.[296] However, according to this model the Fermi-level varies over 640 meV upon doping which is large compared to expected bandwidths in conjugated polymers and further investigation of the changes of the DoS upon molecular doping are necessary.[296,299]

Based on a sequential ion-exchange doping protocol developed in our group (Jacobs *et al.*, manuscript in preparation, see sections 3.1.1 and 3.2.3), an alignment process of PBTTT via high-temperature rubbing (established by Yuxuan Huang, section 3.2.3) and the multifunctional thermoelectric devices (section 3.2.3) and measurement routines (section 3.3.1) established in this thesis, ongoing investigations of the impact of polymer alignment on charge and thermoelectric transport in molecularly doped PBTTT-C_{12} in the high charge density limit are presented.

6.2 Optical and structural characterization

In order to characterize the degree of alignment of the aligned PBTTT-C_{12} films that were obtained via high-temperature rubbing as discussed in section 3.2.3, both polarized UV-Vis absorption spectroscopy as well as grazing incident wide-angle X-ray scattering (GIWAXS) measurements have been employed (experimental details in section 3.4). From the polarized UV-Vis absorption spectra (Fig. 6.1a) the degree of polymer alignment has been quantified via the dichroic ratio $R = \frac{A_{\parallel}}{A_{\perp}}$ (Fig. 6.1b), where $A_{\parallel}$ and $A_{\perp}$ denote the film absorbance for incident light polarized parallel and perpendicular to the rubbing direction respectively. Considering that for polythiophene-based polymers

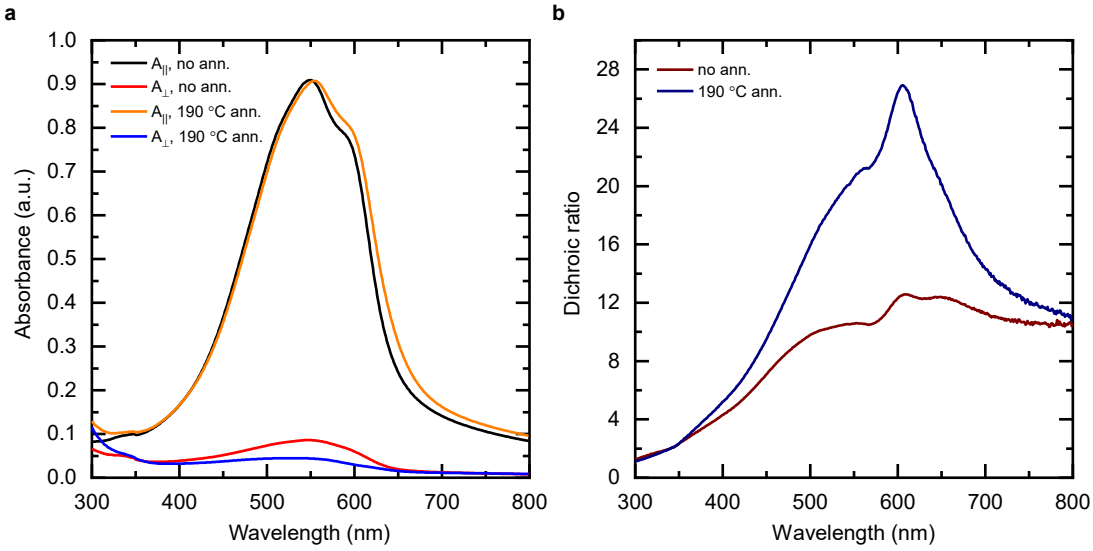

Figure 6.1. Polarized UV-Vis absorption spectra of aligned PBTTT films. The polarized UV-Vis absorption spectra of aligned PBTTT films with (190 °C ann.) and without (no ann.) an annealing step after rubbing with the incident light polarized parallel ($A_{\parallel}$) and perpendicular ($A_{\perp}$) to the rubbing alignment direction (a) as well as the correspondingly extracted dichroic ratios ($R = \frac{A_{\parallel}}{A_{\perp}}$, (b)) are shown. While the films without an annealing step are already highly aligned, recrystallization upon the annealing step leads to an even higher degree of alignment (R up to 26.9). The measurements have been performed by Yuxuan Huang and Dr. Ian Jacobs.

the transition dipole moment of the polymer backbone π-π^* transition, the most prominent absorption feature of PBTTT in Fig. 6.1a, is oriented parallel to the polymer backbone long axis,[64] the dichroic ratio is a good measure for the alignment of polymer chains. The maximum dichroic ratio of the aligned PBTTT-C_{12} films without annealing after rubbing (no ann.) and with a subsequent annealing step at 190 °C for 20 min, as employed for the thermoelectric devices, is $R \approx 12.6$ and $R \approx 26.9$ respectively. While the films without annealing show dichroic ratios on par with recently reported

rubbed and annealed PBTTT-C_{12} films ($R \approx 10$ without and $R \approx 13$ with 200 °C annealing), here the annealed films show substantially higher dichroic ratios.[254,298,305] In order to compare the dichroic ratios with the degree of alignment obtained from GIWAXS measurements, the dichroic ratio is related to the 2D structural order parameter $S = 2\langle\cos^2(\phi)\rangle - 1 = \frac{R-1}{R+1}$, with ϕ the angle between polymer chain segments and the direction of alignment and the brackets indicating the average over all chain segments in the film.[74,306] The structural order parameter from the polarized UV-Vis absorption spectra of the aligned and annealed films is approximately $S \approx 0.93$, indicating the high degree of polymer chain alignment ($S = 1$ for complete uniaxial alignment).

GIWAXS measurements directly probe the structural features within the crystalline fraction of the polymer film.[307] 2D GIWAXS patterns of the unaligned and annealed (180 °C for 20 min) reference film (Fig. 6.2a) as well as the aligned PBTTT films with the incident X-ray beam parallel (without annealing (Fig. 6.2b), with annealing (Fig. 6.2d)) and perpendicular (without annealing (Fig. 6.2c), with annealing (Fig. 6.2e)) to the rubbing direction have been recorded (section 3.4). The corresponding horizontal (in-plane), vertical (out-of-plane) and circularly averaged 1D GIWAXS profiles are shown in Fig. 6.3. The peak assignment has been done as previously reported.[307] The scattering peaks (q_i) and corresponding d-spacings ($d_i = \frac{2\pi}{q_i}$) of the reference film agree well with previously reported values (Table 1 and 2 in ref. [307]). In particular the strongly edge-on configuration of the PBTTT chains is evident from the in-plane (010) π-π stacking peak with an approximate d-spacing of 3.7 Å and the out-of-plane (h00) lamellar stacking peaks.[307] As analysed in more detail below, strong in-plane polymer alignment is evident from the strong in-plane (010) π-π stacking and weak in-plane (003) backbone stacking peaks for the incident X-ray beam parallel to the alignment direction as well as weak (010) and strong (003) in-plane peaks for the beam perpendicular to the rubbing direction (Figs. 6.2b-e and 6.3b-e). Alignment further causes the evolution of a face-on population in addition to the edge-on chains, as indicated by the out-of-plane (010) π-π stacking and in-plane (h00) lamellar stacking peaks in the 2D GIWAXS patterns with an X-ray beam parallel to the alignment direction (Fig. 6.2b, d). Upon annealing the chains become more edge-on oriented, while a fraction of face-on chains still remains and the stacking distances are mostly unchanged, with a small reduction of the lamellar stacking distance from 19.7 Å to 19.2 Å.

The degree of alignment within the crystalline domains was characterized via the intensities of the (003) backbone stacking peaks in the horizontal 1D line scans (blue lines in Fig. 6.3) that were obtained from the 2D GIWAXS patterns (Fig. 6.2) with the incident X-ray beam parallel and perpendicular to the rubbing alignment direction. The

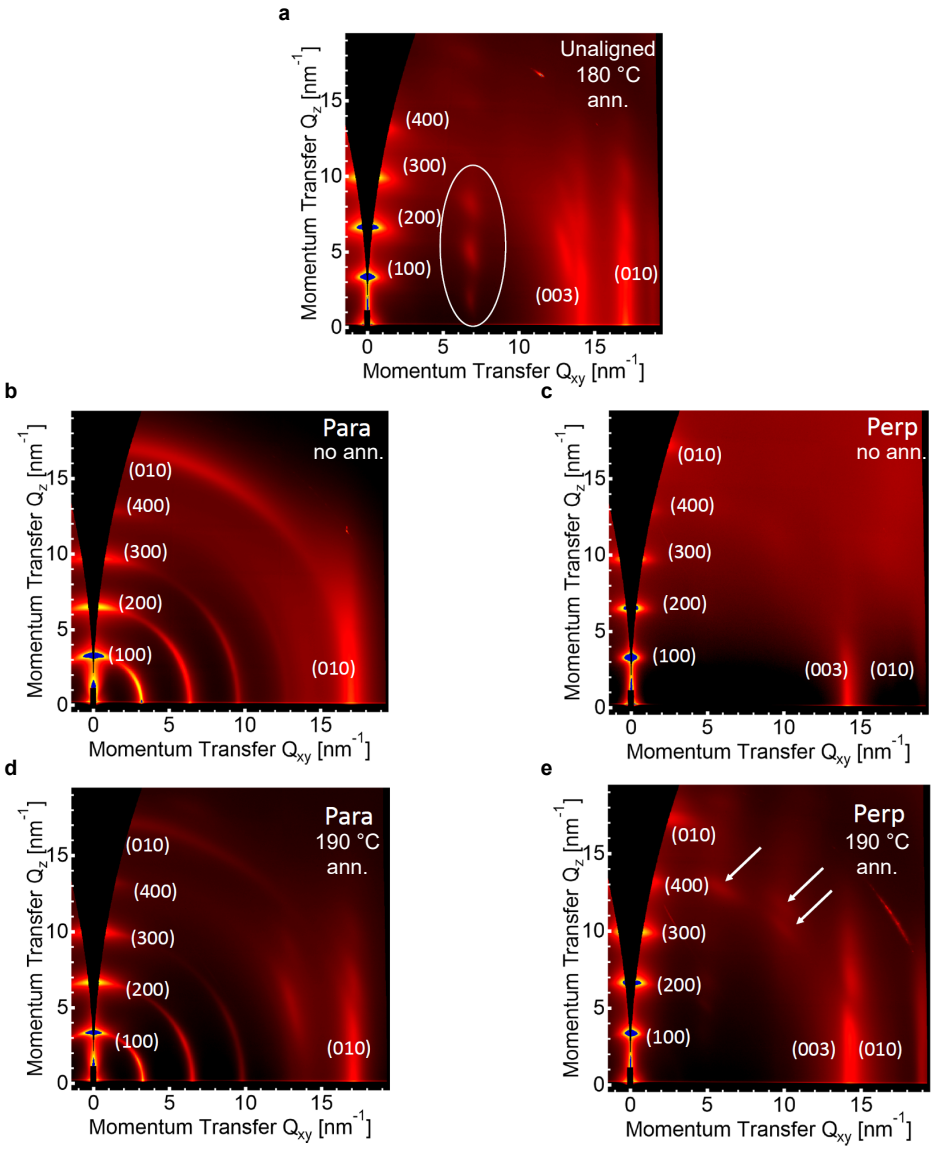

Figure 6.2. 2D grazing incidence wide-angle X-ray scattering patterns of PBTTT films. The 2D GIWAXS patterns of unaligned and annealed (180 °C ann.) PBTTT (a), aligned PBTTT without annealing with the incident X-ray beam oriented parallel (b) and perpendicular (c) to the rubbing direction as well as aligned and subsequently annealed (190 °C ann.) PBTTT with the incident X-ray beam oriented parallel (d) and perpendicular (e) to the rubbing direction are shown. The peak assignments are done as previously reported.[307] Rubbing leads to strong polymer chain alignment as well as a redistribution from pure edge-on (a) to mixed edge-on and face-on stacking (b-e). The annealing step leads to an even higher degree of alignment (see intensity ratio of (003) backbone peak between perpendicular and parallel beam orientation to rubbing direction) as well as more edge-on polymer chain stacking. The white ellipse and arrows indicate features that are only appearing in the specific conditions. The figures have been adapted from Prof. Chris McNeill.

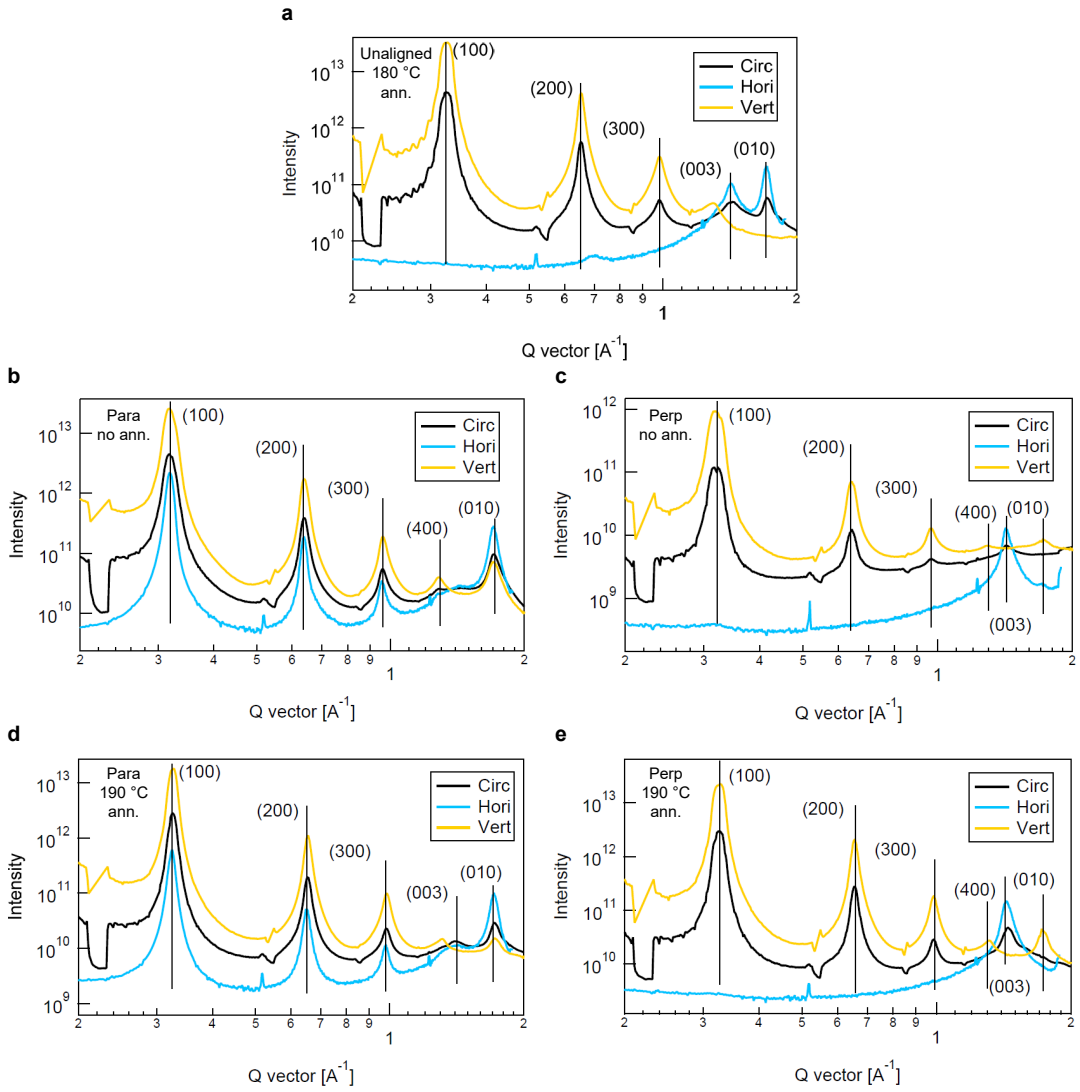

Figure 6.3. 1D GIWAXS profiles of PBTTT films. The 1D GIWAXS profiles of unaligned and annealed (180 °C ann.) PBTTT (a), aligned PBTTT without annealing with the incident X-ray beam oriented parallel (b) and perpendicular (c) to the rubbing direction as well as aligned and subsequently annealed (190 °C ann.) PBTTT with the incident X-ray beam oriented parallel (d) and perpendicular (e) to the rubbing direction along the horizontal axis (Hori, blue lines, in-plane line-cut), the vertical axis (Vert, yellow lines, out-of-plane line-cut) and circularly averaged (Circ, black lines) are shown. The peak assignments are done as previously reported.[307] Rubbing leads to strong polymer chain alignment as well as a redistribution from pure edge-on (a) to mixed edge-on and face-on stacking (b-e). The annealing step leads to an even higher degree of alignment (see intensity ratio of (003) backbone peak between perpendicular and parallel beam orientation to rubbing direction) as well as more edge-on polymer chain stacking. The stacking distances are mostly unchanged, with a small reduction of the lamellar stacking distance from 19.7 Å to 19.2 Å upon annealing. The figures have been adapted from Prof. Chris McNeill.

dichroic ratio $R = \frac{I_{\max}}{I_{\min}}$, where $I_{\max}$ and $I_{\min}$ denote the peak areas of the (003) peaks (corrected for the intensity contributions from other scattering peaks as well as the baseline) for the incident beam perpendicular and parallel to the alignment direction respectively. Based on this analysis the dichroic ratio of the aligned PBTTT films without and with annealing have been estimated to be $R \approx 58$ and $R \approx 85$ respectively. The correspondingly estimated structural order parameter ($S \approx \frac{I_{\max}-I_{\min}}{I_{\max}+I_{\min}}$) for aligned PBTTT without and with annealing is $S \approx 0.97$ and $S \approx 0.98$ respectively. A more accurate and conservative estimation of the structural parameter can be obtained from a parameterization of the intensity distribution of orientations along the alignment direction ($I(\phi)$ of the (003) peak from Fig. 6.2c, e) or ϕ-scans, focusing on a particular scattering peak (e.g. (003)) and subsequently rotating the sample around the surface normal.[74,306] The structural order parameter can then be expressed as:[74,306]

$$S = 2 \cdot \langle \cos^2(\phi) \rangle - 1 = 2 \cdot \frac{\int_0^{\pi} I(\phi) \cos^2(\phi) d\phi}{\int_0^{\pi} I(\phi) d\phi} - 1, \tag{6.4}$$

where $I(\phi)$ denotes the X-ray scattering intensity at a particular ϕ. However, assuming a Gaussian intensity distribution $I(\phi)$ for the scattering profiles of the (003) backbone peaks in Fig. 6.2c, e with a full-width half-maximum of approximately 10° also leads to a structural order parameter of $S \approx 0.97$, rendering the above approximations as good estimates. Evidently, the structural order parameters from the GIWAXS measurements are slightly higher than those from the polarized UV-Vis absorption spectra, considering that the former only probe the crystalline domains while the latter probe both crystalline and amorphous fractions of the aligned PBTTT films.

In conclusion, the optical and structural characterization has revealed very high degrees of alignment of the rubbed and annealed PBTTT films, rendering them as a suitable system to investigate the impact of polymer chain alignment on charge and thermoelectric transport in molecularly doped conjugated polymers.

After the PBTTT film preparation both unaligned as well as aligned films were molecularly doped employing a sequential ion-exchange doping process (similar to ref. [42]) based on $FeCl_3$ (in acetonitrile) as an oxidizing agent and the ionic liquid BMP-TFSI (in acetonitrile) for the ion-exchange process (see section 3.2.3). The details of this ion-exchange doping process will be reported elsewhere (Jacobs *et al.*, manuscript in preparation (2020)). The ion-exchange process allows to increase the doping efficiency of the binary conjugated polymer-molecular dopant system, which is primarily governed by the redox potential between the conjugated polymer and the dopant,[295] e.g. as reported by Yamashita *et al.*:[42]

$$\mathrm{PBTTT} + \mathrm{F4TCNQ} \rightleftharpoons [\mathrm{PBTTT}^{+} + \mathrm{F4TCNQ}^{-}], \tag{6.5}$$

with F4TCNQ as a molecular dopant, with a LUMO energy of approximately −5.24 eV below the HOMO energy of PBTTT (−5.1 eV).[295] The ion exchange of $TFSI^-$ and $F4TCNQ^-$ to lower the free energy of the system (as presented by Yamashita *et al.*), decreases the population $[PBTTT^+ + F4TCNQ^-]$ and therefore promotes the forward reaction in Eq. 6.5, increasing the doping efficiency. Hence, if the ionic liquid ($[X^+Y^-]$) allows an energy lowering upon ion exchange the doping process is essentially a two step process with the oxidation of PBTTT and subsequent ion-exchange, e.g. as demonstrated by Yamashita *et al.*:[42]

$$\begin{aligned} PBTTT + F4TCNQ + X^+ + Y^- &\rightarrow [PBTTT^+ + F4TCNQ^-] + X^+ + Y^-, \\ [PBTTT^+ + F4TCNQ^-] + X^+ + Y^- &\rightarrow [PBTTT^+ + Y^-] + X^+ + F4TCNQ^-. \end{aligned} \tag{6.6}$$

For the purpose of the further discussion of the temperature-dependent conductivity and Seebeck coefficient of the molecularly doped unaligned and aligned PBTTT films, it should be noted that the amount of residual molecular dopant anions ($FeCl_4^-$) in the PBTTT films has been found to be negligible ($< 10^{19}$ cm^{-3} from UV-Vis absorption and X-ray photoemission spectroscopy) and that the lower bound of the charge density of the doped films has been found to be approximately $5.4 \pm 0.5 \cdot 10^{20}$ cm^{-3} from UV-Vis spectroscopy (Jacobs *et al.*, manuscript in preparation (2020)). Furthermore, the doping process does not perturb the structural order of the PBTTT films, while an increase of the lamellar stacking distance is observed due to incorporation of the ionic liquid anions ($TFSI^-$) into the voids of the PBTTT lamellar stacks (based on GIWAXS measurements, Jacobs *et al.*, manuscript in preparation (2020)).[42,293] Furthermore, the charge density in the PBTTT active layer of the multifunctional devices employed for the characterization of charge and thermoelectric transport (sections 3.2.3 and 3.3.1) could be tuned via the doping concentration, which will be briefly discussed at the end of the following section.

6.3 Temperature-dependent charge and thermoelectric transport

Based on the optical and structural characterization the ion-exchange-doped PBTTT films display a suitable system to study the impact of polymer chain alignment on charge and thermoelectric transport in the high charge density limit, with the carrier density on the order of the monomer density (approximately $8.9 \cdot 10^{20}$ cm^{-3} for PBTTT films).[54] Ongoing investigations of the temperature dependence of the electrical conductivity and Seebeck coefficient of these systems in the temperature range of 200-300 K employing

the multifunctional device architecture and measurement routines developed in this thesis (sections 3.2.3 and 3.3.1) are presented. These results are put into context with measurements based on the established device architecture and measurement routines performed by Chen Chen, PhD student in Prof. Henning Sirringhaus's group, in the temperature range of 10-300 K at different doping densities.

The four-point-probe (4pp) electrical conductivity (σ_{4pp}) of the annealed unaligned and aligned PBTTT films doped via the BMP-TFSI-$FeCl_3$-based ion-exchange doping process to the highest doping level is shown in Fig. 6.4. As outlined in the previous

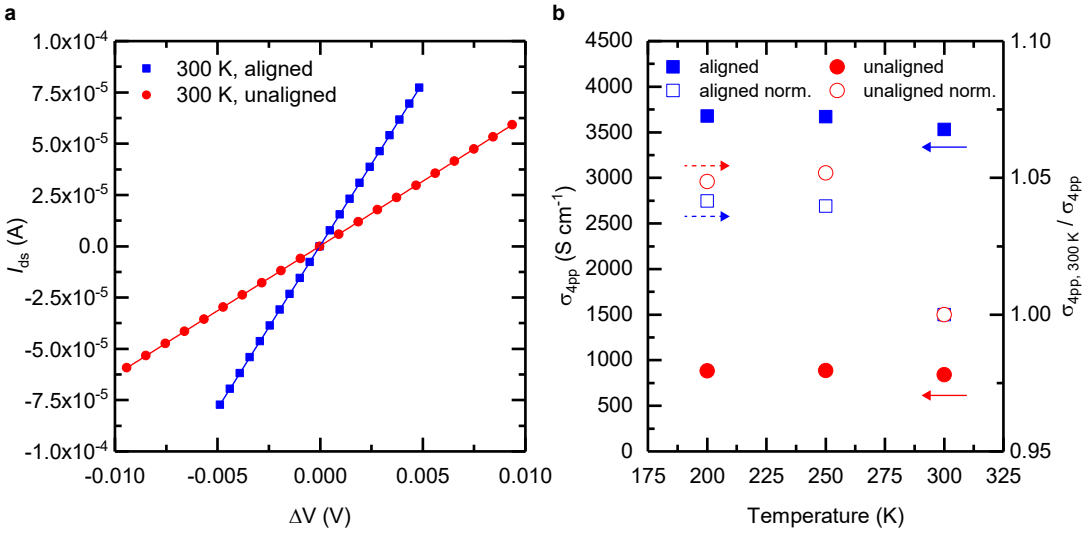

Figure 6.4. Temperature-dependent conductivity of molecularly doped unaligned and aligned PBTTT films. *I-V* scans of the molecularly doped unaligned and aligned annealed PBTTT films at 300 K (a) to extract the 4pp conductivity (σ_{4pp}) as well as the temperature-dependent 4pp conductivities (b) are shown. The conductivity increases notably upon alignment (approximately by a factor of 4.2 at 300 K). Within the temperature range investigated here, the conductivity is nearly temperature independent, slightly increasing with decreasing temperature as evident from the normalized conductivities ($\sigma_{4pp}/\sigma_{4pp,\,300\,K}$) corresponding to the right *y*-axis in panel (b).

section the lower bound of the charge density in these films has been estimated from UV-Vis absorption spectroscopy to be approximately $5.4\pm0.5\cdot10^{20}$ cm^{-3} and is therefore comparable to the monomer density. The 4pp conductivity has been obtained from *I-V* scans according to Eq. 3.2 (section 3.3.1), with $h = 60$ nm and $h = 100$ nm for the film thickness of the aligned and unaligned films from atomic force microscopy respectively and $\Delta V = V_{P1} - V_{P2}$ the measured potential between the two longitudinal Hall bar voltage probes. A notable increase of the conductivity at 300 K from around 842 S cm^{-1} to 3531 S cm^{-1} by a factor of ~ 4.2 is observed upon alignment. While the conductivity for the unaligned PBTTT film is high compared to a conductivity

of 620 S cm^{-1} presented by Yamashita *et al.* for a Li-TFSI-F4TCNQ-based ion-exchange doping process,[42] the obtained conductivities are orders of magnitude lower than those reported by Vijayakumar *et al.* for $FeCl_3$-doped aligned PBTTT-C_{12} films with conductivities of approximately $2 \cdot 10^5$ S cm^{-1} and $2.1 \cdot 10^3$ S cm^{-1} parallel and perpendicular to the alignment direction respectively.[254] Since the dichroic ratio from polarized UV-Vis absorption measurements of the annealed and aligned PBTTT films reported here is almost twice as large as those reported by Vijayakumar *et al.* (26.9 versus approx. 13), the origin of this substantial performance difference is currently under investigation. Polarized UV-Vis absorption as well as GIWAXS measurements of the aligned and molecularly doped films are necessary. However, considering that the microstructure of unaligned PBTTT films doped via the ion-exchange doping process has not been perturbed (apart from the commonly observed increased lamellar stacking distance, Jacobs *et al.*, manuscript in preparation (2020)), a substantial change of the structural order parameter from both polarized UV-Vis and GIWAXS measurements is not expected. Within the temperature range investigated here (200-300 K), the conductivity of both molecularly doped aligned and unaligned PBTTT films is nearly temperature independent, slightly increasing with decreasing temperature as evident from the normalized conductivities ($\sigma_{4pp}/\sigma_{4pp,\,300\,K}$, Fig. 6.4b). This qualitative temperature dependence of the conductivity has been observed for several highly doped conducting polymers such as polyacetylene, polyaniline and recently Li-TFSI-F4TCNQ ion-exchange doped PBTTT.[42,308,309] It has typically been found that the local conductivity maximum shifts to lower temperatures and eventually diminishes as the conductivity of the films increases, in line with the presented conductivities.[308,309] This is further supported by the observation that while an absolute maximum in the conductivity within 200 K and 300 K is found for all ion-exchange doped films presented by Yamashita *et al.* (maximum conductivity of 620 S cm^{-1}),[42] particularly the aligned and doped PBTTT films presented here do not show a distinguishable local conductivity maximum in this temperature range.

The Seebeck coefficient ($S = \frac{V_{th}}{\Delta T}$) of the annealed unaligned and aligned, molecularly doped PBTTT films has been measured as discussed in sections 3.2.3 and 3.3.1. The improved device design allowed for high measurement accuracy and precision with relative errors in the Seebeck coefficient as low as 2 % (see also section 3.3.2). Employing the calibration of the sensor resistance thermometers, the Seebeck coefficients have been obtained from linear regression fits of the thermal voltage versus temperature difference, representatively shown for the PBTTT films at 300 K in Fig. 6.5a. The temperature dependence of the Seebeck coefficients and power factors ($PF = S \cdot \sigma^2$) of the molecularly

doped PBTTT films are presented in Fig. 6.5b, c. The Seebeck coefficient increases upon

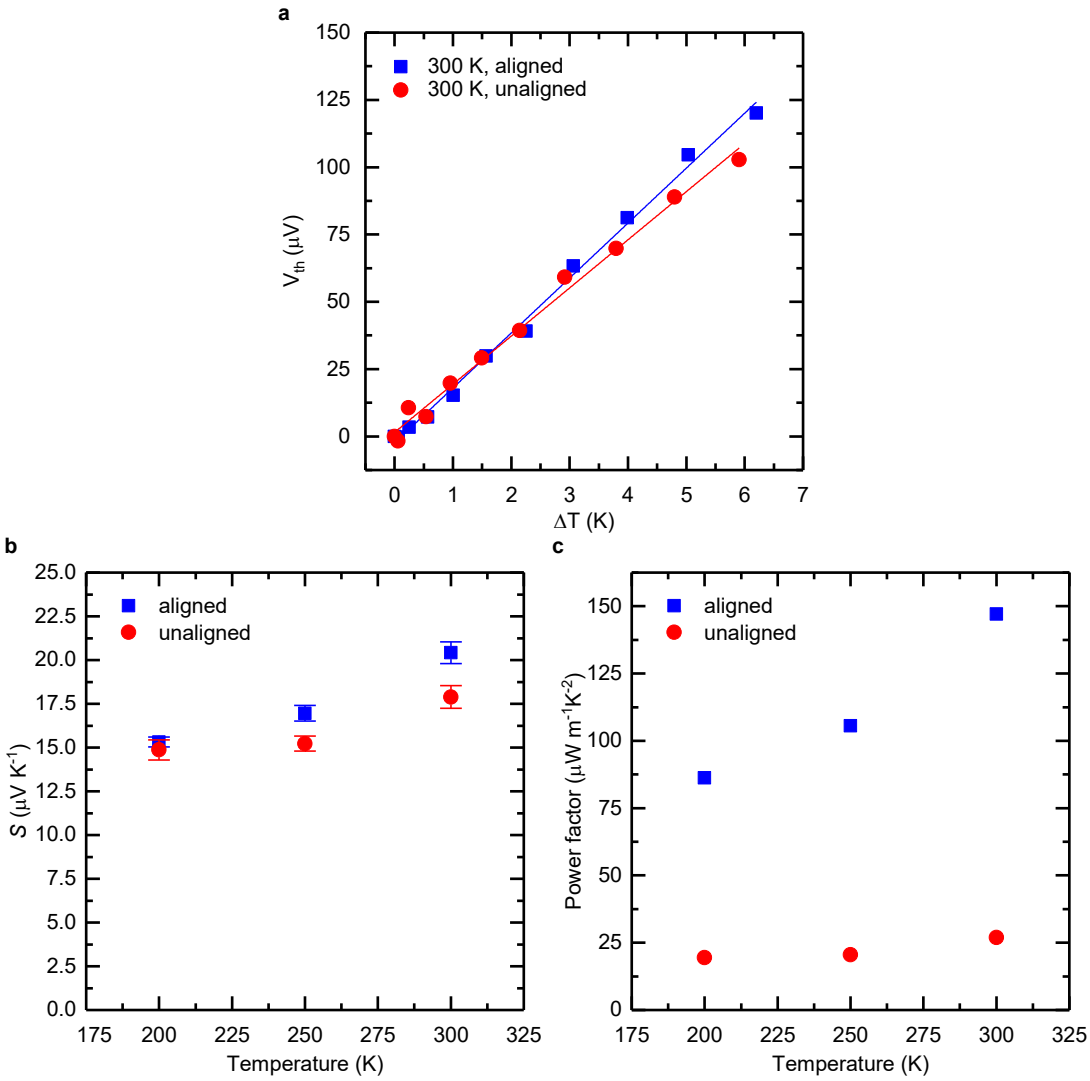

Figure 6.5. Temperature-dependent Seebeck coefficient and power factor of molecularly doped unaligned and aligned PBTTT films. The extraction of the Seebeck coefficient from the slope of the measured thermal voltages (V_{th}) versus temperature differences ΔT of the molecularly doped unaligned and aligned annealed PBTTT films at 300 K (a) as well as their temperature-dependent Seebeck coefficients (b) and power factors ($PF = \sigma \cdot S^2$, (c)) are shown. The voltage offset of the remote pre-amplifier of the Keithley K6430 has been subtracted in panel (a). The error bars shown in panel (b) are the relative errors in the Seebeck coefficient (~ 2 %) as determined in section 3.3.2. The Seebeck coefficient increases approximately by a factor of 1.1 at 300 K upon alignment. The Seebeck coefficient increases with increasing temperature and dominates the temperature dependence of the power factor, which increases substantially upon alignment (approximately by a factor of 5.5 at 300 K).

alignment (approximately by a factor of 1.1 at 300 K) and due to the high charge density

with the Fermi-level (E_F) deep inside the DoS distribution, it shows small magnitudes on the order of 20 μV K^{-1}, much smaller than $\frac{k_B}{e} \sim 86$ μV K^{-1}. While in non-degenerate semiconductors Seebeck coefficients are usually several times $\frac{k_B}{e}$ in magnitude, such low Seebeck coefficients observed here are characteristic for degenerate semiconductors.[211] The Seebeck coefficient increases with increasing temperature, while based on the temperature range investigated here (further measurements are necessary), it does not linearly extrapolate to zero for zero temperature. This is in contrast to recently reported temperature-dependent Seebeck coefficients of ion-exchange-doped unaligned PBTTT films which have been described by Mott's formula (Eq. 2.30 in section 2.3).[302] However, further measurements down to at least 50 K are necessary to establish its precise temperature dependence. The power factor increases substantially upon alignment (approximately by a factor of 5.5 at 300 K) and its temperature dependence is dominated by that of the Seebeck coefficient and therefore it also increases with increasing temperature. With a power factor of nearly 150 μW m^{-1} K^{-2} at 300 K for the aligned PBTTT films, the presented thermoelectric performance is amongst the highest reported for PBTTT (except the recently presented 2 mW m^{-1} K^{-2} for $FeCl_3$-doped aligned PBTTT by Vijayakumar *et al.*).[41,42,254,293,296]

In order to contextualize the presented conductivities and Seebeck coefficients, Fig. 6.6 shows measurements by Chen Chen, PhD student in Prof. Sirrringhaus's group, of the temperature-dependent conductivity and Seebeck coefficient of unaligned PBTTT films molecularly doped via the presented BMP-TFSI-$FeCl_3$-based ion-exchange doping process, with varied doping levels (d1-d7) respectively charge densities by tuning the doping solution concentrations, using the device design and measurement routines developed in this thesis. The seven doping levels (d1-d7) lead to conductivities at 300 K in the range from $0.7 - 779.2$ S cm^{-1}, with significantly different temperature dependences, while transitioning from a non-degenerate to a degenerate transport regime.[43] The unaligned PBTTT film with the highest doping level (d7, Fig. 6.6) is comparable to the unaligned PBTTT film presented in Figs. 6.4 and 6.5. The trends in the temperature dependence of the conductivity and Seebeck coefficient of molecularly doped conducting polymers have been phenomenologically described by heterogeneous transport models.[198,308] As emphasized in several sections of this thesis (e.g. sections 2.1.2 and 4.3), most conjugated polymers and in particular semicrystalline polymers display a coexistence of crystalline and amorphous domains, providing the intuition for the necessity of a heterogeneous transport model. In this model, conductive crystalline regions (subscript c) are envisioned to be in series with amorphous barrier regions in which both non-metallic (subscript n) and disordered metallic (subscript d)

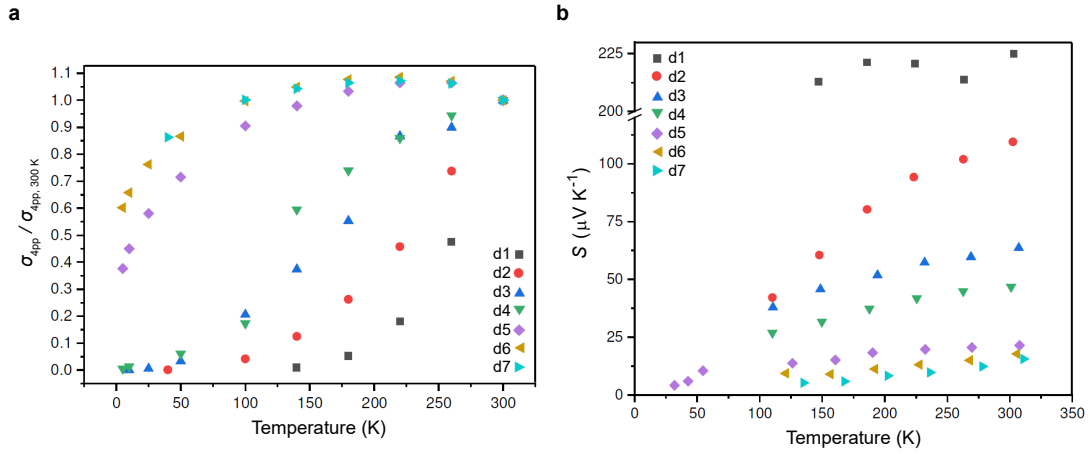

Figure 6.6. Temperature-dependent conductivity and Seebeck coefficient of molecularly doped unaligned PBTTT films. Temperature-dependent normalized 4pp conductivity ($\sigma_{4pp}/\sigma_{4pp,\,300\,K}$, (a)) and Seebeck coefficient (b) of unaligned PBTTT films molecularly doped via the presented BMP-TFSI-$FeCl_3$-based ion-exchange doping process, with varied doping levels (d1-d7) by tuning the doping solution concentrations, measured by Chen Chen using the device design and measurement routines developed in this thesis are shown. The data are presented to contextualize the presented conductivities and Seebeck coefficients in Figs. 6.4 and 6.5. The doping levels (d1-d7) correspond to the following conductivities at 300 K: $\sigma_1 \approx 0.7$ S cm^{-1}, $\sigma_2 \approx 8.2$ S cm^{-1}, $\sigma_3 \approx 49.7$ S cm^{-1}, $\sigma_4 \approx 144.6$ S cm^{-1}, $\sigma_5 \approx 405.6$ S cm^{-1}, $\sigma_6 \approx 630.8$ S cm^{-1}, $\sigma_7 \approx 779.2$ S cm^{-1}. The unaligned PBTTT film with the highest doping level (d7) is comparable to the unaligned PBTTT film shown in Figs. 6.4 and 6.5.

portions are present in parallel and the total conductivity is therefore expressed as:[308]

$$\sigma^{-1} = \rho = f_c\rho_c + \left[(f_n\rho_n)^{-1} + (f_d\rho_d)^{-1}\right]^{-1}, \tag{6.7}$$

with ρ_i the resistivity and $f_i = \frac{L_i A}{L A_i}$ the geometric factor of portion i. Here A and L denote the cross-sectional area and effective total length of the sample, while A_i and L_i are the cross-sectional area and length of portion i. The geometric factors have been assumed to be temperature independent based on the assumption that fibrillar conjugated polymers have fibers with similar properties in which the nature of the electronic states does not change with temperature.[308] For highly conducting polymers, such as those presented in Figs. 6.4 and 6.5 and the unaligned films with high doping level (d5-d7) in Fig. 6.6, it has been proposed to express the conductivity in the crystalline regions as that of a quasi-one-dimensional metal as well as the conductivity of the non-metallic disordered barrier regions by a fluctuation-induced tunneling term (see also section 5.4) and the disordered metallic portion as a constant term due to

elastic disorder scattering:[308]

$$\sigma^{-1} = f_{\mathrm{c}}\rho_{\mathrm{m}} \exp\left(-\frac{T_{\mathrm{m}}}{T}\right) + \left(\left[f_{\mathrm{n}}\rho_{\mathrm{t}} \exp\left(\frac{T_{\mathrm{B}}}{T+T_0}\right)\right]^{-1} + [f_{\mathrm{d}}\rho_{\mathrm{d}}]^{-1}\right)^{-1}. \tag{6.8}$$

Here $k_{\mathrm{B}}T_{\mathrm{m}}$ characterizes the energy of phonons that can backscatter electrons, T_{B} is the temperature for which significant thermal excitation above the tunnel barriers can occur and T_0 is the temperature for which voltage fluctuations across the tunnel barriers due to Johnson noise become relevant.[196,308] For moderately conductive polymers, such as the unaligned PBTTT films with lower doping levels (d1-d4) and conductivities, the contribution of the disordered non-metallic regions to the conductivity has instead been proposed to be modelled by a variable-range hopping term and the disordered metallic contribution has been considered to be absent, considering that the conductivity tends to zero as the temperature tends to zero:[308]

$$\sigma^{-1} = f_{\mathrm{c}}\rho_{\mathrm{m}} \exp\left(-\frac{T_{\mathrm{m}}}{T}\right) + f_{\mathrm{n}}\rho_0 \exp\left[\left(\frac{T_0}{T}\right)^{\gamma}\right]. \tag{6.9}$$

Here ρ_0, T_0 and γ are constants that describe the temperature-activated behaviour of the conductivity. The parameter γ is typically found to be in the range from $\frac{1}{4}$ to $\frac{1}{2}$, while $\frac{1}{4}$ corresponds to 3D Mott variable-range hopping (see section 2.1.1). Similarly to the conductivity, the Seebeck coefficient has been phenomenologically described as:[198]

$$S = X \cdot T + C \cdot T^{\frac{1}{2}}, \tag{6.10}$$

with X and C being constant fitting parameters due to a metallic contribution to the Seebeck coefficient characterized by Mott's formula (Eq. 2.30 in section 2.3)[164,217] and a 3D variable-range hopping contribution to the Seebeck coefficient $S = \frac{k_{\mathrm{B}}^2}{2e}(T_0 T)^{\frac{1}{2}} \cdot \left[\frac{\partial \ln N(E)}{\partial E}\right]_{E=E_{\mathrm{F}}}$, with $N(E)$ the DoS, as also discussed in section 4.5.[155,171,198,270] While the phenomenological heterogeneous transport model appears to describe the temperature dependence of the presented conductivities of unaligned and aligned molecularly doped PBTTT films (also for varying doping levels), a more detailed analysis in terms of the DoS ($g(E)$) and microscopic mobility ($\mu_{\mathrm{E}}(E)$) as introduced in Eq. 6.3 is necessary to gain further insights into the microscopic transport mechanisms.[296] However, for this more detailed analysis further measurements of the temperature-dependent conductivity and Seebeck coefficient of the aligned PBTTT films both along and perpendicular to the rubbing direction as well as with varying doping levels (similar to those presented for unaligned films in Fig. 6.6) need to be performed. Furthermore,

the charge density needs to be determined by a separate set of measurements such as electron spin resonance (ESR) measurements, a Mott-Schottky analysis or ultraviolet photoelectron spectroscopy (UPS).[296,301–304] For closed-shell anions such as $TFSI^-$ the determination of the charge density, particularly in the high charge density limit, is not trivial, since they are ESR silent.[42] While a Mott-Schottky analysis can be employed for low to moderate doping levels, for very high charge densities there will be no capacitive response and UPS measurements have been shown to be more suitable.[303,304]

6.4 Conclusions

In this chapter the foundation for detailed insights into the microscopic transport mechanisms of ion-exchange-doped, aligned PBTTT films has been presented. Both polarized UV-Vis absorption as well as GIWAXS measurements have confirmed the very high degree of alignment in the rubbed PBTTT films with structural order parameters near unity. High charge densities on the order of one carrier per monomer repeat unit have been obtained via ion-exchange doping, which is reflected by the high thermoelectric performance of the aligned PBTTT films. Conductivity, Seebeck coefficient and power factor increase significantly upon polymer chain alignment leading to a power factor of molecularly doped, aligned PBTTT of nearly 150 $\mu W\ m^{-1}\ K^{-2}$ at 300 K. A multifunctional device architecture suitable for 4pp conductivity, Hall and Seebeck coefficient measurements on the same chip has been designed. In combination with the presented measurement routine, this architecture allows highly accurate and precise measurements of the Seebeck coefficient with relative errors of approximately 2 %. The temperature dependence of the electrical conductivity and Seebeck coefficient of both unaligned and aligned, molecularly doped PBTTT films can be phenomenologically explained by a heterogeneous transport model. In order to improve upon this phenomenological description of charge and thermoelectric transport, measurements of the temperature-dependent conductivity and Seebeck coefficient of the aligned PBTTT films both along and perpendicular to the rubbing direction with varying degrees of doping are required. Furthermore, in order to disentangle the DoS and microscopic mobility function, separate measurements of the charge density induced by molecular doping are necessary. These further investigations have the potential to provide a more detailed understanding of the scattering physics and microscopic transport mechanisms in molecularly doped conjugated polymers, which can trigger further improvement of their thermoelectric performance for applications in flexible thermoelectric generators.

Chapter 7

Conclusions and outlook

The high-mobility donor-acceptor copolymers with low energetic disorder, the polymer-sorted semiconducting SWCNT networks as well as the semicrystalline molecularly doped, aligned conjugated polymers, investigated in this thesis, all have significant potential for applications in flexible electronics and thermoelectric generators for clean energy harvesting. Considering that these material systems have only recently emerged, this thesis has focused on providing an improved understanding of their charge and thermoelectric transport via studies of their charge density and temperature-dependent field-effect mobility respectively electrical conductivity as well as their Seebeck coefficient, with particular emphasis on field-effect-modulated on-chip measurements. For the purpose of these investigations several device architectures have been designed and through both the choice of electronic measurement units as well as device designs the accuracy and precision of the on-chip Seebeck coefficient measurements have been further improved, leading to relative errors as low as 2 %. Overall it has been unambiguously demonstrated that the simultaneous study of the charge density and temperature dependence of the field-effect mobility and on-chip field-effect-modulated Seebeck coefficient offers insights into the transport energetics, density of states (DoS) and transport mechanisms including the scattering physics, which cannot be obtained by a restriction to electrical and structural characterizations.

First of all this thesis has established that charge and thermoelectric transport in semicrystalline high-mobility copolymers is incompatible with disorder-based transport models. A common prediction of these models, which typically consider charge carrier hopping between localized states in a broad Gaussian DoS or thermal activation above a mobility edge, is a stronger charge density and temperature dependence of both field-effect mobility and Seebeck coefficient with increasing disorder. However, measurements of the charge density and temperature dependence of the field-effect mobility and gated Seebeck coefficient of the semicrystalline n-type polymer P(NDI2OD-T2) with varying degrees of crystallinity, show a significantly stronger charge density dependence of the mobility for the more crystalline polymer morphology as well as a

temperature-independent Seebeck coefficient between 180 K and 300 K for different degrees of crystallinity. These findings provide instead direct evidence for low-disorder, narrow-band conduction. Furthermore, both mobility and Seebeck coefficient have been explained by the inclusion of short-range electron-electron interactions as well as the consideration of a spatially inhomogeneous DoS. Within this framework the Seebeck coefficient essentially follows a modified Heikes formula for fermions (with spin) and strong on-site Coulomb interaction. The extracted thermally accessible DoS has been interpreted as the thermally accessible DoS within the crystalline domains. Considering that the mobility has been substantially increased via enhanced crystallinity while maintaining the magnitude of the Seebeck coefficient, the extension of crystalline domains provides further potential for enhancing thermoelectric conversion efficiencies. Based on these findings it would be very interesting to investigate the influence of the monomer density on the Seebeck coefficient, while ideally maintaining the polymer stacking and electronic transfer integrals. Such study could provide an improved quantitative understanding of the interrelationship between Seebeck coefficient and monomer density in conjugated polymers and should allow for enhanced thermoelectric performance via higher monomer densities. Furthermore, the impact of the extent of polaron delocalization on the change of the entropy of mixing and hence the Seebeck coefficient should be investigated. The magnitude of the Coulomb repulsion of interacting carriers in semicrystalline conjugated polymers could potentially be quantified from the temperature and charge density dependence of the Seebeck coefficient by extending the presented measurements down to at least 50 K, employing the measurement routines presented in this thesis.

The second part of this thesis has been concerned with the charge and thermoelectric transport in polymer-sorted SWCNT networks. Measurements of the charge density and temperature-dependent field-effect mobility and gated Seebeck coefficient of polymer-sorted monochiral small diameter (6,5) (0.76 nm) and mixed large diameter SWCNT (1.17-1.55 nm) networks with different network densities and length distributions have been reported. By employing Boltzmann transport formalism and incorporating transport in heterogeneous media as well as fluctuation-induced tunneling, both charge and thermoelectric transport in these SWCNT networks has been modelled. Considering the diameter-dependent one-dimensional DoS of the SWCNTs composing the network, the charge density and temperature dependence of the Seebeck coefficient can be simulated and therefore provides direct insights into the transport energetics. As opposed to one-dimensional acoustic and optical phonon scattering in single SWCNTs, the best agreement with the experimental data has been found when considering a carrier relax-

ation time that is anti-proportional to energy, pointing towards a more two-dimensional character of scattering and the potential necessity to consider scattering at SWCNT junctions. It has been presented that trap-free, narrow DoS distribution, large diameter SWCNT networks, which simultaneously display low tunnel barriers and a large thermally accessible DoS, are highly desirable for both electronic and thermoelectric applications.

Further field-effect mobility and gated Seebeck coefficient measurements of monochiral SWCNT networks with large diameters (1.0-1.6 nm) should allow discerning the optimal SWCNT diameters for both electronic and thermoelectric applications. In addition, it is inevitable to investigate the electrical conductivity and Seebeck coefficient of molecularly doped monochiral SWCNT networks with the Fermi-level close to the second van-Hove singularity to maximize their thermoelectric performance. Furthermore, it would be interesting to characterize the thermoelectric performance of large diameter (1.0-1.6 nm) monochiral armchair (n, n) SWCNT networks. Based on the presented findings, the magnitude of the Seebeck coefficient of SWCNT networks is directly related to the 1D DoS of the composing SWCNTs. Since armchair SWCNTs have particularly high peaks (van Hove singularities) in their DoS, their Seebeck coefficient and power factor should be particularly high when the Fermi-level is in the vicinity of these DoS peaks. Evidently, further measurements are necessary to scrutinize this speculation. Concomitantly further advances of the SWCNT sorting yield are necessary for the investigation of the transport coefficients of monochiral armchair as well as monochiral semiconducting SWCNT networks of different diameters.

Finally, ongoing investigations of the impact of polymer chain alignment on charge and thermoelectric transport of the molecularly doped semicrystalline polymer PBTTT have been discussed. Both polarized UV-Vis absorption as well as GIWAXS measurements have corroborated the very high degree of alignment in rubbed PBTTT films, displaying structural order parameters near unity. This effective alignment process leads to a substantial increase of conductivity, Seebeck coefficient and power factor upon polymer chain alignment. Consequently, in combination with the high charge densities on the order of one carrier per monomer repeat unit obtained by ion-exchange doping, a power factor of molecularly doped, aligned PBTTT of nearly 150 μW m^{-1} K^{-2} at 300 K has been observed. While this performance is high compared to most reports on the thermoelectric power factor of conjugated polymers, it is lower than the recently reported 2 mW m^{-1} K^{-2} at 300 K for $FeCl_3$-doped and aligned PBTTT films. This reported performance exceeds even those of unaligned polymer-sorted SWCNT networks by a factor of 2-3, urging for further polarized UV-Vis absorption and GIWAXS measurements of

the molecularly doped and aligned PBTTT films as well as conductive AFM measurements in order to investigate the origin of these performance discrepancies. However, it is worth noting that $FeCl_3$ is highly unstable as a dopant, while the presented stable ion-exchange doped PBTTT films allow more accurate measurements of the electrical conductivity and Seebeck coefficient. For a thorough investigation of the potential of conjugated polymers for thermoelectric applications, doping level respectively charge density dependent measurements of the on-chip thermal conductivity are critical. If the thermal conductivity would not be significantly higher than those typically reported in a range of 0.2 W m^{-1} K^{-1} to 0.7 W m^{-1} K^{-1} for conducting polymers, a power factor of 2 mW m^{-1} K^{-2} at 300 K would correspond to a material figure of merit zT in the range from 0.9 to 3 at 300 K. Since $zT \sim 1$ is considered to be approximately the threshold for feasible practical applications, these conducting polymer systems could potentially be very promising candidates for wearable electronics and low temperature waste heat to electricity conversion.

Further improvement of the thermoelectric performance of these material systems necessitates a microscopic understanding of their charge and thermoelectric transport. While the temperature dependence of the electrical conductivity and Seebeck coefficient of both unaligned and aligned, molecularly doped PBTTT films reported here can be phenomenologically explained by a heterogeneous transport model, this description does not allow detailed insights into the microscopic transport mechanisms. Measurements of the temperature-dependent conductivity and Seebeck coefficient of the aligned PBTTT films both along and perpendicular to the alignment direction with varying degrees of doping are needed for a more detailed understanding. In addition, separate measurements of the charge density induced by molecular doping are necessary to disentangle the DoS and microscopic mobility function, allowing to gain insights into the scattering physics and microscopic transport mechanisms.

Appendix A

Publications and presentations

Publications

[1] X. Jiao, **M. Statz**, L. Lai, S. Schott, C. Jellett, I. McCulloch, H. Sirringhaus, C. R. McNeill, Resolving different physical origins toward crystallite imperfection in semiconducting polymers: Crystallite size vs paracrystallinity. *J. Phys. Chem. B* **124,** 10529-10538 (2020).

[2] **M. Statz**, S. Schneider, F. J. Berger, L. Lai, W. A. Wood, M. Abdi-Jalebi, S. Leingang, H.-J. Himmel, J. Zaumseil and H. Sirringhaus, Charge and thermoelectric transport in polymer-sorted semiconducting single-walled carbon nanotube networks. *ACS Nano* **14,** 15552-15565 (2020).

[3] M. Xiao, B. Kang, S. B. Lee, L. M. Perdigão, A. Luci, D. A. Warr, S. P. Senanayak, M. Nikolka, **M. Statz**, Y. Wu, A. Sadhanala, S. Schott, R. Carey, Q. Wang, M. Lee, C. Kim, A. Onwubiko, C. Jellett, H. Liao, W. Yue, K. Cho, G. Costantini, I. McCulloch and H. Sirringhaus, Anisotropy of charge transport in a uniaxially aligned fused electron-deficient polymer processed by solution shear coating. *Adv. Mater.* **32,** 2000063 (2020).

[4] **M. Statz**, D. Venkateshvaran, X. Jiao, S. Schott, C. R. McNeill, D. Emin, H. Sirringhaus and R. Di Pietro, On the manifestation of electron-electron interactions in the thermoelectric response of semicrystalline conjugated polymers with low energetic disorder. *Commun. Phys.* **1,** 16 (2018).

[5] K. Broch, D. Venkateshvaran, V. Lemaur, Y. Olivier, D. Beljonne, M. Zelazny, I. Nasrallah, D. J. Harkin, **M. Statz**, R. Di Pietro, A. J. Kronemeijer and H. Sirringhaus, Measurements of ambipolar Seebeck coefficients in high-mobility diketopyrrolopyrrole donor-acceptor copolymers. *Adv. Electron. Mater.* **3,** 1700225 (2017).

Presentations

Oral presentations

[1] Virtual MRS Spring/Fall Meeting & Exhibit (2020)
M. Statz, S. Schneider, F. J. Berger, L. Lai, W. A. Wood, M. Abdi-Jalebi, S. Leingang, H.-J. Himmel, J. Zaumseil and H. Sirringhaus. Temperature-dependent thermoelectric transport in polymer-sorted semiconducting carbon nanotube networks with different diameter distributions.

[2] APS March Meeting, Denver (2020, cancelled due to Covid-19)
M. Statz, S. Schneider, F. J. Berger, L. Lai, W. A. Wood, M. Abdi-Jalebi, S. Leingang, H.-J. Himmel, J. Zaumseil and H. Sirringhaus. Temperature-dependent thermoelectric transport in polymer-sorted semiconducting carbon nanotube networks with different diameter distributions.

[3] International Conference on Organic and Hybrid Thermoelectrics, Valencia (2018)
M. Statz, D. Venkateshvaran, H. Sirringhaus, and R. Di Pietro. On the manifestation of electron-electron interactions in the thermoelectric response of semicrystalline conjugated polymers with low energetic disorder. (Invited speaker)

[4] Centre for Advanced Materials for Integrated Energy Systems (CAM-IES) - Symposium: Interfaces in Photovoltaics and Thermoelectrics, Cambridge (2017)
M. Statz, D. Venkateshvaran, M. Nikolka, K. Kang, K. Broch, L. Lai, F. J. Berger, A. Y. Lin, J. Zaumseil, D. Emin, R. Di Pietro and H. Sirringhaus. Thermoelectric transport measurements of conjugated polymers and CNT:polymer blends. (Invited speaker)

[5] CAM-IES - Autumn Symposium, London (2017)
M. Statz, L. Lai, F. J. Berger, A. Y. Lin, K. Kang, M. Nikolka, J. Zaumseil and H. Sirringhaus. Thermoelectric transport measurements in carbon nanotube:polymer blends.

Poster presentations

[1] Cambridge-LMU Strategic Partnership Workshop - Emerging Hybrid 2D Materials: shaping opportunities from quantum engineering to energy applications, Munich (2019)
M. Statz, S. Schneider, F. J. Berger, L. Lai, W. A. Wood, D. Venkateshvaran, X. Jiao, S. Schott, C. R. McNeill, D. Emin, J. Zaumseil, R. Di Pietro and H. Sirringhaus. Thermoelectric transport in semicrystalline conjugated polymers and single-walled carbon nanotube networks.

[2] Gordon Research Conference (GRC & GRS) - Electronic Processes in Organic Materials, Lucca (2018)
M. Statz, D. Venkateshvaran, X. Jiao, S. Schott, C. R. McNeill, D. Emin, H. Sirringhaus and R. Di Pietro. On the manifestation of electron-electron interactions in the thermoelectric response of semicrystalline conjugated polymers with low energetic disorder.

[3] MRS Fall Meeting & Exhibit, Boston (2017)
M. Statz, D. Venkateshvaran, H. Sirringhaus, and R. Di Pietro. Evidence of low disorder, correlated electron transport regime in the thermoelectric response of semicrystalline polymer semiconductors.

[4] CAM-IES May Workshop, Cambridge (2017)
M. Statz, K. Kang, D. Venkateshvaran, K. Broch, C. N. Warwick, R. Di Pietro, M. Nikolka and H. Sirringhaus. Thermoelectrics in organic semiconductors.

References

1. Chiang, C. K. *et al.* Electrical conductivity in doped polyacetylene. *Phys. Rev. Lett.* **39,** 1098–1101 (1977) (cit. on p. 1).
2. Tang, C. W. & Vanslyke, S. A. Organic electroluminescent diodes. *Appl. Phys. Lett.* **51,** 913–915 (1987) (cit. on p. 1).
3. Burroughes, J. H. *et al.* Light-emitting diodes based on conjugated polymers. *Nature* **347,** 539–541 (1990) (cit. on p. 1).
4. Iijima, S. Helical microtubules of graphitic carbon. *Nature* **354,** 56–58 (1991) (cit. on p. 1).
5. Saito, R., Fujita, M., Dresselhaus, G. & Dresselhaus, M. S. Electronic structure of chiral graphene tubules. *Appl. Phys. Lett.* **60,** 2204–2206 (1992) (cit. on pp. 1, 14).
6. Iijima, S. & Ichihashi, T. Single-shell carbon nanotubes of 1-nm diameter. *Nature* **363,** 603–605 (1993) (cit. on p. 1).
7. Tsumura, A., Koezuka, H. & Ando, T. Macromolecular electronic device: Field-effect transistor with a polythiophene thin film. *Appl. Phys. Lett.* **49,** 1210–1212 (1986) (cit. on pp. 1, 10).
8. Fratini, S., Nikolka, M., Salleo, A., Schweicher, G. & Sirringhaus, H. Charge transport in high-mobility conjugated polymers and molecular semiconductors. *Nat. Mater.* **19,** 491–502 (2020) (cit. on pp. 1, 2, 9, 29, 31, 36–38).
9. Tans, S. J., Verschueren, A. R. & Dekker, C. Room-temperature transistor based on a single carbon nanotube. *Nature* **393,** 49–52 (1998) (cit. on p. 1).
10. Peng, L. M., Zhang, Z. & Wang, S. Carbon nanotube electronics: Recent advances. *Mater. Today* **17,** 433–442 (2014) (cit. on pp. 1, 2).

11. Zaumseil, J. Semiconducting single-walled carbon nanotubes or very rigid conjugated polymers: A comparison. *Adv. Electron. Mater.* **5,** 1800514 (2019) (cit. on pp. 1–3, 41–43, 117).

12. Sirringhaus, H. 25th anniversary article: Organic field-effect transistors: The path beyond amorphous silicon. *Adv. Mater.* **26,** 1319–1335 (2014) (cit. on pp. 1, 23, 86).

13. Takeda, Y. *et al.* Fabrication of ultra-thin printed organic TFT CMOS logic circuits optimized for low-voltage wearable sensor applications. *Sci. Rep.* **6,** 25714 (2016) (cit. on pp. 1, 2).

14. Perinot, A., Kshirsagar, P., Malvindi, M. A., Pompa, P. P., Fiammengo, R. & Caironi, M. Direct-written polymer field-effect transistors operating at 20 MHz. *Sci. Rep.* **6,** 38941 (2016) (cit. on p. 1).

15. Yang, Y., Ding, L., Han, J., Zhang, Z. & Peng, L. M. High-performance complementary transistors and medium-scale integrated circuits based on carbon nanotube thin films. *ACS Nano* **11,** 4124–4132 (2017) (cit. on pp. 2, 3, 117).

16. Nikolka, M. *et al.* High operational and environmental stability of high-mobility conjugated polymer field-effect transistors through the use of molecular additives. *Nat. Mater.* **16,** 356–362 (2017) (cit. on p. 2).

17. Javey, A., Guo, J., Wang, Q., Lundstrom, M. & Dai, H. Ballistic carbon nanotube field-effect transistors. *Nature* **424,** 654–657 (2003) (cit. on pp. 2, 40).

18. Javey, A. *et al.* High-field quasiballistic transport in short carbon nanotubes. *Phys. Rev. Lett.* **92,** 106804 (2004) (cit. on pp. 2, 40, 41, 56).

19. Javey, A. *et al.* Self-aligned ballistic molecular transistors and electrically parallel nanotube arrays. *Nano Lett.* **4,** 1319–1322 (2004) (cit. on p. 2).

20. Shulaker, M. M. *et al.* Carbon nanotube computer. *Nature* **501,** 526–530 (2013) (cit. on p. 2).

21. Zhong, D. *et al.* Gigahertz integrated circuits based on carbon nanotube films. *Nat. Electron.* **1,** 40–45 (2018) (cit. on pp. 3, 117).

22. Schroeder, V., Savagatrup, S., He, M., Lin, S. & Swager, T. M. Carbon nanotube chemical sensors. *Chem. Rev.* **119,** 599–663 (2019) (cit. on p. 3).

23. Russ, B., Glaudell, A., Urban, J. J., Chabinyc, M. L. & Segalman, R. A. Organic thermoelectric materials for energy harvesting and temperature control. *Nat. Rev. Mater.* **1,** 16050 (2016) (cit. on pp. 3, 6, 110, 147, 148).

24. Blackburn, J. L., Ferguson, A. J., Cho, C. & Grunlan, J. C. Carbon-nanotube-based thermoelectric materials and devices. *Adv. Mater.* **30,** 1704386 (2018) (cit. on pp. 3, 4, 6, 55, 56, 117, 144, 147).

25. Snyder, G. J. & Toberer, E. S. Complex thermoelectric materials. *Nat. Mater.* **7,** 105–114 (2008) (cit. on pp. 3–5, 144).

26. Urban, J. J. Prospects for thermoelectricity in quantum dot hybrid arrays. *Nat. Nanotechnol.* **10,** 997–1001 (2015) (cit. on p. 4).

27. Tian, Z., Lee, S. & Chen, G. A comprehensive review of heat transfer in thermoelectric materials and devices. *arXiv:1401.0749 [cond-mat.mtrl-sci]* (2014) (cit. on pp. 3, 4).

28. He, J. & Tritt, T. M. Advances in thermoelectric materials research: Looking back and moving forward. *Science* **357,** 1369–1377 (2017) (cit. on pp. 4–6).

29. Crossno, J. *et al.* Observation of the Dirac fluid and the breakdown of the Wiedemann-Franz law in graphene. *Science* **351,** 1058–1061 (2016) (cit. on p. 5).

30. Venkatasubramanian, R., Siivola, E., Colpitts, T. & O'Quinn, B. Thin-film thermoelectric devices with high room-temperature figures of merit. *Nature* **413,** 597–602 (2001) (cit. on p. 5).

31. Harman, T. C., Taylor, P. J., Walsh, M. P. & LaForge, B. E. Quantum dot superlattice thermoelectric materials and devices. *Science* **297,** 2229–2232 (2002) (cit. on p. 5).

32. Hochbaum, A. I. *et al.* Enhanced thermoelectric performance of rough silicon nanowires. *Nature* **451,** 163–167 (2008) (cit. on p. 5).

33. Hicks, L. D. & Dresselhaus, M. S. Effect of quantum-well structures on the thermoelectric figure of merit. *Phys. Rev. B* **47,** 12727–12731 (1993) (cit. on p. 6).

34. Hicks, L. D. & Dresselhaus, M. S. Thermoelectric figure of merit of a one-dimensional conductor. *Phys. Rev. B* **47,** 16631–16634 (1993) (cit. on p. 6).

35. Pei, Y., Shi, X., Lalonde, A., Wang, H., Chen, L. & Snyder, G. J. Convergence of electronic bands for high performance bulk thermoelectrics. *Nature* **473,** 66–69 (2011) (cit. on p. 6).

36. Zhao, L. D. *et al.* Ultralow thermal conductivity and high thermoelectric figure of merit in SnSe crystals. *Nature* **508,** 373–377 (2014) (cit. on p. 6).

37. Xie, X., Li, D., Tsai, T. H., Liu, J., Braun, P. V. & Cahill, D. G. Thermal conductivity, heat capacity, and elastic constants of water-soluble polymers and polymer blends. *Macromolecules* **49,** 972–978 (2016) (cit. on p. 6).

38. Zevalkink, A. *et al.* A practical field guide to thermoelectrics: Fundamentals, synthesis, and characterization. *Appl. Phys. Rev.* **5,** 021303 (2018) (cit. on p. 6).

39. Kim, G. H., Shao, L., Zhang, K. & Pipe, K. P. Engineered doping of organic semiconductors for enhanced thermoelectric efficiency. *Nat. Mater.* **12,** 719–723 (2013) (cit. on p. 6).

40. Bubnova, O. *et al.* Optimization of the thermoelectric figure of merit in the conducting polymer poly(3,4-ethylenedioxythiophene). *Nat. Mater.* **10,** 429–433 (2011) (cit. on p. 6).

41. Patel, S. N. *et al.* Morphology controls the thermoelectric power factor of a doped semiconducting polymer. *Sci. Adv.* **3,** e1700434 (2017) (cit. on pp. 6, 51, 148, 160).

42. Yamashita, Y. *et al.* Efficient molecular doping of polymeric semiconductors driven by anion exchange. *Nature* **572,** 634–638 (2019) (cit. on pp. 6, 148, 155, 156, 158, 160, 163).

43. Tanaka, H. *et al.* Thermoelectric properties of a semicrystalline polymer doped beyond the insulator-to-metal transition by electrolyte gating. *Sci. Adv.* **6,** eaay8065 (2020) (cit. on pp. 6, 160).

44. Yang, C. Y. *et al.* A thermally activated and highly miscible dopant for n-type organic thermoelectrics. *Nat. Commun.* **11,** 1–10 (2020) (cit. on p. 6).

45. Pop, E., Mann, D., Wang, Q., Goodson, K. & Dai, H. Thermal conductance of an individual single-wall carbon nanotube above room temperature. *Nano Lett.* **6,** 96–100 (2006) (cit. on p. 7).

46. MacLeod, B. A. *et al.* Large n- and p-type thermoelectric power factors from doped semiconducting single-walled carbon nanotube thin films. *Energy Environ. Sci.* **10,** 2168–2179 (2017) (cit. on pp. 7, 56, 144, 149).

47. Avery, A. D. *et al.* Tailored semiconducting carbon nanotube networks with enhanced thermoelectric properties. *Nat. Energy* **1,** 1–9 (2016) (cit. on pp. 7, 55, 56, 144).

48. Köhler, A. & Bässler, H. *Electronic Processes in Organic Semiconductors.* 1st ed. (Wiley, Weinheim, 2015) (cit. on pp. 8, 9).

49. Peierls, R. *Quantum Theory of Solids.* 1st ed. (Clarendon Press, Oxford, 1955) (cit. on p. 9).

50. Su, W. P., Schrieffer, J. R. & Heeger, A. J. Solitons in polyacetylene. *Phys. Rev. Lett.* **42,** 1698–1701 (1979) (cit. on pp. 9, 31, 40).

51. Kohler, B. E. A simple model for linear polyene electronic structure. *J. Chem. Phys.* **93,** 5838–5842 (1990) (cit. on p. 9).

52. Hückel, E. Quantentheoretische Beiträge zum Benzolproblem. *Z. Phys.* **70,** 204–286 (1931) (cit. on p. 9).

53. Machida, S.-i. *et al.* Highest-occupied-molecular-orbital band dispersion of rubrene single crystals as observed by angle-resolved ultraviolet photoelectron spectroscopy. *Phys. Rev. Lett.* **104,** 156401 (2010) (cit. on p. 9).

54. Venkateshvaran, D. *et al.* Approaching disorder-free transport in high-mobility conjugated polymers. *Nature* **515,** 384–388 (2014) (cit. on pp. 9, 36, 39, 51–54, 60, 61, 66, 71, 83, 86, 87, 90, 91, 122, 124, 156).

55. Noriega, R. *et al.* A general relationship between disorder, aggregation and charge transport in conjugated polymers. *Nat. Mater.* **12,** 1038–1044 (2013) (cit. on pp. 9, 10, 38, 87).

56. Podzorov, V., Menard, E., Borissov, A., Kiryukhin, V., Rogers, J. A. & Gershenson, M. E. Intrinsic charge transport on the surface of organic semiconductors. *Phys. Rev. Lett.* **93,** 086602 (2004) (cit. on p. 9).

57. Schweicher, G., Olivier, Y., Lemaur, V. & Geerts, Y. H. What currently limits charge carrier mobility in crystals of molecular semiconductors? *Isr. J. Chem.* **54,** 595–620 (2014) (cit. on p. 9).

58. Kuei, B. & Gomez, E. D. Chain conformations and phase behavior of conjugated polymers. *Soft Matter* **13,** 49–67 (2017) (cit. on p. 9).

59. Mei, J. & Bao, Z. Side chain engineering in solution-processable conjugated polymers. *Chem. Mater.* **26,** 604–615 (2014) (cit. on p. 9).

60. Rivnay, J., Noriega, R., Northrup, J. E., Kline, R. J., Toney, M. F. & Salleo, A. Structural origin of gap states in semicrystalline polymers and the implications for charge transport. *Phys. Rev. B* **83,** 121306 (2011) (cit. on p. 9).

61. Vissenberg, M. C. & Matters, M. Theory of the field-effect mobility in amorphous organic transistors. *Phys. Rev. B* **57,** 12964–12967 (1998) (cit. on pp. 10, 26, 32–35, 52, 86, 87, 130).

62. Sirringhaus, H. *et al.* Two-dimensional charge transport in self-organized, high-mobility conjugated polymers. *Nature* **401,** 685–688 (1999) (cit. on p. 10).

63. McCulloch, I. *et al.* Liquid-crystalline semiconducting polymers with high charge-carrier mobility. *Nat. Mater.* **5,** 328–333 (2006) (cit. on pp. 10, 58).

64. Delongchamp, D. M. *et al.* Controlling the orientation of terraced nanoscale "ribbons" of a poly(thiophene) semiconductor. *ACS Nano* **3,** 780–787 (2009) (cit. on pp. 10, 58, 151).

65. Nielsen, C. B., Turbiez, M. & McCulloch, I. Recent advances in the development of semiconducting DPP-containing polymers for transistor applications. *Adv. Mater.* **25,** 1859–1880 (2013) (cit. on pp. 10, 36).

66. Zhao, Y., Guo, Y. & Liu, Y. 25th anniversary article: Recent advances in n-type and ambipolar organic field-effect transistors. *Adv. Mater.* **25,** 5372–5391 (2013) (cit. on pp. 10, 36).

67. Yi, Z., Wang, S. & Liu, Y. Design of high-mobility diketopyrrolopyrrole-based π-conjugated copolymers for organic thin-film transistors. *Adv. Mater.* **27,** 3589–3606 (2015) (cit. on pp. 10, 36, 86, 87).

68. Wang, E., Mammo, W. & Andersson, M. R. 25th anniversary article: Isoindigo-based polymers and small molecules for bulk heterojunction solar cells and field effect transistors. *Adv. Mater.* **26,** 1801–1826 (2014) (cit. on pp. 10, 36).

69. Yan, H. *et al.* A high-mobility electron-transporting polymer for printed transistors. *Nature* **457,** 679–686 (2009) (cit. on pp. 10, 36, 57, 60, 87, 90).

70. Zhang, W. *et al.* Indacenodithiophene semiconducting polymers for high-performance, air-stable transistors. *J. Am. Chem. Soc.* **132,** 11437–11439 (2010) (cit. on p. 10).

71. Zhang, X. *et al.* Molecular origin of high field-effect mobility in an indacenodithiophenebenzothiadiazole copolymer. *Nat. Commun.* **4,** 1–9 (2013) (cit. on p. 10).

72. Luzio, A., Criante, L., D'Innocenzo, V. & Caironi, M. Control of charge transport in a semiconducting copolymer by solvent-induced long-range order. *Sci. Rep.* **3,** 1–6 (2013) (cit. on pp. 10, 38).

73. Steyrleuthner, R. *et al.* The role of regioregularity, crystallinity, and chain orientation on electron transport in a high-mobility n-type copolymer. *J. Am. Chem. Soc.* **136,** 4245–4256 (2014) (cit. on pp. 10, 57, 95).

74. Schott, S. *et al.* Charge-transport anisotropy in a uniaxially aligned diketopyrrolopyrrole-based copolymer. *Adv. Mater.* **27,** 7356–7364 (2015) (cit. on pp. 10, 152, 155).

75. Yamashita, Y. *et al.* Mobility exceeding 10 $cm^2/(V{\cdot}s)$ in donor-acceptor polymer transistors with band-like charge transport. *Chem. Mater.* **28,** 420–424 (2016) (cit. on pp. 10, 38).

76. Khim, D. *et al.* Uniaxial alignment of conjugated polymer films for high-performance organic field-effect transistors. *Adv. Mater.* **30,** 1705463 (2018) (cit. on p. 10).

77. Kroto, H. W., Heath, J. R., O'Brien, S. C., Curl, R. F. & Smalley, R. E. C_{60}: Buckminsterfullerene. *Nature* **318,** 162–163 (1985) (cit. on p. 12).

78. Novoselov, K. S. *et al.* Electric field effect in atomically thin carbon films. *Science* **306,** 666–669 (2004) (cit. on p. 12).

79. Philip Wong, H. S. & Akinwande, D. *Carbon Nanotube and Graphene Device Physics.* 1st ed., 73–97, 105–117 (Cambridge University Press, Cambridge, 2010) (cit. on pp. 12, 14, 16–18, 40, 137, 139).

80. Humphrey, W., Dalke, A. & Schulten, K. VMD: Visual molecular dynamics. *J. Mol. Graph.* **14,** 33–38 (1996) (cit. on p. 13).

81. Peng, X. *et al.* Optically active single-walled carbon nanotubes. *Nat. Nanotechnol.* **2,** 361–365 (2007) (cit. on p. 13).

82. Saito, R., Fujita, M., Dresselhaus, G. & Dresselhaus, M. S. Electronic structure of graphene tubules based on C_{60}. *Phys. Rev. B* **46,** 1804–1811 (1992) (cit. on p. 14).

83. Machón, M., Reich, S., Thomsen, C., Sánchez-Portal, D. & Ordejón, P. Ab initio calculations of the optical properties of 4-Å-diameter single-walled nanotubes. *Phys. Rev. B* **66,** 1–5 (2002) (cit. on p. 14).

84. Saito, R. & Dresselhaus, G. Trigonal warping effect of carbon nanotubes. *Phys. Rev. B* **61,** 2981–2990 (2000) (cit. on pp. 14, 16–18, 118, 123, 127, 134, 136).

85. Maruyama, S. 1D DOS (van Hove singularity). `http://www.photon.t.u-tokyo.ac.jp/~maruyama/kataura/1D_DOS.html` (2002) (cit. on pp. 17, 118, 123, 134, 136).

86. Rao, A. M. *et al.* Diameter-selective Raman scattering from vibrational modes in carbon nanotubes. *Science* **275,** 187–190 (1997) (cit. on p. 17).

87. Wildöer, J. W., Venema, L. C., Rinzler, A. G., Smalley, R. E. & Dekker, C. Electronic structure of atomically resolved carbon nanotubes. *Nature* **391,** 59–62 (1998) (cit. on p. 17).

88. Kataura, H. *et al.* Optical properties of single-wall carbon nanotubes. *Synth. Met.* **103,** 2555–2558 (1999) (cit. on pp. 17–19).

89. Bachilo, S. M., Strano, M. S., Kittrell, C., Hauge, R. H., Smalley, R. E. & Weisman, R. B. Structure-assigned optical spectra of single-walled carbon nanotubes. *Science* **298,** 2361–2366 (2002) (cit. on p. 17).

90. Mintmire, J. W. & White, C. T. Universal density of states for carbon nanotubes. *Phys. Rev. Lett.* **81,** 2506–2509 (1998) (cit. on p. 18).

91. Maruyama, S. Kataura-plot for resonant Raman. `http://www.photon.t.u-tokyo.ac.jp/~maruyama/kataura/kataura.html` (2002) (cit. on pp. 18, 19).

92. Blase, X., Benedict, L. X., Shirley, E. L. & Louie, S. G. Hybridization effects and metallicity in small radius carbon nanotubes. *Phys. Rev. Lett.* **72,** 1878–1881 (1994) (cit. on p. 18).

93. Reich, S., Thomsen, C. & Ordejón, P. Electronic band structure of isolated and bundled carbon nanotubes. *Phys. Rev. B* **65,** 155411 (2002) (cit. on pp. 18, 19).

94. Weisman, R. B. & Bachilo, S. M. Dependence of optical transition energies on structure for single-walled carbon nanotubes in aqueous suspension: An empirical Kataura plot. *Nano Lett.* **3,** 1235–1238 (2003) (cit. on pp. 19, 120, 123, 137, 138, 140).

95. Maultzsch, J., Telg, H., Reich, S. & Thomsen, C. Radial breathing mode of single-walled carbon nanotubes: Optical transition energies and chiral-index assignment. *Phys. Rev. B* **72,** 205438 (2005) (cit. on pp. 19, 120).

96. Nanot, S., Hároz, E. H., Kim, J.-H., Hauge, R. H. & Kono, J. Optoelectronic properties of single-wall carbon nanotubes. *Adv. Mater.* **24,** 4977–4994 (2012) (cit. on pp. 19, 120).

97. Prasek, J. *et al.* Methods for carbon nanotubes synthesis - review. *J. Mater. Chem.* **21,** 15872–15884 (2011) (cit. on pp. 19, 20).

98. Zaumseil, J. Single-walled carbon nanotube networks for flexible and printed electronics. *Semicond. Sci. Technol.* **30,** 074001 (2015) (cit. on pp. 19–21, 23).

99. Nikolaev, P. *et al.* Gas-phase catalytic growth of single-walled carbon nanotubes from carbon monoxide. *Chem. Phys. Lett.* **313,** 91–97 (1999) (cit. on p. 20).

100. Bronikowski, M. J., Willis, P. A., Colbert, D. T., Smith, K. A. & Smalley, R. E. Gas-phase production of carbon single-walled nanotubes from carbon monoxide via the HiPco process: A parametric study. *J. Vac. Sci. Technol.* **19,** 1800–1805 (2001) (cit. on p. 20).

101. Lolli, G., Zhang, L., Balzano, L., Sakulchaicharoen, N., Tan, Y. & Resasco, D. E. Tailoring (n,m) structure of single-walled carbon nanotubes by modifying reaction conditions and the nature of the support of CoMo catalysts. *J. Phys. Chem. B* **110,** 2108–2115 (2006) (cit. on p. 20).

102. Journet, C. *et al.* Large-scale production of single-walled carbon nanotubes by the electric-arc technique. *Nature* **388,** 756–758 (1997) (cit. on p. 20).

103. Guo, T., Nikolaev, P., Thess, A., Colbert, D. T. & Smalley, R. E. Catalytic growth of single-walled nanotubes by laser vaporization. *Chem. Phys. Lett.* **243,** 49–54 (1995) (cit. on p. 20).

104. Ando, Y., Zhao, X., Hirahara, K., Suenaga, K., Bandow, S. & Iijima, S. Mass production of single-wall carbon nanotubes by the arc plasma jet method. *Chem. Phys. Lett.* **323,** 580–585 (2000) (cit. on p. 20).

105. Kim, K. S., Cota-Sanchez, G., Kingston, C. T., Imris, M., Simard, B. & Soucy, G. Large-scale production of single-walled carbon nanotubes by induction thermal plasma. *J. Phys. D. Appl. Phys.* **40,** 2375–2387 (2007) (cit. on p. 20).

106. Kim, K. S., Kingston, C. T., Ruth, D., Barnes, M. & Simard, B. Synthesis of high quality single-walled carbon nanotubes with purity enhancement and diameter control by liquid precursor Ar-H_2 plasma spraying. *Chem. Eng. J.* **250,** 331–341 (2014) (cit. on p. 20).

107. Mistry, K. S., Larsen, B. A. & Blackburn, J. L. High-yield dispersions of large-diameter semiconducting single-walled carbon nanotubes with tunable narrow chirality distributions. *ACS Nano* **7,** 2231–2239 (2013) (cit. on pp. 20, 119).

108. Hersam, M. C. Progress towards monodisperse single-walled carbon nanotubes. *Nat. Nanotechnol.* **3,** 387–394 (2008) (cit. on pp. 20, 21).

109. Wang, H. & Bao, Z. Conjugated polymer sorting of semiconducting carbon nanotubes and their electronic applications. *Nano Today* **10,** 737–758 (2015) (cit. on pp. 20, 21).

110. Yang, F., Wang, M., Zhang, D., Yang, J., Zheng, M. & Li, Y. Chirality pure carbon nanotubes: Growth, sorting, and characterization. *Chem. Rev.* **120,** 2693–2758 (2020) (cit. on pp. 20, 22).

111. Jin, S. H. *et al.* Using nanoscale thermocapillary flows to create arrays of purely semiconducting single-walled carbon nanotubes. *Nat. Nanotechnol.* **8,** 347–355 (2013) (cit. on p. 20).

112. Coleman, J. N. Liquid-phase exfoliation of nanotubes and graphene. *Adv. Funct. Mater.* **19,** 3680–3695 (2009) (cit. on p. 20).

113. Graf, A. *et al.* Large scale, selective dispersion of long single-walled carbon nanotubes with high photoluminescence quantum yield by shear force mixing. *Carbon* **105,** 593–599 (2016) (cit. on pp. 20, 58, 119, 121).

114. Zheng, M. *et al.* Structure-based carbon nanotube sorting by sequence-dependent DNA assembly. *Science* **302,** 1545–1548 (2003) (cit. on p. 21).

115. Zheng, M. *et al.* DNA-assisted dispersion and separation of carbon nanotubes. *Nat. Mater.* **2,** 338–342 (2003) (cit. on p. 21).

116. Tu, X., Manohar, S., Jagota, A. & Zheng, M. DNA sequence motifs for structure-specific recognition and separation of carbon nanotubes. *Nature* **460,** 250–253 (2009) (cit. on p. 21).

117. Ao, G., Streit, J. K., Fagan, J. A. & Zheng, M. Differentiating left- and right-handed carbon nanotubes by DNA. *J. Am. Chem. Soc.* **138,** 16677–16685 (2016) (cit. on p. 21).

118. Arnold, M. S., Green, A. A., Hulvat, J. F., Stupp, S. I. & Hersam, M. C. Sorting carbon nanotubes by electronic structure using density differentiation. *Nat. Nanotechnol.* **1,** 60–65 (2006) (cit. on pp. 21, 55, 117).

119. Liu, H., Nishide, D., Tanaka, T. & Kataura, H. Large-scale single-chirality separation of single-wall carbon nanotubes by simple gel chromatography. *Nat. Commun.* **2,** 1–8 (2011) (cit. on p. 21).

120. Nish, A., Hwang, J. Y., Doig, J. & Nicholas, R. J. Highly selective dispersion of single-walled carbon nanotubes using aromatic polymers. *Nat. Nanotechnol.* **2,** 640–646 (2007) (cit. on pp. 21, 55, 117).

121. Lee, H. W. *et al.* Selective dispersion of high purity semiconducting single-walled carbon nanotubes with regioregular poly(3-alkylthiophene)s. *Nat. Commun.* **2,** 1–8 (2011) (cit. on pp. 21, 22).

122. Jakubka, F. *et al.* Effect of polymer molecular weight and solution parameters on selective dispersion of single-walled carbon nanotubes. *ACS Macro Lett.* **1,** 815–819 (2012) (cit. on p. 22).

123. Gomulya, W. *et al.* Semiconducting single-walled carbon nanotubes on demand by polymer wrapping. *Adv. Mater.* **25,** 2948–2956 (2013) (cit. on p. 22).

124. Lei, T., Chen, X., Pitner, G., Wong, H. S. & Bao, Z. Removable and recyclable conjugated polymers for highly selective and high-yield dispersion and release of low-cost carbon nanotubes. *J. Am. Chem. Soc.* **138,** 802–805 (2016) (cit. on p. 22).

125. Ozawa, H., Ide, N., Fujigaya, T., Niidome, Y. & Nakashima, N. One-pot separation of highly enriched (6,5)-single-walled carbon nanotubes using a fluorene-based copolymer. *Chem. Lett.* **40,** 239–241 (2011) (cit. on pp. 22, 55, 119).

126. Ichinose, Y., Eda, J., Yomogida, Y., Liu, Z. & Yanagi, K. Extraction of high-purity single-chirality single-walled carbon nanotubes through precise pH control using carbon dioxide bubbling. *J. Phys. Chem. C* **121,** 13391–13395 (2017) (cit. on p. 22).

127. Zaumseil, J. & Sirringhaus, H. Electron and ambipolar transport in organic field-effect transistors. *Chem. Rev.* **107,** 1296–1323 (2007) (cit. on pp. 23, 24).

128. Horowitz, G., Hajlaoui, R., Bouchriha, H., Bourguiga, R. & Hajlaoui, M. Concept of 'threshold voltage' in organic field-effect transistors. *Adv. Mater.* **10,** 923–927 (1998) (cit. on p. 24).

129. Sze, S. M. & Ng, K. K. *Physics of Semiconductor Devices.* 3rd ed., 293–373 (Wiley, Hoboken, 2007) (cit. on p. 24).

130. Choi, H. H., Cho, K., Frisbie, C. D., Sirringhaus, H. & Podzorov, V. Critical assessment of charge mobility extraction in FETs. *Nat. Mater.* **17,** 2–7 (2018) (cit. on pp. 25, 26, 73).

131. Bittle, E. G., Basham, J. I., Jackson, T. N., Jurchescu, O. D. & Gundlach, D. J. Mobility overestimation due to gated contacts in organic field-effect transistors. *Nat. Commun.* **7,** 1–7 (2016) (cit. on p. 25).

132. Natali, D. & Caironi, M. Charge injection in solution-processed organic field-effect transistors: Physics, models and characterization methods. *Adv. Mater.* **24,** 1357–1387 (2012) (cit. on p. 26).

133. Liu, C., Xu, Y. & Noh, Y. Y. Contact engineering in organic field-effect transistors. *Mater. Today* **18,** 79–96 (2015) (cit. on p. 26).

134. Liu, C. *et al.* Device physics of contact issues for the overestimation and underestimation of carrier mobility in field-effect transistors. *Phys. Rev. Appl.* **8,** 034020 (2017) (cit. on pp. 26, 73).

135. Di Pietro, R. *et al.* Coulomb enhanced charge transport in semicrystalline polymer semiconductors. *Adv. Funct. Mater.* **26,** 8011–8022 (2016) (cit. on pp. 26, 36–39, 52, 57, 87, 91, 94, 96, 99–101, 106, 108, 130).

136. Shimotani, H. *et al.* Continuous band-filling control and one-dimensional transport in metallic and semiconducting carbon nanotube tangled films. *Adv. Funct. Mater.* **24,** 3305–3311 (2014) (cit. on pp. 26, 41, 56, 117, 128).

137. Shimizu, S. *et al.* Thermoelectric detection of multi-subband density of states in semiconducting and metallic single-walled carbon nanotubes. *Small* **12,** 3388–3392 (2016) (cit. on pp. 26, 41, 56, 117, 128, 144).

138. Di Pietro, R. *et al.* Simultaneous extraction of charge density dependent mobility and variable contact resistance from thin film transistors. *Appl. Phys. Lett.* **104,** 193501 (2014) (cit. on pp. 26, 27, 66, 73, 92, 125).

139. Fratini, S., Mayou, D. & Ciuchi, S. The transient localization scenario for charge transport in crystalline organic materials. *Adv. Funct. Mater.* **26,** 2292–2315 (2016) (cit. on pp. 29–31).

140. Coropceanu, V., Cornil, J., da Silva Filho, D. A., Olivier, Y., Silbey, R. & Brédas, J.-L. Charge transport in organic semiconductors. *Chem. Rev.* **107,** 926–952 (2007) (cit. on pp. 29–34).

141. Sirringhaus, H. Device physics of solution-processed organic field-effect transistors. *Adv. Mater.* **17,** 2411–2425 (2005) (cit. on pp. 29, 32).

142. Brédas, J.-L., Beljonne, D., Coropceanu, V. & Cornil, J. Charge-transfer and energy-transfer processes in π-conjugated oligomers and polymers: A molecular picture. *Chem. Rev.* **104,** 4971–5004 (2004) (cit. on p. 29).

143. Sirringhaus, H., Sakanoue, T. & Chang, J.-F. Charge-transport physics of high-mobility molecular semiconductors. *Phys. Status Solidi B* **249,** 1655–1676 (2012) (cit. on pp. 29–31).

144. Chang, J. F., Sirringhaus, H., Giles, M., Heeney, M. & McCulloch, I. Relative importance of polaron activation and disorder on charge transport in high-mobility conjugated polymer field-effect transistors. *Phys. Rev. B* **76,** 205204 (2007) (cit. on pp. 29, 32, 33, 53, 86, 94, 97, 98, 110).

145. Fornari, R. P., Blom, P. W. & Troisi, A. How many parameters actually affect the mobility of conjugated polymers? *Phys. Rev. Lett.* **118,** 086601 (2017) (cit. on pp. 29, 36, 37).

146. Troisi, A. Charge transport in high mobility molecular semiconductors: Classical models and new theories. *Chem. Soc. Rev.* **40,** 2347–2358 (2011) (cit. on pp. 30, 32).

147. Holstein, T. Studies of polaron motion: Part I. The molecular-crystal model. *Ann. Phys. (N. Y.)* **8,** 325–342 (1959) (cit. on p. 31).

148. Holstein, T. Studies of polaron motion: Part II. The "small" polaron. *Ann. Phys. (N. Y.)* **8,** 343–389 (1959) (cit. on p. 31).

149. Emin, D. Phonon-assisted transition rates I. Optical-phonon-assisted hopping in solids. *Adv. Phys.* **24,** 305–348 (1975) (cit. on pp. 31, 34, 53, 86).

150. Hannewald, K., Stojanović, V. M., Schellekens, J. M., Bobbert, P. A., Kresse, G. & Hafner, J. Theory of polaron bandwidth narrowing in organic molecular crystals. *Phys. Rev. B* **69,** 075211 (2004) (cit. on p. 31).

151. Fratini, S. & Ciuchi, S. Bandlike motion and mobility saturation in organic molecular semiconductors. *Phys. Rev. Lett.* **103,** 266601 (2009) (cit. on p. 31).

152. Ciuchi, S. & Fratini, S. Electronic transport and quantum localization effects in organic semiconductors. *Phys. Rev. B* **86,** 245201 (2012) (cit. on p. 31).

153. Marcus, R. A. Electron transfer reactions in chemistry. Theory and experiment. *Rev. Mod. Phys.* **65,** 599–610 (1993) (cit. on pp. 32, 86).

154. Ambegaokar, V., Halperin, B. I. & Langer, J. S. Hopping conductivity in disordered systems. *Phys. Rev. B* **4,** 2612–2620 (1971) (cit. on pp. 32, 34, 35, 87).

155. Mott, N. The mobility edge since 1967. *J. Phys. C* **20,** 3075 (1987) (cit. on pp. 32, 36, 100–102, 162).

156. Bässler, H. Charge transport in disordered organic photoconductors a Monte Carlo simulation study. *Phys. Status Solidi B* **175,** 15–56 (1993) (cit. on pp. 32–34).

157. Yu, Z. G., Smith, D. L., Saxena, A., Martin, R. L. & Bishop, A. R. Molecular geometry fluctuation model for the mobility of conjugated polymers. *Phys. Rev. Lett.* **84,** 721–724 (2000) (cit. on p. 32).

158. Arkhipov, V. I., Emelianova, E. V. & Adriaenssens, G. J. Effective transport energy versus the energy of most probable jumps in disordered hopping systems. *Phys. Rev. B* **64,** 125125 (2001) (cit. on pp. 32, 86).

159. Pasveer, W. F. *et al.* Unified description of charge-carrier mobilities in disordered semiconducting polymers. *Phys. Rev. Lett.* **94,** 206601 (2005) (cit. on pp. 32, 34, 35, 86, 87, 105).

160. Coehoorn, R., Pasveer, W. F., Bobbert, P. A. & Michels, M. A. Charge-carrier concentration dependence of the hopping mobility in organic materials with Gaussian disorder. *Phys. Rev. B* **72,** 155206 (2005) (cit. on p. 32).

161. Fishchuk, I. I., Arkhipov, V. I., Kadashchuk, A., Heremans, P. & Bässler, H. Analytic model of hopping mobility at large charge carrier concentrations in disordered organic semiconductors: Polarons versus bare charge carriers. *Phys. Rev. B* **76,** 045210 (2007) (cit. on pp. 32, 52, 86).

162. Fishchuk, I. I. *et al.* Unified description for hopping transport in organic semiconductors including both energetic disorder and polaronic contributions. *Phys. Rev. B* **88,** 125202 (2013) (cit. on pp. 32, 34).

163. Anderson, P. W. Absence of diffusion in certain random lattices. *Phys. Rev.* **109,** 1492–1505 (1958) (cit. on p. 32).

164. Mott, N. F. & Davis, E. A. *Electronic processes in non-crystalline materials.* 2nd ed., (Oxford University Press, New York, 1979) (cit. on pp. 32, 48, 86, 100, 101, 162).

165. Salleo, A. *et al.* Intrinsic hole mobility and trapping in a regioregular poly(thiophene). *Phys. Rev. B* **70,** 115311 (2004) (cit. on p. 32).

166. Novikov, S. V., Dunlap, D. H., Kenkre, V. M., Parris, P. E. & Vannikov, A. V. Essential role of correlations in governing charge transport in disordered organic materials. *Phys. Rev. Lett.* **81,** 4472–4475 (1998) (cit. on p. 33).

167. Miller, A. & Abrahams, E. Impurity conduction at low concentrations. *Phys. Rev.* **120,** 745–755 (1960) (cit. on pp. 33, 86).

168. Emin, D. Phonon-assisted jump rate in noncrystalline solids. *Phys. Rev. Lett.* **32,** 303–307 (1974) (cit. on pp. 34, 86).

169. Baranovskii, S. D. Theoretical description of charge transport in disordered organic semiconductors. *Phys. Status Solidi B* **251,** 487–525 (2014) (cit. on p. 34).

170. Kirkpatrick, S. Percolation and conduction. *Rev. Mod. Phys.* **45,** 574–588 (1973) (cit. on pp. 34, 35, 131).

171. Van Lien, N. & Toi, D. D. Coulomb correlation effects in variable-range hopping thermopower. *Phys. Lett. A* **261,** 108–113 (1999) (cit. on pp. 36, 100, 102, 162).

172. Statz, M. *et al.* On the manifestation of electron-electron interactions in the thermoelectric response of semicrystalline conjugated polymers with low energetic disorder. *Commun. Phys.* **1,** 16 (2018) (cit. on pp. 36, 37, 51, 52, 71, 85, 118, 124, 125, 127, 128, 130, 133, 134, 137).

173. Fornari, R. P. & Troisi, A. Narrower bands with better charge transport: The counterintuitive behavior of semiconducting copolymers. *Adv. Mater.* **26,** 7627–7631 (2014) (cit. on pp. 36, 37, 39).

174. Kronemeijer, A. J. *et al.* Two-dimensional carrier distribution in top-gate polymer field-effect transistors: Correlation between width of density of localized states and Urbach energy. *Adv. Mater.* **26,** 728–733 (2014) (cit. on pp. 36, 39, 52, 66, 73, 98, 100, 122, 125).

175. Tanaka, H. *et al.* Microscopic observation of efficient charge transport processes across domain boundaries in donor-acceptor-type conjugated polymers. *Commun. Phys.* **2,** 1–10 (2019) (cit. on p. 36).

176. Fornari, R. P. & Troisi, A. Theory of charge hopping along a disordered polymer chain. *Phys. Chem. Chem. Phys.* **16,** 9997–10007 (2014) (cit. on pp. 36, 39).

177. Poelking, C. *et al.* Characterization of charge-carrier transport in semicrystalline polymers: Electronic couplings, site energies, and charge-carrier dynamics in poly(bithiophene-*alt*-thienothiophene) [PBTTT]. *J. Phys. Chem. C* **117,** 1633–1640 (2013) (cit. on p. 37).

178. Liu, T. & Troisi, A. Understanding the microscopic origin of the very high charge mobility in PBTTT: Tolerance of thermal disorder. *Adv. Funct. Mater.* **24,** 925–933 (2014) (cit. on p. 37).

179. Gu, K., Snyder, C. R., Onorato, J., Luscombe, C. K., Bosse, A. W. & Loo, Y. L. Assessing the Huang-Brown description of tie chains for charge transport in conjugated polymers. *ACS Macro Lett.* **7,** 1333–1338 (2018) (cit. on p. 38).

180. Beni, G. Thermoelectric power of the narrow-band Hubbard chain at arbitrary electron density: Atomic limit. *Phys. Rev. B* **10,** 2186–2189 (1974) (cit. on pp. 38, 54, 113).

181. Chaikin, P. M. & Beni, G. Thermopower in the correlated hopping regime. *Phys. Rev. B* **13,** 647–651 (1976) (cit. on pp. 38, 53, 54, 109).

182. Li, S., Yu, Z., Rutherglen, C. & Burke, P. J. Electrical properties of 0.4 cm long single-walled carbon nanotubes. *Nano Lett.* **4,** 2003–2007 (2004) (cit. on p. 40).

183. Perebeinos, V., Tersoff, J. & Avouris, P. Electron-phonon interaction and transport in semiconducting carbon nanotubes. *Phys. Rev. Lett.* **94,** 086802 (2005) (cit. on pp. 40, 41, 117, 118, 131, 137).

184. Zhou, X., Park, J. Y., Huang, S., Liu, J. & McEuen, P. L. Band structure, phonon scattering, and the performance limit of single-walled carbon nanotube transistors. *Phys. Rev. Lett.* **95,** 146805 (2005) (cit. on pp. 40, 41, 117, 131).

185. Jiang, J. *et al.* Electron-phonon matrix elements in single-wall carbon nanotubes. *Phys. Rev. B* **72,** 235408 (2005) (cit. on pp. 40, 41).

186. Perebeinos, V., Rotkin, S. V., Petrov, A. G. & Avouris, P. The effects of substrate phonon mode scattering on transport in carbon nanotubes. *Nano Lett.* **9,** 312–316 (2009) (cit. on p. 40).

187. Yao, Z., Kane, C. L. & Dekker, C. High-field electrical transport in single-wall carbon nanotubes. *Phys. Rev. Lett.* **84,** 2941 (2000) (cit. on p. 41).

188. Kumar, S., Murthy, J. Y. & Alam, M. A. Percolating conduction in finite nanotube networks. *Phys. Rev. Lett.* **95,** 066802 (2005) (cit. on p. 41).

189. Hecht, D., Hu, L. & Grüner, G. Conductivity scaling with bundle length and diameter in single walled carbon nanotube networks. *Appl. Phys. Lett.* **89,** 133112 (2006) (cit. on p. 41).

190. Behnam, A. & Ural, A. Computational study of geometry-dependent resistivity scaling in single-walled carbon nanotube films. *Phys. Rev. B* **75,** 125432 (2007) (cit. on p. 41).

191. Hicks, J., Behnam, A. & Ural, A. Resistivity in percolation networks of one-dimensional elements with a length distribution. *Phys. Rev. E* **79,** 012102 (2009) (cit. on p. 41).

192. Topinka, M. A., Rowell, M. W., Goldhaber-Gordon, D., McGehee, M. D., Hecht, D. S. & Gruner, G. Charge transport in interpenetrating networks of semiconducting and metallic carbon nanotubes. *Nano Lett.* **9,** 1866–1871 (2009) (cit. on p. 41).

193. Fuhrer, M. S. *et al.* Crossed nanotube junctions. *Science* **288,** 494–497 (2000) (cit. on pp. 41, 43).

194. Znidarsic, A. *et al.* Spatially resolved transport properties of pristine and doped single-walled carbon nanotube networks. *J. Phys. Chem. C* **117,** 13324–13330 (2013) (cit. on pp. 41, 43, 56, 131, 132, 143).

195. Kaiser, A., Düsberg, G. & Roth, S. Heterogeneous model for conduction in carbon nanotubes. *Phys. Rev. B* **57,** 1418–1421 (1998) (cit. on pp. 42, 55).

196. Sheng, P. Fluctuation-induced tunneling conduction in disordered materials. *Phys. Rev. B* **21,** 2180–2195 (1980) (cit. on pp. 42, 117, 130, 131, 162).

197. Kim, G. *et al.* Magnetoresistance of an entangled single-wall carbon-nanotube network. *Phys. Rev. B* **58,** 16064–16069 (1998) (cit. on pp. 42, 117).

198. Kaiser, A. B. Thermoelectric power and conductivity of heterogeneous conducting polymers. *Phys. Rev. B* **40,** 2806–2813 (1989) (cit. on pp. 42, 55, 118, 130, 133, 160, 162).

199. Yanagi, K. *et al.* Transport mechanisms in metallic and semiconducting single-wall carbon nanotube networks. *ACS Nano* **4,** 4027–4032 (2010) (cit. on p. 42).

200. Rother, M., Schießl, S. P., Zakharko, Y., Gannott, F. & Zaumseil, J. Understanding charge transport in mixed networks of semiconducting carbon nanotubes. *ACS Appl. Mater. Interfaces* **8,** 5571–5579 (2016) (cit. on pp. 42, 117).

201. Chortos, A. *et al.* Universal selective dispersion of semiconducting carbon nanotubes from commercial sources using a supramolecular polymer. *ACS Nano* **11,** 5660–5669 (2017) (cit. on p. 42).

202. Schießl, S. P. *et al.* Modeling carrier density dependent charge transport in semiconducting carbon nanotube networks. *Phys. Rev. Mater.* **1,** 046003 (2017) (cit. on pp. 42, 43, 117, 128, 136).

203. Brohmann, M. *et al.* Temperature-dependent charge transport in polymer-sorted semiconducting carbon nanotube networks with different diameter distributions. *J. Phys. Chem. C* **122,** 19886–19896 (2018) (cit. on pp. 42, 43, 59, 73, 117, 119, 128, 130).

204. Brohmann, M., Berger, F. J., Matthiesen, M., Schießl, S. P., Schneider, S. & Zaumseil, J. Charge transport in mixed semiconducting carbon nanotube networks with tailored mixing ratios. *ACS Nano* **13,** 7323–7332 (2019) (cit. on pp. 42, 43, 58, 59, 130, 143, 144).

205. Zorn, N. F. *et al.* Probing mobile charge carriers in semiconducting carbon nanotube networks by charge modulation spectroscopy. *ACS Nano* **14,** 2412–2423 (2020) (cit. on pp. 42, 117).

206. Nirmalraj, P. N., Lyons, P. E., De, S., Coleman, J. N. & Boland, J. J. Electrical connectivity in single-walled carbon nanotube networks. *Nano Lett.* **9,** 3890–3895 (2009) (cit. on pp. 43, 56).

207. Kim, W., Javey, A., Vermesh, O., Wang, Q., Li, Y. & Dai, H. Hysteresis caused by water molecules in carbon nanotube field-effect transistors. *Nano Lett.* **3,** 193–198 (2003) (cit. on pp. 44, 122).

208. Aguirre, C. M. *et al.* The role of the oxygen/water redox couple in suppressing electron conduction in field-effect transistors. *Adv. Mater.* **21,** 3087–3091 (2009) (cit. on pp. 44, 122).

209. Held, M., Schießl, S. P., Miehler, D., Gannott, F. & Zaumseil, J. Polymer/metal oxide hybrid dielectrics for low voltage field-effect transistors with solution-processed, high-mobility semiconductors. *Appl. Phys. Lett.* **107,** 083301 (2015) (cit. on pp. 44, 60, 63, 124).

210. Callen, H. B. *Thermodynamics and an Introduction to Thermostatistics.* 2nd ed., 320–322 (Wiley, New York, 1985) (cit. on pp. 44, 45, 88).

211. Emin, D. *Seebeck Effect* in *Wiley Encyclopedia of Electrical and Electronics Engineering* (ed Webster, J.) 8–11 (Wiley, New York, 1999) (cit. on pp. 44, 45, 47, 48, 52, 53, 90, 160).

212. Kubo, R. Statistical-mechanical theory of irreversible processes. I. General theory and simple applications to magnetic and conduction problems. *J. Phys. Soc. Jpn.* **12,** 570–586 (1957) (cit. on pp. 44, 46).

213. Kubo, R., Yokota, M. & Nakajima, S. Statistical-mechanical theory of irreversible processes. II. Response to thermal disturbance. *J. Phys. Soc. Jpn.* **12,** 1203–1211 (1957) (cit. on pp. 44, 46, 54, 149).

214. Onsager, L. Reciprocal relations in irreversible processes. I. *Phys. Rev.* **37,** 405–426 (1931) (cit. on p. 44).

215. Onsager, L. Reciprocal relations in irreversible processes. II. *Phys. Rev.* **38,** 2265–2279 (1931) (cit. on p. 44).

216. Ashcroft, N. W. & Mermin, N. D. *Solid State Physics.* 33rd ed., 243–258 (Holt, Rinehart and Winston, New York, 1976) (cit. on pp. 46, 48, 49, 88, 137).

217. Fritzsche, H. A general expression for the thermoelectric power. *Solid State Commun.* **9,** 1813–1815 (1971) (cit. on pp. 46–48, 88, 118, 137, 162).

218. Cohen, M. H., Economou, E. N. & Soukoulis, C. M. Microscopic mobility. *Phys. Rev. B* **30,** 4493–4500 (1984) (cit. on pp. 46, 149, 150).

219. Pernstich, K. P., Rössner, B. & Batlogg, B. Field-effect-modulated Seebeck coefficient in organic semiconductors. *Nat. Mater.* **7,** 321–325 (2008) (cit. on pp. 47, 48, 51).

220. Brandt, M., Herbst, P., Angerer, H., Ambacher, O. & Stutzmann, M. Thermopower investigation of n- and p-type GaN. *Phys. Rev. B* **58,** 7786–7791 (1998) (cit. on p. 48).

221. Kang, S. D. & Snyder, G. J. Charge-transport model for conducting polymers. *Nat. Mater.* **16,** 252–257 (2017) (cit. on pp. 48, 51, 100, 101, 103, 137, 149).

222. Cutler, M. & Mott, N. F. Observation of Anderson localization in an electron gas. *Phys. Rev.* **181,** 1336–1340 (1969) (cit. on p. 48).

223. Lu, N., Li, L. & Liu, M. A review of carrier thermoelectric-transport theory in organic semiconductors. *Phys. Chem. Chem. Phys.* **18,** 19503–19525 (2016) (cit. on pp. 51, 52).

224. Germs, W. C., Guo, K., Janssen, R. A. & Kemerink, M. Unusual thermoelectric behavior indicating a hopping to bandlike transport transition in pentacene. *Phys. Rev. Lett.* **109,** 016601 (2012) (cit. on p. 51).

225. Warwick, C. N., Venkateshvaran, D. & Sirringhaus, H. Accurate on-chip measurement of the Seebeck coefficient of high mobility small molecule organic semiconductors. *APL Mater.* **3,** 096104 (2015) (cit. on p. 51).

226. Zhang, F. *et al.* Modulated thermoelectric properties of organic semiconductors using field-effect transistors. *Adv. Funct. Mater.* **25,** 3004–3012 (2015) (cit. on p. 51).

227. Broch, K. *et al.* Measurements of ambipolar Seebeck coefficients in high-mobility diketopyrrolopyrrole donor-acceptor copolymers. *Adv. Electron. Mater.* **3,** 1700225 (2017) (cit. on pp. 51, 53).

228. Arkhipov, V. I., Heremans, P., Emelianova, E. V., Adriaenssens, G. J. & Bässler, H. Charge carrier mobility in doped semiconducting polymers. *Appl. Phys. Lett.* **82,** 3245–3247 (2003) (cit. on pp. 51, 105, 118, 149).

229. Glaudell, A. M., Cochran, J. E., Patel, S. N. & Chabinyc, M. L. Impact of the doping method on conductivity and thermopower in semiconducting polythiophenes. *Adv. Energy Mater.* **5,** 1401072 (2015) (cit. on pp. 51, 100–102, 149).

230. Roichman, Y. & Tessler, N. Generalized Einstein relation for disordered semiconductors - implications for device performance. *Appl. Phys. Lett.* **80,** 1948–1950 (2002) (cit. on p. 52).

231. Schmechel, R. Hopping transport in doped organic semiconductors: A theoretical approach and its application to *p*-doped zinc-phthalocyanine. *J. Appl. Phys.* **93,** 4653–4660 (2003) (cit. on p. 52).

232. Kim, G. & Pipe, K. P. Thermoelectric model to characterize carrier transport in organic semiconductors. *Phys. Rev. B* **86,** 085208 (2012) (cit. on pp. 52, 105).

233. Mendels, D. & Tessler, N. Thermoelectricity in disordered organic semiconductors under the premise of the Gaussian disorder model and its variants. *J. Phys. Chem. Lett.* **5,** 3247–3253 (2014) (cit. on p. 52).

234. Lu, N., Li, L. & Liu, M. Universal carrier thermoelectric-transport model based on percolation theory in organic semiconductors. *Phys. Rev. B* **91,** 195205 (2015) (cit. on pp. 52, 105).

235. Heikes, R. R. & Ure, R. W. *Thermoelectricity. Science and engineering.* 1st ed., 75–82 (Interscience Publishers, New York, London, 1961) (cit. on pp. 53, 95, 98, 125, 128).

236. Emin, D. Enhanced Seebeck coefficient from carrier-induced vibrational softening. *Phys. Rev. B* **59,** 6205–6210 (1999) (cit. on p. 53).

237. Von Mühlenen, A., Errien, N., Schaer, M., Bussac, M. N. & Zuppiroli, L. Thermopower measurements on pentacene transistors. *Phys. Rev. B* **75,** 115338 (2007) (cit. on p. 53).

238. Hone, J. *et al.* Thermoelectric power of single-walled carbon nanotubes. *Phys. Rev. Lett.* **80,** 1042–1045 (1998) (cit. on pp. 55, 117).

239. Kaiser, A. B., Park, Y. W., Kim, G. T., Choi, E. S., Düsberg, G. & Roth, S. Electronic transport in carbon nanotube ropes and mats. *Synth. Met.* **103,** 2547–2550 (1999) (cit. on pp. 55, 117, 118, 133).

240. Small, J. P., Perez, K. M. & Kim, P. Modulation of thermoelectric power of individual carbon nanotubes. *Phys. Rev. Lett.* **91,** 256801 (2003) (cit. on p. 55).

241. Blackburn, J. L., Kang, S. D., Roos, M. J., Norton-Baker, B., Miller, E. M. & Ferguson, A. J. Intrinsic and extrinsically limited thermoelectric transport within semiconducting single-walled carbon nanotube networks. *Adv. Electron. Mater.* **5,** 1800910 (2019) (cit. on pp. 55, 56, 117, 132).

242. Sivan, U. & Imry, Y. Multichannel Landauer formula for thermoelectric transport with application to thermopower near the mobility edge. *Phys. Rev. B* **33,** 551–558 (1986) (cit. on p. 55).

243. Hayashi, D. *et al.* Thermoelectric properties of single-wall carbon nanotube films: Effects of diameter and wet environment. *Appl. Phys. Express* **9,** 025102 (2016) (cit. on p. 55).

244. Hayashi, D. *et al.* Thermoelectric properties of single-wall carbon nanotube networks. *Jpn. J. Appl. Phys.* **58,** 075003 (2019) (cit. on p. 55).

245. Hung, N. T., Nugraha, A. R., Hasdeo, E. H., Dresselhaus, M. S. & Saito, R. Diameter dependence of thermoelectric power of semiconducting carbon nanotubes. *Phys. Rev. B* **92,** 165426 (2015) (cit. on pp. 56, 117, 133, 137).

246. Yamamoto, T. & Fukuyama, H. Possible high thermoelectric power in semiconducting carbon nanotubes - A case study of doped one-dimensional semiconductors. *J. Phys. Soc. Jpn.* **87,** 24707 (2018) (cit. on p. 56).

247. Yamamoto, T. & Fukuyama, H. Bipolar thermoelectric effects in semiconducting carbon nanotubes: Description in terms of one-dimensional Dirac electrons. *J. Phys. Soc. Jpn.* **87,** 114710 (2018) (cit. on p. 56).

248. Chen, Z., Zheng, Y., Yan, H. & Facchetti, A. Naphthalenedicarboximide- vs perylenedicarboximide-based copolymers. Synthesis and semiconducting properties in bottom-gate n-channel organic transistors. *J. Am. Chem. Soc.* **131,** 8–9 (2009) (cit. on pp. 57, 60).

249. Peters, A., Kaifer, E. & Himmel, H.-J. 1,2,4,5-Tetrakis(tetramethylguanidino)-benzene: Synthesis and properties of a new molecular electron donor. *Eur. J. Org. Chem.* **2008,** 5907–5914 (2008) (cit. on p. 58).

250. Himmel, H. J. Guanidines as reagents in proton-coupled electron-transfer reactions and redox catalysts. *Synlett* **29,** 1957–1977 (2018) (cit. on p. 58).

251. McCulloch, I. *et al.* Semiconducting thienothiophene copolymers: Design, synthesis, morphology, and performance in thin-film organic transistors. *Adv. Mater.* **21,** 1091–1109 (2009) (cit. on p. 58).

252. Cochran, J. E. *et al.* Molecular interactions and ordering in electrically doped polymers: Blends of PBTTT and F4TCNQ. *Macromolecules* **47,** 6836–6846 (2014) (cit. on p. 58).

253. Vijayakumar, V. *et al.* Effect of alkyl side chain length on doping kinetics, thermopower, and charge transport properties in highly oriented F4TCNQ-doped PBTTT films. *ACS Appl. Mater. Interfaces* **11,** 4942–4953 (2019) (cit. on p. 58).

254. Vijayakumar, V. *et al.* Bringing conducting polymers to high order: Toward conductivities beyond 10^5 S cm^{-1} and thermoelectric power factors of 2 mW m^{-1} K^{-2}. *Adv. Energy Mater.* **9,** 1900266 (2019) (cit. on pp. 58, 148, 149, 152, 158, 160).

255. Chang, J. F., Gwinner, M. C., Caironi, M., Sakanoue, T. & Sirringhaus, H. Conjugated-polymer-based lateral heterostructures defined by high-resolution photolithography. *Adv. Funct. Mater.* **20,** 2825–2832 (2010) (cit. on pp. 60, 61, 63).

256. Veres, J., Ogier, S. D., Leeming, S. W., Cupertino, D. C. & Khaffaf, S. M. Low-k insulators as the choice of dielectrics in organic field-effect transistors. *Adv. Funct. Mater.* **13,** 199–204 (2003) (cit. on pp. 60, 87).

257. Venkateshvaran, D., Kronemeijer, A. J., Moriarty, J., Emin, D. & Sirringhaus, H. Field-effect modulated Seebeck coefficient measurements in an organic polymer using a microfabricated on-chip architecture. *APL Mater.* **2,** 032102 (2014) (cit. on pp. 60, 61, 66, 91).

258. Schießl, S. P., Rother, M., Lüttgens, J. & Zaumseil, J. Extracting the field-effect mobilities of random semiconducting single-walled carbon nanotube networks: A critical comparison of methods. *Appl. Phys. Lett.* **111,** 193301 (2017) (cit. on pp. 63, 122, 127).

259. Boukai, A. I., Bunimovich, Y., Tahir-Kheli, J., Yu, J. K., Goddard, W. A. & Heath, J. R. Silicon nanowires as efficient thermoelectric materials. *Nature* **451,** 168–171 (2008) (cit. on p. 66).

260. Isenberg, I., Russell, B. R. & Greene, R. F. Improved method for measuring Hall coefficients. *Rev. Sci. Instrum.* **19,** 685–688 (1948) (cit. on p. 77).

261. Kirby, N. M. *et al.* A low-background-intensity focusing small-angle X-ray scattering undulator beamline. *J. Appl. Crystallogr.* **46,** 1670–1680 (2013) (cit. on p. 82).

262. Ilavsky, J. Nika: Software for two-dimensional data reduction. *J. Appl. Crystallogr.* **45,** 324–328 (2012) (cit. on p. 82).

263. Jackson, W. B., Amer, N. M., Boccara, A. C. & Fournier, D. Photothermal deflection spectroscopy and detection. *Appl. Opt.* **20,** 1333–1344 (1981) (cit. on p. 83).

264. Caironi, M. *et al.* Very low degree of energetic disorder as the origin of high mobility in an n-channel polymer semiconductor. *Adv. Funct. Mater.* **21,** 3371–3381 (2011) (cit. on pp. 87, 95).

265. Steyrleuthner, R. *et al.* Aggregation in a high-mobility n-type low-bandgap copolymer with implications on semicrystalline morphology. *J. Am. Chem. Soc.* **134,** 18303–18317 (2012) (cit. on p. 87).

266. Lu, G. *et al.* Dual-characteristic transistors based on semiconducting polymer blends. *Adv. Electron. Mater.* **2,** 1600267 (2016) (cit. on p. 87).

267. Emin, D. *Polarons.* 1st ed., 125–134 (Cambridge University Press, Cambridge, 2013) (cit. on p. 90).

268. Rivnay, J. *et al.* Unconventional face-on texture and exceptional in-plane order of a high mobility n-type polymer. *Adv. Mater.* **22,** 4359–4363 (2010) (cit. on pp. 92, 93).

269. Rivnay, J. *et al.* Drastic control of texture in a high performance n-type polymeric semiconductor and implications for charge transport. *Macromolecules* **44,** 5246–5255 (2011) (cit. on pp. 92, 93).

270. Burns, M. J. & Chaikin, P. M. Interaction effects and thermoelectric power in low-temperature hopping. *J. Phys. C* **18,** L743–L749 (1985) (cit. on pp. 102, 162).

271. Emin, D. Pair breaking in semiclassical singlet small-bipolaron hopping. *Phys. Rev. B* **53,** 1260–1268 (1996) (cit. on pp. 107, 108).

272. Green, M. A. Intrinsic concentration, effective densities of states, and effective mass in silicon. *J. Appl. Phys.* **67,** 2944–2954 (1990) (cit. on p. 109).

273. Statz, M. *et al.* Charge and thermoelectric transport in polymer-sorted semiconducting single-walled carbon nanotube networks. *ACS Nano* **14,** 15552–15565 (2020) (cit. on p. 115).

274. Franklin, A. D. Nanomaterials in transistors: From high-performance to thin-film applications. *Science* **349,** aab2750 (2015) (cit. on p. 117).

275. Blackburn, J. L. Semiconducting single-walled carbon nanotubes in solar energy harvesting. *ACS Energy Lett.* **2,** 1598–1613 (2017) (cit. on p. 117).

276. Hu, L., Hecht, D. S. & Grüner, G. Percolation in transparent and conducting carbon nanotube networks. *Nano Lett.* **4,** 2513–2517 (2004) (cit. on p. 117).

277. Schneider, S. *et al.* Efficient n-doping and hole blocking in single-walled carbon nanotube transistors with 1,2,4,5-tetrakis(tetramethylguanidino)benzene. *ACS Nano* **12,** 5895–5902 (2018) (cit. on pp. 118, 122, 127, 143).

278. Guo, J. A quantum-mechanical treatment of phonon scattering in carbon nanotube transistors. *J. Appl. Phys.* **98,** 063519 (2005) (cit. on pp. 118, 137).

279. Popov, V. N. & Lambin, P. Intraband electron-phonon scattering in single-walled carbon nanotubes. *Phys. Rev. B* **74,** 075415 (2006) (cit. on pp. 118, 137).

280. Yu, H., Hermann, S., Schulz, S. E., Gessner, T., Dong, Z. & Li, W. J. Optimizing sonication parameters for dispersion of single-walled carbon nanotubes. *Chem. Phys.* **408,** 11–16 (2012) (cit. on p. 121).

281. Urbach, F. The long-wavelength edge of photographic sensitivity and of the electronic absorption of solids. *Phys. Rev.* **92,** 1324 (1953) (cit. on p. 122).

282. Blackburn, J. L. *et al.* Transparent conductive single-walled carbon nanotube networks with precisely tunable ratios of semiconducting and metallic nanotubes. *ACS Nano* **2,** 1266–1274 (2008) (cit. on p. 130).

283. Gao, J. & Loo, Y.-L. Temperature-dependent electrical transport in polymer-sorted semiconducting carbon nanotube networks. *Adv. Funct. Mater.* **25,** 105–110 (2015) (cit. on p. 130).

284. Ferguson, A. J., Reid, O. G., Nanayakkara, S. U., Ihly, R. & Blackburn, J. L. Efficiency of charge-transfer doping in organic semiconductors probed with quantitative microwave and direct-current conductance. *J. Phys. Chem. Lett.* **9,** 6864–6870 (2018) (cit. on p. 131).

285. Bernasconi, J. Electrical conductivity in disordered systems. *Phys. Rev. B* **7,** 2252–2260 (1973) (cit. on p. 131).

286. Tanaka, Y., Hirana, Y., Niidome, Y., Kato, K., Saito, S. & Nakashima, N. Experimentally determined redox potentials of individual (n, m) single-walled carbon nanotubes. *Angew. Chem. Int. Ed.* **48,** 7655–7659 (2009) (cit. on pp. 137, 140).

287. Hwang, E. H. & Das Sarma, S. Acoustic phonon scattering limited carrier mobility in two-dimensional extrinsic graphene. *Phys. Rev. B* **77,** 115449 (2008) (cit. on p. 142).

288. Kaasbjerg, K., Thygesen, K. S. & Jacobsen, K. W. Unraveling the acoustic electron-phonon interaction in graphene. *Phys. Rev. B* **85,** 165440 (2012) (cit. on p. 142).

289. Li, H. *et al.* Separation of specific single-enantiomer single-wall carbon nanotubes in the large-diameter regime. *ACS Nano* **14,** 948–963 (2020) (cit. on pp. 144, 145).

290. Pingel, P. & Neher, D. Comprehensive picture of *p*-type doping of P3HT with the molecular acceptor F4TCNQ. *Phys. Rev. B* **87,** 115209 (2013) (cit. on pp. 148, 149).

291. Salzmann, I., Heimel, G., Oehzelt, M., Winkler, S. & Koch, N. Molecular electrical doping of organic semiconductors: Fundamental mechanisms and emerging dopant design rules. *Acc. Chem. Res.* **49,** 370–378 (2016) (cit. on pp. 148, 149).

292. Jacobs, I. E. *et al.* Comparison of solution-mixed and sequentially processed P3HT:F4TCNQ films: Effect of doping-induced aggregation on film morphology. *J. Mater. Chem. C* **4,** 3454–3466 (2016) (cit. on p. 148).

293. Kang, K. *et al.* 2D coherent charge transport in highly ordered conducting polymers doped by solid state diffusion. *Nat. Mater.* **15,** 896–902 (2016) (cit. on pp. 148, 156, 160).

294. Chew, A. R., Ghosh, R., Shang, Z., Spano, F. C. & Salleo, A. Sequential doping reveals the importance of amorphous chain rigidity in charge transport of semi-crystalline polymers. *J. Phys. Chem. Lett.* **8,** 4974–4980 (2017) (cit. on p. 148).

295. Jacobs, I. E. & Moulé, A. J. Controlling molecular doping in organic semiconductors. *Adv. Mater.* **29,** 1703063 (2017) (cit. on pp. 148, 155, 156).

296. Kang, K. *et al.* Investigation of the thermoelectric response in conducting polymers doped by solid-state diffusion. *Mater. Today Phys.* **8,** 112–122 (2019) (cit. on pp. 148–150, 160, 162, 163).

297. Cho, E. *et al.* Three-dimensional packing structure and electronic properties of biaxially oriented poly(2,5-bis(3-alkylthiophene-2-yl)thieno[3,2-*b*]thiophene) films. *J. Am. Chem. Soc.* **134,** 6177–6190 (2012) (cit. on p. 148).

298. Hamidi-Sakr, A. *et al.* A versatile method to fabricate highly in-plane aligned conducting polymer films with anisotropic charge transport and thermoelectric properties: The key role of alkyl side chain layers on the doping mechanism. *Adv. Funct. Mater.* **27,** 1700173 (2017) (cit. on pp. 148, 152).

299. Thomas, E. M., Popere, B. C., Fang, H., Chabinyc, M. L. & Segalman, R. A. Role of disorder induced by doping on the thermoelectric properties of semiconducting polymers. *Chem. Mater.* **30,** 2965–2972 (2018) (cit. on pp. 149, 150).

300. Arkhipov, V. I., Heremans, P., Emelianova, E. V. & Bässler, H. Effect of doping on the density-of-states distribution and carrier hopping in disordered organic semiconductors. *Phys. Rev. B* **71,** 045214 (2005) (cit. on p. 149).

301. Fujimoto, R. *et al.* Control of molecular doping in conjugated polymers by thermal annealing. *Org. Electron.* **47,** 139–146 (2017) (cit. on pp. 150, 163).

302. Watanabe, S., Ohno, M., Yamashita, Y., Terashige, T., Okamoto, H. & Takeya, J. Validity of the Mott formula and the origin of thermopower in π-conjugated semicrystalline polymers. *Phys. Rev. B* **10,** 241201 (2019) (cit. on pp. 150, 160, 163).

303. Tietze, M. L., Burtone, L., Riede, M., Lüssem, B. & Leo, K. Fermi level shift and doping efficiency in *p*-doped small molecule organic semiconductors: A photoelectron spectroscopy and theoretical study. *Phys. Rev. B* **86,** 35320 (2012) (cit. on pp. 150, 163).

304. Tietze, M. L. *et al.* Elementary steps in electrical doping of organic semiconductors. *Nat. Commun.* **9,** 1–9 (2018) (cit. on pp. 150, 163).

305. Biniek, L., Leclerc, N., Heiser, T., Bechara, R. & Brinkmann, M. Large scale alignment and charge transport anisotropy of pBTTT films oriented by high temperature rubbing. *Macromolecules* **46,** 4014–4023 (2013) (cit. on p. 152).

306. O'Connor, B. *et al.* Anisotropic structure and charge transport in highly strain-aligned regioregular poly(3-hexylthiophene). *Adv. Funct. Mater.* **21,** 3697–3705 (2011) (cit. on pp. 152, 155).

307. Chabinyc, M. L., Toney, M. F., Kline, R. J., McCulloch, I. & Heeney, M. X-ray scattering study of thin films of poly(2,5-bis(3-alkylthiophen-2-yl) thieno[3,2-*b*]thiophene). *J. Am. Chem. Soc.* **129,** 3226–3237 (2007) (cit. on pp. 152–154).

308. Kaiser, A. B. Systematic conductivity behavior in conducting polymers: Effects of heterogeneous disorder. *Adv. Mater.* **13,** 927–941 (2001) (cit. on pp. 158, 160–162).

309. Lee, K., Cho, S., Sung, H. P., Heeger, A. J., Lee, C. W. & Lee, S. H. Metallic transport in polyaniline. *Nature* **441,** 65–68 (2006) (cit. on p. 158).